



ISSN 1605-2730  
E-ISSN 1605-8119

# **MATERIALS PHYSICS AND MECHANICS**

**Vol. 48, No. 3, 2022**

# MATERIALS PHYSICS AND MECHANICS

## Principal Editors:

**Dmitrii Indeitsev**  
*Institute of Problems of Mechanical Engineering  
of the Russian Academy of Science (RAS), Russia*

**Andrei Rudskoi**  
*Peter the Great St.Petersburg Polytechnic University, Russia*

## Founder and Honorary Editor: Ilya Ovid'ko (1961-2017)

*Institute of Problems of Mechanical Engineering  
of the Russian Academy of Sciences (RAS), Russia*

## Associate Editors:

**Anna Kolesnikova**  
*Institute of Problems of Mechanical Engineering  
of the Russian Academy of Sciences (RAS), Russia*

**Alexander Nemov**  
*Peter the Great St.Petersburg Polytechnic University, Russia*

## Editorial Board:

**E.C. Aifantis**  
*Aristotle University of Thessaloniki, Greece*

**K.E. Aifantis**  
*University of Florida, USA*

**U. Balachandran**  
*Argonne National Laboratory, USA*

**A. Bellosi**  
*Research Institute for Ceramics Technology, Italy*

**A.K. Belyaev**  
*Institute of Problems of Mechanical Engineering (RAS), Russia*

**S.V. Bobylev**  
*Institute of Problems of Mechanical Engineering (RAS), Russia*

**A.I. Borovkov**  
*Peter the Great St.Petersburg Polytechnic University, Russia*

**G.-M. Chow**  
*National University of Singapore, Singapore*

**Yu. Estrin**  
*Monash University, Australia*

**A.B. Freidin**  
*Institute of Problems of Mechanical Engineering (RAS), Russia*

**Y. Gogotsi**  
*Drexel University, USA*

**I.G. Goryacheva**  
*Institute of Problems of Mechanics (RAS), Russia*

**D. Hui**  
*University of New Orleans, USA*

**G. Kiriakidis**  
*IESL/FORTH, Greece*

**D.M. Klimov**  
*Institute of Problems of Mechanics (RAS), Russia*

**G.E. Kodzhaspirov**  
*Peter the Great St.Petersburg Polytechnic University, Russia*

**S.A. Kukushkin**  
*Institute of Problems of Mechanical Engineering (RAS), Russia*

**T.G. Langdon**  
*University of Southampton, U.K.*

**V.P. Matveenko**  
*Institute of Continuous Media Mechanics (RAS), Russia*

**A.I. Melker**  
*Peter the Great St.Petersburg Polytechnic University, Russia*

**Yu.I. Meshcheryakov**  
*Institute of Problems of Mechanical Engineering (RAS), Russia*

**N.F. Morozov**  
*St.Petersburg State University, Russia*

**R.R. Mulyukov**  
*Institute for Metals Superplasticity Problems (RAS), Russia*

**Yu.V. Petrov**  
*St.Petersburg State University, Russia*

**N.M. Pugno**  
*Politecnico di Torino, Italy*

**B.B. Rath**  
*Naval Research Laboratory, USA*

**A.E. Romanov**  
*Ioffe Physico-Technical Institute (RAS), Russia*

**A.M. Sastry**  
*University of Michigan, Ann Arbor, USA*

**B.A. Schrefler**  
*University of Padua, Italy*

**N.V. Skiba**  
*Institute of Problems of Mechanics (RAS), Russia*

**A.G. Sheinerman**  
*Institute of Problems of Mechanics (RAS), Russia*

**R.Z. Valiev**  
*Ufa State Aviation Technical University, Russia*

**K. Zhou**  
*Nanyang Technological University, Singapore*

## "Materials Physics and Mechanics" Editorial Office:

**Phone:** +7(812)552 77 78, ext. 224 **E-mail:** mpmjournal@spbstu.ru **Web-site:** <http://www.mpm.spbstu.ru>

International scientific journal "Materials Physics and Mechanics" is published by Peter the Great St.Petersburg Polytechnic University in collaboration with Institute of Problems of Mechanical Engineering of the Russian Academy of Sciences in both hard copy and electronic versions.

The journal provides an international medium for the publication of reviews and original research papers written in English and focused on the following topics:

- Mechanics of composite and nanostructured materials.
- Physics of strength and plasticity of composite and nanostructured materials.
- Mechanics of deformation and fracture processes in conventional materials (solids).
- Physics of strength and plasticity of conventional materials (solids).
- Physics and mechanics of defects in composite, nanostructured, and conventional materials.
- Mechanics and physics of materials in coupled fields.

Owner organizations: Peter the Great St. Petersburg Polytechnic University; Institute of Problems of Mechanical Engineering RAS.

*Materials Physics and Mechanics is indexed in Chemical Abstracts, Cambridge Scientific Abstracts, Web of Science Emerging Sources Citation Index (ESCI) and Elsevier Bibliographic Databases (in particular, SCOPUS).*



# **МЕХАНИКА И ФИЗИКА МАТЕРИАЛОВ**

## **Materials Physics and Mechanics**

**Том 48, номер 3, 2022 год**

Учредители:

ФГАОУ ВО «Санкт-Петербургский политехнический университет Петра Великого»  
ФГБУН «Институт проблем машиноведения Российской Академии Наук»

## Редакционная коллегия журнала

### Главные редакторы:

д.ф.-м.н., чл.-корр. РАН **Д.А. Индейцев**  
Институт проблем машиноведения Российской Академии Наук  
(РАН)

д.т.н., академик РАН **А.И. Рудской**  
Санкт-Петербургский политехнический университет  
Петра Великого

**Основатель и почетный редактор:** д.ф.-м.н. **И.А. Овидько (1961-2017)**

Институт проблем машиноведения Российской Академии Наук (РАН)

### Ответственные редакторы

д.ф.-м.н. **А.Л. Колесникова**  
Институт проблем машиноведения Российской Академии Наук  
(РАН)

к.т.н. **А.С. Немов**  
Санкт-Петербургский политехнический университет Петра  
Великого

### Международная редакционная коллегия:

д.ф.-м.н., проф. **А.К. Беляев**  
Институт проблем машиноведения РАН, Россия  
д.ф.-м.н. **С.В. Бобылев**  
Институт проблем машиноведения РАН, Россия  
к.т.н., проф. **А.И. Боровков**  
Санкт-Петербургский политехнический у-т Петра Великого, Россия  
д.ф.-м.н., проф. **Р.З. Валнев**  
Уфимский государственный технический университет, Россия  
д.ф.-м.н., академик РАН **И.Г. Горячева**  
Институт проблем механики РАН, Россия  
д.ф.-м.н., академик РАН **Д.М. Климов**  
Институт проблем механики РАН, Россия  
д.т.н., проф. **Г.Е. Коджаспиров**  
Санкт-Петербургский политехнический у-т Петра Великого, Россия  
д.ф.-м.н., проф. **С.А. Кукушкин**  
Институт проблем машиноведения РАН, Россия  
д.ф.-м.н., академик РАН **В.П. Матвеев**  
Институт механики сплошных сред РАН, Россия  
д.ф.-м.н., проф. **А.И. Мелькер**  
Санкт-Петербургский политехнический у-т Петра Великого, Россия  
д.ф.-м.н., проф. **Ю.И. Мещеряков**  
Институт проблем машиноведения РАН, Россия  
д.ф.-м.н., академик РАН **Н.Ф. Морозов**  
Санкт-Петербургский государственный университет, Россия  
д.ф.-м.н., чл.-корр. РАН **Р.Р. Мулюков**  
Институт проблем сверхпластичности металлов РАН, Россия  
д.ф.-м.н., чл.-корр. РАН **Ю.В. Петров**  
Санкт-Петербургский государственный университет, Россия  
д.ф.-м.н., проф. **А.Е. Романов**  
Физико-технический институт им. А.Ф. Иоффе РАН, Россия  
д.ф.-м.н. **Н.В. Скиба**  
Институт проблем машиноведения РАН, Россия  
д.ф.-м.н., проф. **А.Б. Фрейдин**  
Институт проблем машиноведения РАН, Россия  
д.ф.-м.н. **А.Г. Шейнман**  
Институт проблем машиноведения РАН, Россия

Prof., Dr. **E.C. Aifantis**  
Aristotle University of Thessaloniki, Greece  
Dr. **K.E. Aifantis**  
University of Florida, USA  
Dr. **U. Balachandran**  
Argonne National Laboratory, USA  
Dr. **A. Bellosi**  
Research Institute for Ceramics Technology, Italy  
Prof., Dr. **G.-M. Chow**  
National University of Singapore, Singapore  
Prof., Dr. **Yu. Estrin**  
Monash University, Australia  
Prof., Dr. **Y. Gogotsi**  
Drexel University, USA  
Prof., Dr. **D. Hui**  
University of New Orleans, USA  
Prof., Dr. **G. Kiriakidis**  
IESL/FORTH, Greece  
Prof., Dr. **T.G. Langdon**  
University of Southampton, UK  
Prof., Dr. **N.M. Pugno**  
Politecnico di Torino, Italy  
Dr. **B.B. Rath**  
Naval Research Laboratory, USA  
Prof., Dr. **A.M. Sastry**  
University of Michigan, Ann Arbor, USA  
Prof., Dr. **B.A. Schrefler**  
University of Padua, Italy  
Prof. Dr. **K. Zhou**  
Nanyang Technological University, Singapore

Тел.: +7(812)552 77 78, доб. 224 E-mail: [mpmjournal@spbstu.ru](mailto:mpmjournal@spbstu.ru) Web-site: <http://www.mpm.spbstu.ru>

### Тематика журнала

Международный научный журнал "Materials Physics and Mechanics" издается Санкт-Петербургским политехническим университетом Петра Великого в сотрудничестве с Институтом проблем машиноведения Российской Академии Наук в печатном виде и электронной форме. Журнал публикует обзорные и оригинальные научные статьи на английском языке по следующим тематикам:

- Механика композиционных и наноструктурированных материалов.
- Физика прочности и пластичности композиционных и наноструктурированных материалов.
- Механика процессов деформации и разрушения в традиционных материалах (твердых телах).
- Физика прочности и пластичности традиционных материалов (твердых тел).
- Физика и механика дефектов в композиционных, наноструктурированных и традиционных материалах.
- Механика и физика материалов в связанных полях.

Редколлегия принимает статьи, которые нигде ранее не опубликованы и не направлены для опубликования в другие научные издания. Все представляемые в редакцию журнала "Механика и физика материалов" статьи рецензируются. Статьи могут отправляться авторам на доработку. Не принятые к опубликованию статьи авторам не возвращаются.

Журнал "Механика и физика материалов" ("Materials Physics and Mechanics") включен в систему цитирования Web of Science Emerging Sources Citation Index (ESCI), SCOPUS и PИИЦ.

© 2022, Санкт-Петербургский политехнический университет Петра Великого

© 2022, Институт проблем машиноведения Российской Академии Наук

## Contents

<b>Effect of Si<sup>+</sup> ion irradiation of <math>\alpha</math>-Ga<sub>2</sub>O<sub>3</sub> epitaxial layers on their hydrogen sensitivity.....</b>	<b>301-307</b>
N.N. Yakovlev, A.V. Almaev, P.N. Butenko, A.N. Mikhaylov, A.I. Pechnikov, S.I. Stepanov, R.B. Timashov, A.V. Chikiryaka, V.I. Nikolaev	
<b>Non-equilibrium phonon gas in a chalcogenide semiconductor with exponential temperature dependence of conductivity .....</b>	<b>308-314</b>
K.D. Mynbaev, N.V. Sovtus	
<b>Optimization of powder metallurgy process parameters to enhance the mechanical properties of AZ91 magnesium alloy .....</b>	<b>315-327</b>
Naveen Kumar, Ajaya Bharti	
<b>A study on mechanical and dielectric properties of B<sub>4</sub>C and Al dispersed single-layered epoxy-based polymer composites fabricated through molding and curing route .....</b>	<b>328-341</b>
S. Vignesh, J.T. Winowlin Jappes, S. Nagaveena, K. Sankaranarayanan, R. Krishna Sharma, N.C. Brintha	
<b>Comparison of mechanical strain measurement accuracy of fiber-optic sensor and smart-layer .....</b>	<b>342-354</b>
G.S. Shipunov, M.A. Baranov, A.S. Nikiforov, F.R. Khabibrakhmanova	
<b>Deformation and mechanical stresses in a magnet with thin-walled quasi-force-free winding .....</b>	<b>355-366</b>
G.A. Shneerson, A.V. Khlybov, A.A. Belov, A.P. Nenashev, A.A. Parfentiev, S.A. Shimanskiy	
<b>Preparation and characterization of undoped and antimony doped tin oxide thin films synthesized by spray pyrolysis .....</b>	<b>367-378</b>
H. Habieb, N. Hamdadou	
<b>On the problem of evaluating the behavior of multicomponent materials in mixed boundary conditions in contact problems.....</b>	<b>379-385</b>
V.A. Babeshko, O.V. Evdokimova, O.M. Babeshko	
<b>The nanofluids' viscosity prediction through particle-media interaction layer.....</b>	<b>386-396</b>
V.V. Syzrantsev, A.T. Arymbaeva, A.P. Zavjalov, K.V. Zobov	
<b>Study numerical and experimental of stress concentration factor on isotropic plate with hole.....</b>	<b>397-406</b>
M.N. Misbah, R.C. Ariesta, T. Yulianto, D. Setyawan, W.H.A. Putra	
<b>An out-of-plane oscillating beam nanoresonator with ultrahigh intrinsic quality factor ...</b>	<b>407-418</b>
Chu Manh Hoang, Nguyen Van Duong, Dang Van Hieu	
<b>Ab initio calculations of electronic band structure of ideal and defective CdMnS .....</b>	<b>419-427</b>
Matanat A. Mehrabova, Natig T. Panahov, Niyazi H. Hasanov	
<b>Seismic behavior of heritage building with isotropic and orthotropic material properties: a comparative analysis .....</b>	<b>428-442</b>
Kamran, Shakeel Ahmad, Rehan A. Khan	

**Calculation of the stress level in modeling the inter-dislocation interaction of aluminum bronze..... 443-451**  
A.Yu. Nikonov, A.A. Bibko, D.V. Lychagin

**Influence of Ni-Al interphase boundary orientation on the interdiffusion rate at temperatures above aluminum melting point: a molecular dynamics study ..... 452-458**  
G.M. Poletaev, R.Y. Rakitin

# Effect of Si<sup>+</sup> ion irradiation of $\alpha$ -Ga<sub>2</sub>O<sub>3</sub> epitaxial layers on their hydrogen sensitivity

N.N. Yakovlev<sup>1</sup>✉, A.V. Almaev<sup>1,2</sup>, P.N. Butenko<sup>1,3</sup>, A.N. Mikhaylov<sup>4</sup>, A.I. Pechnikov<sup>3</sup>,  
S.I. Stepanov<sup>3</sup>, R.B. Timashov<sup>3</sup>, A.V. Chikiryaka<sup>3</sup>, V.I. Nikolaev<sup>3,5</sup>

<sup>1</sup>Tomsk State University, Tomsk, Russia

<sup>2</sup>Fokon LLC, Kaluga, Russia

<sup>3</sup>Ioffe Institute, Saint Petersburg, Russia

<sup>4</sup>Lobachevsky State University, Nizhny Novgorod, Russia

<sup>5</sup>Perfect Crystals LLC, Saint Petersburg, Russia

✉ [nik\\_mr\\_x@mail.ru](mailto:nik_mr_x@mail.ru)

**Abstract.** The effect of Si<sup>+</sup> ion irradiation of  $\alpha$ -Ga<sub>2</sub>O<sub>3</sub> at doses of  $8 \cdot 10^{12} \text{ cm}^{-2}$ ,  $8 \cdot 10^{14} \text{ cm}^{-2}$ , and energy of 100 keV on the gas-sensitive properties has been studied. It is shown that irradiation of  $\alpha$ -Ga<sub>2</sub>O<sub>3</sub> layer grown by halide vapor phase epitaxy with implanted Si<sup>+</sup> ions allows effective control of its sensitivity to H<sub>2</sub>, response, and recovery times, as well as varying the operating temperatures. The maximum sensitivity to H<sub>2</sub> occurred for samples with Si<sup>+</sup> ion irradiation dose of  $8 \cdot 10^{12} \text{ cm}^{-2}$  at 400°C. The mechanism of sensitivity of  $\alpha$ -Ga<sub>2</sub>O<sub>3</sub> epitaxial layers irradiated with Si<sup>+</sup> to H<sub>2</sub> is discussed.

**Keywords:**  $\alpha$ -Ga<sub>2</sub>O<sub>3</sub>, halide vapor phase epitaxy, ion implantation, gas sensitivity

**Acknowledgements.** This work was supported by the Russian Science Foundation (project № 20-79-10043).

**Citation:** Yakovlev NN, Almaev AV, Butenko PN, Mikhaylov AN, Pechnikov AI, Stepanov SI, Timashov RB, Chikiryaka AV, Nikolaev VI. Effect of Si<sup>+</sup> ion irradiation of  $\alpha$ -Ga<sub>2</sub>O<sub>3</sub> epitaxial layers on their hydrogen sensitivity. *Materials Physics and Mechanics*. 2022;48(3): 301-307. DOI: 10.18149/MPM.4832022\_1.

## 1. Introduction

Gallium oxide with a corundum-like structure ( $\alpha$ -Ga<sub>2</sub>O<sub>3</sub>) is a promising ultra-wide bandgap semiconductor. It is of interest for the development of both power diodes, field-effect transistors (FETs) [1] and solar-blind photodetectors, gas sensors [2,3]. The sensitivity of epitaxial layers of metastable  $\alpha$ - and  $\epsilon(\kappa)$ -Ga<sub>2</sub>O<sub>3</sub> to gases, including H<sub>2</sub>, depends largely on the donor's concentration ( $N_d$ ) [4]. Sn [5,6] and Si [7-10] are known to be used as donor impurities in this case. The atomic radii of Ga and Si differ by only 3.6 % [7], which provides a better embedding of Si atoms into the  $\alpha$ -Ga<sub>2</sub>O<sub>3</sub> lattice. The electron mobility ( $\mu_n$ ) of  $\alpha$ -Ga<sub>2</sub>O<sub>3</sub>:Si is higher than  $\mu_n$  ( $\alpha$ -Ga<sub>2</sub>O<sub>3</sub>:Sn) [11]. Besides, the  $\alpha$ -Ga<sub>2</sub>O<sub>3</sub> phase doped with Si, contrary to one doped with Sn, demonstrates stable electrophysical characteristics at high temperatures up to 500°C [7]. The method of donor introduction into Ga<sub>2</sub>O<sub>3</sub>, which provides

fine control of  $N_d$  and allows localized area handling, is ion implantation [10]. This paper is focused on the study of the  $\text{Si}^+$  implantation effect on the gas-sensitive properties of  $\alpha\text{-Ga}_2\text{O}_3$ .

## 2. Materials and methods

Layers of unintentionally doped (UID)  $\alpha\text{-Ga}_2\text{O}_3$ , 2  $\mu\text{m}$  thick, were deposited on sapphire substrates by halide vapor-phase epitaxy (HVPE) at 500°C. Metallic Ga, gaseous HCl, and  $\text{O}_2$  were used as precursors. Two modes of  $\alpha\text{-Ga}_2\text{O}_3$  layers irradiation with  $\text{Si}^+$  ions at the same energy  $E = 100$  keV with doses ( $D$ )  $D_1 = 8 \cdot 10^{12}$   $\text{cm}^{-2}$  and  $D_2 = 8 \cdot 10^{14}$   $\text{cm}^{-2}$  were chosen. TRIM (Transport of Ions in Matter) software was used to simulate the ion implantation process in  $\alpha\text{-Ga}_2\text{O}_3$  layers. Initial and irradiated plates were used to fabricate  $2 \times 1$   $\text{mm}^2$  samples. After that Pt contacts were deposited on their surface, resulting in the formation of planar metal-semiconductor-metal (MSM) structures on a sapphire substrate.

Rapid thermal annealing (RTA) was applied to stabilize the conductive properties of the samples, in the mode: 30 s at  $T = 400^\circ\text{C}$  in a stream of pure dry air. Measurements of current-voltage characteristics (I-V characteristics) and time dependences of the samples' current were carried out in dark conditions and in a sealed microprobe chamber equipped with an objective table with a heater. A mixture of pure dry air, obtained by an appropriate generator, and  $\text{H}_2$ , in which the gas concentration was set using a gas mixture generator, was passed through the chamber.

## 3. Results and discussion

TRIM calculations showed that the maximum values of  $\text{Si}^+$  concentration in  $\alpha\text{-Ga}_2\text{O}_3$  layers for  $D_1$  is  $9 \cdot 10^{17}$   $\text{cm}^{-3}$  and for  $D_2$  is  $9 \cdot 10^{19}$   $\text{cm}^{-3}$  corresponding to a depth ( $d$ ) of 75 nm. The concentration of defects caused by  $\text{Si}^+$  irradiation of  $\alpha\text{-Ga}_2\text{O}_3$  layers exceeds the concentration of impurity atoms by 3 orders of magnitude. The defects are concentrated mainly in the subsurface  $\alpha\text{-Ga}_2\text{O}_3$  layer, i.e., at  $d \leq 75$  nm.

The current ( $I$ ) in the studied structures at  $D = 0$  ( $D_0$ ) and  $D_1$  increases exponentially with temperature. When the dose increases up to  $D_2$ , the current of the samples weakly depends on temperature ( $T$ ). At  $T \leq 200^\circ\text{C}$   $I$  practically does not depend on  $D$ , and in high temperatures the range  $T = 250 - 400^\circ\text{C}$  it drops with  $D$  exponentially. The I-V characteristics of the samples at  $D_0$  and  $D_1$  in the voltage ( $U$ ) range  $U = 0-50$  V are approximated by the power law:  $I \propto U^l$ .  $l$  decreases from  $1.20 \pm 0.02$  to  $1.00 \pm 0.02$  with increasing  $T$  from  $25^\circ\text{C}$  to  $250^\circ\text{C}$  and  $350^\circ\text{C}$  for  $D_0$  and  $D_1$  respectively and remains constant as  $T$  increases further. When the dose rises up to  $D_2$ ,  $l = 1.5 \pm 0.1$  in the range  $T = 200-400^\circ\text{C}$ .

Exposure of the samples to  $\text{H}_2$  leads to a reversible increase in  $I$ . Figure 1 shows the temperature dependences of the response ( $S$ ) of  $\alpha\text{-Ga}_2\text{O}_3$  samples to 3 vol.%  $\text{H}_2$  at different  $D$ . The ratio  $I_g/I_0$  was taken as the response to  $\text{H}_2$ , where  $I_g$  is the current value of samples in a gas mixture of pure dry air +  $\text{H}_2$ ;  $I_0$  is the current value of samples in pure dry air. The samples at  $D_0$  exhibited a weak response to  $\text{H}_2$  in the range  $T = 100-400^\circ\text{C}$ . A significant increase in response to  $\text{H}_2$  occurred for the samples at  $D_1$ . However, the response of these samples could be registered in the range  $T = 200-400^\circ\text{C}$  only. For these samples at  $400^\circ\text{C}$ , the response to 3 vol. %  $\text{H}_2$  reached 69.3 a.u. As the dose increased up to  $D_2$ , the response of the samples dropped but was evident over the entire range  $T = 25-400^\circ\text{C}$ .

To evaluate the response rates of  $\alpha\text{-Ga}_2\text{O}_3$  samples being exposed to  $\text{H}_2$ , the response times  $t_{res}$  and recovery times  $t_{rec}$  were determined. They were chosen as the periods necessary to reach the level of  $0.9 \times I_g$  after  $\text{H}_2$  was supplied into the chamber and to reach the level of  $1.1 \times I_0$  after the start of pumping pure air through the measuring chamber, respectively.

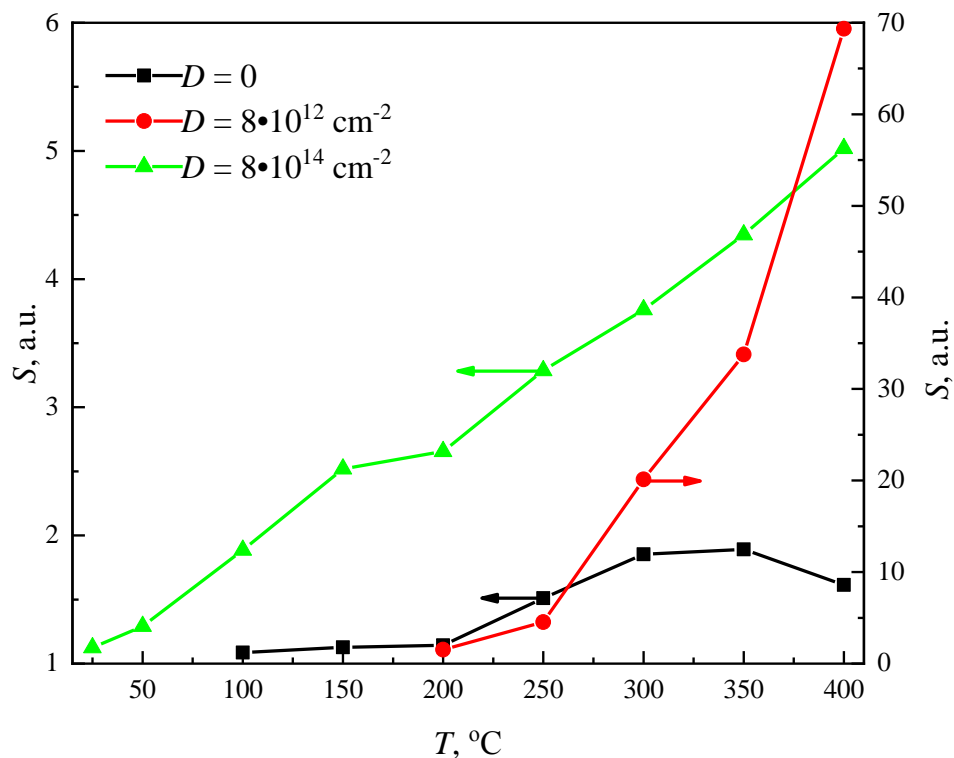


**Fig. 1.** Temperature dependences of the response ( $S$ ) of  $\alpha$ -Ga<sub>2</sub>O<sub>3</sub> samples exposed to 3 vol.% H<sub>2</sub> at different Si<sup>+</sup> irradiation doses.

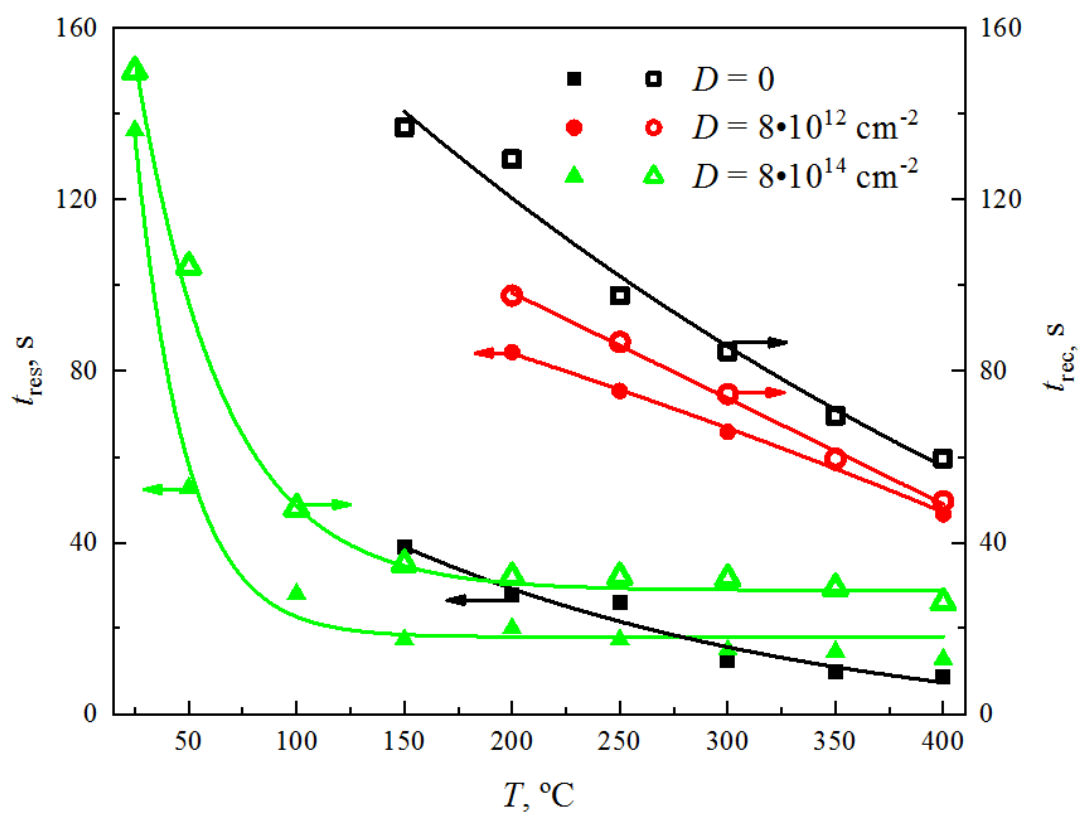


**Fig. 2.** Temperature dependences of the response ( $t_{res}$ ) and recovery ( $t_{rec}$ ) times of  $\alpha$ -Ga<sub>2</sub>O<sub>3</sub> samples exposed to 3 vol.% H<sub>2</sub> at different Si<sup>+</sup> irradiation doses

Figure 2 compares the temperature dependences of  $t_{res}$  and  $t_{rec}$  for  $\alpha$ -Ga<sub>2</sub>O<sub>3</sub> samples at  $D_0$ ,  $D_1$ , and  $D_2$ . For all these curves  $t_{res}$  and  $t_{rec}$  decrease exponentially with increasing in  $T$ . The  $\alpha$ -Ga<sub>2</sub>O<sub>3</sub> samples with the highest response to H<sub>2</sub>, at  $D_1$  demonstrate the largest  $t_{res}$ . At  $T \geq 300^\circ\text{C}$ , at  $D_0$  and  $D_2$ , in both cases,  $t_{res}$  do not exceed 25 s. Unirradiated  $\alpha$ -Ga<sub>2</sub>O<sub>3</sub> samples are characterized by the highest  $t_{rec}$  values.

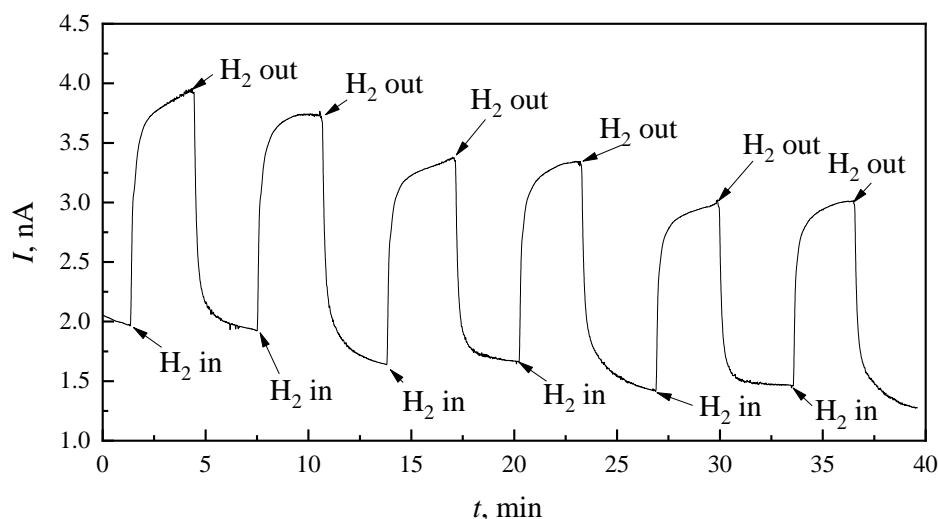


**Fig. 3.** Time dependence of the current ( $I$ ) of  $\alpha$ -Ga<sub>2</sub>O<sub>3</sub> sample after Si<sup>+</sup> irradiation with  $D = 8 \cdot 10^{14} \text{ cm}^{-2}$  at six-fold exposure to 0.5 vol.% H<sub>2</sub> and  $T = 400^\circ\text{C}$

Time dependence of the current of  $\alpha$ -Ga<sub>2</sub>O<sub>3</sub> sample at  $D_2$  at six-fold exposure to 0.5 vol. % H<sub>2</sub> and  $T = 400^\circ\text{C}$  is depicted in Fig. 3. For these samples,  $I_0$  decreased by 26.3 % and  $I_g$  decreased by 23.7 % after the sixth H<sub>2</sub> feed into the chamber. Due to the difference in the rate of decrease of  $I_0$  and  $I_g$  over time,  $S$  increases by 1.07 a.u. For  $\alpha$ -Ga<sub>2</sub>O<sub>3</sub> samples at  $D_1$ , the opposite effects of current change with time were observed. After the sixth H<sub>2</sub> feed,  $I_0$  increased by 21.9 % and  $I_g$  increased by 139.8 % compared to the first feed. Such a significant increase in  $I_g$  led to an increase in  $S$  by 2.03 a.u.

The gas sensitivity of  $\beta$ -Ga<sub>2</sub>O<sub>3</sub> structures can be described by two mechanisms [12]. The first one is realized by chemisorption of gas molecules on the semiconductor surface, resulting in the change of charge state of the surface at  $T = 25$ - $900^\circ\text{C}$  and/or the concentration of oxygen vacancies in the material at  $T = 700$ - $1100^\circ\text{C}$ . This mechanism predominates for structures with a developed surface in which the surface conductivity contribution exceeds the bulk one. This is valid for thin and porous films, and low-dimensional structures, but is also observed for single crystals at extremely high temperatures [13]. The second mechanism is based on a change in the conditions for the flow of electron current through the potential barrier at the interface of the gallium oxide and metal (gate) with catalytic activity. This mechanism is typical of relatively thick, epitaxial gallium oxide layers [14]. Such structures are sensitive to H<sub>2</sub> due to weak diffusion limitations for H in the metal. It is believed that during adsorption on a metal surface, H<sub>2</sub> molecules dissociate into H atoms, which diffuse through the metal layer to the heterogeneous interface with the semiconductor, where they form a dipole layer that reduces the height of the potential barrier for electrons.

The thickness of the Pt contacts in the considered MSM structures was  $\sim 300$  nm. The estimates showed that at the temperatures applied in this study, the time required for the diffusion of H atoms through the Pt layer does not exceed 0.055 s. While for some other molecules (CO, NH<sub>3</sub>, NO, and NO<sub>2</sub>) and their possible fragments this time is significantly longer. A Schottky barrier is formed at the Pt /  $\alpha$ -Ga<sub>2</sub>O<sub>3</sub> interface [13]. The saturation current of such a barrier in the air is  $I_{S0} = AA^*T^2 \exp[-\Phi_{b0}/(kT)](kT)$ , where  $A$  is the contact

area;  $A^*$  is Richardson constant;  $e$  is electron charge;  $k$  is Boltzmann constant;  $\Phi_{b0}$  is the potential barrier height at the Pt /  $\alpha$ -Ga<sub>2</sub>O<sub>3</sub> interface in an atmosphere of pure dry air. In a pure dry air + H<sub>2</sub> gas mixture,  $\Phi_{b0}$  decreases by the value of  $e\Delta V_H$  and  $\Phi_{bH}(n_{H_2}) = \Phi_{b0} - e\Delta V_H(n_{H_2})$ , where  $\Phi_{bH}$  is the height of the potential barrier at the Pt /  $\alpha$ -Ga<sub>2</sub>O<sub>3</sub> interface when exposed to H<sub>2</sub>. It is not difficult to show that  $S(n_{H_2}) = \exp[e\Delta V_H(n_{H_2})/kT]$ . As  $T$  increases from 100°C to 350°C at  $D_0$ ,  $e\Delta V_H$  increases from 0.003 eV to 0.034 eV.

To increase the response of  $\alpha$ -Ga<sub>2</sub>O<sub>3</sub> to H<sub>2</sub> an increase in  $\Delta V_H$  is necessary. It is shown [14,15], that  $\Delta V_H = p \times \theta_H \times N_i/\epsilon_0$ , where  $p$  is the dipole moment created by the H atom on the heterogeneous interface;  $\theta_H$  is the coverage of the Pt /  $\alpha$ -Ga<sub>2</sub>O<sub>3</sub> interface by H atoms,  $\theta_H \leq 1$  and  $\theta_H = n_H/N_i$ ;  $n_H$  is the surface density of H atoms adsorbed on the interface;  $N_i$  is the surface density of adsorption centers for H on the interface;  $\epsilon_0$  is the dielectric constant. At  $T = 350^\circ\text{C}$  and  $n_{H_2} = 3$  vol. %  $p \approx 6.67 \cdot 10^{-30}$  C $\times$ m [15,16]. The dependences of  $e\Delta V_H$  on H<sub>2</sub> concentration are approximated by power functions,  $e\Delta V_H \sim n_{H_2}^m$ , and at  $n_{H_2} > 1$  vol. % tend to saturation, where  $m$  is the exponent,  $m = 0.32$  at  $D_1$ . Hence, we can assume that when  $n_{H_2} = 3$  vol. %  $\theta_H \rightarrow 1$ . The  $N_i$  values obtained at  $T = 350^\circ\text{C}$  were  $4.54 \cdot 10^{14}$  cm<sup>-2</sup>,  $2.51 \cdot 10^{15}$  cm<sup>-2</sup>, and  $1.05 \cdot 10^{15}$  cm<sup>-2</sup>, respectively, at  $D_0$ ,  $D_1$ , and  $D_2$ . Irradiation of  $\alpha$ -Ga<sub>2</sub>O<sub>3</sub> with Si<sup>+</sup> ions leads to an increase in  $N_i$  and as a consequence the response to H<sub>2</sub> and other gases increases. When a dose is further increased up to  $D_2$ , the surface of  $\alpha$ -Ga<sub>2</sub>O<sub>3</sub> develops defects that decrease  $I$  and  $N_i$ . A similar mechanism of influence of ion irradiation on gas-sensitive properties was observed earlier for SnO<sub>2</sub> [17,18].

#### 4. Conclusions

It was found that Si<sup>+</sup> ion irradiation of  $\alpha$ -Ga<sub>2</sub>O<sub>3</sub> epitaxial layers with a dose of  $8 \cdot 10^{12}$  cm<sup>-2</sup> and energy of 100 keV leads to a magnification from 3 to 43 times in the H<sub>2</sub> response of MSM Pt/ $\alpha$ -Ga<sub>2</sub>O<sub>3</sub>/Pt structures with increasing the heating temperature from 250°C to 400°C. When the irradiation dose is increased up to  $8 \cdot 10^{14}$  cm<sup>-2</sup>, a significant decrease in the H<sub>2</sub> response, response, and recovery times are observed. We attribute the observed effect to an increase in the density of adsorption centers for H atoms on the Pt /  $\alpha$ -Ga<sub>2</sub>O<sub>3</sub> interface when  $\alpha$ -Ga<sub>2</sub>O<sub>3</sub> is irradiated with Si<sup>+</sup> ions at a dose of  $8 \cdot 10^{12}$  cm<sup>-2</sup>. A further increase in dose up to  $8 \cdot 10^{14}$  cm<sup>-2</sup> generates defects on the semiconductor surface which reduce the density of adsorption centers for H on the Pt /  $\alpha$ -Ga<sub>2</sub>O<sub>3</sub> interface.

#### References

1. Kaneko K, Fujita S, Hitora T. A power device material of corundum-structured  $\alpha$ -Ga<sub>2</sub>O<sub>3</sub> fabricated by MIST EPITAXY® technique. *Jpn. J. Appl. Phys.* 2018;57(2S2): 02CB18.
2. Hou X, Zou Y, Ding M, Qin Y, Zhang Z, Ma X, Tan P, Yu S, Zhou X, Zhao X, Xu G, Sun H, Long SJ. Review of polymorphous Ga<sub>2</sub>O<sub>3</sub> materials and their solar-blind photodetector applications. *Phys. D: Appl. Phys.* 2021;54(4): 043001.
3. Almaev A, Nikolaev V, Stepanov S, Pechnikov A, Chikiryaka A, Yakovlev N, Kalygina V, Kopyev V, Chernikov E. Hydrogen influence on electrical properties of Pt-contacted  $\alpha$ -Ga<sub>2</sub>O<sub>3</sub>/ $\epsilon$ -Ga<sub>2</sub>O<sub>3</sub> structures grown on patterned sapphire substrates. *J. Phys. D: Appl. Phys.* 2020;53(41): 414004.
4. Yakovlev N, Nikolaev V, Stepanov S, Almaev A, Pechnikov A, Chernikov E, Kushnarev B. Effect of Oxygen on the Electrical Conductivity of Pt-Contacted  $\alpha$ -Ga<sub>2</sub>O<sub>3</sub>/ $\epsilon$ ( $\kappa$ )-Ga<sub>2</sub>O<sub>3</sub> MSM Structures on Patterned Sapphire Substrates. *IEEE Sensors Journal.* 2021;21(13): 14636
5. Polyakov A, Smirnov N, Shchemerov I, Yakimov E, Nikolaev V, Stepanov S, Pechnikov A, Chernykh A, Shcherbachev K, Shikoh A, Kochkova A, Vasilev A, Pearton S. Deep trap spectra of Sn-doped  $\alpha$ -Ga<sub>2</sub>O<sub>3</sub> grown by halide vapor phase epitaxy on sapphire. *APL Materials.* 2019;7(5): 051103.

6. Polyakov A, Nikolaev V, Stepanov S, Pechnikov A, Yakimov E, Smirnov N, Shchemerov I, Vasilev A, Kochkova A, Chernykh A, Pearton S. Electrical Properties and Deep Traps in  $\alpha$ -Ga<sub>2</sub>O<sub>3</sub>:Sn Films Grown on Sapphire by Halide Vapor Phase Epitaxy. *ECS J. Solid State Sci. Technol.* 2020;9(4): 045003.
7. Dong L, Yu J, Zhang Y, Jia R. Elements (Si, Sn, and Mg) doped  $\alpha$ -Ga<sub>2</sub>O<sub>3</sub>: First-principles investigations and predictions. *Comput. Mater. Sci.* 2019;156: 273.
8. Tadjer M, Lyons J, Nepal N, Freitas Jr. J, Koehler A, Foster G. Theory and Characterization of Doping and Defects in  $\beta$ -Ga<sub>2</sub>O<sub>3</sub>. *ECS J. Solid State Sci. Technol.* 2019;8(7): Q3187.
9. VÍllora E, Shimamura K, Yoshikawa Y, Ujiie T, Aoki K. Electrical conductivity and carrier concentration control in  $\beta$ -Ga<sub>2</sub>O<sub>3</sub> by Si doping. *Appl. Phys. Lett.* 2008;92(20): 202120.
10. Nikolskaya A, Okulich E, Korolev D, Stepanov A, Nikolichev D, Mikhaylov A, Tetelbaum D, Almaev A, Bolzan C, Buaczik Jr. A, Giulian R, Grande P, Kumar A, Kumar M, Gogova D. Ion implantation in  $\beta$ -Ga<sub>2</sub>O<sub>3</sub>: Physics and technology. *J. Vac. Sci. Technol. A*, 2021;39(3): 030802.
11. Uchida T, Kaneko K, Fujita S. Electrical characterization of Si-doped n-type  $\alpha$ -Ga<sub>2</sub>O<sub>3</sub> on sapphire substrates. *MRS Advances.* 2018;3(3): 171.
12. Krawczyk M, Korbutowicz R, Szukiewicz R, Suchorska-Woźniak P, Kuchowicz M, Teterycz H. P-type Inversion at the Surface of  $\beta$ -Ga<sub>2</sub>O<sub>3</sub> Epitaxial Layer Modified with Au Nanoparticles. *Sensors.* 2022;22(3): 932.
13. Afzal A.  $\beta$ -Ga<sub>2</sub>O<sub>3</sub> nanowires and thin films for metal oxide semiconductor gas sensors: Sensing mechanisms and performance enhancement strategies. *J. Materiomics.* 2019;5(4): 542.
14. Jang S, Jung S, Kim J, Ren F, Pearton S, Baik K. Hydrogen Sensing Characteristics of Pt Schottky Diodes on (-201) and (010) Ga<sub>2</sub>O<sub>3</sub> Single Crystals. *ECS J. Solid State Sci. Technol.* 2018;7(7): Q3180.
15. Lundström I, Petersson L-G. Chemical sensors with catalytic metal gates. *J. Vac. Sci. Technol.* 1996;14(3): 1539.
16. Eriksson M, Lundström I, Ekedahl L-G. A model of the Temkin isotherm behavior for hydrogen adsorption at Pd-SiO<sub>2</sub> interfaces. *J. Appl. Phys.* 1997;82(6): 3143.
17. Kim J-H, Mirzaei A, Kim J-Y, Lee J-H, Kim HW, Hishita S, Kim S. Enhancement of gas sensing by implantation of Sb-ions in SnO<sub>2</sub> nanowires. *Sens. Actuators B Chem.* 2020;304: 127307.
18. Kwon Y, Kang S, Wu P, Peng Y, Kim S, Kim H. Selective Improvement of NO<sub>2</sub> Gas Sensing Behavior in SnO<sub>2</sub> Nanowires by Ion-Beam Irradiation. *ACS Appl. Mater. Interfaces.* 2016;8(21): 13646.

## THE AUTHORS

### **Yakovlev N.N.**

e-mail: nik\_mr\_x@mail.ru

ORCID: 0000-0002-5190-0178

### **Almaev A.V.**

e-mail: almaev\_alex@mail.ru

ORCID: 0000-0002-3502-8770

**Butenko P.N.**

e-mail: pavel@butenko.info

ORCID: 0000-0003-1364-3016

**Mikhaylov A.N.**

e-mail: mian@nifti.unn.ru

ORCID: 0000-0001-5505-7352

**Pechnikov A.I.**

e-mail: alpechn@yahoo.com

ORCID: -

**Stepanov S.I.**

e-mail: s.i.stepanov@googlemail.com

ORCID: -

**Timashov R.B.**

e-mail: timashov@inbox.ru

ORCID: -

**Chikiryaka A.V.**

e-mail: chikiryaka@mail.ru

ORCID: -

**Nikolaev V.I.**

e-mail: nikolaev.v@mail.ioffe.ru

ORCID: -

# Non-equilibrium phonon gas in a chalcogenide semiconductor with exponential temperature dependence of conductivity

K.D. Mynbaev✉, N.V. Sovtus

Ioffe Physical Technical Institute of the Russian Academy of Sciences, 26, Polytekhnicheskaya St.,  
St. Petersburg, 194021, Russia  
✉ [mynkad@mail.ioffe.ru](mailto:mynkad@mail.ioffe.ru)

**Abstract.** The distribution function for a phonon gas in the non-equilibrium case of current crowding in a chalcogenide glassy semiconductor is considered. The approximate internal energy of the gas and its heat capacity is calculated. The change in the heat capacity caused by phase changes, which according to the results of the numerical calculations, are similar to the second-order phase transition, is analyzed. The law of temperature variation with time is calculated for a homogeneous current crowding without a heat sink, taking into account the exponential dependence of the conductivity on the temperature. It is shown that the temperature dependences of the concentration and energy of phonons do not undergo significant changes and are linear. The results of this work should be useful in developing chalcogenide glass-based phase-change memory devices, where strong heating by an electric current is possible and, as a consequence, a significant effect of phonons on the current flow should occur.

**Keywords:** chalcogenide glasses, current filament, phonon gas

**Acknowledgments.** No external financial support was provided for this study.

**Citation:** Mynbaev K.D., Sovtus N.V. Non-equilibrium phonon gas in a chalcogenide semiconductor with exponential temperature dependence of conductivity. *Materials Physics and Mechanics*. 2022;48(3): 308-314. DOI: 10.18149/MPM.4832022\_2.

## 1. Introduction

The phenomenon of current crowding (filamentation) in chalcogenide glassy semiconductors (CGSs) has been studied since the discovery of the switching effect in these materials in the 1960s [1]. With the switching effect in a CGS, the conductivity  $\sigma$  increases sharply, and this low-resistance state can persist for an indefinitely long time, which is the memory effect. This effect is used in the development of the new generation of memory devices based on phase-change memory (PCM) technology; these devices are expected to be faster and more durable than current ones [2-4] and can be used in photonic applications [5,6].

Current crowding in CGS has been studied both experimentally and theoretically, and, most extensively, in application to GeSbTe (GST)-related materials [7-9]. For these materials, the transition from the crystalline state into the amorphous state, which implies structural transformation in the Ge sublattice called an 'umbrella flip', means that the octahedral elementary cell transforms into a tetrahedral one [10]. Crystallization temperature for the GST family of materials varies between  $\sim 120$  and  $\sim 140^\circ\text{C}$  while melting points typically range from  $\sim 600$  to  $\sim 620$  K [11]. With recording using PCM, an initially amorphous CGS film is

crystallized by exposure to external action (optical or electrical pulse) with an intensity sufficient to heat the material to a point slightly above the glass-transition temperature. Subsequent exposure to a short pulse melts the CGS so upon quenching it gets converted into the amorphous state, and a recorded bit is just an amorphized mark against the crystalline background [10].

Current filament forms at the switching effect, and not only leads to the appearance of the area with low resistivity but also allows one to describe the system using the model of negative differential conductivity. The basic, thermal model of current crowding in CGS states that the formation of the filament along the central axis of a disk-shaped semiconductor sample is due to a sharp non-uniform temperature distribution across the disk. The temperature of the filament is directly proportional to the squared temperature of the maximum temperature in the center of the filament. Indeed, in [1,12], the effect of current crowding in a CGS placed in a uniform electric field was considered in detail, and it was shown that crowding occurs due to a sharp distribution of temperature  $T$  along with the radial coordinate  $r$ . This distribution is well described by an exponential function of time  $t$  and  $r$ , and the current value in the filament appears to be inversely proportional to the value of the applied electric field  $F$ . However, current crowding in [1,12] was considered without taking into account the behavior of phonons in a semiconductor, while during switching and crowding a phase transition occurs in the system, and the amorphous state becomes crystalline [13]. An ensemble of phonons will necessarily be present in a crystalline semiconductor. In the equilibrium, they are distributed according to the Bose-Einstein law; however, with sharp heating, their distribution is not in equilibrium.

In this work, we analyze the behavior of an ensemble of phonons taking into account the time dependence of the filament temperature. The time-dependent non-equilibrium Boltzmann function for phonons and values of the internal energy of a phonon gas and its heat capacity is obtained. The results of this work can be useful in developing CGS-based PCM devices, where strong heating by an electric current is possible and, as a consequence, a significant effect of phonons on the current flow should occur.

## 2. Results and discussion

As mentioned above, the temperature distribution involves not only radial coordinate  $r$  but also time  $t$ . This distribution was studied, e.g., in [12]. The layout of a sample with current flow and radial temperature distribution is shown in Fig. 1. The contacts are considered to be smaller than the semiconductor sample and the current filament is smaller than the contacts (Fig. 1a). The dependence of the conductivity on the reciprocal temperature leads to strongly pronounced current re-distribution along with  $r$ . We consider a disk-shaped sample of CGS with a thickness  $L$  of the order of 1  $\mu\text{m}$ , where the temperature is exponentially distributed along with  $r$  during the current crowding (Fig. 1b). For this sample, the expression  $\sigma = \sigma_0 \exp(-\Delta E/k_B T)$  is used for the dependence of  $\sigma$  on  $T$ . Here,  $\sigma_0$  is the initial conductivity,  $\Delta E$  is the activation energy of conductivity, and  $k_B$  is the Boltzmann constant. To take into account the contribution of the phonon gas to the redistribution of heat in the sample, it is necessary to describe its behavior by introducing a stationary non-equilibrium function  $f(r, \nu) = f_0(r, \nu) + \Delta f$ , where  $\nu$  is the velocity,  $f_0(r, \nu) = 1/(\exp(\hbar\omega/k_B T) - 1)$ ,  $f_0(r, \nu) = 1/(\exp(\hbar\omega) - 1)$ ,  $\Delta f$  is a correction ( $\hbar$  is the Planck constant,  $\omega$  is the frequency).

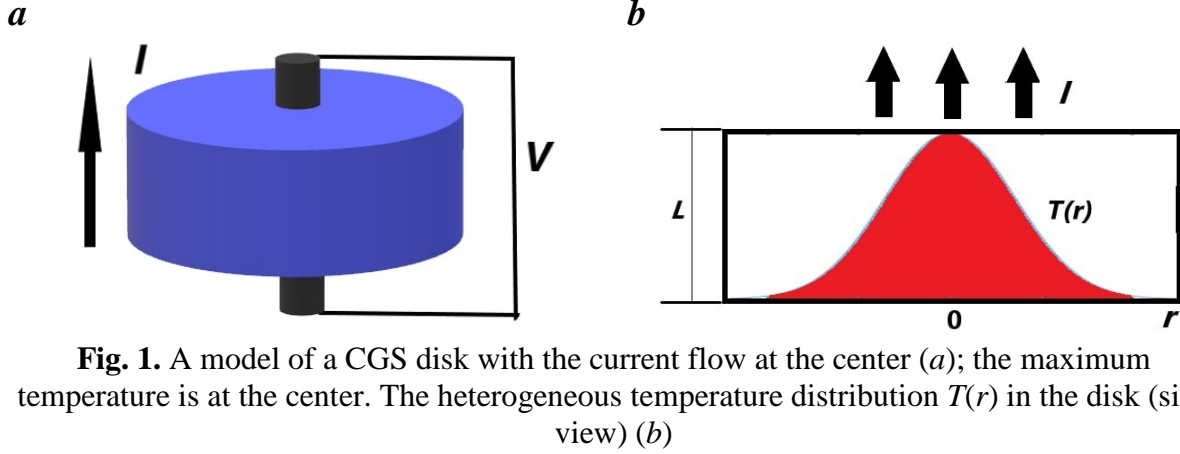


**Fig. 1.** A model of a CGS disk with the current flow at the center (a); the maximum temperature is at the center. The heterogeneous temperature distribution  $T(r)$  in the disk (side view) (b)

To find a non-equilibrium kinetic distribution function, we should solve the Boltzmann kinetic equation:

$$\frac{\partial f}{\partial t} + v \frac{\partial f}{\partial r} + \frac{F}{m} \frac{\partial f}{\partial v} = -\frac{f-f_0}{\tau_0}. \quad (1)$$

Using the simplest way to obtain a new function, we assume that heating in a certain region of the CGS is uniform, and then (1) is transformed into the expression  $\frac{\partial f}{\partial t} = -\frac{f-f_0}{\tau_0}$ , where  $\tau_0$  is the relaxation time.

In the case of uniform and fast quasi-adiabatic heating, the thermal conductivity equation takes the form  $dy/du = \beta \exp(-1/y)$ , where  $y = k_B Tu/\Delta E$ ,  $u = \alpha t/L^2$  is the dimensionless time,  $\alpha$  is thermal diffusivity,  $\beta = F^2/F_s^2 \exp(F/F_0)$ ,  $F_s^2 = 2\lambda\Delta E/\sigma_0 Lk_B$ ,  $\lambda$  is the coefficient of heat removal,  $F_0 \approx 10^{-6}$  V/m [9]. The heating here is considered to be more intensive than heat removal. We will solve the equation in the first approximation assuming that thermal diffusivity does not change with time. Let us expand the formula in the exponent near a certain high-temperature value  $y_m$ :  $\frac{\partial y}{\partial u} = \beta \exp\left(\frac{y-2y_m}{y_m^2}\right)$ . The solution to this differential equation is the function:

$$y(u) = 2y_m^2 \ln(t_m) - y_m^2 \ln\left(y_m^2 \exp\left(\frac{-y_0}{y_m^2}\right)\right) - y_m^2 \ln\left(1 - \frac{u}{u_d}\right) \approx y_0 + y_m^2 \frac{u}{u_d}, \quad (2)$$

where  $u_d = \frac{y_m^2 \exp\left(\frac{-y_0}{y_m^2}\right)}{\beta \exp\left(\frac{-1}{y_m}\right)}$  defines the time when the temperature of the heated area turns to infinity.

We will look for a non-equilibrium distribution function at high temperatures that are larger than Debye temperatures  $T_D$ , which for various materials typically fall into the range 90 K (lead) to 1860 K (diamond):

$$f_0 = \frac{1}{\exp\left(\frac{\hbar\omega}{k_B T}\right) - 1} \approx \frac{\Delta E y}{\hbar\omega}. \quad (3)$$

Taking into account Eqs. (2) and (3), the solution of the simplified Eq. (1) is the function:

$$f_1(t) = \frac{\Delta E y_0}{\hbar\omega} + \frac{y_m^2 \Delta E u}{u_d \hbar\omega} + \frac{\Delta E y_m^2 \tau}{\hbar\omega u_d} \left( \exp\left(\frac{-u}{\tau}\right) - 1 \right). \quad (4)$$

In what follows, the dimensionless time  $\tau = \alpha\tau_0/L^2$  will be used as the relaxation time. For the calculations, the authors took the CGS parameters used in [12], which are characteristic of GST CGSs.

Let us consider our crystal to be volumetric ('bulk') for the analytical calculation of the thermodynamic parameters of the phonon gas. In a bulk crystal, the internal energy of a phonon gas  $U = \int_0^{\omega_d} \hbar\omega f_1(\omega) g(\omega) d\omega$ , where  $g(\omega)$  is the density of phonon states,

$$\omega_d = v \left( \frac{6\pi^2 N}{V} \right)^{1/3}.$$

Here  $N$  is the number of unit cells in the crystal, and  $V$  is its volume.

The density of phonon states can be determined using the formula  $g(\omega) = \frac{3V\omega^2}{2\pi^2 v^3} = \frac{9N\omega^2}{\omega_d}$ . Substituting the expressions for  $g(\omega)$  and  $f_i(T)$  into the integral for  $U$ , we obtain:

$$U = 3Nk_B \left[ T + \frac{k_B T_m^2 \tau}{\Delta E u_d} \left( \exp \left( \frac{-(T-T_0)u_d \Delta E}{k_B T_m^2 \tau} \right) - 1 \right) \right], \quad (5)$$

where  $T_m$  is the maximum temperature of the filament. With an increase in temperature, the internal energy increases, this process can be described as isochoric heating, since the phonon gas does not increase its volume during the temperature increase. For an ideal gas of molecules, the isochoric heat capacity is a constant value. The heat capacity of a phonon gas is calculated as  $C=dU/dT$ , that is:

$$C = 3Nk_B \left[ 1 - \exp \left( \frac{-(T-T_0)u_d \Delta E}{k_B T_m^2 \tau} \right) \right]. \quad (6)$$

Figure 2a shows the results of the calculations. Hereinafter, in the calculations, we assumed  $L = 10^{-5}$  m,  $\Delta E = 0.5$  eV,  $\sigma_0 = 10^6$   $\Omega \cdot m$ , thermal conductivity  $\kappa = 20$  W/K,  $n = N/V = 1.25 \times 10^{29}$  m<sup>-3</sup>,  $\alpha = 10^6$  m<sup>2</sup>/s,  $T_0 = 300$  K,  $T_m = 700$  K,  $T_D = 500$  K. It is seen how fast  $C$  increases with time ( $\tau \sim 10^{-6}$  s here is assumed to be a constant value of  $3Nk_B$ ). A similar sharp jump in the heat capacity can be observed during a second-order phase transition. The temperature rise with time in the analytical case is described by a polynomial of the first order.

The pressure in the isochoric process can be estimated using the expression  $p = 2U/3V$ . From Fig. 2b it follows that under the given conditions it is of the order of  $10^9$  Pa. Pressure and internal energy have an extremum at  $T = T_0$ . The heat capacity at this temperature is zero, which is typical for an adiabatic process. However, as has already been shown, the process almost instantly becomes isochoric.

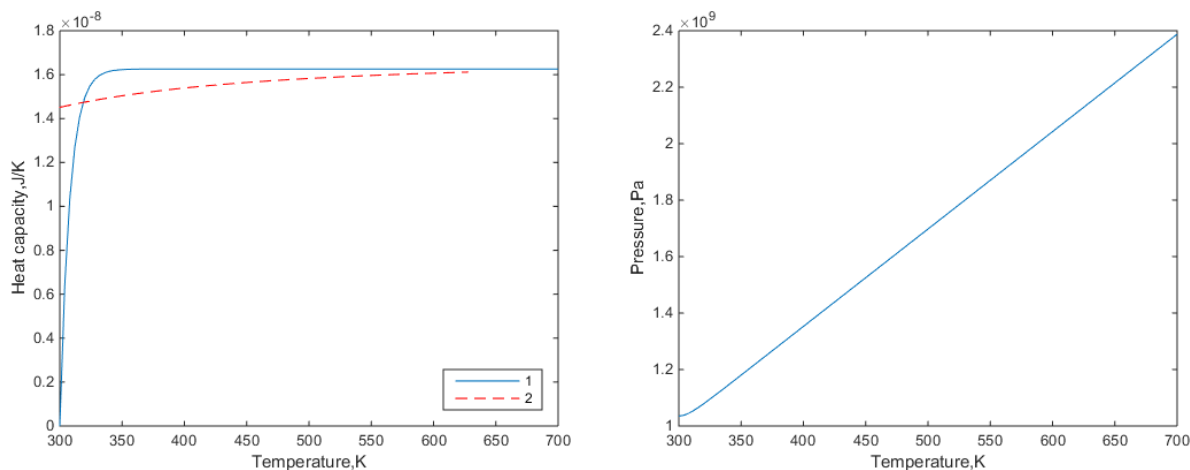


**Fig. 2.** Analytically (1) and numerically (2) calculated dependences of heat capacity of the phonon gas  $C$  on the temperature (a) and analytically obtained pressure dependence of the gas on the temperature (b)

The phonon concentration can be calculated as ( $\gamma = \alpha/u_d$ ):

$$n_{ph} = \frac{9N}{V\omega_d^3} \int_0^{\omega_d} \omega^2 f_1(\omega) d\omega = \frac{9Nk_B}{2V\hbar\omega_d} \left[ T + \frac{k_B T_m^2 \gamma \tau_0}{\Delta E L^2} \left( \exp \left( \frac{-(T-T_0)\Delta E}{k_B T_m^2 \tau} \right) - 1 \right) \right]. \quad (7)$$

Let us turn to the results of the numerical calculations of thermodynamic coefficients. The calculations were completed using MATLAB. From Eq. (6), the zero value of the heat capacity at the initial moment of time is derived; it indicates the adiabatic nature of the

process of changing the internal energy of the phonon gas near the zero time coordinate. In [12], the heat removal near the zero coordinate was neglected. Figure 3 shows a graph of the temperature obtained when heating according to the law  $\frac{dT}{dt} = \eta \exp(-\frac{\Delta E}{k_B T})$ , where  $\eta = \sigma_0 F^2 \alpha / \kappa$ .

Heating in films with a thickness of the order of micrometers occurs in a few milliseconds. The non-equilibrium distribution function in general form, taking into account the above expressions for  $df/dt$  and  $dT/dt$ , will take the form:

$$f_1(\omega) = f_0(\omega) - \tau \eta \exp(-\frac{\Delta E}{k_B T}) \frac{df}{dT}. \quad (8)$$

Taking into account that the selected value of  $\tau$  is small compared to the heating time  $\frac{\alpha}{L^2} u_d$  up to the temperatures  $T \gg T_0$ , we can assume that the non-equilibrium distribution function does not differ much from the equilibrium function  $f_0$ , and  $\frac{df}{dT} = \frac{df_0}{dT}$ . Then,

$$f_1 = f_0 - \frac{\tau \eta \hbar \omega \exp(-\frac{\hbar \omega - \Delta E}{k_B T})}{k_B T^2 (\exp(\frac{\hbar \omega}{k_B T}) - 1)^2}. \quad (9)$$

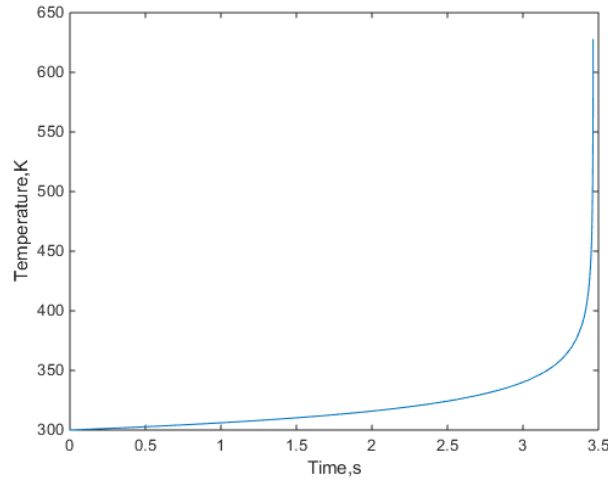


**Fig. 3.** Numerically calculated heating time dependence of the semiconductor temperature

The formula for the heat capacity  $C$  takes the form

$$C = \frac{9N}{\omega_d^3} \int_0^{\omega_d} \frac{df_1}{dT} \hbar \omega^3 d\omega.$$

The temperature dependences for internal energy  $U$  are shown in Fig. 4a. Internal energies are of the same order of magnitude, and their dependence on the temperature resembles those of an ideal gas. In Fig. 4b, it is seen that the phonon concentration exceeds the concentration of unit cells and increases linearly with time, which corresponds to the behavior of phonons at high temperatures ( $T > T_d$ ).

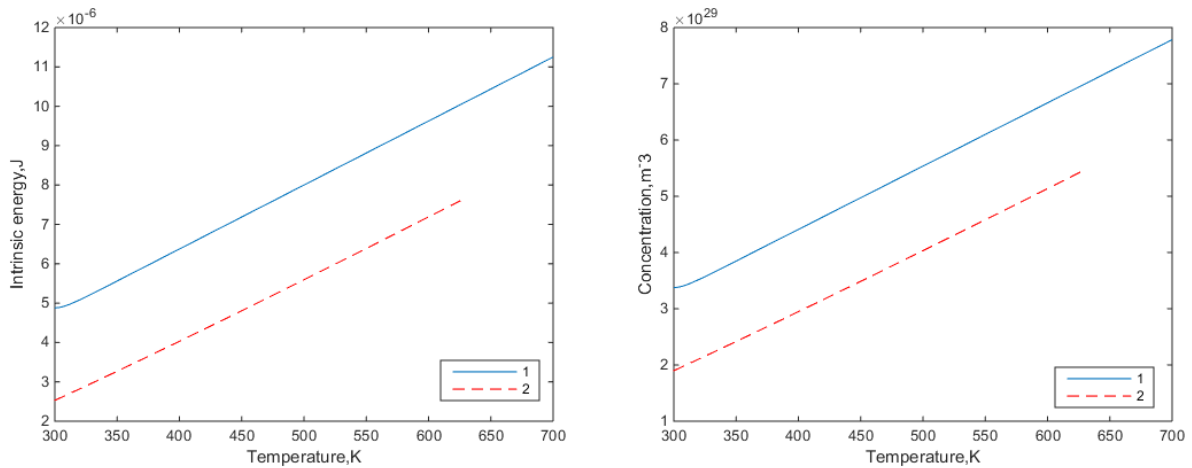


**Fig. 4.** Analytically (1) and numerically (2) calculated dependences of the internal energy of the phonon gas  $U$  on the semiconductor temperature (a) and the temperature dependence of the phonon concentration (b)

### 3. Discussion

From Figure 2a, it follows that the numerically calculated heat capacity does not experience such a sharp jump as its analytical counterpart. As the former grows, it tends to the limiting value of  $3Nk_B$ . However, a sharp change, similar to an increase in the analytically calculated heat capacity, does not occur, although at high temperatures both values tend to be the same value. The temperature of the sample, calculated numerically (Fig. 3) and analytically (not shown, but basically represented by Eq. (2)), differed greatly in the nature of their time dependence. We believe the data for the numerically calculated heat capacity are more credible, since they approximately reproduce the nature of the dependence for the derivative  $dU/dT$ , and both dependences become similar at  $T > T_0$ . The analytical dependence indicates a rapid increase in the temperature at the initial moment of time, while in the numerical dependence, a rapid increase in temperature occurs after some time  $t \gg t_d$ , where  $t_d$  is the characteristic time of the increase.

### 4. Conclusion

For the conditions of current crowding in a CGS, we have calculated the thermodynamic parameters of the phonon gas. It is shown that the numerically calculated heat capacity of the gas increases sharply upon heating a CGS with a conductivity that exponentially depends on the temperature, which can be interpreted as a manifestation of a second-order phase transition. The solution was obtained for a region with a uniform heating temperature. Due to its high conductivity, this region corresponds to the current filament. The temperature dependences of the concentration and energy of phonons do not undergo significant changes and are linear. The disadvantage of the obtained analytical solution is its applicability only in a limited temperature range.

### References

1. Bogoslovskiy NA, Tsandin KD. Physics of switching and memory effects in chalcogenide glassy semiconductors. *Semiconductors*. 2012;46(5): 559-590.
2. Noé P, Vallée C, Hippert F, Fillot F, Raty J-Y. Phase-change materials for non-volatile memory devices: From technological challenges to materials science issues. *Semiconductor Science and Technology*. 2018;33(1): 013002.
3. Le Gallo M, Sebastian A. An overview of phase-change memory. *Journal of Physics D: Applied Physics*. 2020;53(21): 213002.

4. Zhang W, Mazzarello R, Wuttig M, Ma E. Designing crystallization in phase-change materials for universal memory and neuro-inspired computing. *Nature Review Materials*. 2019;4: 150-168.
5. Wuttig M, Bhaskaran H, Taubner T. Phase-change materials for non-volatile photonic applications. *Nature Photonics*. 2017;11(8): 465-476.
6. Guo P, Sarangan AM, Agha IA. Review of germanium-antimony-telluride phase change materials for non-volatile memories and optical modulators. *Applied Sciences*. 2019;9(30): 530.
7. Almasov N, Bogoslovskiy N, Korobova N, Kozyukhin S, Fefelov S, Kazakova L, Jakovlev S, Tsendin K, Guseinov N. Switching and memory effects in partly crystallized amorphous Ge<sub>2</sub>Sb<sub>2</sub>Te<sub>5</sub> films in a current controlled mode. *Journal of Non-Crystalline Solids*. 2012;358(23): 3299-3303.
8. Bogoslovskiy NA, Tsendin KD. Dynamics of the current filament formation and its steady-state characteristics in chalcogenide based PCM. *Solid-State Electronics*. 2017;129: 10-15.
9. Sovtus N, Mynbaev K. Analytical description of quantum effects at current filamentation in chalcogenide glasses. *Materials Physics and Mechanics*. 2020;46(1): 202-206.
10. Kolobov AV, Fons P, Frenkel AI, Ankudinov AL, Tominaga J, Uruga T. Understanding the phase-change mechanism of rewritable optical media. *Nature Materials*. 2004;3: 703-708.
11. Yamada N, Ohno E, Nishiuchi K, Akahira N, Takao M. Rapid-phase transitions of GeTe-Sb<sub>2</sub>Te<sub>3</sub> pseudobinary amorphous thin films for an optical disk memory. *Journal of Applied Physics*. 1991;69: 2849-2856.
12. Sovtus NV, Mynbaev KD. Parameters of lateral and unsteady cord currents in a cylindrical chalcogenide glassy semiconductor. *Semiconductors*. 2019;53(12): 1651-1655.
13. Yamada N, Ohno E, Akahira N, Nishiuchi K, Nagata K, Takao M. High Speed Overwritable Phase Change Optical Disk Material. *Japanese Journal of Applied Physics*. 1987;26(S4): 61-66.

#### THE AUTHORS

**Mynbaev K.D.**

e-mail: mynkad@mail.ioffe.ru  
ORCID: 0000-0002-9853-8874

**Sovtus N.V.**

e-mail: spnick93@mail.ru  
ORCID: -

# Optimization of powder metallurgy process parameters to enhance the mechanical properties of AZ91 magnesium alloy

Naveen Kumar✉, Ajaya Bharti

Applied Mechanics Department, Motilal Nehru National Institute of Technology Allahabad, Prayagraj,  
India-211004

✉ [chaudhary56naveen@gmail.com](mailto:chaudhary56naveen@gmail.com)

**Abstract.** In the present work, optimization of powder metallurgy process parameters, i.e., compaction pressure, sintering time, and sintering temperature, for magnesium alloy AZ91 is done using Taguchi Design of Experiment and ANOVA techniques. Regression equation for determining ultimate compressive stress and hardness of AZ91 Magnesium alloy was formulated and validated experimentally. Out of the nine sets of parameters present in the current design, H8 (450 MPa compaction pressure, 450° sintering temperature, and 60 minutes sintering time) was found to be the best set of parameters for both the hardness and ultimate compressive stress. Still, the optimum set of parameters was not present in the current design of experiments. The optimum set of parameters obtained after analyzing the main effect plots for means is a combination of 450 MPa compaction pressure, 450° sintering temperature, and 90 minutes of sintering time. The optimum value of hardness and ultimate compressive stress obtained from the regression equations is 81.81 Hv and 138.90 MPa, respectively. Experimental value of ultimate compressive stress and hardness for samples processed at optimal parameters is 144.89 MPa and 82.12. Compression test results obtained from regression analysis are 4.31% less than the experimental results. Micro-hardness results obtained from regression analysis are 0.4% less than the experimental results. This shows that the regression analysis results are in good agreement with experimental results.

**Keywords:** ANOVA, AZ91 magnesium alloy, powder metallurgy, Taguchi

**Acknowledgements.** No external funding was received for this study.

**Citation:** Kumar N, Bharti A. Optimization of powder metallurgy process parameters to enhance the mechanical properties of AZ91 magnesium alloy. *Materials Physics and Mechanics*. 2022;48(3): 315-327. DOI: 10.18149/MPM.4832022\_3.

## 1. Introduction

Most industries, especially automobiles, aircraft, and space, are looking for lightweight structural material so that the overall weight of vehicles can be reduced and payload capacity can be increased [1-4]. Magnesium is one such material because It has the highest strength to weight ratio compared to other structural materials, i.e., aluminium, copper, and steel [5-8]. The low-density high strength to weight ratio of magnesium leads to the enormous increase in the demand for magnesium-based materials [7,9-12]. With the increase in demand for magnesium alloys and composites, there is an urgent need for an efficient reprocessing technique. Conventional reprocessing techniques (casting) have low material utilization (nearly 50%) and high energy consumption. Researchers worldwide are working on the

development of a more efficient reprocessing technique. Powder metallurgy is found to be one of the most efficient reprocessing techniques for metallic materials especially aluminium.

Powder metallurgy offers various advantages over other processes such as high material utilization, less scrap, near-net-shape products, less machining required, low power consumption, high control over density, easy handling, etc. [13-16]. In the powder metallurgy technique, blended powders are compressed at high pressure to produce green compacts, and then these green compacts are sintered to produce the final material [17-19]. Parameters such as compaction pressure, sintering temperature, and sintering time are very important in the powder metallurgy process. These parameters have a high effect on the properties of powder metallurgy products [20-22].

Burke et al. studied the effect of compaction pressure on the properties of AZ31 magnesium alloy [23]. Density and hardness increased on increasing the compaction pressure. Durai et al. investigated the effect of sintering temperature on Mg-Zr alloy properties [24]. Strength and hardness increased on increasing the sintering temperature. Gunes et al. studied the effect of sintering time on pure Magnesium properties. Hardness increased, and wear rate decreased on increasing the sintering time [25]. Kucuk et al. optimized the above-mentioned powder metallurgy process parameters for the fabrication of magnesium matrix composites and observed that the powder compaction pressure is the most influencing parameter followed by sintering temperature and sintering time [26].

There is not much literature available on the reprocessing of magnesium-based materials by powder metallurgy process. Kumar et al. in their review paper on the recycling and foaming of aluminium-based materials explained various methods of recycling aluminium by powder metallurgy, those methods can be used for the reprocessing of magnesium-based materials [27]. In the present work, optimization of powder metallurgy process parameters, i.e., compaction pressure, sintering time, and sintering temperature, for the reprocessing of magnesium alloy AZ91 is done using Taguchi Design of Experiment and ANOVA techniques. Regression equations for determining ultimate compressive stress and hardness of AZ91 Magnesium alloy were also formulated and validated experimentally.

## 2. Materials and methods

**Sample preparation.** AZ91 magnesium alloy powder produced by grinding the machining scrap was purchased from Jagada Industries, Virudhunagar, India. Powder was non-uniform with a mess size of 50 (particle size < 300 $\mu$ m). Nine different types of samples with different sets of process parameters were prepared by powder metallurgy technique [28]. Block diagram of powder metallurgy process is shown in Fig. 1.

Table 1. Parameters used and their levels

Parameter	Level 1	Level 2	Level 3
Compaction Pressure (MPa)	350	400	450
Sintering Temperature ( $^{\circ}$ C)	400	450	500
Sintering Time (Min)	60	90	120

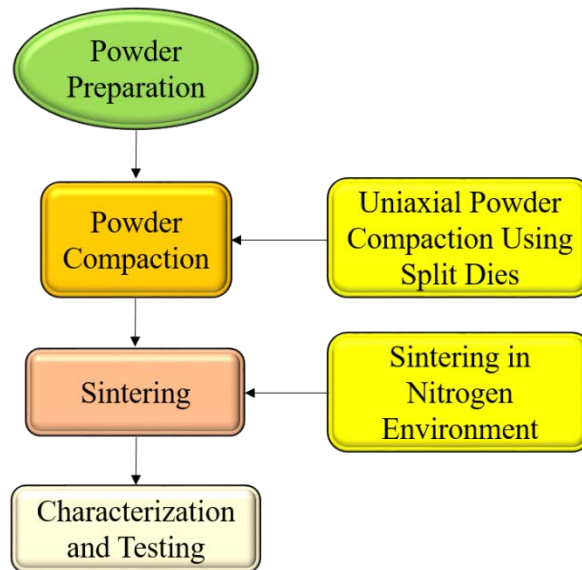


**Fig. 1.** Flow chart of powder metallurgy process

Three parameters, i.e., compaction pressure, sintering temperature, and sintering time, were used for optimization based on the literature survey. Three levels were selected for all three parameters. Parameters used and their levels are given below in Table 1. Taguchi Design of Experiment (DOE) technique was used for preparing the experimental plan. Nine different combinations of parameters used for sample preparation based on the Taguchi DOE method are given in Table 2. For all the nine types of samples, the powders were compacted in a split powder compaction die using Universal Testing Machine at the respective compression pressure to obtain the green compacts. The obtained green compacts were sintered in a muffle furnace in the presence of Nitrogen gas for the respective time at the respective temperature level as given in Table 2.

Table 2. Design of Experiment data based on Taguchi L9 orthogonal array

S. No.	Compaction Pressure (MPa)	Sintering Temperature (°C)	Sintering Time (Min)	Sample Code
1	350	400	60	A1
2	350	450	90	B2
3	350	500	120	C3
4	400	400	90	D4
5	400	450	120	E5
6	400	500	60	F6
7	450	400	120	G7
8	450	450	60	H8
9	450	500	90	I9

**Characterization and testing.** Specimens prepared after compaction and sintering were characterized and tested for investigating the mechanical properties of materials. For all nine types of specimens, the microscopic analysis was done to study the microscopic changes in the materials during compaction and sintering based on the optical micrographs obtained after grinding, polishing, and etching. Optical microscopy was done using an inverted digital metallurgical microscope available at GLA Mathura. Micro-hardness testing was also done for all the samples using Vicker's micro-hardness tester available at Mechanical Engineering Department, MNNIT Allahabad, according to ASTM B933-16. All nine types of samples

were then tested for compressive strength. Compressions tests were done on cylindrical samples according to ASTM E9 with the same length to diameter ratio (0.8) for all the samples using Universal Testing Machine available at Applied Mechanics Department, MNNIT Allahabad.

**Taguchi method.** The Taguchi DOE is an excellent method to design the experiments. Using the Taguchi DOE, sufficient information can be obtained by conducting less number of experiments [26]. In this method, parameters are categorized as controllable and uncontrollable. The effect of multiple parameters at two or more than two levels can be studied simultaneously using this method. There is always a target value of performance characteristic or property of any product or process. In this method, variability around the target value is reduced by optimizing the affecting factors. The optimum level of factors can be found by studying the main effect plots for each factor. The percentage effect of affecting factors can be found by analyzing the experimental results by the Analysis of Variance (ANOVA) technique.

Performance characteristics or properties of any product or process always belong to one of the following three categories:

1. The bigger, the better (In this target value is infinite);
2. The smaller, the better (In this target value is zero);
3. The nominal values are better (In this, a specific target value is given).

Signal to noise ratio (SN ratio) is an important statistical relation used in the Taguchi method to determine the optimum level of parameters. The high value of the SN ratio implies that the value of the signal is high, and the value of the noise is low. So, the parameter levels, which give the maximum values of the SN ratio, are the optimum parameters. Statistical formulas for calculating SN ratios for three different types of performance characteristics are given below.

For "the bigger, the better" characteristic:

$$SN = 10 \log \left[ \frac{1}{n} \sum_{n=1}^n \frac{1}{y^2} \right].$$

For "the smaller, the better" characteristic:

$$SN = -10 \log \left[ \frac{1}{n} \sum_{n=1}^n \frac{1}{y^2} \right].$$

For "the nominal values are better" characteristic:

$$SN = -10 \log \left( \overline{y^2} / S \right).$$

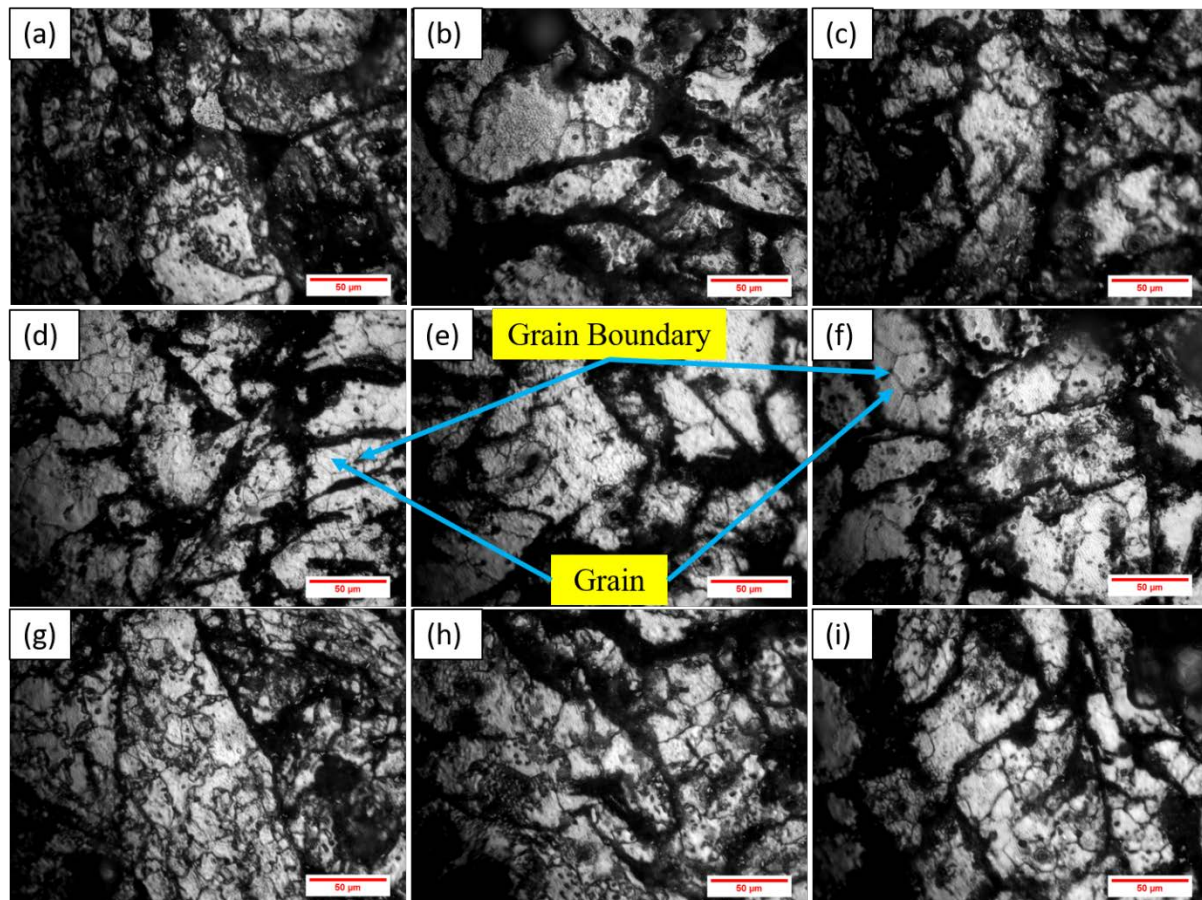
Where n is the number of repeated experimental tests, y is the performance value and S is the target value.

### 3. Results and Discussion

**Optical Microscopy.** Figure 2 shows the optical micrographs of all the specimens. It can be seen from the micrographs of specimens A1, B2, and C3 that grain size increased with an increase in sintering time and temperature because of recrystallization and grain growth in the material at high temperatures.

Group of specimens D4, E5, and F6 and G7, H8, and I9 show a similar effect of sintering time and temperature on the grain size of the material. The average grain size of all the specimens is given in Table 3. As the compaction pressure increases, grain size reduces because of the deformation in the material at high pressure. This can be seen in the micrographs of specimens A1, D4, and G7. Group of specimens B2, E5, and H8 and C3, F6, and I9 show a similar effect of compaction on the grain size of the material. Micrographs of the specimens A1, B2, and C3 show that there is high porosity in the material because of the

low compaction pressure. As the compaction pressure increases, porosity in the material also decreases. This can also be seen from the micrographs that porosity decreases with increases in the sintering time and temperature also. This is because of the proper diffusion in the material, as the diffusion is a time and temperature-dependent phenomenon.



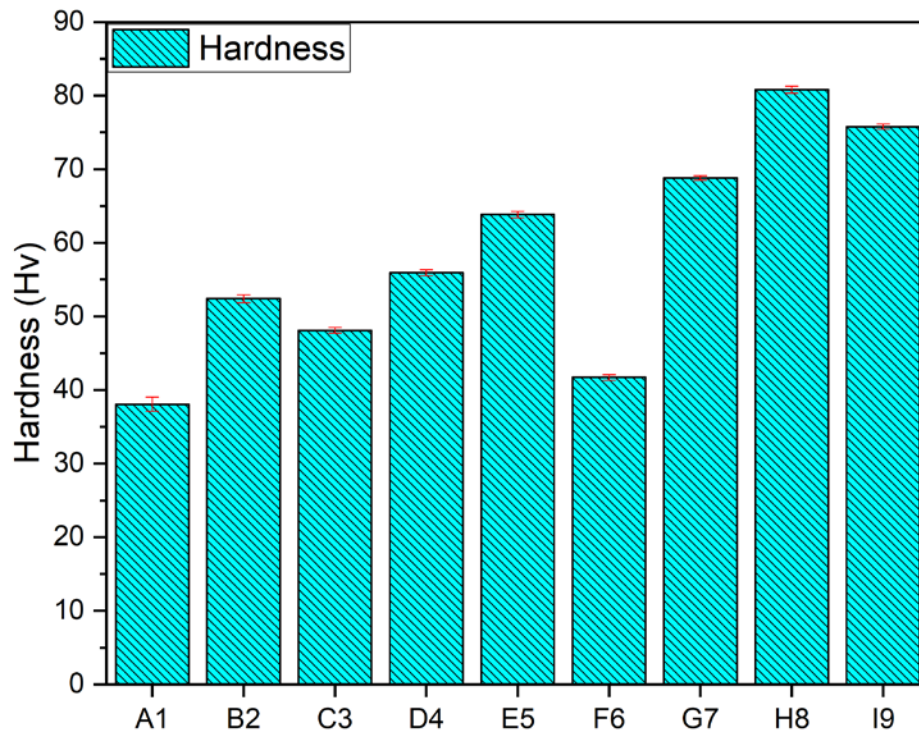
**Fig. 2.** Optical micrograph of specimens (a) A1, (b) B2, (c) C3, (d) D4, (e) E5, (f) F6, (g) G7, (h) H8 and (i) I9

Table 3. Average grain size (in  $\mu\text{m}$ ) of specimens

A1	B2	C3	D4	E5	F6	G7	H8	I9
24.78	25.09	26.50	16.24	18.83	24.21	15.94	17.82	23.34

**Microhardness.** The microhardness value of all the specimens is given in Fig. 3. This can be seen from the graph that the maximum and minimum values of error bars are too close, therefore, it can be understood that the sample has a homogeneous microstructure.

Microhardness values of the specimens increased with an increase in the compaction pressure. This is because of the grain size reduction and densification in the material on increasing compression pressure as seen in the optical micrographs of the specimens. On increasing the sintering time and temperature, hardness first increased because of the better diffusion bonding in the material at the high temperature. On further increase in sintering time and temperature, hardness started to decrease because of the recrystallization and grain growth in the material as shown in the optical micrographs of the specimens. The highest hardness value of 80.8Hv was obtained in specimen H8. Similar results were observed by other researchers also [29].



**Fig. 3.** Microhardness values of specimens

**Compression test.** Figure 4 shows the compressive stress vs. compressive strain curves of the specimens. Like hardness, similar effects of compaction pressure, sintering temperature, and sintering time had been seen on the ultimate compressive stress also. The highest ultimate compressive stress (UCS) of 136.44MPa was obtained for specimen H8. Similar results were observed by other researchers also [29]. The highest compressive strain was obtained in specimen I9 because of the proper diffusion and grain growth in the material at high sintering temperature.

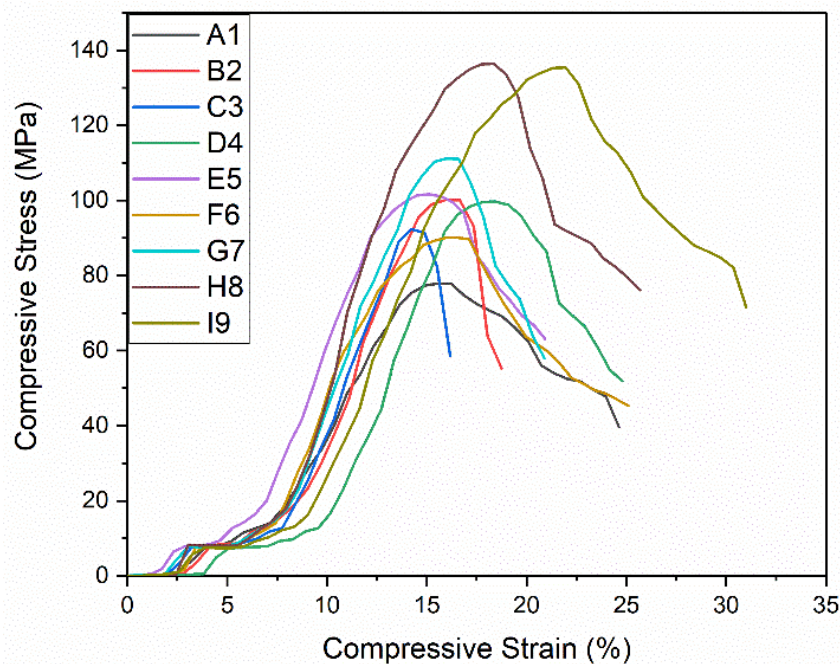


**Fig. 4.** Compressive stress vs. compressive strain curves of specimens

**Statistical analysis.** Statistical data obtained after the analysis of Taguchi DOE are given below in Table 4. This can be seen from the table that the maximum value of the SN ratio for both the hardness and ultimate compressive stress was obtained for specimen H8. This shows that, out of these nine sets of process parameters, parameters used for the fabrication of specimen H8 are optimum process parameters.

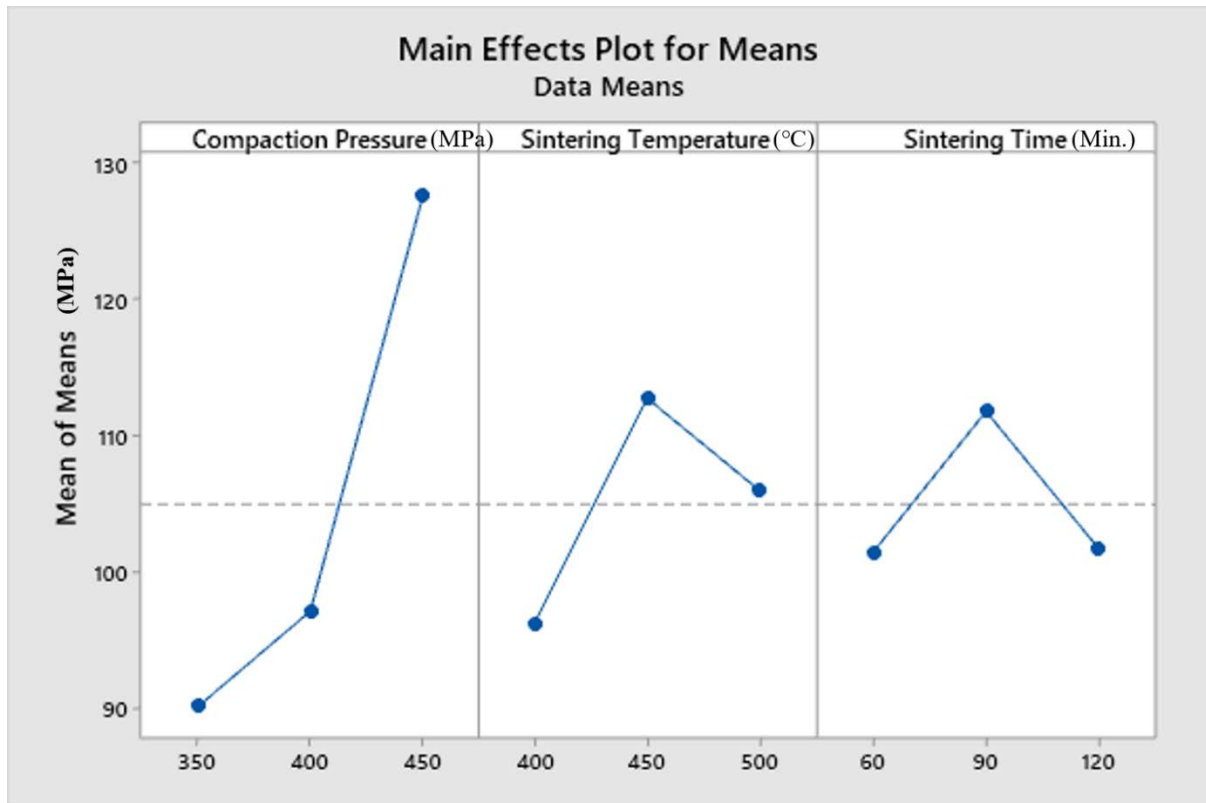
The main effect plots for means for ultimate compressive stress and hardness are given in Fig. 5 and Fig. 6 respectively. This can be seen from the graph that hardness and ultimate compressive stress continuously increased with the increase in the compaction pressure. So, out of the selected three levels of compaction pressure, 450 MPa compaction pressure is the optimum compaction pressure for the reprocessing of the AZ91 magnesium alloy with respect to hardness and compressive stress. Sintering temperature and sintering time have a mixed effect on hardness and compressive stress. Hardness and compressive stress first increased with the increase in the sintering temperature and sintering time. But on the further increase in sintering temperature and sintering time, hardness and compressive stress reduced because of recrystallization and grain growth in the material.

Table 4. Statistical results for hardness and ultimate compressive stress

S. No.	Sample ID	Hardness (Hv)	UCS (MPa)	SN Ratio for Hardness	SN Ratio for UCS
1	A1	38.05	77.864	31.607	37.8267
2	B2	52.4	100.153	34.386	40.0133
3	C3	48.11	92.329	33.644	39.3068
4	D4	55.93	99.724	34.952	39.9760
5	E5	63.85	101.636	36.103	40.1410
6	F6	41.72	90.068	32.406	39.0914
7	G7	68.79	111.120	36.750	40.9159
8	H8	80.8	136.440	38.148	42.6988
9	I9	75.79	135.461	37.592	42.6363

So, out of the selected three levels of sintering temperature and sintering time, the second level of both the sintering temperature (450°) and sintering time (90 minutes) are the optimum levels of process parameters. So, the optimum set of process parameters is not available in the present nine sets of process parameters. The optimum set of process parameters for the given design will be a combination of the 3<sup>rd</sup> level of compaction pressure (450 MPa), 2<sup>nd</sup> level of both the sintering temperature (450°), and sintering time (90 minutes).

Response data for mean UCS values and mean hardness values are given in Table 5 and Table 6. Ranks of parameters based on their effect on UCS and hardness are in the response tables for means. This can be seen that compaction pressure is ranked first in the response table for means for both the UCS and hardness, followed by sintering temperature and sintering time. This shows that compaction pressure is the most important parameter in powder metallurgy process, followed by sintering temperature and sintering time.



**Fig. 5.** Main effect plots for ultimate compressive stress

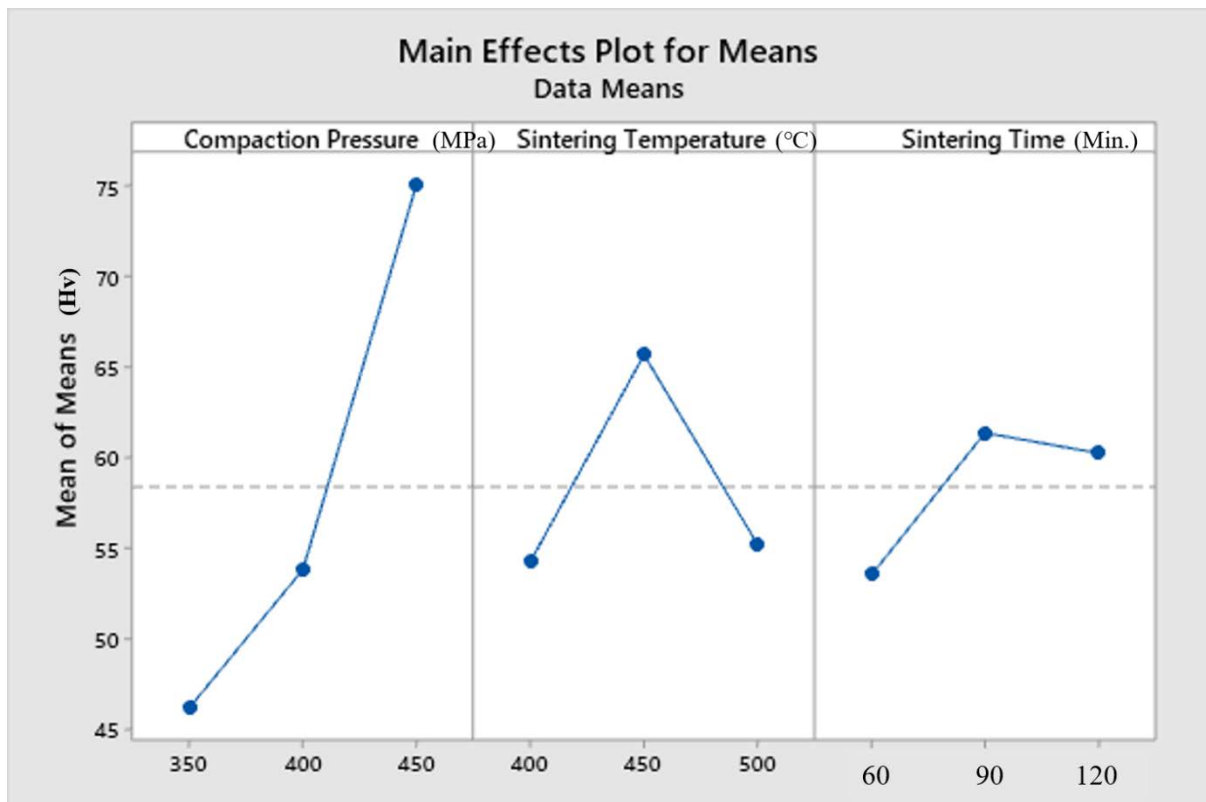


**Fig. 6.** Main effect plots for ultimate compressive stress for hardness

Table 5. Response data for mean UCS values

Level	Compaction Pressure	Sintering Temperature	Sintering Time
1	90.12	96.24	101.46
2	97.14	112.74	111.78
3	127.67	105.95	101.70
Delta	37.56	16.51	10.32
Rank	1	2	3

Table 6 Response data for mean hardness values

Level	Compaction Pressure	Sintering Temperature	Sintering Time
1	46.19	54.26	53.52
2	53.83	65.68	61.37
3	75.13	55.21	60.25
Delta	28.94	11.43	7.85
Rank	1	2	3

The analysis of variance data for UCS and hardness are given in Table 7 and Table 8 respectively. F and P values in the analysis of variance data are the measure of the effectiveness of parameters. Parameter with high effectiveness has a high value of F and low value of P. F-values also confirm the same order of the effectiveness of parameters, as obtained from response data for means for UCS and hardness.

Table 7. Analysis of variance data for UCS

Source	DF	Adj SS	Adj MS	F-Value	P-Value
Compaction Pressure	2	2392.2	1196.10	19.47	0.049
Sintering Temperature	2	413.0	206.51	3.36	0.229
Sintering Time	2	208.3	104.14	1.70	0.371
Error	2	122.9	61.44		
Total	8	3136.4			

The regression equation for UCS obtained after ANOVA analysis is given below. Optimum value of UCS can be obtained by using this equation by putting the value of optimum levels of process parameters. Optimum value of ultimate compressive stress, obtained from the equation using compaction pressure as 450 MPa, sintering temperature as 450°, and sintering time as 90 minutes, is 138.90 MPa.

$$UCS = 160.2 - 3.659 X + 1.845 Y + 4.08 Z + 0.004701 X^2 - 0.002849 Y^2 - 0.008814 Z^2 + 0.001816 XY - 0.006034 XZ,$$

where:

UCS = Ultimate Compressive Stress (MPa)

X = Compaction Pressure (MPa)

Y = Sintering Temperature (°)

Z = Sintering Time (minutes)

Table 8. Analysis of variance data for hardness

Source	DF	Adj SS	Adj MS	F-Value	P-Value
Compaction Pressure	2	1349.40	674.70	16.18	0.058
Sintering Temperature	2	241.23	120.62	2.89	0.257
Sintering Time	2	108.13	54.07	1.30	0.435
Error	2	83.39	41.69		
Total	8	1782.15			

The regression equation for hardness obtained after ANOVA analysis is given below. Optimum value of hardness can be obtained by using this equation by putting the value of optimum levels of process parameters as the optimum set of parameters is not present in the current design of the experiment. Optimum value of hardness, obtained from the regression equation, using compaction pressure as 450 MPa, sintering temperature as 450°, and sintering time as 90 minutes, is 81.41 Hv.

$$H = -37.84 - 2.342 X + 1.775 Y + 2.548 Z + 0.002729 X^2 - 0.002919 Y^2 - 0.002248 Z^2 + 0.001971 XY - 0.004873 XZ,$$

where:

- H = Hardness (Hv)
- X = Compaction Pressure (MPa)
- Y = Sintering Temperature (°)
- Z = Sintering Time (minutes)

#### 4. Experimental validation

Experimental validation of results obtained from regression equations for hardness and UCS was done. Samples were produced using the obtained optimal parameters and hardness and compression tests were performed. Regression analysis results and experimental results are given in Table 9. It can be observed that the percentage error between the experimental results and results obtained from the regression equation is less than 10% for both the hardness and UCS. So, regression equations are giving satisfactory results and can be used to determine the value of hardness and ultimate compressive stress at other sets of parameters.

Table 9 Difference between experimental and regression analysis results

	Ultimate Compressive Stress (MPa)	Hardness (Hv)
Regression Analysis Results	138.9	81.81
Experimental Results	144.89	82.12
Error	4.31%	0.4%

#### 5. Conclusions

The following conclusions are drawn after the characterization and testing of the AZ91 magnesium alloy samples prepared by powder metallurgy technique:

- Out of the present nine sets of process parameters, H8 is the best set of process parameters for both the hardness and compressive stress. But the optimum set of the parameters is not present in the current design of the experiment.
- Optimum level of compaction pressure for both the hardness and compressive stress is 3<sup>rd</sup> level (450 MPa).
- Optimum level of sintering temperature for both the hardness and compressive stress is 2<sup>nd</sup> level (450°).

- Optimum level of sintering time for both the hardness and compressive stress is 2nd level (90 minutes).
- Out of the three selected parameters, compaction pressure is the most effective process parameter for both the hardness and ultimate compressive stress, followed by sintering temperature and sintering time.
- Optimum values of hardness and ultimate compressive stress obtained from the regression equations are 81.81 Hv and 138.90 MPa respectively.
- Experimental value of ultimate compressive stress and hardness for samples processed at optimal parameters is 144.89 MPa and 82.12.
- Compression test results obtained from regression analysis are 4.31% less than the experimental results.
- Micro-hardness results obtained from regression analysis are 0.4% less than the experimental results.
- This shows that the regression analysis results are in good agreement with experimental results.

## References

1. Cai H, Guo F. Study on microstructure and strengthening mechanism of AZ91-Y magnesium alloy. *Materials Research Express*. 2018;5(3): 036501.
2. Ghasali E, Alizadeh M, Niazmand M, Ebadzadeh T. Fabrication of magnesium-boron carbide metal matrix composite by powder metallurgy route: Comparison between microwave and spark plasma sintering. *Journal of Alloys and Compounds*. 2016;697(1): 200-207.
3. Goh CS, Wei J, Lee LC, Gupta M. Development of novel carbon nanotube reinforced magnesium nanocomposites using the powder metallurgy technique. *Nanotechnology*. 2006;17: 7-12.
4. Guleryuz LF, Ozan S, Uzunsoy D, Ipek R. An Investigation of The Microstructure and Mechanical Properties of B4C Reinforced PM Magnesium Matrix Composites. *Powder Metallurgy and Metal Ceramics*. 2012;51: 456-462.
5. Akcamli N, Senyurt B. Fabrication and characterization of in-situ Al<sub>3</sub>Ni intermetallic and CeO<sub>2</sub> particulate-reinforced aluminum matrix composites. *Ceramics International*. 2021;47(15): 21197-21206.
6. Ao M, Liu H, Dong C. The effect of La<sub>2</sub>O<sub>3</sub> addition on intermetallic-free aluminium matrix composites reinforced with TiC and Al<sub>2</sub>O<sub>3</sub> ceramic particles. *Ceramics International*. 2019;45(9): 12001-12009.
7. Blawert C, Hort N, Kainer KU. Automotive applications of Magnesium and its alloys. *Transactions of the Indian Institute of Metals. Met*. 2004;57(4): 397-408.
8. Kandpal BC. Production Technologies of Metal Matrix: A review. *International Journal of Research in Mechanical Engineering & Technology*. 2014;4(2).
9. Musfirah AH, Jaharah AG. Magnesium and Aluminum Alloys in Automotive Industry. *Journal of Applied Sciences Research*. 2012;8(9): 4865-4875.
10. Nie KB, Wang XJ, Hu XS, Xu L, Wu K. Microstructure and tensile properties of micro-SiC particles reinforced magnesium matrix composites produced by semisolid stirring assisted ultrasonic vibration. *Materials Science and Engineering A*. 2011;528: 29-30.
11. Kulekci MK. Magnesium and its alloys applications in automotive industry. *The International Journal of Advanced Manufacturing Technology*. 2008;39: 851-865.
12. Rashad M, Pan F, Asif M, She J, Ullah A. Improved mechanical proprieties of "magnesium based composites" with titanium aluminum hybrids. *Journal of Magnesium and Alloys*. 2015;3: 1-9.

13. Kumar D, Bharti A, Azam SM, Kumar N, Tripathi H. Investigations of Mechanical Properties of Copper Matrix Hybrid Composite. In: *Advances in Mechanical Engineering*. 2020. p.671-676.
14. Kumar N, Bharti A, Saxena KK. A re-analysis of effect of various process parameters on the mechanical properties of Mg based MMCs fabricated by powder metallurgy technique. *Materials Today: Proceedings*. 2020;26(2): 1953-1959.
15. Kumar N, Bharti A, Saxena KK. A re-investigation: Effect of powder metallurgy parameters on the physical and mechanical properties of aluminium matrix composites. *Materials Today: Proceedings*. 2021;44(1): 2188-2193.
16. Wang HY, Jiang QC, Wang Y, Ma BX, Zhao F. Fabrication of TiB<sub>2</sub> particulate reinforced magnesium matrix composites by powder metallurgy. *Materials Letters*. 2004;58: 3509-3513.
17. Kumar N, Bharti A, Dixit M, Nigam A. Effect of Powder Metallurgy Process and its Parameters on the Mechanical and Electrical Properties of Copper-Based Materials: Literature Review. *Powder Metallurgy and Metal Ceramics*. 2020;59: 401-410.
18. Kumar N, Bharti A, Tripathi H. Investigation of Microstructural and Mechanical Properties of Magnesium Matrix Hybrid Composite. In: *Advances in Mechanical Engineering*. 2020. p. 661-669.
19. Yu H, Zhou H, Sun Y. Microstructures and mechanical properties of ultrafine-grained Ti/AZ31 magnesium matrix composite prepared by powder metallurgy. *Advanced Powder Technology*. 2018;29(12): 3241-3249.
20. Erçetin A, Özgün O, Aslantas K, Aykutoğlu G. The microstructure, degradation behavior and cytotoxicity effect of Mg-Sn-Zn alloys in vitro tests. *SN Applied Sciences*. 2020;2(2).
21. Erçetin A. A novel Mg-Sn-Zn-Al-Mn magnesium alloy with superior corrosion properties. *Metallurgical Research & Technology*. 2011;118(5): 504.
22. Ozgun O, Aslantas K, Ercetin A. Powder metallurgy Mg-Sn alloys: Production and characterization. *Scientia Iranica*. 2020;27(3): 1255-1265.
23. Burke P, Kipouros GJ. Development of Magnesium Powder Metallurgy AZ31 Alloy Using Commercially Available Powders. *High. Temp. Mater. Proc.* 2011;30(1): 51-56.
24. Durai TJ, Sivapragash M, Sahayaraj ME. Effect of Sintering Temperature on Mechanical Properties of Mg-Zr Alloy. *International Journal of Mechanical and Production Engineering Research and Development*. 2017;7(5): 117-122.
25. Gunes I, Uygunoglu T, Erdogan M. Effect of Sintering Duration on Some Properties of Pure Magnesium. *Powder Metallurgy and Metal Ceramics*. 2015;54(3-4): 156-165.
26. Kucuk O, Elfarah TTK, Islak S, Ozorak C. Optimization by Using Taguchi Method of the Production of Magnesium-Matrix Carbide Reinforced Composites by Powder Metallurgy Method. *Metals*. 2017;7: 352.
27. Kumar N, Bharti A. Review on Powder Metallurgy: A Novel Technique for Recycling and Foaming of Aluminium-Based Materials. *Powder Metallurgy and Metal Ceramics*. 2021;60(1-2): 52-59.
28. Lee WJ, Kim YJ, Kang NH, Park IM, Park YH. Finite-element modeling of the particle clustering effect in a powder-metallurgy-processed ceramic-particle-reinforced metal matrix composite on its mechanical properties. *Mechanics of Composite Materials*. 2011;46: 639-648.
29. Erçetin A. Application of the hot press method to produce new Mg alloys: Characterization, mechanical properties, and effect of Al addition. *Journal of Materials Engineering and Performance*. 2021;30(6): 4254-4262.

## THE AUTHORS

**Kumar N.**

e-mail: [chaudhary56naveen@gmail.com](mailto:chaudhary56naveen@gmail.com)

ORCID: - 0000-0002-6918-4384

**Bharti A.**

e-mail: [abharti@mnnit.ac.in](mailto:abharti@mnnit.ac.in)

ORCID: - 0000-0003-2809-9674

# A study on mechanical and dielectric properties of B<sub>4</sub>C and Al dispersed single-layered epoxy-based polymer composites fabricated through molding and curing route

S. Vignesh<sup>1</sup>, J.T. Winowlin Jappes<sup>1</sup>✉, S. Nagaveena<sup>2</sup>, K. Sankaranarayanan<sup>1</sup>,  
R. Krishna Sharma<sup>3</sup>, N.C. Brintha<sup>4</sup>

<sup>1</sup>Department of Mechanical Engineering, Kalasalingam Academy of Research and Education, Tamilnadu, India-626126

<sup>2</sup>Department of Nanoscience and Nanotechnology, S.T. Hindu College, Nagercoil, Tamilnadu-629002

<sup>3</sup>Department of Physics, S.T. Hindu College, Nagercoil, Tamilnadu, India-629002

<sup>4</sup>Department of Computer Science & Engineering, Kalasalingam Academy of Research and Education, Tamilnadu, India-626126

✉vickyrsnair@gmail.com

**Abstract.** The work aims in developing epoxy composites with different compositions of boron carbide (5, 10, 15, and 20 wt.%) added with aluminium (10 wt %) for studying the mechanical and dielectric behavior. It was found that the tensile strength of the samples initially increased with an increase in reinforcements and then decreased with an increase in B<sub>4</sub>C content beyond 10 wt. %. Flexural strength, on the other hand, increased with the addition of B<sub>4</sub>C particles. Moreover, the impact strength of the samples decreased with an increase in the addition of the B<sub>4</sub>C particles. The dielectric properties were studied by considering various factors like temperature and frequency. The samples were subjected to frequencies 100Hz, 1kHz, 10kHz, 100kHz, and 1MHz, and temperatures ranged from 40°C to 150°C. As a result, it was found that the dielectric loss factor was increased with increasing temperature. Further, at higher frequencies, an increase in the dielectric constant and a decrease in the dielectric loss factor were evidenced which concluded the material's suitability for energy storage applications.

**Keywords:** conducting polymers, dielectric properties, mechanical properties, molding, particle dispersed

**Acknowledgements.** The author acknowledges the support rendered by King Mongkut's University of Technology North Bangkok, Bangkok, Thailand and The S.T. Hindu College, Nagercoil, for providing necessary research support.

**Citation:** Vignesh S., Winowlin Jappes J.T., Nagaveena S., Sankaranarayanan K., Krishna Sharma R., Brintha N.C. A study on mechanical and dielectric properties of B<sub>4</sub>C and Al dispersed single-layered epoxy-based polymer composites fabricated through molding and curing route. *Materials Physics and Mechanics*. 2022;48(3): 328-341. DOI: 10.18149/MPM.4832022\_4.

## 1. Introduction

Increasing demand in the field of industrial packaging and microelectronics particularly in energy storage has led to the quest in searching for advanced novel materials. In industrial packaging, the materials are expected to be mechanically excellent in their characteristics, and in electronics, the need is for electrically conductive polymeric materials with a conductive core and an insulating shell. Several kinds of research are underway in particulate reinforced polymer-based composites in which the primary phase is the polymer matrix whereas, the secondary phase possessing a good dielectric constant is made to disperse in the primary phase through conventional fabrication routes. Researchers have revealed the possibility of consuming these polymers possessing electrical conductivity with the aid of their secondary phases but also not trading off the weight of the material [1-2]. Epoxy, is a polymeric hinderer of the flow of electrons owing to the inherent low dielectric constant but mechanically possesses wide characteristics [3-5]. However, scientists revealed the ability to increase the dielectric constant of the polymer through the mode of particulate addition utmost to 50 vol.% [6]. On the other hand, reports revealed the detriment of mechanical properties owing to the augmented addition of the fillers [7-9]. Works suggest the addition of particles improves the dielectric properties through the following two notions such as (i) establishing contact between particles, and (ii) making the electron move across a hindrance, widely called electron tunneling. However the former and the latter mechanism can be made possible by generating a 3D-conductive network facilitated by the closeness of the filler particles and transportation of electrons amidst closest particles through a thin layer hindrance by polymer [10].

Here the subject of concern is not restricted to conductivity but also the mechanical property of the material being produced. Hence the proper choice of dispersing reinforcement should be taken. Particularly Boron carbide (B<sub>4</sub>C) based hard materials are seeking attention in the field of structural, tribological-interactive applications [11-20]. Moreover, its excellent hardness and density make it suitable for ballistic applications as well. Anyhow, B<sub>4</sub>C finds less use owing to its increased brittleness [21-23].

Also, aluminum (Al), possessing very less weight, excellent electrical conductivity, and good thermal conductivity can be used in electrical and electronic applications as it has the ability to withstand heat resulting from high operating voltage. The electrical and mechanical characteristics of aluminium along with epoxy were studied and revealed the yield in dielectric properties with respect to that of filler concentrations [24]. Nevertheless, the works are almost void in the case of augmentation of B<sub>4</sub>C and aluminium for the dielectric property through the molding and curing route. Hence in this work, an attempt is made to study the mechanical and electrical properties of the B<sub>4</sub>C and Al dispersed epoxy-based single-layered polymer composite of varying compositions of B<sub>4</sub>C and Al.

## 2. Materials and Methods

**Materials.** The work was carried out using commercially available B<sub>4</sub>C (10µm), Al powder (10µm), epoxy LY566, and its corresponding hardener. The procured metallic powders were subjected to a scanning electron microscope equipped with an electro dispersive spectrum analyzer using JEOL-JSM-5600LV scanning electron microscope equipped with EDS under 20kV and exposure time of 50s and are depicted in Fig. 1 and Fig. 2. The matrix and particle reinforcement were made with different compositions tabulated as shown in Table 1. The different samples were fabricated through the molding and curing method which is depicted in Fig. 3.

Before the fabrication of the composite material, the epoxy matrix and the reinforcement particles were mixed mechanically and were subjected to the ultrasonic dispersion technique for 45 minutes. The initial mixing was then followed by the addition of

hardener to the mixture and was further stirred mechanically for 15 minutes at a uniform speed of 200rpm. The epoxy matrix and the hardener used were mixed in a ratio of 2:1. Subsequently, the liquid mixture of matrix and dispersed particles was poured into a glass mold of 300mm × 130mm × 5mm. Further, the samples from the composite were cut as per the ASTM standard and were subjected to mechanical, electrical, and fractography studies and the result are discussed in the forthcoming chapters.

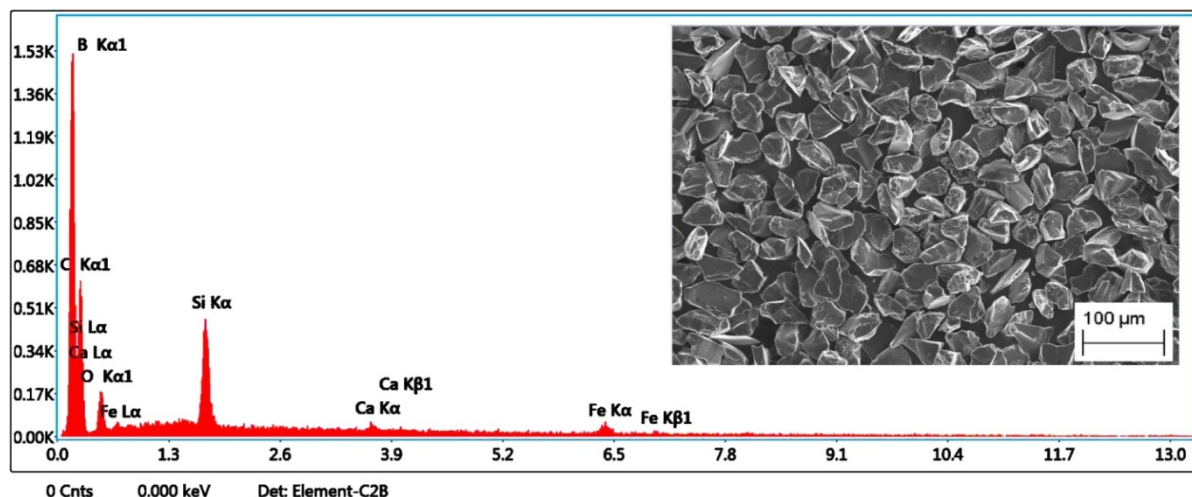


**Fig. 1.** SEM & EDS spectra depicting the particle size and composition of B<sub>4</sub>C particles

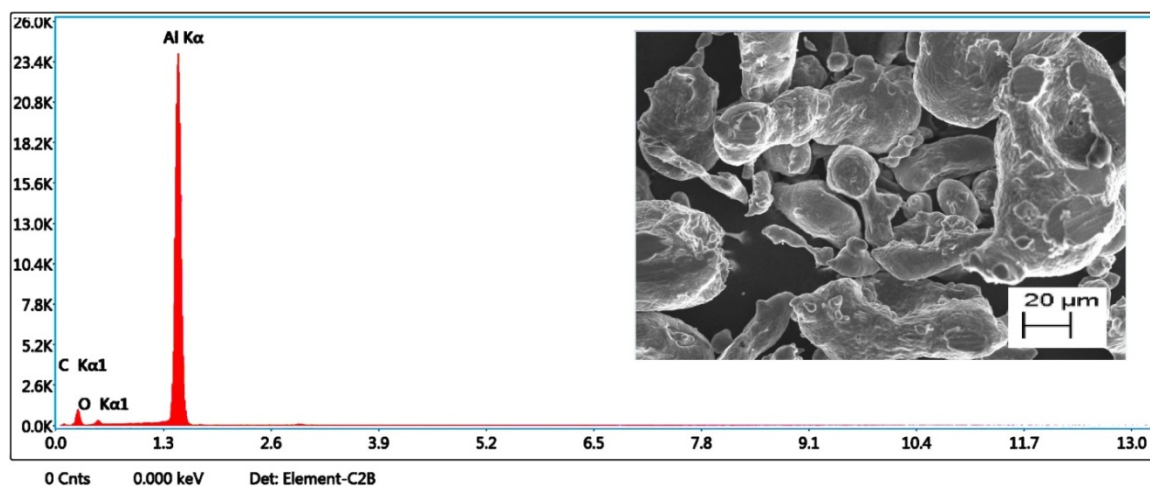


**Fig.2.** SEM & EDS spectra depicting the particle size and composition of Al particles

Table 1. Composition of the samples prepared

Samples	Composition (in wt %)				Weight (g)			
	B <sub>4</sub> C	Al	Epoxy	Hardener	B <sub>4</sub> C	Al	Epoxy	Hardener
<b>A</b>	5	10	57	28	6	12	120	60
<b>B</b>	10	10	54	26	12	12	120	60
<b>C</b>	15	10	50	25	18	12	120	60
<b>D</b>	20	10	47	23	24	12	120	60

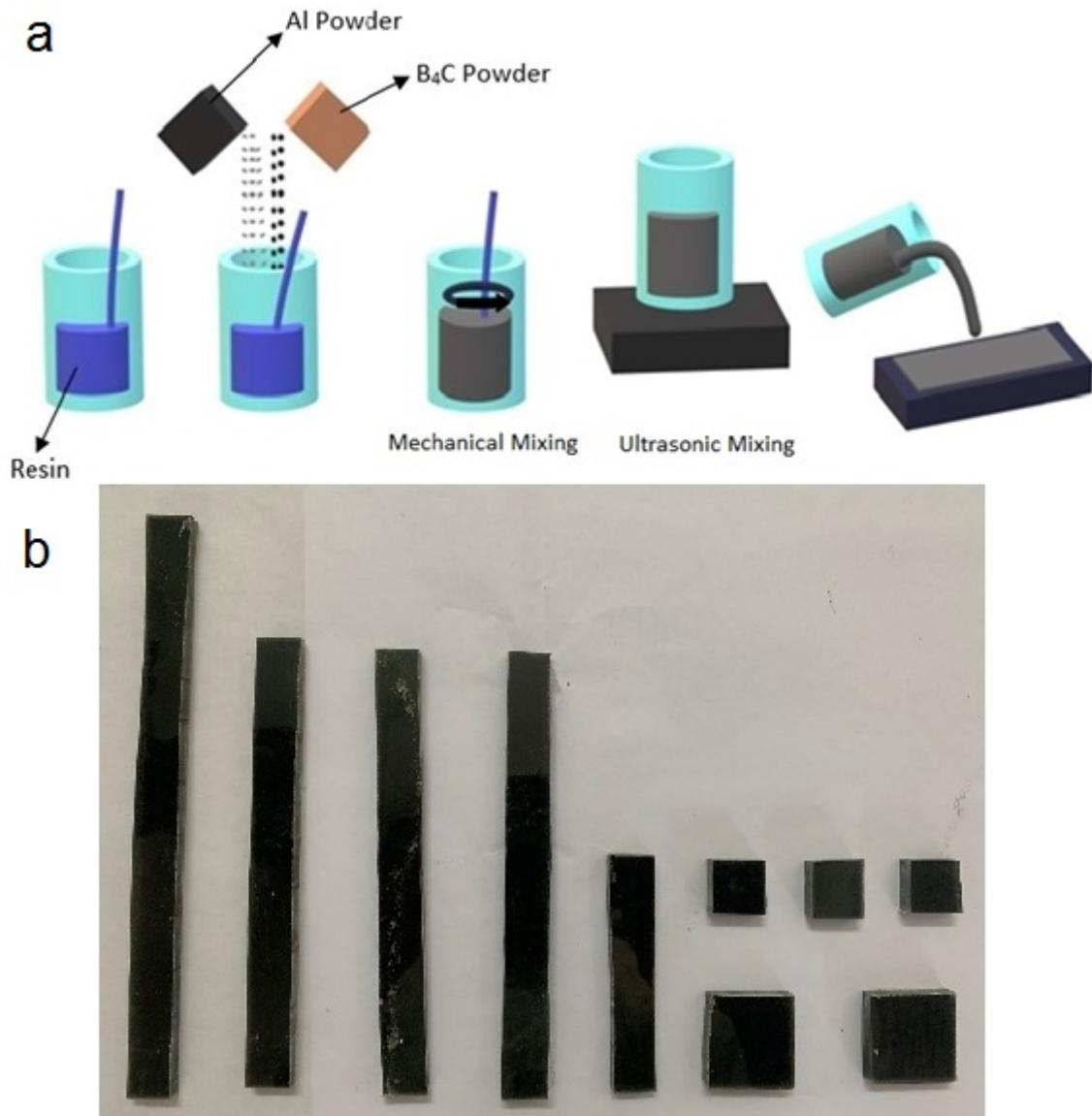


**Fig. 3.** a – composite fabrication method through molding and curing,  
b – as prepared composite specimen

**Mechanical Testing.** The samples prepared were tested for their tensile strength, flexural strength, and impact strength (Izod-v notch samples) after carefully adhering to the ASTM D638, ASTM D790, and ASTM D256 standards respectively. The mechanical studies were carried out in 4 samples, and the results are discussed in the forthcoming sections. The fractography of the tested samples was done by JEOL-JSM-5600LV scanning electron microscope under 15kV and exposure time of 50s. The fractured sections were carefully cut from the samples and were subjected to SEM in order to study the fractography, which is depicted in Fig. 3b.

**Electrical Characterization.** The prepared samples were subjected to electrical characterization to study the capacitance  $C_p$  and dielectric loss factor  $\tan\delta$  at various temperatures ranging from 40°C to 150°C along with a range of frequencies from 100Hz, 1kHz, 10kHz, 100kHz, and 1MHz using an LCR Meter Agilent 4284A through the parallel plate capacitor method. Annealing was done to the samples while holding the same in the sample holder at 160°C prior to observations. The readings were taken during the cooling process of the sample, and it should be noted that the temperature was controlled with an accuracy of

$\pm 0.5^\circ\text{C}$ . Air capacitance  $C_a$  was measured and using the relation  $\epsilon_r = C_p/C_a$  the dielectric constant of the samples was measured. It should be also noted that the AC conductivity of the samples was determined by the relation

$$\sigma_{AC} = \epsilon_0 \epsilon_r \omega \tan \delta,$$

where  $\epsilon_0$  is the permittivity of free space and  $\omega$  is the angular frequency and is given by  $\omega = 2\pi f$ ,  $f$  is the applied frequency.

### 3. Results & discussions

**Tensile, flexural & impact properties.** Figure 4 depicts the tensile and flexural characteristics of the samples prepared. The tensile strength of the sample clearly notifies that the addition of  $B_4C$  beyond 10 wt. % decrements the tensile characteristics of the samples whereas an increase in addition of  $B_4C$  from 5 wt. % to 10 wt. % increases the tensile strength. On the other hand, the ductility of the samples was reduced upon increased augmentation of  $B_4C$ . The increment in tensile strength was attributed due to the better dispersion of the particles in the sample. It is also possible to achieve the tensile characteristics, as the addition of aluminium could result in an improved modulus of tensile. However, the rest of the samples with the increased addition of  $B_4C$  resulted in reduced tensile properties which could be attributed due to the following causes: Primary contribution to the reduction could be the agglomeration of the reinforcement particles owing to the increased addition of the same [25] and the secondary contribution could be a decline in the surface area of contact between the particle and the matrix because of the agglomeration. The former reason was found to be there in the samples and is evident from the tensile fractography as in Fig. 5.

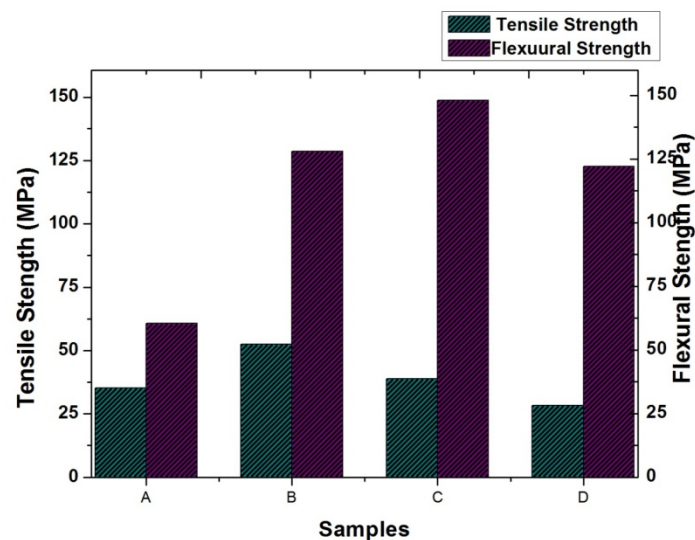


**Fig. 4.** Tensile & Flexural Strength of samples A, B, C & D

Moreover, it is also evident from Fig. 6 that some known pattern like chevron is significantly visible in the tested sample. It is obvious that the chevron-like pattern signifies the failure due to brittleness [26] as the presence of Al and  $B_4C$  in epoxy will have both ductility and brittleness which is inherent by their nature. It is also noted from the fractography that the sample exhibited forceful separation between epoxy and reinforcement particulates. Moreover, the sharp protruded shapes as evident from Fig. 7, that emerged upon the action of loading led to cracking and crack propagation as a result ended with brittle fracture even though with the presence of ductile aluminium particles [27].

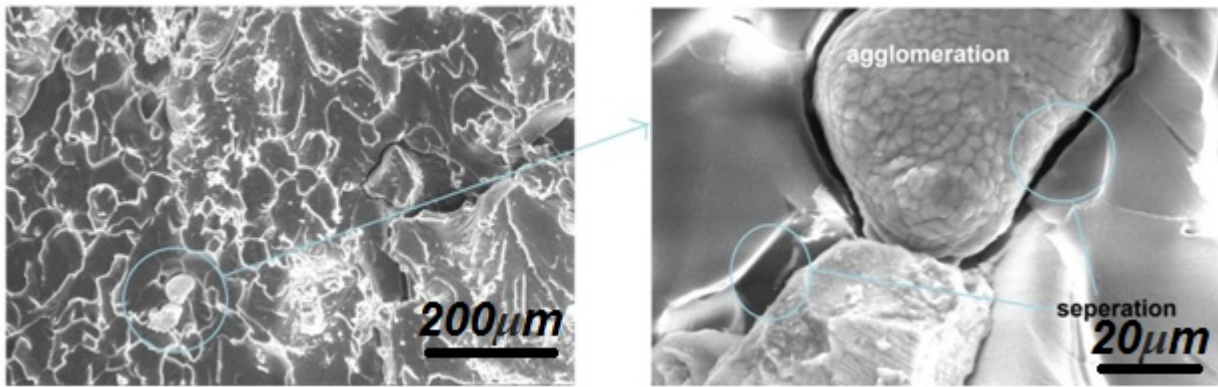


**Fig. 5.** SEM micrograph depicting agglomeration and separation of B<sub>4</sub>C particles (after tensile testing)

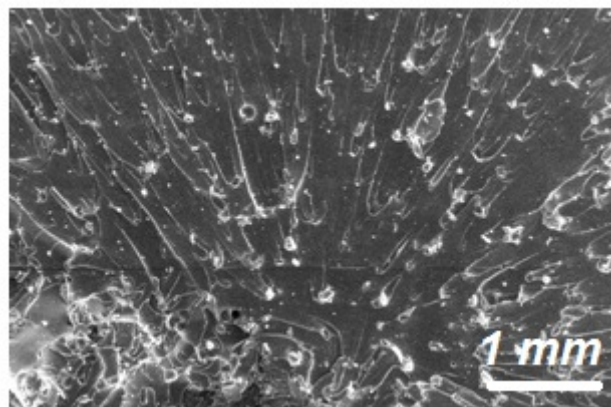


**Fig. 6.** SEM micrograph depicting Chevron-like patterns of B<sub>4</sub>C particles

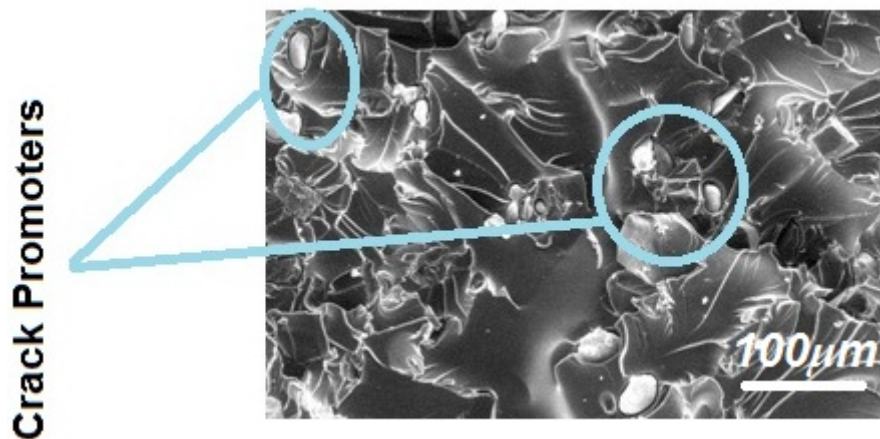


**Fig. 7.** SEM micrograph depicting sharp-edged crack promoters

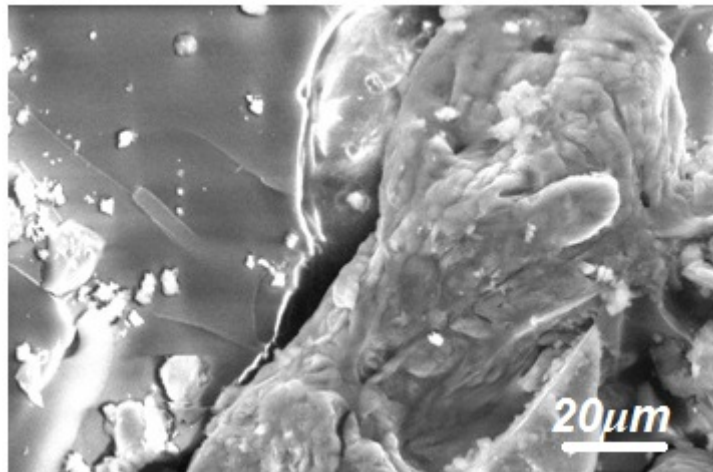


**Fig. 8.** SEM micrograph depicting the separation of B<sub>4</sub>C & Al particles from the epoxy matrix

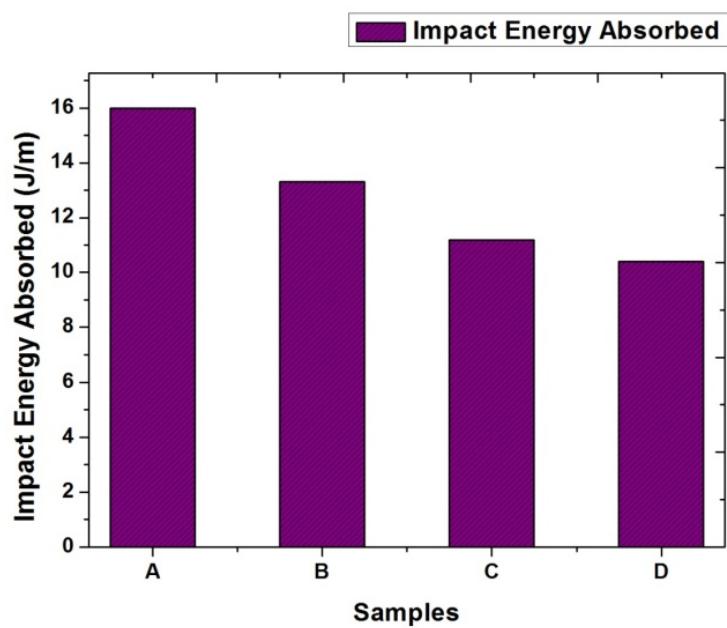


**Fig. 9.** Impact Energy Absorbed of different samples

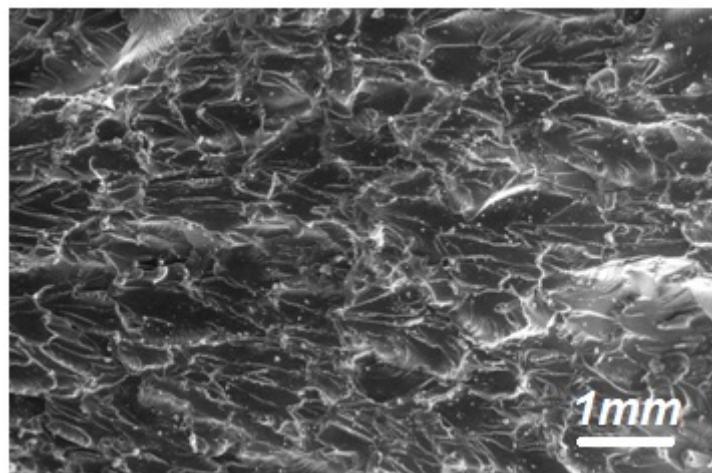


**Fig. 10.** SEM micrograph depicting mountain-like pattern causing brittle failure

The flexural strength of the specimen depicted in Fig. 4 clearly shows the increase in flexural strength with the increased addition of B<sub>4</sub>C particles. The added particles, upon loading, during the test, resulted in the de-lamination of the reinforcements from the epoxy matrix as evident from the Fig. 8, and thus contributed to the reduced flexural strength of the sample A. Since, the sample A incorporated with the least amount of B<sub>4</sub>C has resulted with the least dispersion and is more prone to separation at the zone where de-lamination take place. On the other hand, the impact strength of the samples decreased with an increase in the addition of the B<sub>4</sub>C particles as in Fig. 9. It is because the increase in tensile strength results in the detrimental value of impact strength of the specimen. It is also evident from Fig. 10 that the fractography resembles mountain-like patterns tend to propagate cracks through the v-notch resulting in the brittle failure of the specimen.

**Electrical Properties.** The fabricated samples A to D were subjected to AC conductivity studies to measure the dielectric constant, dielectric loss factor, and electrical conductivity for five different frequencies at different temperatures, and the results are tabulated in Table 2. The parameters were tested with respect to their temperature dependency and are shown in Figs. 11-13. In general, the dielectric properties were found to increase with respect to that temperature. It was also observed from Figs. 11-12, the dielectric constant tends to increase with respect to frequency and the dielectric loss factor decreased with augmented frequency. However, on the other hand, the AC conductivity of the samples increased with an increase in frequency.

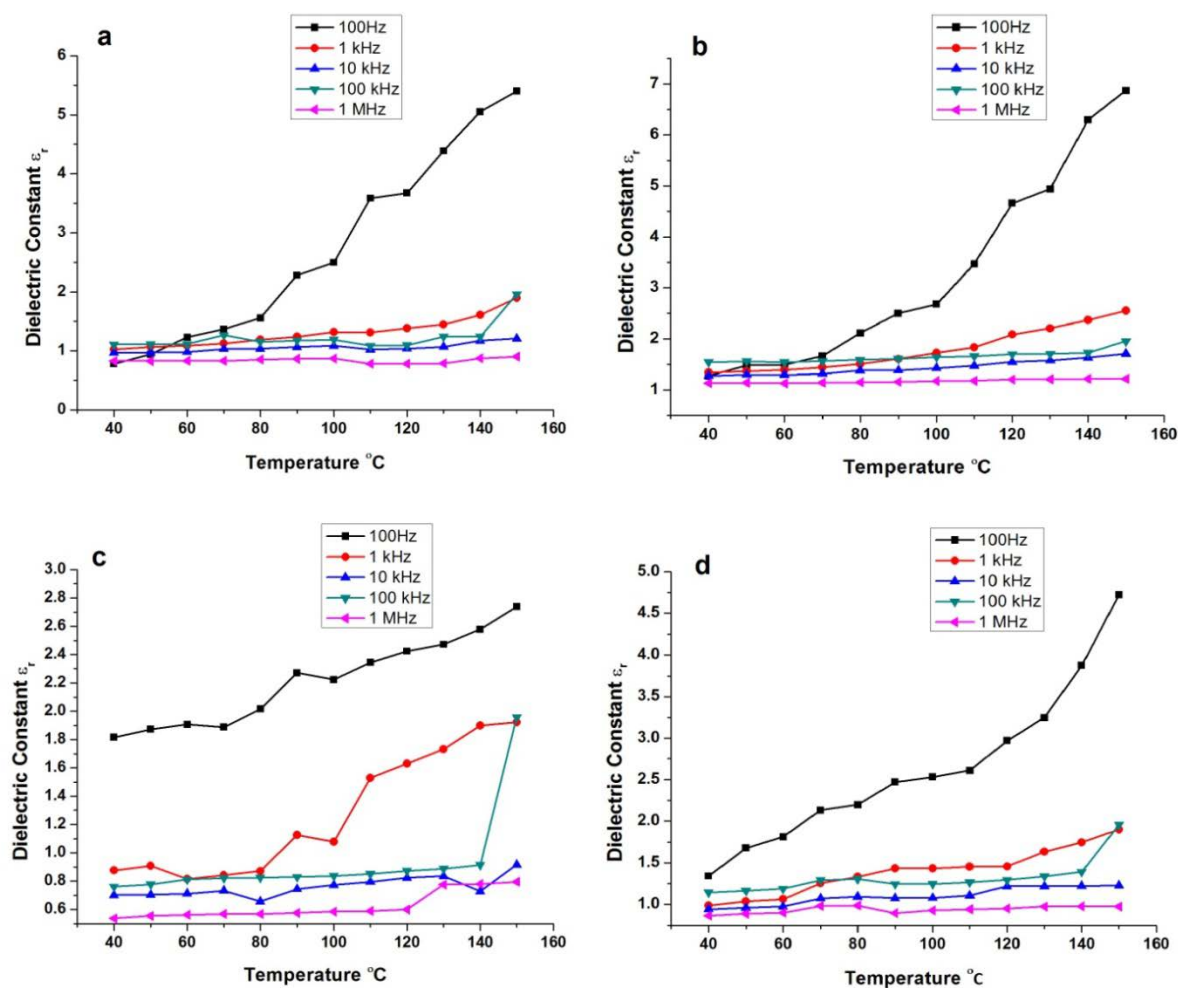


**Fig. 11.** Dielectric constants for samples viz., a) Sample A, b) Sample B, c) Sample C and d) Sample D

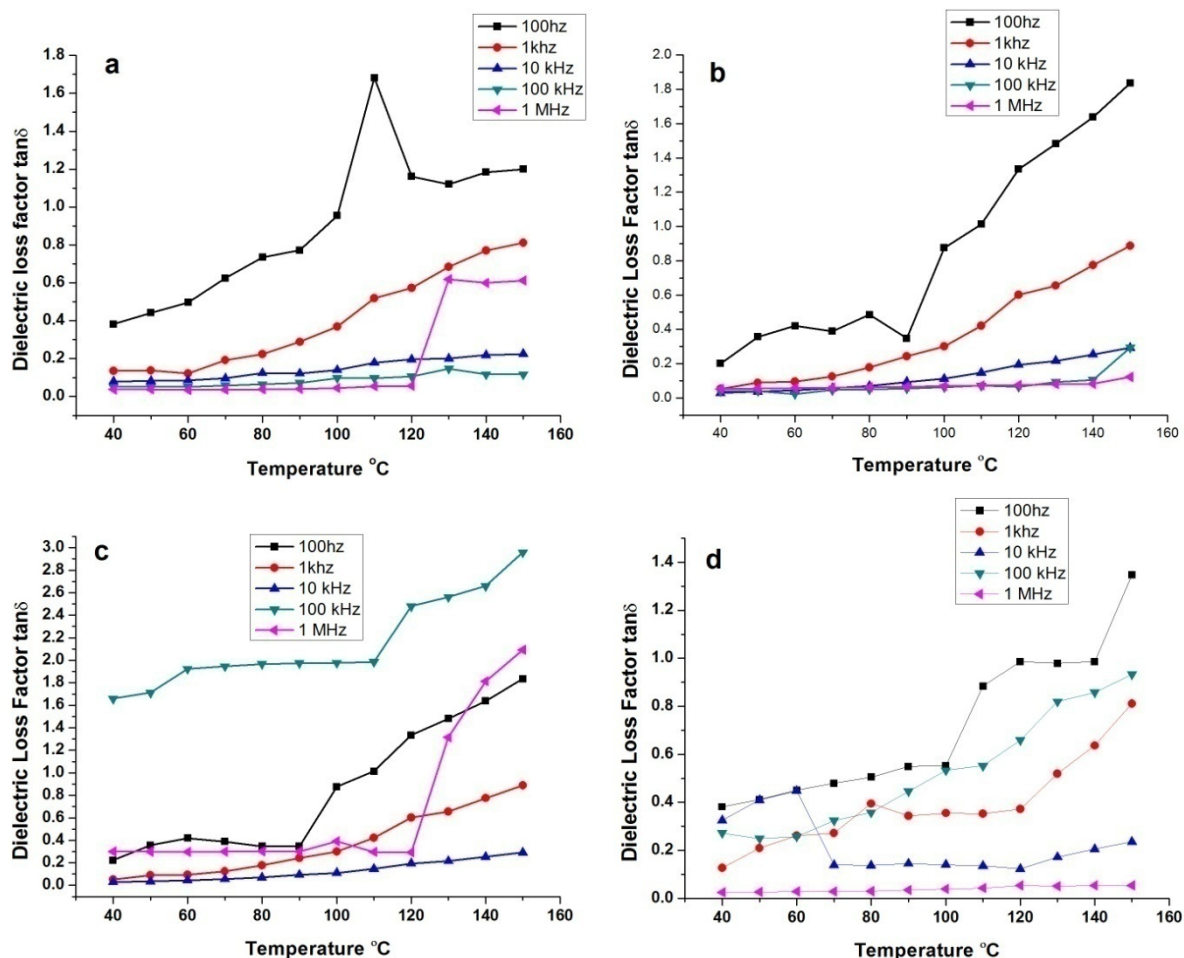


**Fig. 12.** Dielectric loss factor for samples viz., a) Sample A, b) Sample B, c) Sample C and d) Sample D

The presence of different varieties of polarizations in the materials, in general, contributes to the dielectric behavior of the same [28]. Moreover, it is well known that the dielectric constant of epoxy increases predominantly by reducing the free volume of the matrix and is accompanied by improving the polarization of the matrix [29-30]. However, in all the samples, the presence of reinforcement particles contributes to the reduction in the free volume of the epoxy matrix by occupying the volume owing to uniform dispersion. It should be also noted that the existence of these particles provides polarization change thus resulting in a high dielectric constant. Moreover, the higher dielectric constant at lower frequencies is owing to space charge polarization and rotational polarization as well [31]. It should be also noted that the orientation of dipoles would be enhanced upon the effect of temperature, tending to yield the dipole moment [32]. The increase in frequency will give rise to electronic polarization thereby reducing the dielectric constant values in some samples. Further, research suggests that an increase in the dielectric constant of the materials makes the material suitable for energy storage applications to a larger extent. Also, the dielectric characteristics of polymers greatly rely upon the mechanisms of polarization that includes electronic, atomic, dipolar interfacial, and ionic [39]. Moreover, the polarization due to orientation is a predominant factor in achieving better dielectric properties, particularly epoxy-based composites [40] and this could be the possible reason for the improvement of the dielectric characteristics of the sample.

It should be taken into account that dielectric loss factors, are a phenomenon of dissipating heat at the expense of electric energy. Insulating material will tend to have less dielectric loss [33-34]. However, the increase in dielectric constant and dielectric loss could not be explained as a dependence function of filler content concentration. In general, particularly in the case of insulator-conductor composites, it is obvious that tunneling of electrons from a bunch to another bunch would be possible when separated by polymer layers having less number of conductive particles [35-36]. In the case of insulator-conductor composites, it is obvious that the tunneling of electrons is the underlying reason for the AC conductivity performance, due to which the conductivity of the samples increased with an increase in frequency [37-38].

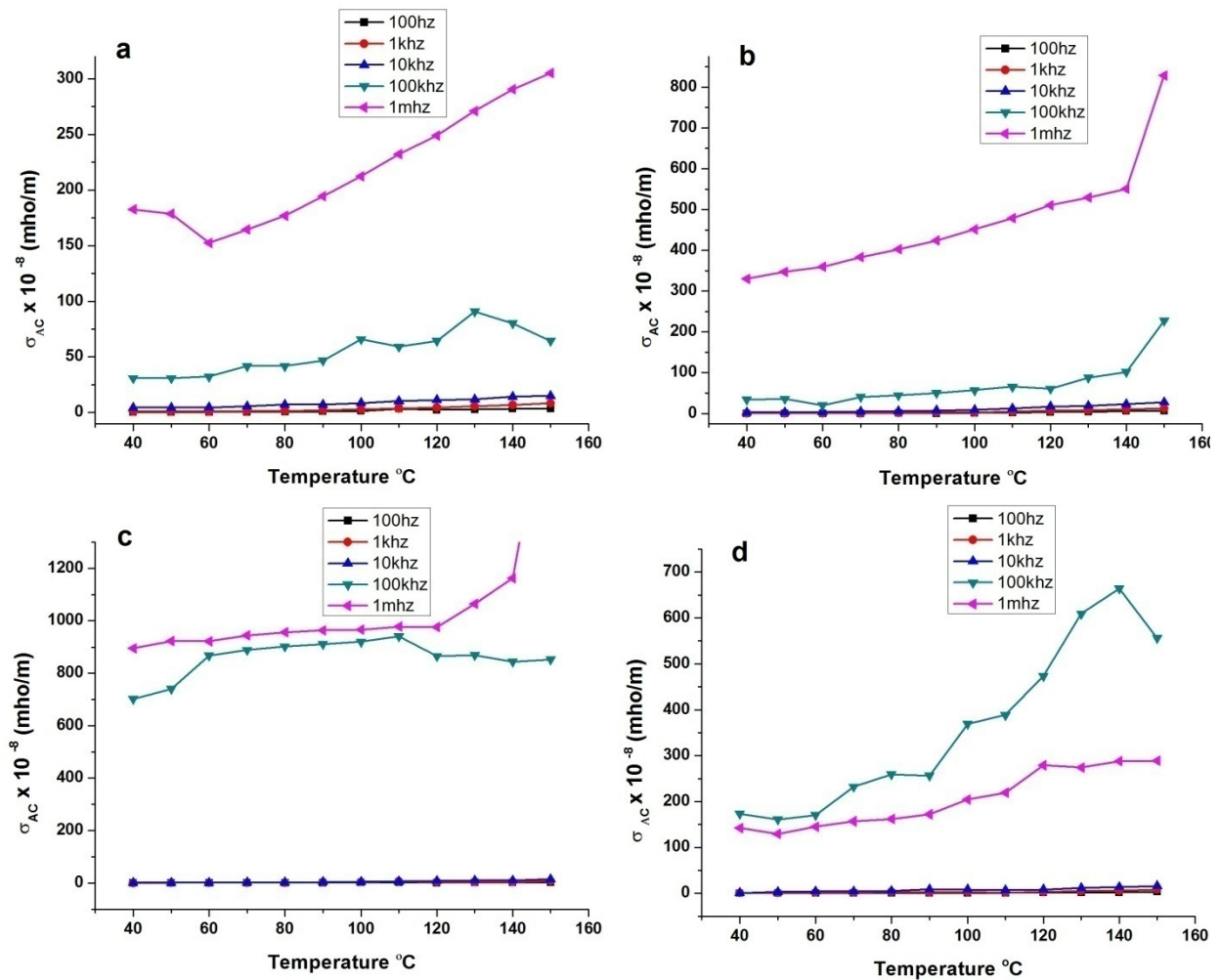


**Fig. 13.** AC Electrical Conductivity ( $\sigma_{AC} \times 10^{-8}$  mho/m) for samples viz., a) Sample A, b) Sample B, c) Sample C and d) Sample D

Table 2. Dielectric constant, dielectric loss factor, and AC conductivity of the prepared samples

Temp	Dielectric Constant					Dielectric loss factor					AC conductivity				
	100Hz	1 kHz	10 kHz	100 kHz	1 MHz	100hz	1khz	10 kHz	100 kHz	1 MHz	100Hz	1 kHz	10 kHz	100 kHz	1 MHz
150	6.871	2.554	1.707	1.958	1.219	1.835	0.887	0.293	0.293	0.122	7.010	12.597	27.769	227.068	828.516
140	6.295	2.374	1.633	1.729	1.215	1.638	0.775	0.254	0.106	0.082	5.734	10.225	23.046	101.410	550.772
130	4.940	2.208	1.577	1.708	1.208	1.482	0.655	0.216	0.092	0.079	4.071	8.044	18.924	87.681	529.371
120	4.661	2.091	1.550	1.698	1.203	1.334	0.602	0.194	0.064	0.076	3.458	6.999	16.740	60.602	510.416
110	3.470	1.836	1.475	1.662	1.180	1.012	0.421	0.146	0.071	0.073	1.953	4.300	11.995	65.704	478.426
100	2.683	1.726	1.427	1.639	1.176	0.876	0.301	0.111	0.063	0.069	1.307	2.886	8.775	57.127	451.343
90	2.503	1.606	1.386	1.612	1.162	0.347	0.244	0.094	0.056	0.066	0.483	2.179	7.243	50.475	423.915
80	2.118	1.511	1.381	1.589	1.151	0.485	0.179	0.069	0.050	0.063	0.571	1.500	5.274	44.260	402.598
70	1.662	1.445	1.319	1.566	1.139	0.388	0.125	0.057	0.046	0.061	0.359	1.005	4.145	40.144	383.280
60	1.495	1.394	1.294	1.546	1.129	0.420	0.095	0.046	0.023	0.057	0.349	0.736	3.289	19.858	359.595
50	1.484	1.370	1.302	1.564	1.145	0.356	0.089	0.037	0.041	0.055	0.294	0.676	2.643	35.474	346.971
40	1.273	1.345	1.278	1.541	1.134	0.201	0.052	0.030	0.040	0.052	0.142	0.392	2.118	33.926	329.850

#### 4. Conclusions

In summary, the tensile strength of the samples initially increased with an increase in reinforcements and then decreased with an increase in B<sub>4</sub>C content beyond 10 wt %. Flexural strength, on the other hand, is found to increase with the addition of B<sub>4</sub>C particles. The impact strength of the samples decreased with an increase in the addition of the B<sub>4</sub>C particles. The dielectric constant increased and the dielectric loss factor decreased with increased frequency. However, the AC conductivity of the samples increased with an increase in frequency. The trend in the increase in dielectric constant with higher frequencies and temperature makes the material suitable for energy storage applications.

#### References

1. Singh V, Kulkarni AR, Rama Mohan TR. Dielectric properties of aluminum–epoxy composites. *Journal of applied polymer science*. 2003;90(13): 3602-3608.
2. Elimat ZM, Zihlif AM, Ragosta G. Study of ac electrical properties of aluminium–epoxy composites. *Journal of Physics D: Applied Physics*. 2008;41(16): 165408.
3. Sharma A, Cheon JS, Jung JP. Epoxy polymer solder pastes for micro-electronic packaging applications. *Journal of Welding and Joining*. 2019;37(2): 7-14.
4. Zhang R. *Novel conductive adhesives for electronic packaging applications: A way towards economical, highly conductive, low temperature and flexible interconnects*. Georgia Institute of Technology; 2011.
5. Aradhana R, Mohanty S, Nayak SK. A review on epoxy-based electrically conductive adhesives. *International Journal of Adhesion and Adhesives*. 2020;99: 102596.
6. Wang Z, Zhou W, Sui X, Dong L, Cai H, Zuo J, Liu X, Chen Q. Dielectric studies of al nanoparticle reinforced epoxy resin composites. *Polymer Composites*. 2018;39(3): 887-894.
7. Zhang LB, Wang JQ, Wang HG, Xu Y, Wang ZF, Li ZP, Mi YJ, Yang SR. Preparation, mechanical and thermal properties of functionalized graphene/polyimide nanocomposites. *Composites Part A: Applied Science and Manufacturing*. 2012;43(9): 1537-1545.
8. Shang J, Zhang Y, Yu L, Luan X, Shen B, Zhang Z, Lv F, Chu PK. Fabrication and enhanced dielectric properties of graphene–polyvinylidene fluoride functional hybrid films with a polyaniline interlayer. *Journal of Materials Chemistry A*. 2013;1(3): 884-890.
9. Xie P, Li Y, Qiu J. Preparation and dielectric behavior of polyvinylidene fluoride composite filled with modified graphite nanoplatelet. *Journal of Applied Polymer Science*. 2014;131(24).
10. Xu S. *Electrically Conductive Adhesives. Literature Review*. 2002.
11. Thevenot F. A review on boron carbide. *Key Engineering Materials*. 1991;56: 59-88.
12. Chen M, McCauley JW, Hemker KJ. Shock-induced localized amorphization in boron carbide. *Science*. 2003;299(5612): 1563-1566.
13. Way H. Media-milled nanoparticles boosts ceramic armor. *American Ceramic Society Bulletin*. 2008;87(5): 20-24.
14. Suri AK, Subramanian C, Sonber JK, Murthy TC. Synthesis and consolidation of boron carbide: a review. *International Materials Reviews*. 2010;55(1): 4-10.
15. Domnich V, Reynaud S, Haber RA, Chhowalla M. Boron carbide: structure, properties, and stability under stress. *Journal of the American Ceramic Society*. 2011;94(11): 3605-3628.
16. Leo S, Tallon C, Stone N, Franks GV. Near-net-shaping methods for ceramic elements of (body) armor systems. *Journal of the American Ceramic Society*. 2014;97(10): 3013-3033.
17. Hallam D, Heaton A, James B, Smith P, Yeomans J. The correlation of indentation behaviour with ballistic performance for spark plasma sintered armour ceramics. *Journal of the European Ceramic Society*. 2015;35(8): 2243-2252.

18. Moshtaghioun BM, Gomez-Garcia D, Dominguez-Rodriguez A, Todd RI. Abrasive wear rate of boron carbide ceramics: Influence of microstructural and mechanical aspects on their tribological response. *Journal of the European Ceramic Society*. 2016;36(16): 3925-3928.
19. Hayun S. Reaction-bonded boron carbide for lightweight armor: The interrelationship between processing, microstructure, and mechanical properties. *American Ceramic Society Bulletin*. 2017;96(6): 20-26.
20. Akter S, Goto A, Mizoue T. Smoking and the risk of type 2 diabetes in Japan: a systematic review and meta-analysis. *Journal of Epidemiology*. 2017;27(12): 553-561.
21. Moshtaghioun BM, Gomez-Garcia D, Dominguez-Rodriguez A, Todd RI. Grain size dependence of hardness and fracture toughness in pure near fully-dense boron carbide ceramics. *J Eur Ceram Soc*. 2016;36(7): 1829-1834.
22. Lawn BR. *Fracture of brittle solids*. Cambridge Solid State Science Series; 1993.
23. Wachtman JB, Cannon WR, Matthewson MJ. *Mechanical properties of ceramics*. John Wiley & Sons; 2009.
24. Samanta B, Kumar P, Nanda D, Sahu R. Dielectric properties of Epoxy-Al composites for embedded capacitor applications. *Results in Physics*. 2019;14: 102384.
25. Kiani MA, Ahmadi SJ, Outokesh M, Adeli R, Mohammadi A. Preparation and characteristics of epoxy/clay/B4C nanocomposite at high concentration of boron carbide for neutron shielding application. *Radiation Physics and Chemistry*. 2017;141: 223-228.
26. Suzuki A, Arai Y, Takata N, Kobashi M. Structural design and bonding strength evaluation of Al/epoxy resin joint via interpenetrating phase layer. *Journal of Materials Processing Technology*. 2018;262: 11-18.
27. Abenojar J, Martínez MA, Velasco F, Pascual-Sánchez V, Martín-Martínez JM. Effect of boron carbide filler on the curing and mechanical properties of an epoxy resin. *The Journal of Adhesion*. 2009;85(4-5): 216-238.
28. Nagaveena S, Mahadevan CK. Preparation by a facile method and characterization of amorphous and crystalline nickel sulfide nanophases. *Journal of Alloys and Compounds*. 2014;582: 447-456.
29. Hougham G, Tesoro G, Viehbeck A. Influence of free volume change on the relative permittivity and refractive index in fluoropolyimides. *Macromolecules*. 1996;29(10): 3453-3456.
30. Chang HC, Lin HT, Lin CH. Benzoxazine-based phosphinated bisphenols and their application in preparing flame-retardant, low dielectric cyanate ester thermosets. *Polymer Chemistry*. 2012;3(4): 970-978.
31. Tareev BM. *Physics of dielectric materials*. Mir publishers; 1975.
32. Kar T, Choudhary RN, Sharma S. Structural and Electrical Properties of Ba<sub>2</sub>Na<sub>3</sub>RNb<sub>10</sub>O<sub>30</sub> [R= Dy, Y] Ceramics. *Indian Journal of Physics*. 1999;73: 453-459.
33. Wang B, Liu L, Huang L, Chi L, Liang G, Yuan L, Gu A. Fabrication and origin of high-k carbon nanotube/epoxy composites with low dielectric loss through layer-by-layer casting technique. *Carbon*. 2015;85: 28-37.
34. Jiao Y, Yuan L, Liang G, Gu A. Dispersing carbon nanotubes in the unfavorable phase of an immiscible reverse-phase blend with Haake instrument to fabricate high-k nanocomposites with extremely low dielectric loss and percolation threshold. *Chemical Engineering Journal*. 2016;285: 650-659.
35. Hummel RE. *Electronic properties of materials*. New York: Springer; 2011.
36. Musameh SM, Abdelazeez MK, Ahmad MS, Zihlif AM, Malinconico M, Martuscelli E, Ragosta G. Some electrical properties of aluminum-epoxy composite. *Materials Science and Engineering: B*. 1991;10(1): 29-33.
37. Ortiz-Lopez J, Gómez-Aguilar R. Dielectric permittivity and AC conductivity in polycrystalline and amorphous C60. *Revista mexicana de física*. 2003;49(6): 529-536.

38. Shekharam T, Rao VL, Yellaiah G, Kumar TM, Nagabhushanam M. AC conductivity, dielectric and impedance studies of Cd<sub>0.8-x</sub>Pb<sub>x</sub>Zn<sub>0.2</sub>S mixed semiconductor compounds. *Journal of alloys and compounds*. 2014;617: 952-960.

39. Yang L, Li X, Allahyarov E, Taylor PL, Zhang QM, Zhu L. Novel polymer ferroelectric behavior via crystal isomorphism and the nanoconfinement effect. *Polymer*. 2013;54(7): 1709-1728.

40. Bonarddd S, Moreno-Serna V, Kortaberria G, Díaz Díaz D, Leiva A, Saldías C. Dipolar glass polymers containing polarizable groups as dielectric materials for energy storage applications. A minireview. *Polymers*. 2019;11(2): 317.

## THE AUTHORS

### **Vignesh S.**

e-mail: vickyrsnair@gmail.com

ORCID: 0000-0002-8368-6110

### **Winowlin Jappes J.T.**

e-mail: winowlin@klu.ac.in

ORCID: 0000-0003-2247-4605

### **Nagaveena S.**

e-mail: nagaveena3@gmail.com

ORCID: -

### **Sankaranarayanan K.**

e-mail: vignesh@klu.ac.in

ORCID: -

### **Krishna Sharma R.**

e-mail: krishsharma5555@gmail.com

ORCID: -

### **Brintha N.C.**

e-mail: brinthachris\_2k@yahoo.com

ORCID: -

# Comparison of mechanical strain measurement accuracy of fiber-optic sensor and smart-layer

G.S. Shipunov, M.A. Baranov✉, A.S. Nikiforov, F.R. Khabibrakhmanova

Perm National Research Polytechnic University, 29 Komsomolsky Ave., Perm, Russia, 614990

✉ maximbaranov.123@gmail.com

**Abstract.** Due to its fragility, fiber optic sensor (FOS) embedded into constructions made of carbon fiber reinforced polymer, can be broken both while it is manufacturing at the point of embedding into construction, and during its operation. This can lead to the inability to further monitoring of the construction strains. Usage of a specific thin Smart-layer for protection of FOS is proposed by the authors. For the Smart-layer manufacturing, 3D printing technology was used. The spectra of fiber Bragg grating (FBG) before and after layer printing have been analyzed, remaining compression strains were recorded. A mechanical test of a sample with surface-mounted FOS along with a Smart-layer was performed in order to measure the precision of strain detection by the Smart-layer. Some inaccuracy in strain detection was found during the analysis of the results. In order to find out the error in strain measured by a Smart-layer, a mechanical test of a full-sized bulkhead in a complex stress-strain state was performed

**Keywords:** fiber optic sensor, structural health monitoring, fused deposition method, Smart-layer, carbon fiber reinforced polymer

**Acknowledgements.** *The results were obtained during the fulfillment of the state task of the Ministry of Science and Higher Education of the Russian Federation for the implementation of fundamental scientific research (project No. FSNM-2020-0026).*

**Citation:** Shipunov GS, Baranov MA, Nikiforov AS, Khabibrakhmanova FR. Comparison of mechanical strain measurement accuracy of fiber-optic sensor and smart-layer. *Materials Physics and Mechanics*. 2022;48(3): 342-354. DOI: 10.18149/MPM.4832022\_5.

## 1. Introduction

Nowadays, the safety and reliability of structures used in civilian, space, and aviation branches, are of principal concern. In order to meet these requirements, periodic non-destructive examinations are usually performed. However, such periodic examinations cannot totally ensure the integrity of a structure and guarantee the safety of its usage [1-3]. This was the reason for scientists to start research on so-called "Structural health monitoring systems" (SHM) based on different kinds of sensors (strain gauges or fiber optic sensors (FOS)), mounted at / embedded into the structure if it is possible.

Monitoring systems based on FOS are widely used in the aviation industry [4]. For example, some experimental investigations of FOS embedded into composite parts of helicopters, are presented and summarized in the article [5]. The problem of embedding optical fiber into carbon fiber reinforced polymer (CFRP) has been considered by the authors; the data provided by FOS embedded into a helicopter longeron prone to exfoliation caused by

dynamic stress has been published. Monitoring of cracks in helicopter hulls caused by metal fatigue with the help of a fiber Bragg grating-based FOS network has been described in the article [6]. Practical usage of FOS for structural monitoring of propeller aircraft and sailing yacht parts has been considered in the article [7]. FOS were embedded into a 35-meter carbon mast of a yacht and mounted at the surface of Jetstream airplane wing. Data from the sensors of the airplane were obtained in real-time while flying in extreme conditions. Another case, when sensors were embedded into airplane wings, is described in the article [8]. Bragg grating-based FOS were used for real-time measurement of dynamic strains during wing testing in a wind tunnel. Readings from the FOS were compared with those from strain gauges and piezoelectric sensors. Good convergence of all the systems has been observed during bench testing. The process of embedding 20 FOS into a longeron of UAV was described in the article [9]. The authors covered the process of development and building of FOS data transmission system mounted at UAV, and described the flight tests when data from FOS were transmitted to the ground-based receiver and deciphered.

Thus, FOS-based monitoring systems are essential for monitoring different kinds of structures. However, most authors mention some difficulties when mounting FOS at the surface or embedding them into a structure. Particularly, they note the fragility of optical fiber, the complexity of accurate sensor positioning, and ensuring the integrity of FOS emerging from a CFRP construction [10-12].

For solving the problems mentioned, the authors use different kinds of "wrappings" for FOS protection. Acellent Technologies, Inc. developed a Smart-layer that allows protection of various types of sensors (FOS, piezoelectric) and their outputs to ensure the accuracy of the sensing element in the monitored environment [13]. In [14], the company mentioned described their own technology for creating the Smart-layer, consisting of a network of piezoelectric sensors that were placed between a polyimide film and coated with epoxy resin. This technology ensures the integrity of the sensors. It can be used for surface monitoring of structures, but it cannot be used for embedding sensors directly into CFRP structures since polyimide films have poor adhesion to carbon fiber reinforced polymers. The thickness of such a layer can be up to 2-4 mm, so it can significantly affect the physical and mechanical characteristics of such structures.

Yoon H.J. et al. used Brillouin backscattering-based FOS for analysis of longitudinal strains of a 40.26-meter long railway bridge when a train had been moving on it at a speed of 15 kilometers per hour [15]. FOS were wrapped into Hytrel thermoplastic elastomer buffer, additionally protected with 0.3 mm thick polyethylene film, and mounted on a rail. The values of longitudinal strains obtained from FOS were compared to the results from strain gauges.

The authors of the article [16] used two fiber Bragg gratings wrapped into a 250 mm length glass tube for diagnosing the stress-strain state of a bridge. The glass tube was fixed to the concrete surface of the bridge with bolts. The authors note that such glass tube containing FOS allows obtaining a full picture of the stress-strain state, however, the cost of such tubes is rather high. Therefore, in their work [17] the authors explored the possibility of manufacturing simple and inexpensive wrapping for FOS capable of providing high quality and reproducibility of strain measurement. While developing such kind of wrapping, the authors defined the following requirements: it should be suitable both for surface mounting (i. e., withstand harsh environmental conditions) and direct embedding into concrete. The authors used photopolymeric resin 3D printing technology. At first, U-shaped substrate was made, and optical fiber was placed inside. Afterward, the substrate was filled with Duralco glue. The thickness of such a package reached 5 mm. The authors conducted some mechanical tests of the concrete beams with sensor packages mounted. After having obtained the test results, they decided to modify the design of the package. The authors then printed U-shaped substrate and cover plate separately. Optical fiber was placed on U-shaped substrate,

covered with glue, and protected by a plate. The thickness of the resulting package was comparable to that of the first version. However, the authors note that FOS sensitivity has decreased. Hence, the authors compared the results of concrete beam mechanical testing with different types of sensor packages. They note that both types are suitable for surface mounting and embedding into constructions; the second design is more advanced and durable, but less sensitive than the first one.

The analysis of the articles mentioned can lead to the conclusion that nowadays FOS packages are manufactured mainly by the technology of gluing together polyamide film layers, and by using additive technologies. This is due to the fact that additive methods are gaining in popularity over the past decades. 3D manufacturing methods such as fused deposition method (FDM) and stereolithography (SLA) are the most common thanks to the possibility of rapid prototyping, low cost of the final part, and the use of various engineering plastics with the required characteristics [18].

Thus, different types of FOS wrappings can provide protection for sensors. However, the majority of packages were designed for surface monitoring of different types of constructions (bridges, rails, pipes) or embedding into concrete, so their dimensions are quite large, and their thickness is up to 3-5 mm. They are not suitable for embedding into CFRP, since such a process can significantly change the physical and mechanical properties of CFRP structures. Hence, the development of thin Smart-layers is a relevant task nowadays.

Several prototypes of Smart-layers have been developed and manufactured at the Research and Educational Center of Aviation Composite Technologies at Perm National Research Polytechnic University. They were embedded into sample constructions made of CFRP and tested. It has been discovered that the embedding process has a negligible effect on the physical and mechanical characteristics of the structures. However, the correctness of strain measurement by the Smart-layers is still the issue of further research. Thus, the aim of this paper is to investigate the effect of the wrapping on the measurement accuracy of FOS.

## **2. Smart-layer manufacturing**

Since Smart-layer is intended to be used both at the surface and inside CFRP, it is necessary to consider the temperature used for manufacturing CFRP samples and constructions. Usually, it is 130-180°C, so the melting point of materials used for building Smart-layers has to be higher than this.

Considering the condition mentioned, it was decided to use the nylon filament (ePA from eSUN) which is printed at 230-260°C and therefore meets the requirements.

Smart-layers were manufactured on a CreatBot F430 FDM 3D printer, which has the following characteristics: bed heat temperature of 120°C, max nozzle heat temperature of 420°C, and hot-chamber device with a constant temperature of 70°C. This 3D printer is a part of the unique research facility "Research complex for scientific and technological research in the field of creating products made of polymer composite materials".

Smart-layer manufacturing consisted of two stages. At the first stage, the lower half of the layer containing a rectangular-shaped groove with dimensions of 0.2×0.16 millimeters was printed, as shown in Fig. 1a. For ensuring the precise placement of the optical fiber inside Smart-layer, the fiber was stretched, loaded into the groove, and had both its ends fixed with sticky tape to the printer bed.

In the second stage, the printing program was resumed and the upper half of the Smart-layer was printed. Fig. 1b represents Smart-layer's second half print scheme. The optical fiber containing fiber Bragg grating (FBG) for a Smart-layer was manufactured by "Inversia Sensor" company. The fiber had a 0.02 mm thick polyamide covering, thus its operating temperature range is from -200°C to 350°C. The FBG length was 5 mm, its resonant wavelength was 1528.17 nm, the reflection coefficient was 70.49%, the spectrum peak

width was 0.155 mm, suppression of side peaks was 9.6 dB. The diameter of the optical fiber was 0.156 mm.

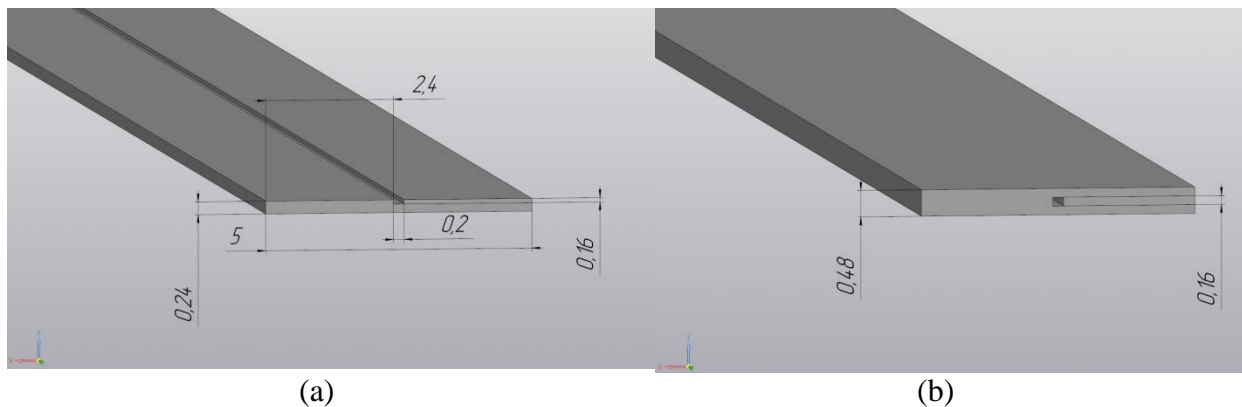


**Fig. 1.** Smart-layer manufacturing scheme: Smart-layer's first half print scheme (a); Smart-layer's second half print scheme (b)

Printing was performed with the following parameters: the substrate temperature was 120°C, printing temperature was 270°C, printing speed was 60 mm/s. It is necessary to mention that optical fiber was rigidly fixed inside the Smart-layer (without any slippage) due to the shrinking of the plastic used. The manufactured layer is presented in Fig. 2. After completion of the printing process, it was connected to a laser source for testing. As it is shown in Fig. 2, optical fiber remained intact and was still capable of transmitting the light.

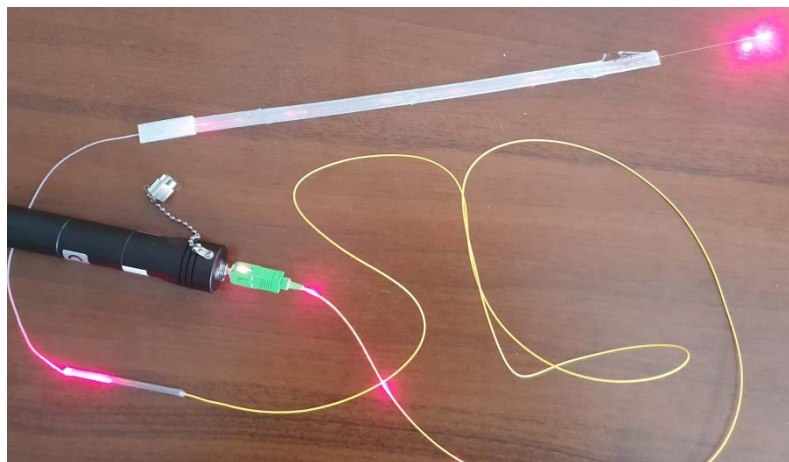


**Fig. 2.** Smart-layer manufactured of nylon by using FDM printing technology

It is known that plastic shrinks after printing because of cooling, so fiber Bragg grating in the Smart-layer is expected to have some residual compression strains. For investigating the impact of residual strains on a spectrum of fiber Bragg grating, the corresponding spectra were studied before and after printing. They are presented in Fig. 3.

The shift of the spectrum peak in the sealed FBG compared to the one of the original FBG allows determining the shift of the resonant wavelength of the signal reflected from the sensor which is caused by the combined impact of mechanical strain and temperature. Analysis of the spectrum obtained revealed a 2.175 nm change in resonant wavelength. More detailed analysis showed that FBG sealing didn't result in peak split; therefore, the double refraction effect did not happen. Double refraction can be caused by temperature strains and material shrinking in the process of manufacturing [19]. Double refraction usually leads to profile strain and some changes in the shape of the peak, which, in turn, lowers measurement

precision and results in doubling the reflection spectrum, which complicates determining the value measured. The next stage of the research is aimed at comparing strains registered during mechanical tests by FOS and Smart-layer.

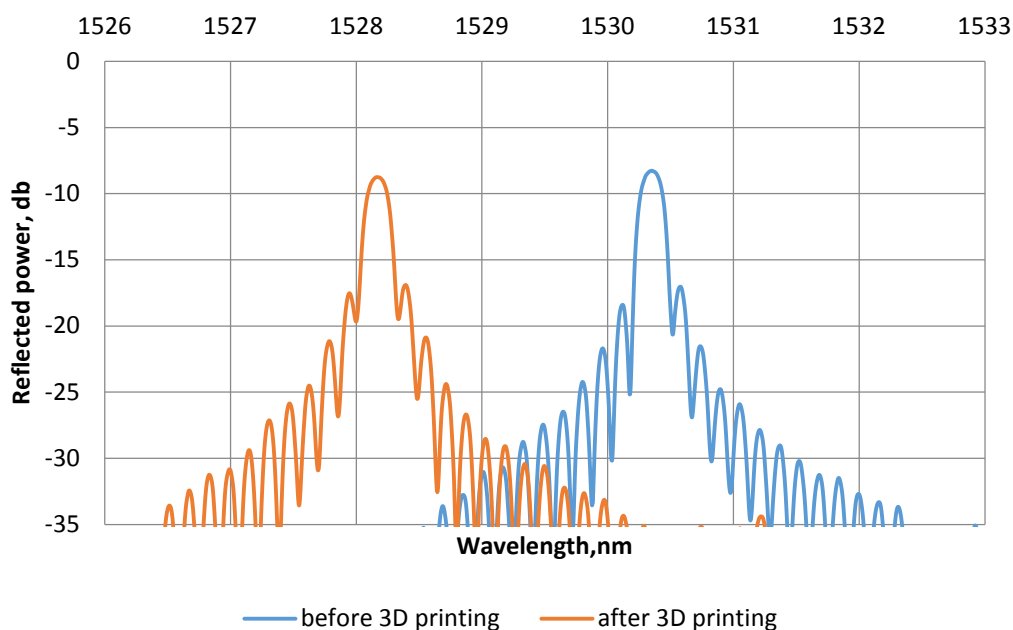


**Fig. 3.** Distribution of reflected signal wavelength before and after 3D printing

### 3. Comparison of fiber-optic sensor and Smart-layer measurements of strain under single-axis load

For detecting possible errors in registering strains by Smart-layer, a CFRP plate with reinforcement scheme  $[0,45]_5$  was made. It was cut into six  $310 \times 22.5 \times 2.3$  mm samples. Five of them were used for determining the critical load that breaks the sample when applied. Finding out the critical load value is necessary to avoid the destruction of control sample with FOS and Smart-layer.

Statistical processing of experimental data was performed according to the following set of correlations (1):

$$\left\{ \begin{array}{l} \bar{x} = \frac{1}{n} \sum_{i=1}^n x_i, \\ s = \sqrt{\frac{1}{n-1} \sum_{i=1}^n (x_i - \bar{x})^2}, \\ v = \frac{s}{\bar{x}} \cdot 100 (\%), \end{array} \right. \quad (1)$$

where  $\bar{x}$  is the mean value;  $s$  is standard deviation of a value;  $v$  is coefficient of variation.

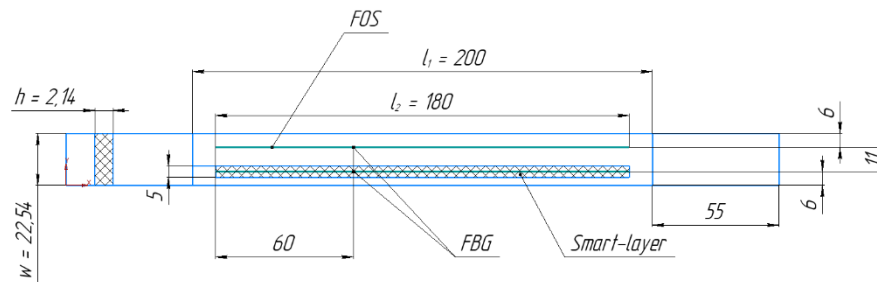
The results of statistical processing of all the data obtained as the result of mechanical tests of the samples are presented in Table 1.

According to the mechanical stretching tests of the five samples, the mean value of critical load was 34.85 kN. The load on the control sample was limited up to 15% of the critical value stated above. Optical fiber and Smart-layer were mounted in such a way that every grating was equally distant from the symmetrical center of the tested sample. The fiber and the Smart-layer were fixed with epoxy resin. The arrangement of FOS and Smart-layer at

the CFRP sample is schematically presented in Fig. 4a. The photo of the sample secured in the testing unit is presented in Fig. 4b.

Table 1. Statistical Processing of Mechanical Test Results

$n = 5$	$\sigma_{\max}, MPa$	$F_{\max}, kN$	$h, mm$	$w, mm$
$\bar{x}$	665.45	34.85	2.32	22.7
$s$	26.68	0.46	0.06	0.06
$v, \%$	4	1.32	2.75	0.28



(a)



(b)

**Fig. 4.** The arrangement of FOS and Smart-layer. (a) FOS placement scheme; (b) control sample with FOS and Smart-layer secured in the testing unit

During mechanical tests of the control sample, a special construction monitoring system was used. It was developed by our research team and consists of a monitored object with mounted Smart-layer and FOS; the interrogator device that is necessary for data exchange with FOS in the Smart-layer; special software that initiates data transfer between the optical fiber and the interrogator, and subsequently processes the data received [20].

The interrogator is a device measuring wavelengths of the light reflected from the fiber Bragg gratings. It operates by measuring the power of the light beam at the output of periodically rearranged selective optical filter in the measured range of wavelengths. The interrogator creates a ray of light directed at sensor (Bragg grating). The reflected signal is

processed by the interrogator and is transferred to the computer. The information received from FOS is presented with the help of specialized software.

The resonant wavelength of Bragg grating  $\lambda_\beta$  depends on the effective refractive index and the grating period. It is expressed by the following correlation [21]:

$$\lambda_\beta = 2n\Lambda, \quad (2)$$

where  $n$  is effective refractive index,  $\Lambda$  is period of fiber Bragg grating. The shift of the spectrum position is defined by the following correlation:

$$\Delta\lambda_\beta = 2\left(\Lambda \frac{\partial n}{\partial l} + n \frac{\partial \Lambda}{\partial l}\right)\Delta l + 2\left(\Lambda \frac{\partial n}{\partial T} + n \frac{\partial \Lambda}{\partial T}\right)\Delta T. \quad (3)$$

The first summand of equation (3) is the impact of strain on the optic fiber. Its physical meaning lies in the change in grating period and refractive index, caused by the optical elasticity effect. The second summand represents the temperature impact on Bragg grating. The Bragg wavelength shift is caused by thermal expansion of quartz that leads to a change in the grating period and refractive index. According to [22], equation (3) can be presented as the following:

$$\Delta\lambda_\beta = \lambda_\beta(1 - p_e)\varepsilon + \lambda_\beta(\alpha + \xi)\Delta T, \quad (4)$$

where  $p_e$  is effective optical elasticity constant,  $\alpha$  is linear thermal expansion coefficient,  $\xi$  is thermo-optic coefficient,  $\varepsilon$  is strain.

As the testing was conducted in normal conditions, there were no temperature changes during the experiment. Therefore, the second summand of the equation (4) can be neglected, so the equation (4) takes the following form:

$$\Delta\lambda_\beta = \lambda_\beta(1 - p_e)\varepsilon. \quad (5)$$

The effective optical elasticity coefficient is defined by the following:

$$p_e = \frac{n^2}{2}(p_{12} - \nu(p_{11} + p_{12})), \quad (6)$$

where  $p_{11}$ ,  $p_{12}$  are Pockels coefficients of elastic-optical tensor.

Substituting the values of Pockels coefficients ( $p_{11}=0.113$ ,  $p_{12}=0.252$ ,  $\nu=0.16$ ,  $n=1.4682$ ) into the equation (4) and excluding temperature strains, we get the formula for strain calculation for any given time:

$$\varepsilon = \frac{1}{0.78} \frac{\Delta\lambda_\beta}{\lambda_\beta}. \quad (7)$$

During the mechanical tests, dependencies of strains (registered by FOS and Smart-layer) upon time have been obtained. They are presented in Fig. 5.

During the test, when 5 kN load was applied to the sample, the strain registered by the fiber optic sensor was  $\varepsilon = 0.099\%$ , and the one registered by Smart-layer was  $\varepsilon = 0.1\%$ .

It should be noted that the accuracy of strain measurement by FOS is not considered in this work since the error of such measurements described in prior research works, does not exceed 6% [23]. The aim of this work is to identify the difference in strain values obtained from Smart-layer and FOS. The analysis of the data obtained leads to the conclusion that the error in strain values measured by Smart-layer is 8.23%. Thus, this error has to be taken into account when Smart-layers are used, and the monitoring system has to be calibrated considering the error of strain measurement.

It is known that full-scale constructions can be in a complex stress-strain state, so the error of strain measurement by Smart-layer on such constructions is to be found.

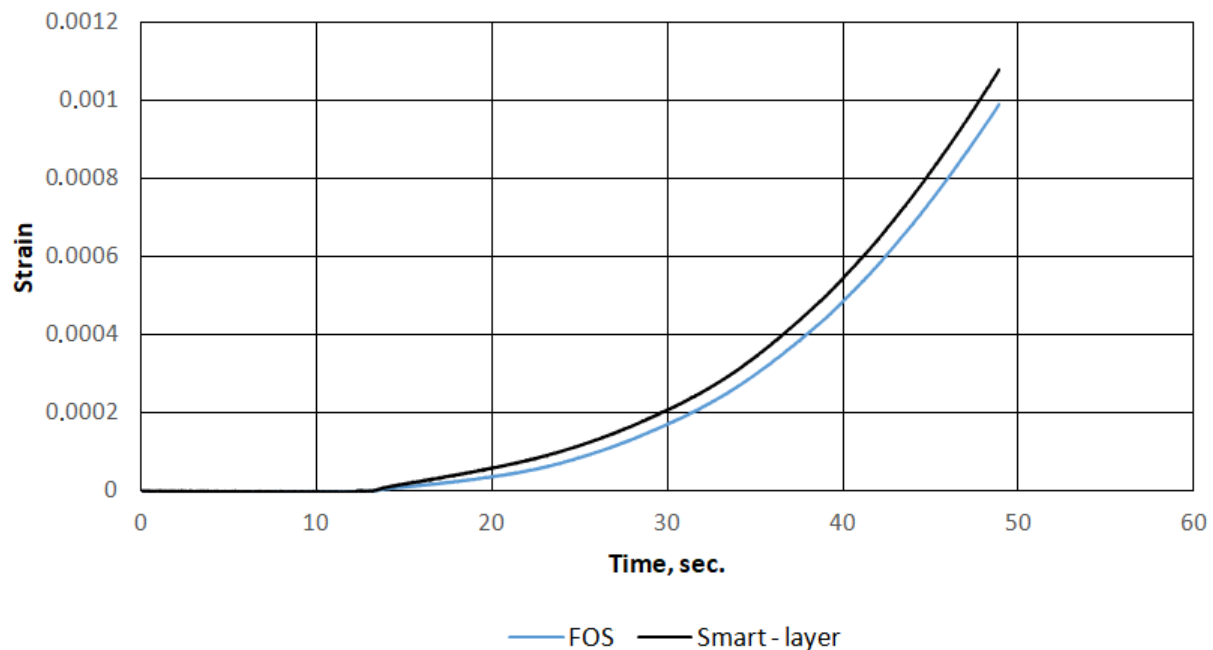


**Fig. 5.** Dependencies of strain value (registered by FOS and Smart-layer) upon time

#### 4. Comparison of fiber-optic sensor and Smart-layer measurements of strain in combined stress-strain state of a bulkhead

The next stage of research is finding out the accuracy of strain measurement by Smart-layer which is mounted on a full-scale construction along with FOS. A CFRP bulkhead was chosen as the construction for the tests. A CFRP bulkhead is a U-shaped ring. The bulkhead is made of textile carbon fiber reinforced plastic with epoxy resin using resin transfer molding (RTM). The bulkhead consists of a solid circular U-shaped body and two flanges having some technological notches and mounting holes. The necessity of this experiment arises from possible confirmation of precise registration of strains in structure experiencing a complex (combined) stress-strain state.

For conducting mechanical tests, the bulkhead was secured on vertical supports. FOS and Smart-layer were mounted on a 740-mm long bulkhead segment. Static load was applied in the middle of the segment. FOS and Smart-layer were mounted at an equal 60 mm distance from the sector symmetry center. The sensor mounting scheme is presented in Fig. 6. Static load was also applied to the symmetry center of the bulkhead sector. A graduated load scheme was used in the experiment. It included 5 stages of load application. At the first stage of the experiment, a 150 N weight was placed on the platform attached to the bulkhead with a stud. At subsequent stages, the same weight was added until the load reached 750 N.

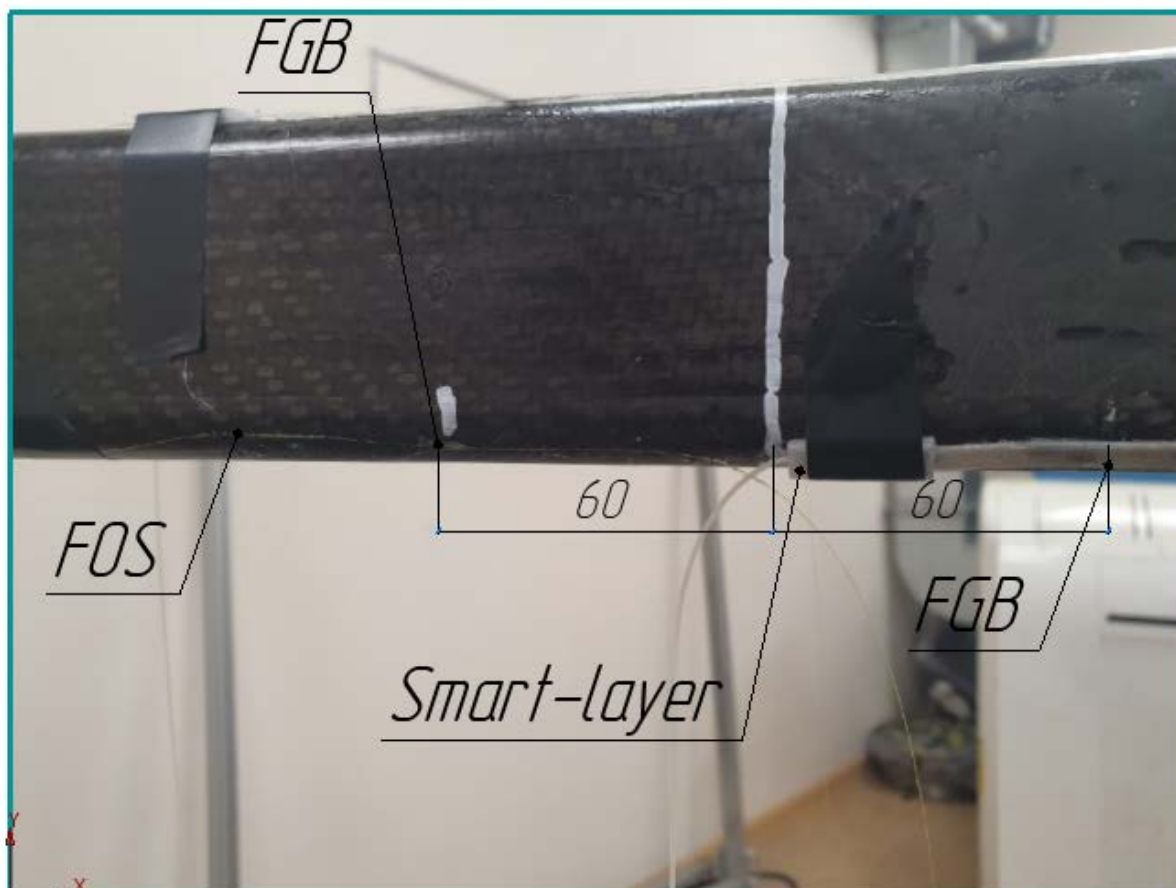


**Fig.6.** Mechanical test of the bulkhead. FOS placement scheme and application of load to the bulkhead segment center

During mechanical tests, for each stage of load application, the values of strain measured by Smart-layer and FOS, were obtained. They are presented in Fig. 7.

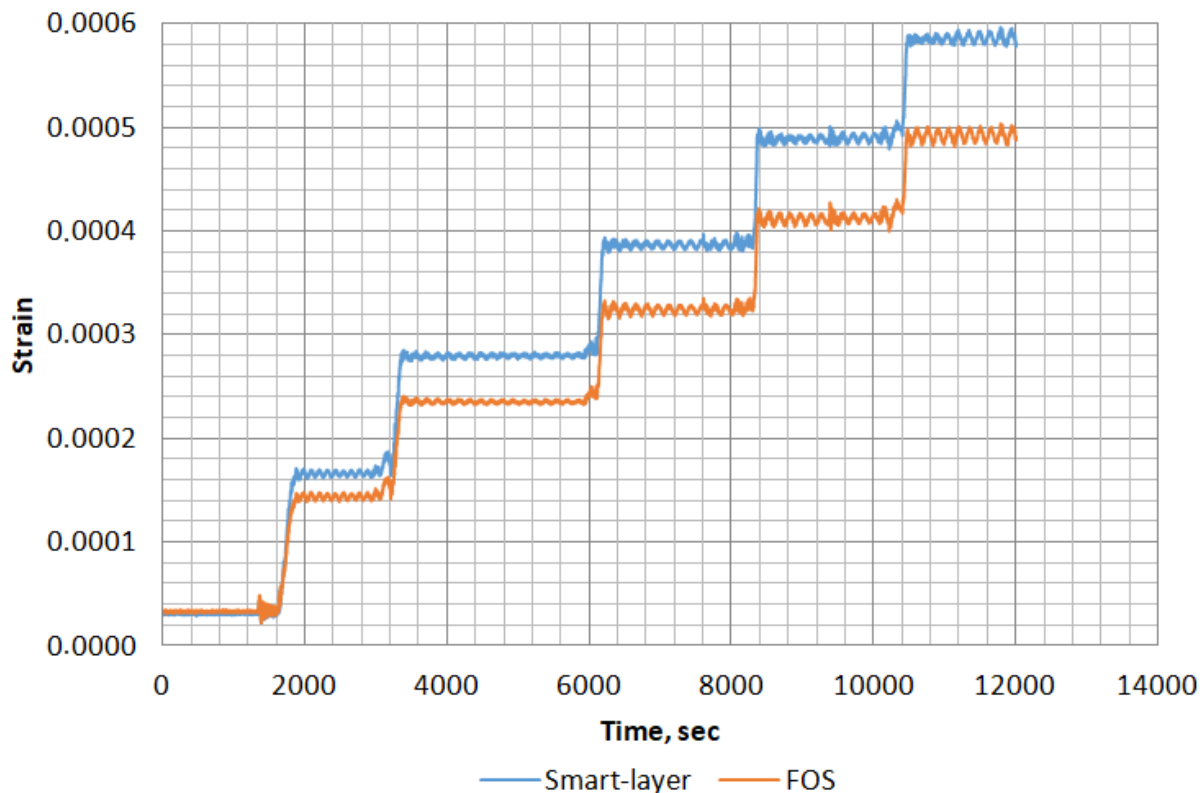


**Fig. 7.** Dependence of strain value (registered by FOS and Smart-layer) upon time during the process of graduated load application

For every pair of strain values (registered by FOS and Smart-layer), their difference and percentage deviation were calculated. Under 150 N load, strain registered by Smart-layer and FOS was 0.017% and 0.015% correspondingly. The difference between readings was 0.002%, and percentage deviation was 11.76%. At the next stage, the load applied to the bulkhead, was doubled. The difference between readings, in this case, was 0.004%, and percentage deviation was 14.29%. At the following three stages, the load was increased by 150 N every time. The difference between readings was 0.005%, 0.007%, 0.008% correspondingly. The percentage deviation was 13.16%, 14.29%, and 13.79% correspondingly. The measurement results obtained during the mechanical test are presented in Table 2.

**Table 2.** Strains Registered by FOS and Smart-layer During Graduated Load Application

$F, N$	$\varepsilon_{Smart-layer}, \%$	$\varepsilon_{FOS}, \%$	$\Delta\varepsilon, \%$	Percentage deviation, %
150	0.017	0.015	0.002	11.76
300	0.028	0.024	0.004	14.29
450	0.038	0.033	0.005	13.16
600	0.049	0.042	0.007	14.29
750	0.058	0.05	0.008	13.79

On the basis of the results obtained it can be concluded that the maximal difference between sensor readings was 14.29% (under 300 N and 600 N load), and minimal difference was 11.76% (under 150 N load). It should be noted that the difference between FOS and

Smart-layer readings has demonstrated continuous, almost linear growth as the load increased. However, there has not been found any obvious correlation between load value and percentage deviation. Hence, it can be supposed that in the case of further load increase, measurement error of Smart-layer compared to FOS will remain within 11.76% – 14.29% range.

## 5. Summary and Conclusion

Thus, within the research presented in the article, a Smart-layer has been manufactured using 3D printing technology. Spectra of the light waves reflected from Bragg grating before and after the printing have been analyzed. Some residual strains in the layer have been found, as indicated by a shift of resonant wavelength. Based on the shapes of spectra peaks, it can be stated that the double refraction effect doesn't appear when sealing FBG.

The mechanical test on stretching the sample with mounted FOS and Smart-layer has been carried out. The dependence of strain upon time under quasi-static single-axis load was obtained and analyzed; the measurement error of Smart-layer has been found to be 8.23%.

In order to find out the dependence of Smart-layer and FOS response deviation upon load in case of the complex stress-strain state, a mechanical test of a CFRP bulkhead has been carried out. A graduated 5-staged load was used in the experiment. For every stage, the values of the registered strains, the difference between sensor readings, and the percent deviation of the values have been recorded. During the analysis of the results obtained, it has been found that the difference of registered values of strain lies in a range from 11.76% to 14.29%, and the average difference is 13.46%.

As the result of mechanical tests, error of strain measurement by Smart-layer has been found out both for single-axis quasi-static and complex load; calibration coefficient that allows registering strain more precisely has been calculated. On the basis of the results obtained, the following conclusion can be drawn: the use of the proposed Smart-layer instead of FOS has been proved to be more innovative and efficient, due to time saving during FOS mounting. Moreover, it excludes the possibility of their damage during their mounting and dismantling.

The next stage of the research is to embed the FOS and Smart-layer into a sample and determine the error of strain measurement during mechanical tests, as well as carrying out mechanical tests of full-sized constructions made of CFRP and fitted with FOS and Smart-layer.

## References

1. Yu F, Okabe Y. Linear damage localization in CFRP laminates using one single fiber-optic Bragg grating acoustic emission sensor. *Compos. Struct.* 2020;238: 1-10.
2. Tserpes KI, Karachalios V, Giannopoulos I, Prentzias V, Ruzek R. Strain and damage monitoring in CFRP fuselage panels using fiber Bragg grating sensors. Part I: Design, manufacturing and impact testing. *Compos. Struct.* 2014;107: 726-736.
3. Han T, Wu G, Lu Y. Crack monitoring using short-gauged Brillouin fiber optic sensor. *Measurement.* 2021;179: 1-13.
4. Di Sante R. Fibre optic sensors for structural health monitoring of aircraft composite structures: Recent advances and applications. *Sensors.* 2015;15(8): 18666-18713.
5. Ghoshal A, Ayers J, Gurvich M, Urban M, Bordick N. Experimental investigations in embedded sensing of composite components in aerospace vehicles. *Compos. Part B Eng.* 2015;71: 52-62.
6. Sbarufatti C, Manes A and Giglio M. Application of sensor technologies for local and distributed structural health monitoring. *Struct. Control Health Monit.* 2013;21(7): 1057-1083.

7. Read IJ, Foote PD. Sea and flight trials of optical fibre Bragg grating strain sensing systems. *Smart Mater. Struct.* 2001;10(5): 1085-1094.
8. Lee JR, Ryu CY, Koo BY, Kang SG, Hong CS, Kim CG. In-flight health monitoring of a subscale wing using a fiber Bragg grating sensor system. *Smart Mater. Struct.* 2003;12(1): 147-155.
9. Alvarez-Montoya J, Carvajal-Castrillón A, Sierra-Pérez J. In-flight and wireless damage detection in a UAV composite wing using fiber optic sensors and strain field pattern recognition. *Mech. Syst. Signal Process.* 2020;136: 1-26.
10. Rufai O, Chandarana N, Gautam M, Potluri P, Gresil M. Cure monitoring and structural health monitoring of composites using micro-braided distributed optical fibre. *Compos. Struct.* 2020;254: 1-9.
11. Shipunov GS, Baranov MA, Nikiforov AS, Golovin D V., Tihonova AA. Study smart-layer effect on the physical and mechanical characteristics of the samples from polymer composite materials under quasi-static loading. *PNRPU Mech. Bull.* 2020;2020(4): 188-200.
12. Shipunov GS, Baranov MA, Nikiforov AS, Tikhonova AA, Osokin VM, Tret'yakov AA. Creation of a SMART Layer prototype with fiber-optic sensors for monitoring the stress-strain state of structures fabricated from polymeric composite materials and an estimation of its technical characteristics. *J. Opt. Technol.* 2021;88(4): 209-214.
13. Qing XP, Beard SJ, Kumar A, Chan HL, Ikegami R. Advances in the development of built-in diagnostic system for filament wound composite structures. *Compos. Sci. Technol.* 2006;66(11-12): 1694-1702.
14. Qing X, Kumar A, Zhang C, Gonzalez IF, Guo G, Chang FK. A hybrid piezoelectric/fiber optic diagnostic system for structural health monitoring. *Smart Mater. Struct.* 2005;14(3): 98-103.
15. Yoon HJ, Song KY, Choi C, Na HS, Kim JS. Real-Time Distributed Strain Monitoring of a Railway Bridge during Train Passage by Using a Distributed Optical Fiber Sensor Based on Brillouin Optical Correlation Domain Analysis. *J. Sensors.* 2016;2016: 1-10.
16. Scott RH, Banerji P, Chikermane S, Srinivasan S, Basheer PAM, Surre F et al. Commissioning and evaluation of a fiber-optic sensor system for bridge monitoring. *IEEE Sens. J.* 2013;13(7): 2555–2562.
17. Scott RH, Chikermane S, Vidakovic M, McKinley B, Sun T, Banerji P et al. Development of low cost packaged fibre optic sensors for use in reinforced concrete structures. *Meas. J. Int. Meas. Confed.* 2019;135: 617-624.
18. Prabhakar MM, Saravanan AK, Lenin AH, Leno IJ, Mayandi K, Ramalingam PS. A short review on 3D printing methods, process parameters and materials. *Mater. Today Proc.* 2020;45: 6108-6114.
19. Matveenko VP, Kosheleva NA, Serovaev GS, Fedorov AY. Numerical analysis of the strain values obtained by FBG embedded in a composite material using assumptions about uniaxial stress state of the optical fiber and capillary on the Bragg grating. *Frat. Ed. Integrata Strutt.* 2019;13(49): 177-89.
20. Voronkov AA, Anoshkin AN, Nikhamkin MA, Shipunov GS, Sazhenkov NA, Nikiforov AS. Registration of dynamic deformations of a composite material by fiber-optic sensors. *AIP Conf. Proc.* 2020;2216: 1-6.
21. Alemohammad H. Opto-Mechanical Modeling of Fiber Bragg Grating Sensors. In: *Opto-Mechanical Fiber Optic Sensors: Research, Technology, and Applications in Mechanical Sensing*. Canada: Elsevier; 2018. p.1–26.
22. Takeda S, Sato M, Ogasawara T. Simultaneous measurement of strain and temperature using a tilted fiber Bragg grating. *Sensors Actuators A Phys.* 2022;335: 113346.
23. Matveenko VP, Shardakov IN, Voronkov AA, Kosheleva NA, Lobanov DS, Serovaev GS, Spaskova EM, Shipunov GS. Measurement of strains by optical fiber Bragg grating

sensors embedded into polymer composite material. *Struct. Control Health Monit.* 2018;25(3): 1-11.

## THE AUTHORS

### **Shipunov G.S.**

e-mail: gsshipunov@gmail.com

ORCID: 0000-0002-2322-1872

### **Baranov M.A.**

e-mail: maximbaranov.123@gmail.com

ORCID: 0000-0002-5600-1526

### **Nikiforov A.S.**

e-mail: aleksandr.niciforov@gmail.com

ORCID: 0000-0001-5360-2484

### **Khabibrakhmanova F.R.**

e-mail: faridhin@mail.ru

ORCID: 0000-0002-8078-6757

# Deformation and mechanical stresses in a magnet with thin-walled quasi-force-free winding

G.A. Shneerson✉, A.V. Khlybov, A.A. Belov, A.P. Nenashev, A.A. Parfentiev,  
S.A. Shimanskiy

Peter the Great St. Petersburg Polytechnic University, 29 Politechnicheskaya St., St. Petersburg, 195251, Russia

✉ gashneerson@mail.ru

**Abstract.** The factors leading to an increase in the mechanical stress in the winding of solenoids are considered on the example of a thin-walled magnet with a multi-turn quasi-force-free winding. This example is compared with an ideal system in the form of a solenoid with unlimited length and continuous current distribution. A method for measuring submicron-sized dynamic deformations of the winding in a pulsed field has been developed and verified by comparing experiment results and calculations. Numerical modelling allowed us to distinguish the influence of local edge effects determined by characteristics of the field distribution in the inter-turn gaps. Numerical calculations have shown how the mechanical properties of the material surrounding the coil affect the stress in the winding. The possibility of reducing the stress by increasing Young's modulus of the material was confirmed. The influence on the strength of axial forces that arise near the edges of the turns and lead to compression of the turns in the axial direction is revealed.

**Keywords:** quasi-force-free magnetic fields, mechanical stresses, local effects, influence of Young's modulus on strength

**Acknowledgements.** *The work was carried out with the financial support of the Russian Science Foundation, project № 18-19-00230*

**Citation:** Shneerson GA, Khlybov AV, Belov AA, Nenashev AP, Parfentiev AA, Shimanskiy SA. Research of deformations and strains in a magnet with a thin-walled quasi-forceless winding. *Materials Physics and Mechanics*. 2022;48(3): 355-366. DOI: 10.18149/MPM.4832022\_6.

## 1. Introduction

Generating strong and superstrong magnetic fields remains a challenge due to potential winding failure in magnets, induced by electromagnetic forces. Balanced (quasi-force-free) windings allow for achieving higher magnetic fields without destroying the magnet [1,2]. However, the configurations available for constructing such windings have certain drawbacks lowering their strength characteristics compared to the initial idealized models. The main issues to be resolved to produce magnets with quasi-force-free windings are outlined in [3]. Following the results obtained in [3], this study aims to continue the investigations of mechanical stresses and strains in a real quasi-force-free winding operating in a pulsed magnetic field. Here, this problem is solved for a peculiar magnetic system comprising a thin-walled multi-turn magnet with balanced winding. The stresses arising in the winding placed in

the magnetic field are characterized by the parameter  $\eta = 1\mu_0\sigma_M / B_m^2$ , which is equal to the ratio of the equivalent mechanical stress (calculated by the formula for the von Mises) to the magnetic pressure of the generated field with the maximum flux density  $B_m$ . According to the prototype model of a quasi-force-free magnet, which corresponds to the limiting case when a balanced thin-walled solid winding without gaps has an unlimited length and is placed in a strictly uniform field, this parameter is close to 0.17–0.2 given an arbitrarily small ratio of winding thickness  $\Delta$  to radius  $R$  [2,3]. For reference, this ratio for a single-turn magnet is  $R/\Delta \gg 1$ .

Earlier studies were performed for the simplest magnet with an inner radius of 10 mm and a balanced (quasi-force-free) three-turn winding made of a thin copper band 0.7 mm thick and 11 mm wide [3]. The findings obtained indicate that the arising stresses and strains are affected by the factors taking center stage in the transition from the prototype model mentioned above to a real multi-turn system. One particular factor is the effect of electromagnetic forces due to normal components of the flux density appearing in such a winding. These effects are most pronounced in a solenoid with thin-walled winding. In this paper, we consider deformation in the midplane of a thin-walled winding with a large length-to-diameter ratio. The field is nearly uniform in this region, which allows excluding the influence that transverse components of the magnetic field, caused by the 'integral' effect from the finite length of the solenoid, have on the magnitude and distribution of electromagnetic forces. In this case, the role of the 'local' effect, i.e., the nonuniformity of the field due to inter-turn gaps, is preserved. Estimates of the resulting electromagnetic forces are given in [4]. The second factor affecting the stresses is the reduced mechanical strength of the winding with gaps between the turns compared to the prototype. Previous studies have shown that filling the space adjacent to the winding with a dielectric medium with a sufficiently large Young's modulus not only provides insulation but also increases the stiffness of the mechanical system [2]. The real winding of a multi-turn magnet is a complex multi-component system. Computer simulation allows calculating the strain taking into account the real three-dimensional structure of the magnetic system and finding the value of the strength parameter  $\eta$ . Varying the computational conditions, we can gain the data on the effectiveness of combining the effects of local field nonuniformity and dielectric medium characteristics on the value of the strength parameter. Additional crucial steps are measuring the strain during the discharge and comparing the obtained data with the results of computer simulation. This way, it is possible to assess the suitability of the adopted computational models for describing the deformation in the winding during discharge and estimate the winding's strength characteristics. The calculations can then serve for obtaining comparative estimates of structural parameters of the winding on its strength characteristics.

## 2. Technique for measuring strain under discharge

There are but scarce studies describing indirect measurements for residual strain in the winding of a multi-turn magnet: by measuring the resistance and inductance after the pulse has stopped in comparison with their initial values [5,6].

Studies on the deformation of magnets with quasi-force-free winding in [7] were carried out using a laser interferometer, recording the boundary displacement in a balanced conductor in the direction of the normal to its surface. These experiments helped identify the characteristics of the quasi-force-free system, for example, the means for adjusting it via an additional external field. However, because the solenoid is displaced during discharge, this method does not allow monitoring of the relative elastic strain and the stresses arising in the conductor. This effect can be eliminated by measuring the strain component tangential to the boundary with a sensor that shifts along with the conductor.

A fiber-optic interferometric sensor, described in [8], has been developed to measure strain. Let us briefly discuss this device. It is a two-arm fiber-optic Mach-Zehnder interferometer. A fiber sensing element is installed in the signal arm of the interferometer so that it is in direct mechanical contact with the measurement sample. The element is a short segment of uncoated optical fiber, glued with slight prestrain to the measurement sample. The sensing elements are equipped with fiber-optic connectors for attaching them to the interferometer. The sensors do not need expensive components and meet all the measurement requirements and conditions: they have a small gauge length, the sensing elements are positioned away from the magnetic system, and are only slightly susceptible to electromagnetic interference during discharge. The sensors allow monitoring of the dynamic displacements in the frequency band up to 100 kHz scale with submicron accuracy. The optical circuit of the device is shown in Fig. 1.

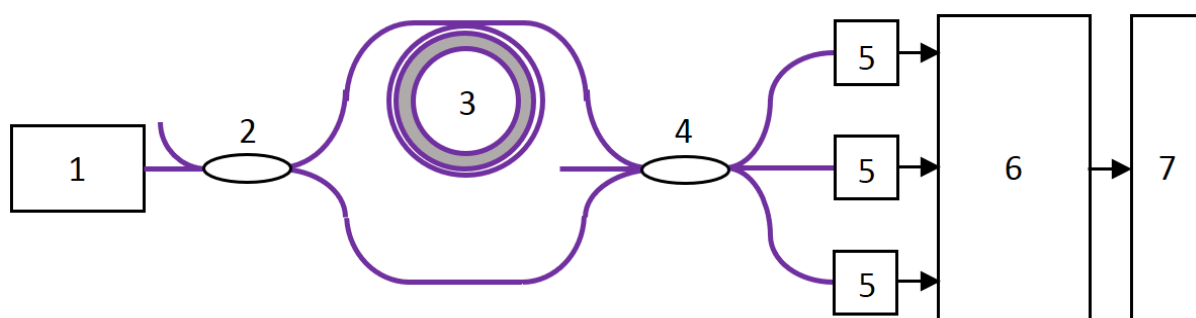


**Fig. 1.** Schematic of fiber-optic displacement sensor: laser 1, 2×2 fiber coupler 2, measurement sample 3, 3×3 fiber couple 4, photodetectors 5, multichannel ADC module 6, computer 7

Variations in the length of the sensing element due to deformations of the winding tend to modulate the phase shift between the interfering light waves in accordance with a calculated proportionality constant whose value is determined strictly by the photoelastic properties of the fiber in the sensing element:

$$\Delta l = \delta\varphi \cdot \left[ \frac{\lambda}{2\pi n} \cdot \frac{1}{1 - \frac{n^2}{2} \cdot (p_{12} - \mu(p_{11} + p_{12}))} \right]. \quad (1)$$

This formula is obtained from the description of the photoelastic tensor in a strained fiber [9]. Here  $\lambda$  is the wavelength,  $n$  is the refractive index of the fiber core at this wavelength,  $\mu$  is Poisson's ratio determining the elastic properties of the material,  $p_{11}$ ,  $p_{12}$  are the components of the photoelastic tensor of the fiber material (quartz). The expression in braces amounts to  $2.158 \cdot 10^{-7}$  m/rad for the given wavelength of 1550 nm.

The optical phase shifts in the arms of the interferometer were calculated numerically based on the data from three detection channels. A symmetric 3×3 fused coupler and a three-channel photodetector were used for this purpose. This technique for phase measurement was first proposed in [10]. The signals of the three detection channels output from the 3×3 coupler, phase-shifted by 120 degrees relative to each other, are extracted and converted to digital simultaneously so that the phase can be determined over a wide frequency band. After a digital low-pass filter is applied to the signals from the detection channels, the time-dependent phase signal can be calculated by the following analytical formula, including the normalization of the signals from the detection channels and differentiation with respect to time, summation of derivatives, and integration over time.

$$\varphi(t) = \int_0^t \frac{u \cdot (\dot{v} - \dot{w}) + v \cdot (\dot{w} - \dot{u}) + w \cdot (\dot{u} - \dot{v})}{u^2 + v^2 + w^2} d\tau. \quad (2)$$

Here  $u(\tau)$ ,  $v(\tau)$ ,  $w(\tau)$  are time functions that are normalized signals of the detection channels; the overdot denotes the time derivative.

### 3. Test experiments

The technique was tested by measuring the strain in the sample that was an external electrode of a coaxial system comprising a wire and a thin-walled cylinder. The inner radius of the cylinder was 8 mm, its wall thickness was 0.7 mm. In the ideal case, the test sample is axially symmetric, and the strength of the azimuthal magnetic field at the inner boundary,  $B_\varphi$ , and the magnetic pressure,  $P_M$ , are found by simple formulas:  $B_\varphi = \mu_0 i / 2\pi R$ ,  $P_M = B_\varphi^2 / 2\mu_0$ , where  $i$  is current,  $R$  is the inner radius of the cylinder. The amplitude and duration of the current pulse were selected so as not to overheat the sample. These conditions are met by a current pulse that is a single half-sine wave with a duration of about 0.6 ms, generated by discharging a capacitor battery. Figure 2 shows current and signal waveforms proportional to the variation in the length of the sensing element (one turn of fiber placed on the outer surface of the cylinder). The data given indicate that the results are well-reproducible, also suggesting a more complex nature of deformation than could be expected from the simplest one-dimensional loading model.

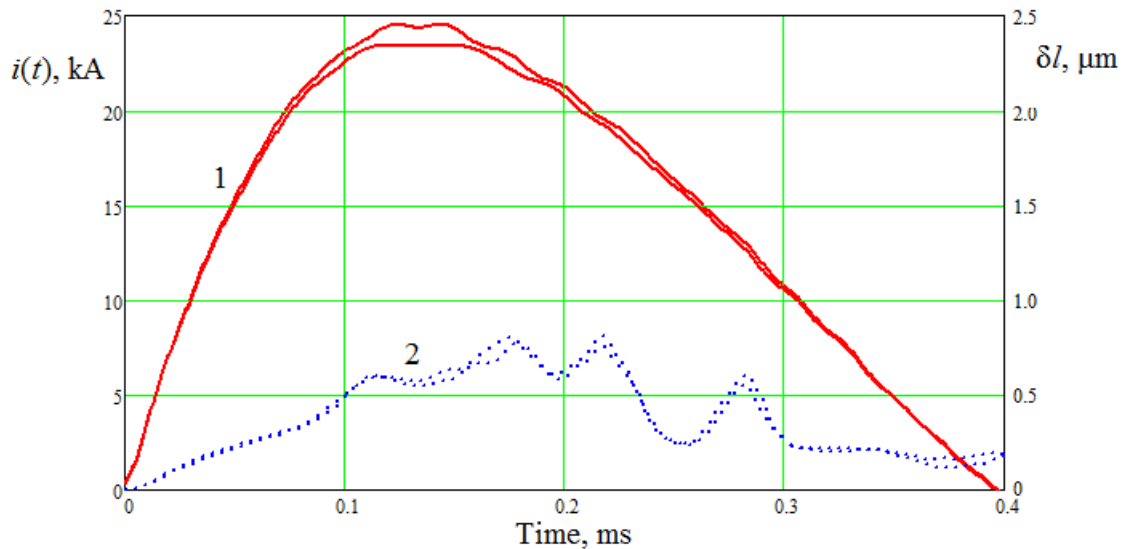


**Fig. 2.** Current waveform in two experiments with a cylinder (1), variations in the length of the sensing element (2)

The relative strain was calculated based on the data on the elongation measured by the strain gauge. Figure 3 shows the time dependence of relative strain as a function of time for one of the experiments (curve 1). We can conclude from the measurement results that high-frequency components of strain in the cylinder wall are observed in addition to the fundamental mode. These components are generated by higher vibrational modes of the mechanical system, comprising the cylindrical conductor along with its mounting components. The amplitude of these vibrations is relatively small, and their frequency is about 5 times higher than that of the fundamental vibrational mode of the cylinder, which can be estimated by the formula  $f \approx (1/2\pi R) \sqrt{E/\gamma}$  where  $\gamma$  is the density of the material,  $E$  is the elastic modulus. In our case,  $f \approx 7.5 \cdot 10^4$  Hz. In view of the above, to identify the fundamental

deformation mode, high-pass filtering of the signal was carried out using a Fourier transform. The corresponding dependence in Fig. 3 (curve 2) gives the strain amplitude value of  $15 \mu\epsilon$ . Curve 3 illustrates the results of numerical calculation for relative strain in the axial symmetry approximation. In accordance with the experimental conditions, the calculations assumed one edge of the sample to be rigidly clamped and the other unclamped.

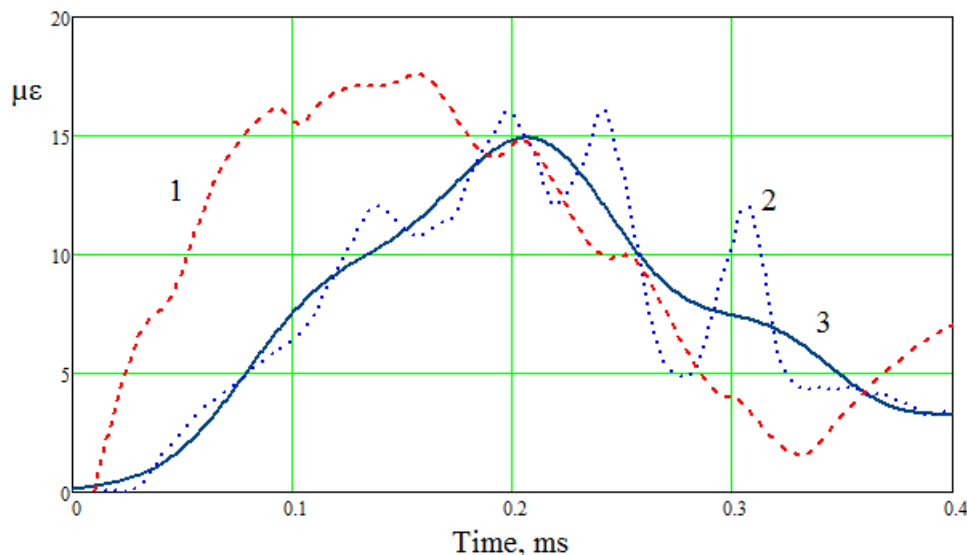


**Fig. 3.** Relative strain  $\Delta R/R$  in cylindrical sample during the test experiment. Result of numerical calculation (1), experiment (2), experimental data after low-pass filter (3)

A certain lag was observed between the times when maximum calculated and measured relative strains were reached in the midplane of the sample. The adopted model proved incapable of explaining the delayed onset of the deformation recorded in the experiments compared to the computational data. The numerical value calculated for the relative strain amplitude is close to the measured one, amounting to  $17 \mu\epsilon$ . Thus, despite the existing discrepancies, the measured and calculated maximum strains agree with each other with an accuracy acceptable for estimating the ratio of the amplitude of mechanical stresses to the amplitude of magnetic pressure.

The relative strain amplitude of a thin-walled cylinder can be estimated by a simple formula describing the static loading mode:

$$\varepsilon = \frac{\Delta R}{R} = P_M \frac{R}{d} = \frac{\mu_0 i^2}{8\pi^2 E R d}, \quad (3)$$

where  $d$  is the thickness of the cylinder wall (0.7 mm),  $E$  is the elastic modulus of copper (110 GPa),  $R$  is the cylinder radius (8 mm). This formula is applicable since the pulse duration (0.6 ms) is tens of times longer than the fundamental vibration period of the tube (about  $13 \mu\text{s}$ ). Calculating the relative strain by this formula for a current with an amplitude of 24.4 kA, we obtain the maximum value  $\Delta R/R = 15.4 \mu\epsilon$ , which is close to the above values. The given formula implies constancy of the relation  $q(t) = \varepsilon(t)^{1/2}/i(t)$ . The experimental data shown in Fig. 4 indicate that the given ratio changes little for almost the entire duration of the pulse.

The agreement between the calculated and measured values of the strain amplitude was also confirmed in experiments with two samples, where the magnetic system had a configuration identical to the one used in [3]. The winding of the samples consists of three series-connected parts (Fig. 5).

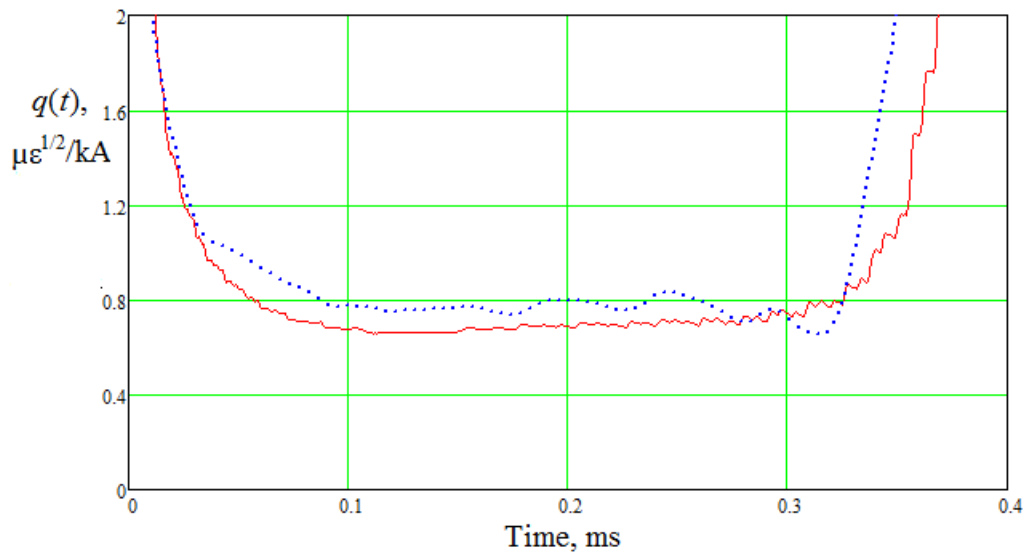


**Fig. 4.** Dependence  $q(t) = \varepsilon(t)^{1/2}/i(t)$  constructed based on the measurements

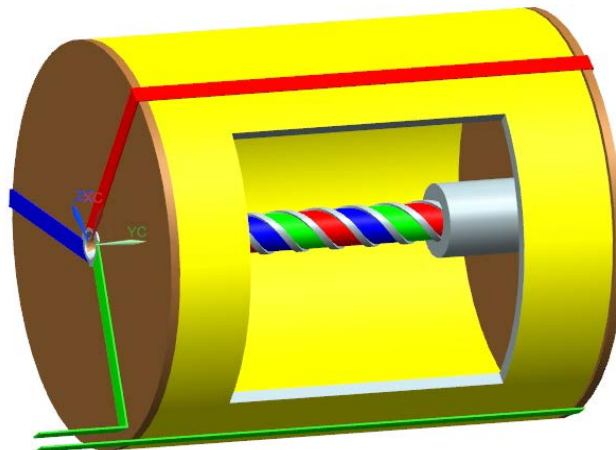


**Fig. 5.** Schematic of three-turn winding with mounting assembly

Each is made of a copper band 11 mm wide and 0.7 mm thick, placed on a dielectric holder in helical grooves 2 mm deep. Ribs 2 mm wide, securing the conductive band, served as insulating layers between the turns. The experiments were carried out both for uncoated windings (Fig. 6) and for windings impregnated with a layer of dielectric coating (bandage) 3 mm thick, made of epoxy resin with an elastic modulus of about 3.8 GPa (Fig. 7). Figures 6 and 8 show the locations where the strain sensors are attached for samples of both types. The sensors in Type I samples were 30 mm long and were placed directly on the surface of the turns. The sensors (41 mm long) in Type II samples were placed in the slots cut in the filling. Figure 9 shows the current waveforms of the sensor signals in three experiments with Type II samples. The same as in the test experiments, the deformation induced by the vibrations of the mounting assembly was detected after the maximum current. They have little effect on the magnitude of strain amplitude.

Figures 10 and 11 compare the measurements of relative strain and the simulation performed in ANSYS software, taking into account the real three-dimensional configurations of the uncoated sample and the sample with slotted coating. The high-frequency component of strain is also detected in experimental samples appears after reaching the maximum strain and has little effect on its value.

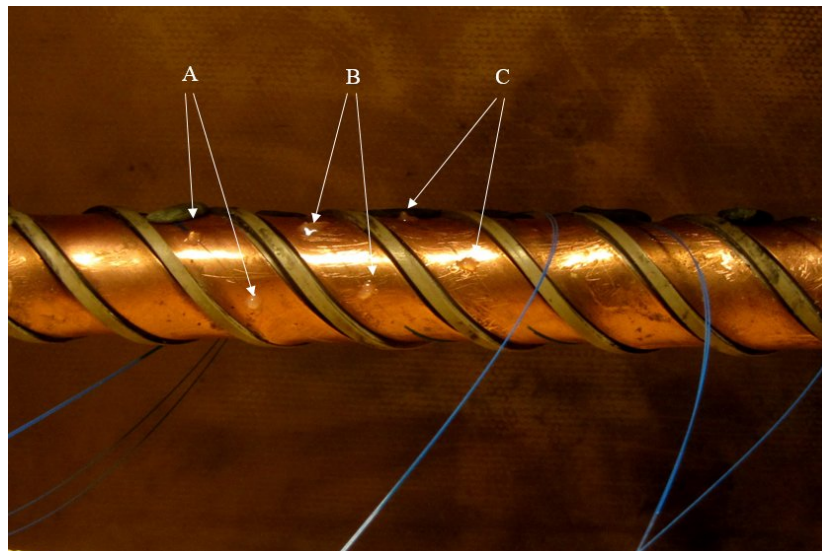


**Fig. 6.** Type I sample (without a dielectric coating layer). The arrows indicate the locations where copper bands are attached to the tips of glass fiber sensors A, B, C



**Fig. 7.** Type II sample (winding is coated with a layer of epoxy resin with slots for placing the sensors)

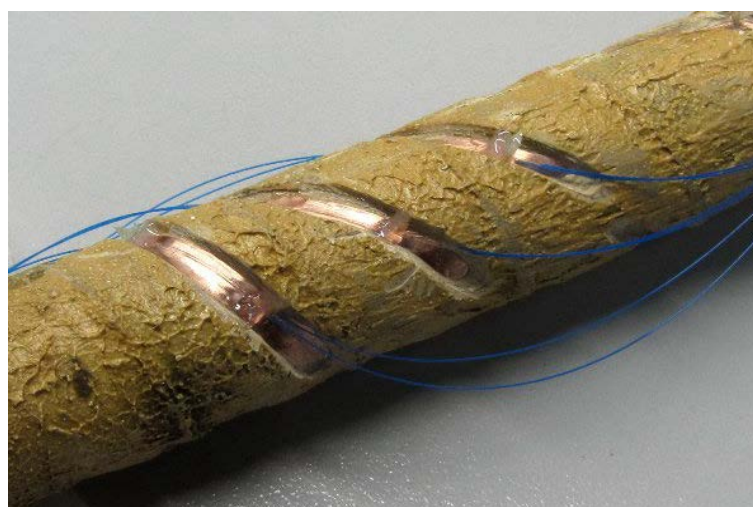


**Fig. 8.** Arrangement of fiber sensing elements in the slots of the sample with outer coating

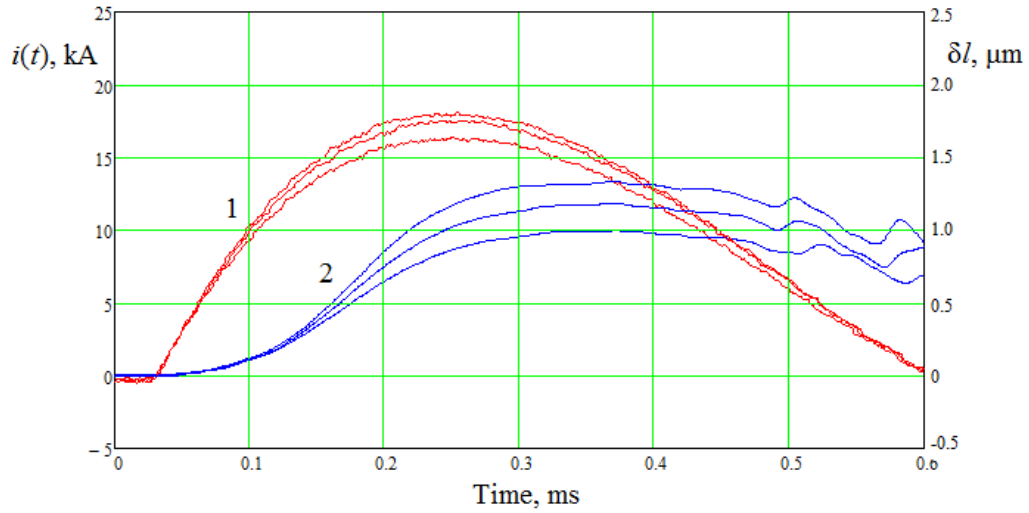


**Fig. 9.** Current and signal waveforms captured from the strain sensors obtained in three experiments with Type II samples: current (1), displacement,  $\mu\text{m}$  (2)

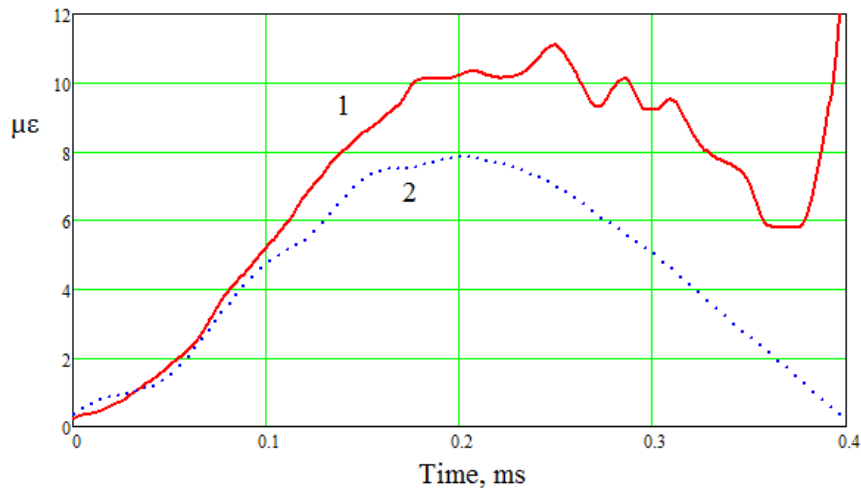


**Fig. 10.** Comparison of the relative strains measured in Type I samples with the computational results: experiment (1), simulation (2)

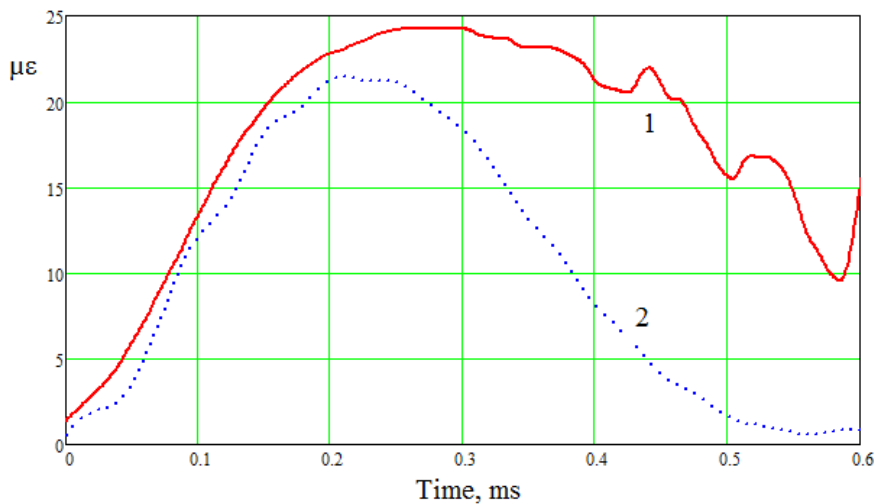


**Fig. 11.** Comparison of relative strains measured in Type II samples with the computational results: experiment (1), simulation (2)

The discrepancies between the strains measured experimentally and the calculated values appear at the late stage of the discharge. We can safely assume that this is because the three-dimensional computational model is inaccurate in accounting for the mounting assembly of the specimen. The difference between the measured and calculated values of strain amplitude is about 20% for experiments with uncoated specimens, and 8% for experiments with coated specimens.

The goal of the experiments consisted in proving that standard methods of computer simulation are applicable to calculating the stress state of the winding. The calculations allow finding the value of normalized stress  $\eta$  and estimate the flux density at which the equivalent stress exceeds the maximum permissible value, for example, the yield strength of the material. Since this quantity (as well as other strength characteristics of a material subjected to critical pulse loads) itself depends on loading mode, temperature conditions, and other factors, estimating it with an error of 10–20% is acceptable for practical purposes. Benchmarking the data obtained by calculation and experiment, we can argue that the computational models used are well applicable to comparative estimates of normalized stresses in magnets of different configurations. In particular, the results obtained can be used to analyze the effects of 'local' field nonuniformities and parameters of the dielectric medium on mechanical stresses in the winding.

#### 4. Numerical experiments illustrating the character of deformation in thin-walled multi-turn quasi-force-free winding

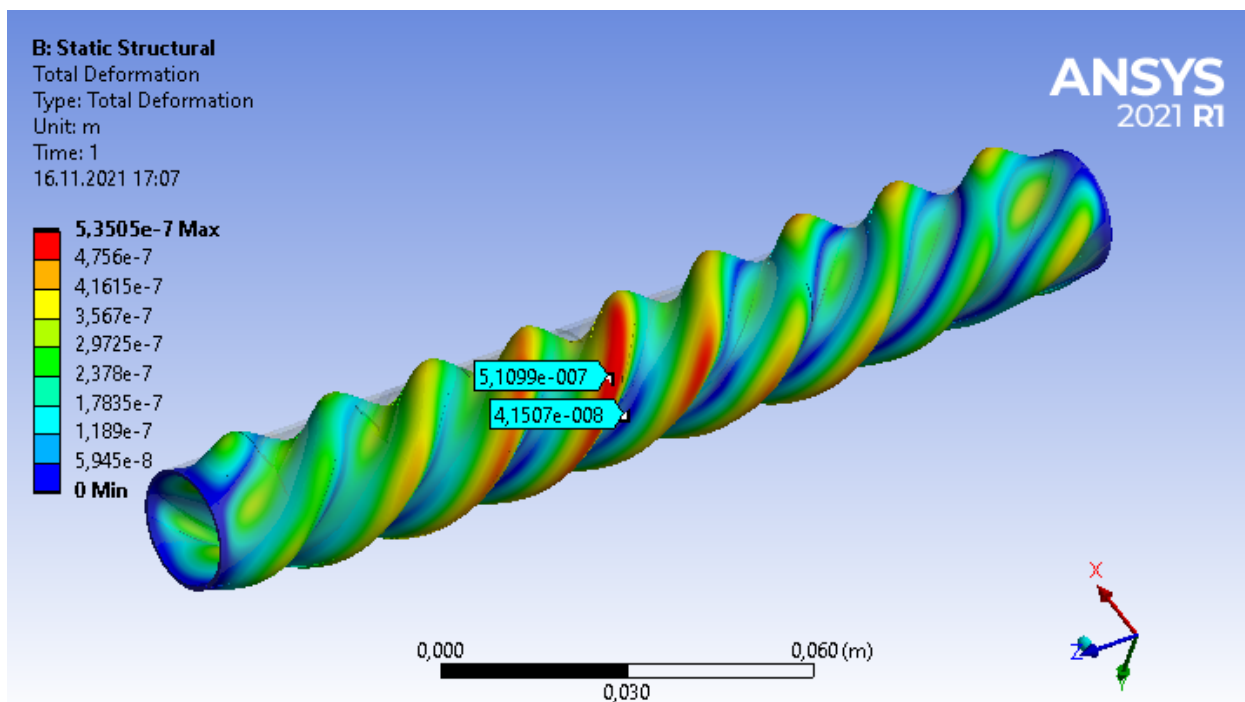
The initial model of balanced winding in the form of a solid thin-walled cylinder can serve as a starting point for multivariate calculations. The normalized stresses (parameter  $\eta$ ) calculated for different configurations are given below. The winding in the first configuration is the same as in the experimental samples and is also clamped only at the edges, but the difference from the prototype model is that no dielectric medium is surrounding the turns. Local field nonuniformities are observed in this system, with no elastic medium increasing the system's stiffness. The factor  $\eta$  in such a magnet amounts to about 40. Its value is given in Table 1 (Row 1); it can be compared with the one for unbalanced winding whose equivalent is a system with longitudinal current, flowing along the axis towards the axial current in the winding and equal to this current. There is no azimuthal field outside the winding in such a system, such that its magnetic pressure would balance the pressure of the poloidal field. The strength parameter reaches the value  $\eta = 200$ .

Table 1. Effect of elastic modulus of the dielectric medium on the mechanical stress in balanced thin-walled winding.

$E$ , GPa	Normalized stress $\eta$	
	$\Delta = 0.7$ mm	$\Delta = 3$ mm
No external medium	40	19.5
3.8	4	1.3
10	3	1
20	2	0.83
40	1.4	0.6

Comparing these data, we can see that the stresses in a balanced system are far smaller than in an unbalanced one. However, the inter-turn gaps dramatically reduce the strength of the system compared to the prototype model. Let us now consider the effect of mechanical characteristics of the windings on the stresses. Assuming that the current distribution remains

invariable, we take a system where the gaps between the turns are filled with a non-conductive material with the same elastic modulus as that of the winding material. While the distribution of electromagnetic forces in such a system is the same as in balanced winding with slots not filled with an elastic medium, the influence of gaps on the strength characteristics of the system is excluded. Consequently, the mechanical stresses are reduced by 50 times compared to the system with slots: the normalized stress takes the value  $\eta \approx 4$ . The transition to a discrete current distribution results in changing the distribution of forces and the nature of the deformation. The deformation of the winding with a thickness of 0.7 mm, magnified by 8400 times, is shown in Fig. 12. The figure shows the influence of axial forces inducing the bending in conductors due to the developing instability. The parameter  $\eta$  increases considerably as a result compared to the value calculated for the prototype model,  $\eta = 0.17\text{--}0.20$ . This result is characteristic of a thin-walled winding with the greatest local nonuniformity of the field and the resulting axial forces. As the winding thickness increases, the axial forces decrease, and the strength of the system against the action of these forces increases. This is confirmed by calculations of mechanical stresses in the winding with turns whose thickness exceeds the thickness of the gap. For example, when the turn thickness increases to 3 mm in a system without a dielectric medium, the parameter  $\eta$  becomes equal to 19.5 instead of 40, and if the gaps are filled with a medium with the same elastic modulus as the winding material, this parameter takes the value  $\eta \approx 1.8$ .



**Fig. 12.** Qualitative picture of deformation in thin-walled winding under the action of axial forces induced by local nonuniformity of the magnetic field

Windings 11 mm wide with a wall thickness  $\Delta$  of 0.7 and 3 mm can serve to trace the influence that the elastic modulus of the dielectric medium is used to fill the gaps between the turns and to construct a support cylinder for arranging the winding. An additional part of the system in both examples is an outer bandage 3 mm thick, made of the same material. The table shows the values of normalized mechanical stresses obtained by calculations for magnets with a variable elastic modulus  $E$ .

It can be seen from Table 1 that given the same distribution and magnitude of electromagnetic forces, the value of the characteristic parameter decreases sharply for a

medium with an elastic modulus  $E = 3.8$  GPa, typical for epoxy resin, subsequently decreasing to a lesser extent as the elastic modulus of the dielectric medium rises to  $E = 40$  GPa.

## 5. Conclusion

The technique developed for measuring small strains in the winding in a pulsed field allowed conducting experiments yielding an acceptable agreement between the measured and calculated strains in a thin-walled magnet with balanced winding. Simulations of mechanical stresses in the system confirmed the expected influence of the factors leading to an increase in stress compared to an ideal system in the form of a solenoid with unlimited length and a continuous current distribution. The role of normal components of the magnetic field, caused by local edge effects in the vicinity of inter-turn gaps and generating longitudinal forces, has been described for a magnet with thin-walled winding. This effect is important since it also preserves its magnitude in systems where the appearance of such components is excluded in the integral picture of the field. Moreover, we have considered the influence that the characteristics of the medium filling the inter-turn gaps have on the stresses in the winding, establishing that normalized stresses close to unity can be achieved in a balanced single-layer multi-turn winding with an increasing elastic modulus of this medium.

## References

1. Shneerson GA, Koltunov OS, Khozikov VYu. Minimizatsiya ostatochnykh napryazheniy v magnitnykh sistemakh s kvazibessilovym raspredeleniyem toka. *ZhTF*. 2002;72(1): 110-116. (in Russian)
2. Shneerson G, Dolotenko M, Krivosheev S. *Strong and Superstrong Pulsed Magnetic Fields Generation*. De Gruyter, Berlin; 2014.
3. Shneerson G, Nenashev P, Parfentiev A, Vechev I, Shimanskiy S. Problems and Possible Ways of Achieving the Design Strength of Quasi-Force-Free Windings. *IEEE Transactions on Plasma Science*. 2018;46(9): 3209-3213.
4. Shneerson G, Krivosheev S, Magazinov S. Electromagnetic Forces Acting on Thin Flat Conductors of Pulse Power Equipment. *IEEE Transactions on Plasma Science*. 2021;49(7): 2148-2152.
5. Jones H, Herlach F, Lee J et al. 50 tesla pulsed magnets using a copper conductor externally reinforced with stainless steel. *IEEE Trans. on Magnetics*. 1988;24(2): 1055-1058.
6. Portugall G, Mainson M, Billette J, Lecouturier F, Frings P, Rikken GLJA. Towards 100T-European Activities in the Development of Non-Destructive Pulsed Magnet. XI Megagauss Conference, Ed. I.R. Smith and B.M. Novac, 2006, London, pp. 53-57.
7. Shneerson G, Koltunov O, Berezkin A, Vechev I, Krivosheev S, Nenashev A, Parfentiev A. Development and Investigation of One-Layer Quasi-Force-Free Magnets // XIV Megagauss Conference, Ed. G.F. Kiuttu, K.W. Struve and J. H. Degnan, 2012, Maui, pp. 46-50.
8. Khlybov AV, Belov AA, Nenashev AP, Shneerson GA, Shimanskiy SA. Measurement of Coil Deformation in Pulsed High Magnetic Field Using a Fiber Optic Interferometer // 2020 IEEE International Conference on Electrical Engineering and Photonics (EExPolytech), St. Petersburg, Russia, 2020, pp. 255-257.
9. Becker T, Ziemann O, Engelbrecht R, Schmauss B. Optical Strain Measurement with Step-Index Polymer Optical Fiber Based on the Phase Measurement of an Intensity-Modulated Signal. *Sensors*. 2018;18(7): 2319.
10. Koo KP, Tveten AB, Dandridge A. Passively stabilized fiber interferometers using 3x3 fiber directional couplers. *Appl. Phys. Lett.* 1982;41: 616.

**THE AUTHORS****Shneerson G.A.**

e-mail: gashneerson@mail.ru

ORCID: 0000-0002-7087-098X

**Khlybov A.V.**

e-mail: a.khlybov@spbstu.ru

ORCID: 0000-0003-4457-7816

**Belov A.A.**

e-mail: belov@spbstu.ru

ORCID: 0000-0003-0617-4514

**Nenashev A.P.**

e-mail: nenashev\_ap@spbstu.ru

ORCID: -

**Parfentiev A.A.**

e-mail: -

ORCID: -

**Shimanskiy S.A.**

e-mail: s.a.shimanskiy@gmail.com

ORCID: -

# Preparation and characterization of undoped and antimony doped tin oxide thin films synthesized by spray pyrolysis

H. Habieb, N. Hamdadou✉

Laboratoire de Micro et de Nanophysique (LaMiN), Ecole Nationale Polytechnique d'Oran Maurice AUDIN,  
BP 1523 El Mnaouer, Oran 31000, Algeria  
✉ nasreddine.hamdadou@enp-oran.dz

**Abstract.** Undoped and antimony doped tin oxide thin films ( $\text{SnO}_2:\text{Sb}$ ) have been deposited by the spray pyrolysis method on glass substrates heated at  $350^\circ\text{C}$ , with various doping concentrations 0 (undoped), 1 at.%, 3 at.%, and 5 at.%. The influence of annealing temperature and various Sb doping rates on the structural, morphological and optical properties have been investigated, using grazing incidence X-ray diffraction (GIXRD), profilometry, atomic force microscopy (AFM), UV-Visible spectrophotometry and photoluminescence measurements (PL). GIXRD diagrams show that the films deposited at various Sb concentrations are polycrystalline with a tetragonal rutile type structure and preferred orientation direction along [110]. It has been also noted that the grain size changes between 11 nm and 25 nm. Atomic force microscopy (AFM) visualization revealed that surface morphology was found to be influenced by the incorporation of Sb and average roughness was varied between 4.580 nm and 10.793 nm. The optical characterization shows that the maximum value of transmittance of 82 % was found for  $\text{SnO}_2: 1 \text{ at.}\% \text{ Sb}$  thin films were annealed at  $400^\circ\text{C}$  for 4 hours and the optical band gap values range from 3.668 eV to 4.224 eV of  $\text{SnO}_2$  films. Room-temperature photoluminescence measurements under excitation at 325 nm show broad emission peak, Photoluminescence (PL) properties influenced by antimony doping for the  $\text{SnO}_2$  films are investigated.

**Keywords:** Transparent Conducting Oxide (TCO), Antimony Doped Tin Oxide Thin Films, Spray Pyrolysis, Annealing Temperature, Grazing Incidence X-ray Diffraction (GIXRD), Profilometer, Atomic Force Microscopy (AFM), Photoluminescence (PL)

**Acknowledgements.** The authors are thankful to LABMAT Laboratory of National Polytechnic School of Oran (ENPO-MA-), Algeria, for the AFM and PL characterization of our samples.

**Citation:** Habieb H, Hamdadou N. Preparation and characterization of undoped and antimony doped tin oxide thin films synthesized by spray pyrolysis. *Materials Physics and Mechanics*. 2022;48(3): 367-378. DOI: 10.18149/MPM.4832022\_7.

## 1. Introduction

Transparent conducting oxides (TCO) like  $\text{In}_2\text{O}_3$ ,  $\text{SnO}_2$ ,  $\text{ZnO}$ ,  $\text{In}_2\text{O}_3:\text{Sn}$  ... etc have been the subject of research over a number of years due to their promising properties. Tin oxide  $\text{SnO}_2$  is a n-type semiconductor with a wide bandgap  $E_g = 3.6 \text{ eV}$  at 300K [1], and electrical resistivity varying from 10 to  $10^6 \Omega\text{cm}$ , depending on the temperature and the stoichiometry of the oxide [2]. In the thin films form,  $\text{SnO}_2$  is a transparent material, characterized by high

© H. Habieb, N. Hamdadou, 2022. Publisher: Peter the Great St. Petersburg Polytechnic University

This is an open access article under the CC BY-NC 4.0 license (<https://creativecommons.org/licenses/by-nc/4.0/>)

optical transmission in the visible range  $\sim 90$ , these properties make it very attractive for several applications, like solar cells, optoelectronic devices, thin-film resistors, antireflection coatings, photochemical devices, electrically conductive glass.  $\text{SnO}_2$  material is usually used in the field of monitoring air pollution and toxic gas detection [3]. Doped and undoped  $\text{SnO}_2$  thin films have been prepared by various techniques such as sol-gel [4-6], reactive radio frequency sputtering (RF) [7], direct current (DC) magnetron sputtering [8], electron beam evaporation [9] and spray pyrolysis [10-12].

In the present study,  $\text{SnO}_2$  thin films are deposited by employing a spray pyrolysis technique. We are principally interested in this chemical technique for its advantages like ease of adding dopant material, reproducibility, high growth rate, and mass production capability for uniform large area coatings, which are desirable for industrial, solar cell, and gas sensors applications. We have made an attempt to synthesize pure and Sb doped  $\text{SnO}_2$  thin films on glass substrates by the chemical spray pyrolysis technique and the influence of annealing temperature and antimony dopant concentration on the structural, morphological and optical properties of the prepared films is reported.

## 2. Experimental methods

**Thin films preparation.** The substrates of dimensions  $7.6 \text{ cm} \times 2.6 \text{ cm} \times 0.1 \text{ cm}$  were carefully initially cleaned chemically, by keeping in distilled water, acetone and ethanol individually each for 5 min. These substrates were further treated ultrasonically with pure water for 9 min to remove surface contamination and dried at room temperature. The substrates were preheated to the required temperature, prior to deposition.

Undoped and antimony doped tin oxide thin films were deposited on glass substrates by using a spray pyrolysis system HOLMARC Model HO-TH-04. The chemical reagents used were stannous (II) chloride dihydrate ( $\text{SnCl}_2 \cdot 2\text{H}_2\text{O}$ , 97%, BIOCHEM Chemopharma, Quebec Canada) and antimony trichloride ( $\text{SbCl}_3$ , 99%, BIOCHEM Chemopharma, France) as host and dopant precursors. Initially, 0.1M of  $\text{SnCl}_2 \cdot 2\text{H}_2\text{O}$  and  $\text{SbCl}_3$  solutions were made separately by dissolving in appropriate amounts of deionized water and methanol  $\text{CH}_3\text{OH}$  volume proportion: 13 ml: 13 ml with adding a few drops of hydrochloric acid HCl to obtain a standardized and transparent working solution. Then the solution was prepared by mixing the existing solutions in appropriate volume ratios, to obtain the targeted concentrations 0 at.%, 1 at.%, 3 at.% and 5 at.% of Sb doped  $\text{SnO}_2$  thin films. The solution was stirred continuously at room temperature for 15 min until it became transparent and homogeneous. After that, the resulting solution was sprayed on the glass substrate at an optimized substrate temperature of  $350^\circ\text{C}$  with an accuracy of  $\pm 1^\circ\text{C}$  for 10 min with a compressed air pressure of 2 bars. The normalized distance between the spray nozzle and the substrates, the flow rate, and the total quantity of spray solution were 12 cm, 200  $\mu\text{l}/\text{min}$ , and 30 ml respectively. During the spraying, the nozzle moved with longitudinal and transverse speeds  $v_x = 400\text{mm}/\text{s}$  and  $v_y = 8\text{mm}/\text{s}$  respectively. The substrate's temperature was maintained using a digital temperature controller. After deposition, the films were annealed in a programmable tubular oven under air and with a heating rate of  $10^\circ\text{C}/\text{min}$  at temperatures  $400^\circ\text{C}$ ,  $450^\circ\text{C}$ ,  $500^\circ\text{C}$ , and  $550^\circ\text{C}$  for 4h.

**Thin films characterization.** A set of complementary investigation methods has been used to characterize the thin films prepared. The structural analysis has been carried out by Inel EQUINOX 3000 diffractometer using grazing incidence X-ray diffraction (GIXRD) with Cu-K $\alpha$  radiation,  $\lambda = 1.54056\text{\AA}$  at room temperature in the scan range of  $2\theta$  between  $20^\circ$  and  $90^\circ$ , continuously with the step width of  $0.03^\circ$  and a fixed incidence angle of  $5^\circ$ . The thickness of all the films was estimated by BRUKER Dektak XT profilometer with standard scan type. The morphology of the films was examined by atomic force microscope (AFM) Nano surf C3000 in tapping mode at room temperature. The optical properties of the deposited films are

measured in the wavelength region of 190-1100 nm of the spectrum at room temperature using spectrophotometer SPECORD 210 Plus UV/VIS/IR. Also, we made a complementary investigation using the room temperature photoluminescence (PL), the films were analyzed by spectrometer HORIBA iHR-550 equipped with CCD detector (400–1000 nm) and the InGaAs detector (800–1600 nm). The He-Cd laser of wavelength 325 nm (UV) or equivalently at energy 3.815 eV and power of 30mW was used as the excitation source.

### 3. Results and discussion

**Structural properties.** The GIXRD patterns obtained for undoped and doped SnO<sub>2</sub>: Sb thin films at doping rates 0 (undoped) and 5 at.% before and after annealing at temperatures 400°C, 450°C, 500°C, and 550°C, are shown in Figs. 1 and 2 respectively.

GIXRD diffractograms recorded on pure SnO<sub>2</sub> thin films with different annealing temperatures deposited at a substrate temperature of 350°C using 0.1 M stanic chloride are shown in Fig. 1. All the peaks in the pattern correspond to tetragonal rutile structure of SnO<sub>2</sub> and are indexed on the basis of ICCD file N° 00-41-1445. It is quite clear from the GIXRD diagrams that all the films are polycrystalline and highly oriented along (110) plane, this result corresponds to those reported by several works [13,14]. Presence of other plane orientations such as (101), (200), (211), (220), (310) and (301) have also been detected [15,16]. Although the intensities of all peaks increase with increasing annealing temperatures, this is related to the increase in the rate of SnO<sub>2</sub> crystallites, this result is in perfect agreement with the work of S. Laghrib et al. [17].

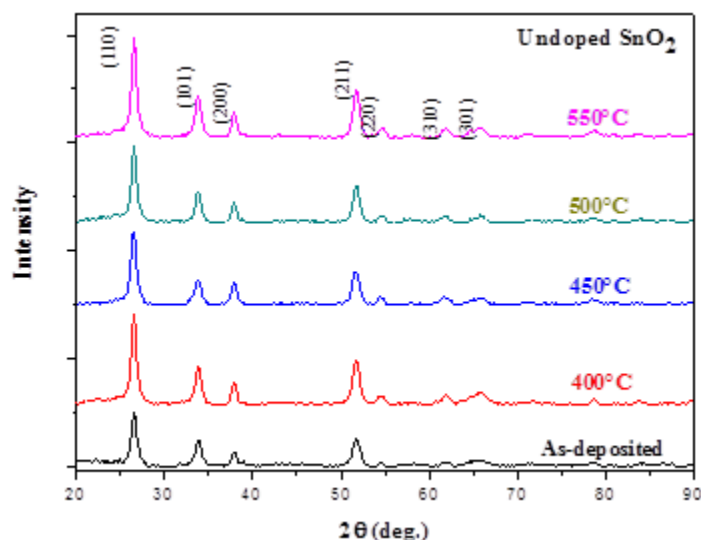


**Fig. 1.** GIXRD patterns of undoped SnO<sub>2</sub> thin films before and after annealing at different temperatures

The GIXRD patterns of as-deposited and annealed Sb-doped SnO<sub>2</sub> thin films are shown in Fig. 2 for 5 at.% of Sb doping rate. It can be seen, that the produced films are polycrystalline and all the diffractograms contain the characteristic SnO<sub>2</sub> peaks only. No phase corresponding to antimony, antimony oxides, or any other antimony compound was detected in the GIXRD patterns, which indicates that O atoms were replaced by Sb atoms in the SnO<sub>2</sub>: Sb thin films. The (110) peak is the strongest peak observed for all the films. The addition of dopants does not affect the preferred [110] orientational growth of the films, the same result was observed by Junji S. et al. [18].

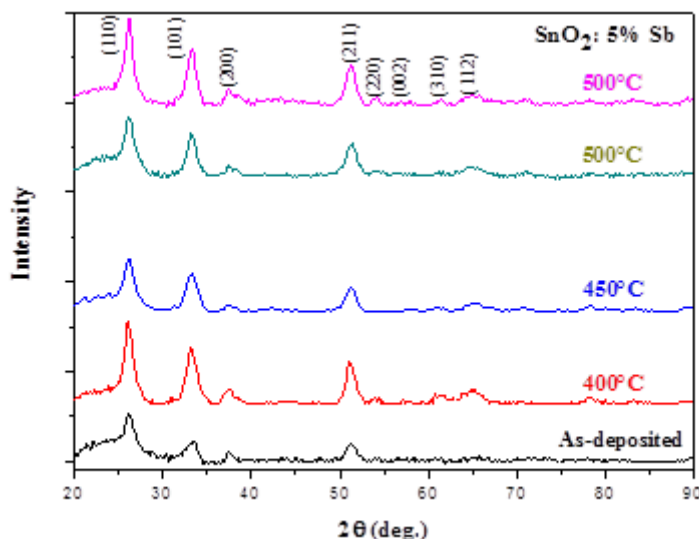


**Fig. 2.** GIXRD patterns of SnO<sub>2</sub>: 5 at.% Sb thin films before and after annealing at different temperatures

Table 1 shows the GIXRD parameters: mean grain size  $D$  (nm), the preferred orientation plane  $F_{hk0}$  (%), lattice parameters  $a$  and  $c$  (Å), and crystalline structure, of undoped and antimony doped SnO<sub>2</sub> thin films with various concentrations of 0 (undoped), 1 at.%, 3 at.%, and 5 at.% for different annealing temperatures.

The lattice parameters  $a$  and  $c$  of the identified structure were calculated by Eq. (1), where  $(hkl)$  is the lattice plane:

$$\frac{1}{d_{hkl}^2} = \frac{h^2 + k^2}{a^2} + \frac{l^2}{c^2}. \quad (1)$$

The lattice parameters values presented in Table 1 are in good agreement with those given in ICDD card N° 00-41-1445. The mean grain size  $D$  of thin films was also calculated, using the Scherrer formula based on GIXRD patterns [19,20]:

$$D = K \frac{\lambda}{\beta \cos \theta}. \quad (2)$$

In which  $K = 0.9$ ,  $\lambda = 1.54056$  Å is the wavelength of the incident radiation,  $\theta$  is the Bragg angle and  $\beta$  is the full width at half maximum (FWHM) of the diffraction peak.  $\beta$  was calculated by the Warren relation [21]:

$$\beta^2 = B^2 - b^2, \quad (3)$$

where  $B$  is the measured peak width and  $b = 0.08^\circ$  is the instrumental peak broadening, due to the instrument of GIXRD. The mean grain sizes of the samples were found between 11nm and 25nm.

The degree of preferential grain orientation according to  $(hk0)$  plane was determined using the following equation:

$$F_{hk0} = \frac{\sum I(h,k,0)/I_0(h,k,0)}{\sum I(h,k,l)/I_0(h,k,l)}, \quad (4)$$

where  $I(hkl)$  is the measured intensity of X-ray diffraction,  $I_0(hkl)$  is the corresponding standard intensity from the ICDD data. The degree of preferential orientation according to the plane  $(hk0)$  of SnO<sub>2</sub>: 3 at.% Sb thin films is in the order of 44%.

**Morphological Properties.** The thin films of undoped and Sb doped SnO<sub>2</sub> at 1 at.%, 3 at.% and 5 at.% respectively, annealed at 400 °C for 4h were examined by the AFM device to characterize the surface roughness. The AFM measurements are carried out in the air in "tapping mode". Figure 3 displays the 2D and 3D AFM images of Sb-doped SnO<sub>2</sub> thin films annealed at 400 °C with a Sb concentrations of 0 (undoped) and 5 at.% obtained over an area of  $2 \times 2 \mu\text{m}^2$ .

Table 1. GIXRD parameters and mean grain size of undoped and antimony doped SnO<sub>2</sub> thin films with various Sb concentrations of 0 (undoped), 1 at.%, 3 at.%, and 5 at.% for different annealing temperatures

Doping rate	T <sub>a</sub> (°C)	Crystalline structure	a, c (Å)	D (nm)	F <sub>hko</sub> (%)
0 at.%	As-prepared	Tetragonal	a = 4.740 c = 3.204	23	64
	400				
	450				
	500				
	550				
1 at.%	As-prepared		a = 4.766 c = 3.195	25	53
	400				
	450				
	500				
	550				
3 at.%	As-prepared		a = 4.780 c = 3.293	11	44
	400				
	450				
	500				
	550				
5 at.%	As-prepared		a = 4.740 c = 3.204	14	43
	400				
	450				
	500				
	550				

The average roughness  $R_a$  and the root mean square  $R_q$  (RMS) parameters were calculated from AFM data using the following relations:

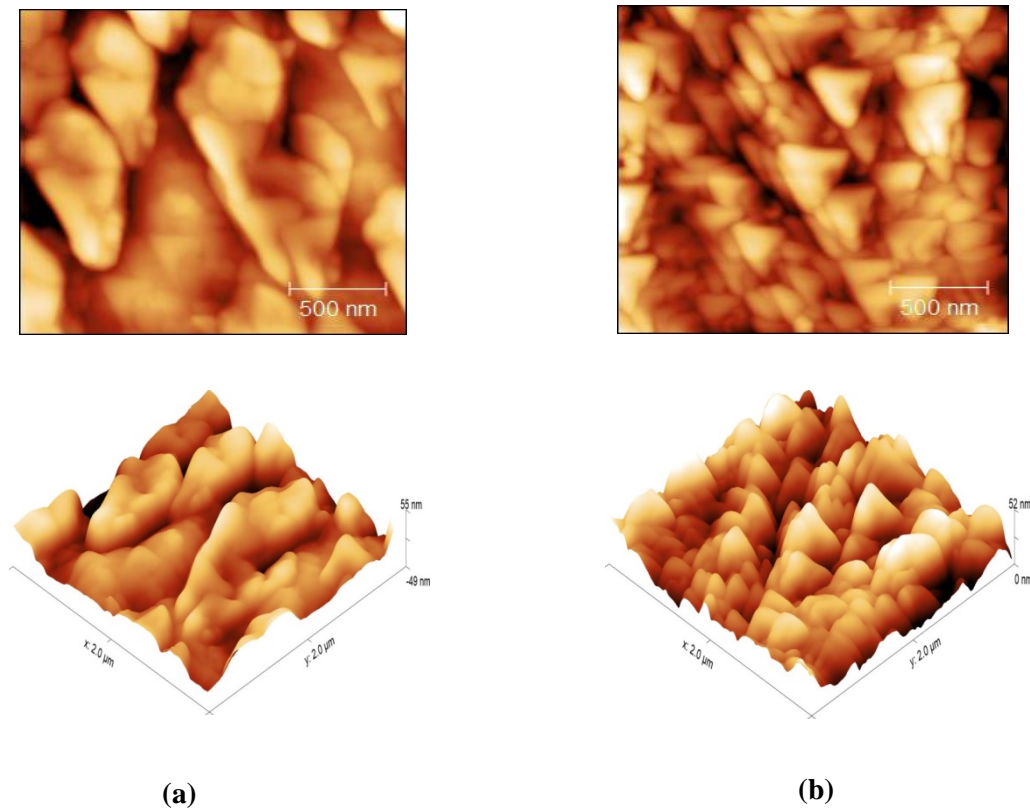
$$R_a = \frac{1}{l} \int_0^l |Z(x)| dx, \quad (5)$$

$$R_q = \sqrt{\frac{1}{l} \int_0^l Z^2(x) dx}, \quad (6)$$

where  $Z(x)$  is the function, that describes the surface profile, analyzed in terms of height  $Z$  and position  $x$  of the sample over the evaluation length  $l$ . The results are collected in Table 2, with thickness values measured by a profilometer as a function of Sb doping.

All samples show a polycrystalline morphology, and the grain size gradually decreases with an increase of Sb concentration. The grain size is seen to be larger than the crystallite size estimated from XRD measurements; however, this is also attributable to the agglomeration of smaller crystallites. Also, we see from the AFM images, a trend of

formation of nanostructures in the form of aggregate with different sizes in relation to doping concentration. It has been suggested that there is homogeneous granulates on all surfaces of the films, these results are in very good agreement with previous works [18]. The root mean square (RMS) surface roughness values for samples with Sb concentrations of 0 (undoped) and 1 at.%, 3 at.%, and 5 at.% were found to be 7.707 nm and 13.563 - 5.725 - 8.334 nm, respectively.



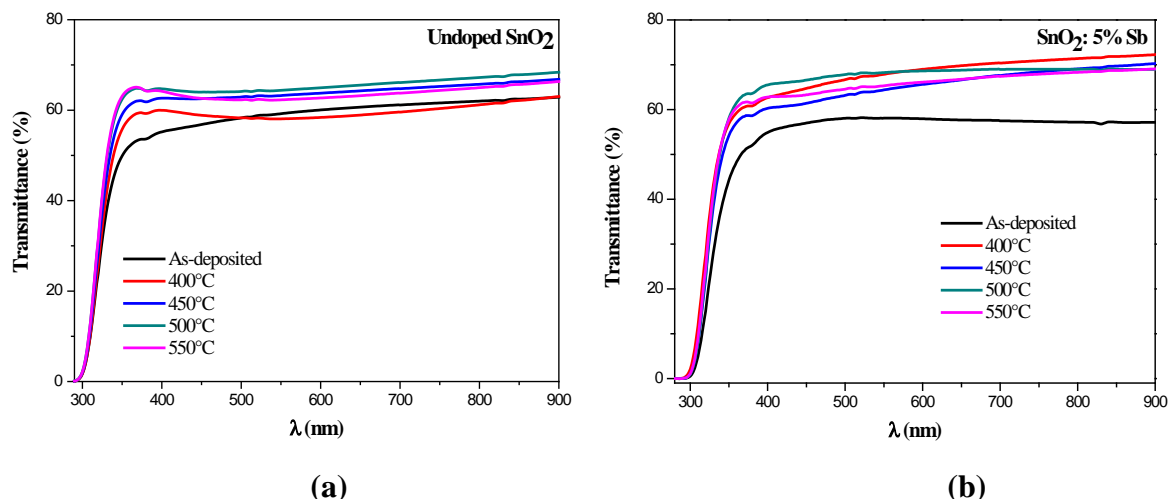
**Fig. 3.** 2D and 3D AFM images of Sb-doped SnO<sub>2</sub> thin films annealed at 400°C with Sb concentration of 0 (undoped) (a) and 5 at.% (b)

Table 2. Surface roughness parameters and thickness of undoped and Sb doped SnO<sub>2</sub> thin films annealed at 400°C for 4h

Sb-doping concentration (at. %)	Thickness (nm)	$R_a$ (nm)	$R_q$ (nm)
0	340	5.709	7.704
1	155	10.793	13.563
3	141	4.580	5.725
5	306	6.694	8.334

**Optical properties.** Figure 4 shows the optical transmittance of the undoped and Sb doped SnO<sub>2</sub> thin films and those deposited at Sb doping concentration 5 at.%, in the wavelength range from 300 to 900 nm.

All the undoped SnO<sub>2</sub> thin films deposited have an average transmittance in the visible range that varies between 58% and 65%, it has been noticed that this transmittance increases with the increase of annealing temperature. The increased transparency observed may be attributed to less scattering effects and better crystallinity.



**Fig. 4.** Optical transmittance spectra of undoped (a) and Sb doped SnO<sub>2</sub> thin films before and after annealing at different temperatures (b)

We have noticed that transmittance increases after doping with 1 at.%, 3 at.% and 5 at.% Sb, and all the films display high transmittance in the visible and near-infrared ranges. It indicates that the highest optical transmittance is of the order of 82% for SnO<sub>2</sub>: 1 at.% Sb thin films annealed at 400°C for 4h.

From the transmission spectra and the thickness determined by the profilometer, we calculate the absorption coefficients  $\alpha$  using the following relation:

$$\alpha = \frac{1}{e} \ln \left( \frac{100}{T(\%)} \right), \quad (7)$$

where  $e$  is the film thickness.

In the low-energy region of the incident photon [1.5–3.5 eV], we notice a decrease in the absorption coefficient. It is clear that the rate of doping reduces the absorption coefficient.

Optical band gap  $E_g$  is an important characterization tool for thin film. The optical band gap of undoped and Sb doped SnO<sub>2</sub> thin films were evaluated from Tauc's equation [22],

$$(\alpha h\nu) = A(h\nu - E_g)^n, \quad (8)$$

where  $A$  is a constant,  $h$  is the Plank's constant,  $\nu$  is the frequency of incident photon and  $\alpha$  is the absorption coefficient. In eq. (8) the exponent  $n$  indicates the nature of band transition, the value of  $n$  is taken as  $\frac{1}{2}$ , for the direct allowed transition nature of undoped and Sb doped SnO<sub>2</sub> thin films. The  $E_g$  values of the films were measured, from extrapolation of the straight line region of the  $(\alpha h\nu)^2$  versus  $h\nu$  graph to intercept the  $h\nu$  axis. The obtained values of optical band gaps of all the films are mentioned in the respective plots, Fig. 5.

The direct bandgap, determined by extrapolating the straight-line portions to the energy axis to  $(\alpha h\nu)^2 = 0$ , is found to be varied between 4.099 and 4.224 eV for pure SnO<sub>2</sub> thin film, which is comparable to the value of  $E_g = 4.119$  eV reported for single-crystal SnO<sub>2</sub> [23], these gap energy values are larger than the value of 3.62 eV for the bulk SnO<sub>2</sub> due to the contribution of quantum size effect of the present SnO<sub>2</sub> thin film [24]. On the one hand, we notice a decrease in the width of the band gap after doping (approximately 3.9 eV for SnO<sub>2</sub>: 1 at.% Sb), this variation can be explained by the Roth effect [25]. And on the other hand, the gap increases again with the increase of the doping rate (3 at. % and 5 at.% Sb), the gap increases following the Burstein Moss effect [26,27], also this increase may occur due to the replacement of Sn<sup>+4</sup> with Sb<sup>+5</sup>, which fills the lower energy levels of the conduction band inside the forbidden gap region that then causes the increased carrier concentration. However,

these results converge on previously published studies, Table 3, that show that doped SnO<sub>2</sub> thin films generally exhibit wider band gap energies on the order of 4 eV [28,29].

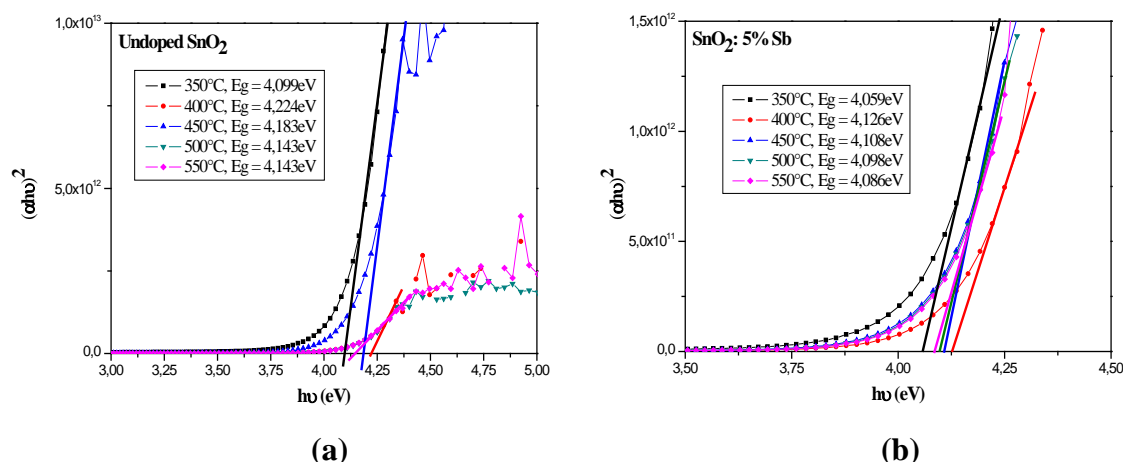


**Fig. 5.** Plots of  $(\alpha h\nu)^2$  vs.  $h\nu$  of undoped (a) and Sb doped SnO<sub>2</sub> (b) thin films for different annealing temperatures

**Table 3.** Comparison of SnO<sub>2</sub> thin films band gap values

Thin films	Deposition method	E <sub>g</sub> (eV)	References
Undoped SnO <sub>2</sub>	Spray pyrolysis	4.09 - 4.22	Our study
	Spin coating	4.38	[30]
	Spin coating	4.10	[6]
	Ultrasonic spray pyrolysis	4.10	[31]
Sb doped SnO <sub>2</sub>	Spray pyrolysis	4.10 - 4.12	Our study
	Radio-frequency magnetron sputtering	4.28 - 4.32	[32]
	/	4.17 - 4.41	[33]

Urbach energy, which characterizes crystalline disorder of films, can be determined by the following relation [34]:

$$\alpha = \alpha_0 \exp\left(\frac{h\nu}{E_u}\right), \quad (9)$$

where  $\alpha_0$  is a constant and  $E_u$  is the Urbach energy. The value of Urbach energy is calculated from the reciprocal value of the slope of the linear portion of  $\ln\alpha$  versus  $h\nu$ . We have found that for all the samples, the values of Urbach energy of undoped and doped SnO<sub>2</sub> films decreases from 0.286 eV to 0.283 eV, 0.319 eV to 0.299 eV, 0.319 eV to 0.305 eV and from 0.300 eV to 0.288 eV, for 0 at.%, 1 at.%, 3 at.% and 5 at.% Sb concentration, this result can be explained by the decrease in disorder in the films.

**Photoluminescence (PL) analysis.** Photoluminescence (PL) spectroscopy is a powerful technique for studying the behavior of SnO<sub>2</sub> luminescence as a function of Sb-doping content. We give in Fig. 6 the emission spectra for Sb-doped SnO<sub>2</sub> thin films annealed at 400°C with Sb concentration of 0 (undoped), 1 at.%, 3 at. % and 5 at.% obtained at room temperature normalized intensity recorded in the energy range (4.1–1.4 eV) corresponding to the wavelength range (~ 300–900 nm). For all the deposited thin films, the emission peaks have high intensity and are positioned at 359, 409, 535, and 718 nm. At room temperature, the high density of oxygen vacancies interacting with interfacial tin leads to the formation of a considerable amount of trapped states within the band gap, giving rise to high PL intensity. The peak at 359 nm (~3.45 eV) is sharp UV-violet luminescence peak, the visible region can

be split into three luminescence bands, peak at 409 nm is violet luminescence peak ( $\sim 3.03$  eV), peak at 534 nm is green luminescence peak ( $\sim 2.32$  eV) and peak at 718 nm ( $\sim 1.73$  eV) is red luminescence peak. According to the literature [35,36], the UV-violet is mainly generated by the electron transition from the donor level formed by oxygen vacancies ( $V_O$ ) to the acceptor level formed by other defects and impurities. The UV-violet peak we observed from undoped  $\text{SnO}_2$ , and think that it is also due to oxygen vacancies ( $V_O$ ). The UV-violet peak for the doped  $\text{SnO}_2$  is due to the difference in the position of the donor level formed by Sb ions and oxygen vacancies ( $V_O$ ). The violet can be related to tin interstitials and oxygen vacancies in the undoped  $\text{SnO}_2$  thin films. For  $\text{SnO}_2$ : Sb films, the origin of the violet peak at 409 nm is attributed to the electron transition from the donor level formed by oxygen vacancies ( $V_O$ ) or  $\text{Sb}^{+5}$  ions to the acceptor level formed by the  $\text{Sb}^{+3}$  ions [37]. In spray deposited polycrystalline oxides, oxygen vacancies are known to be the most common defects and form the donor level [38]. For our samples, because of the pyrolytic decomposition, there should be the existence of oxygen vacancies due to rapid evaporation and oxidation processes. A broad peak observed at 718 nm may be due to other crystal defects which are formed during the growth of samples. As to the origin of the peak at 535 nm of pure  $\text{SnO}_2$  and Sb doped  $\text{SnO}_2$ , maybe it is related to other crystal defects which were formed during the growth of the samples, but it is not yet clear now.

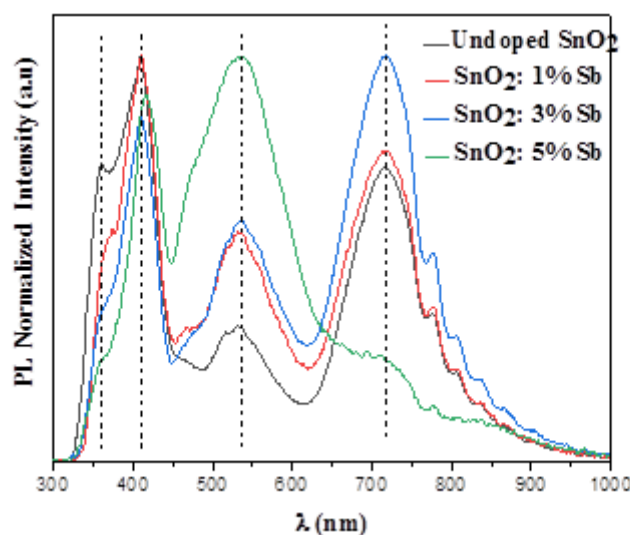


**Fig. 6.** PL emission spectrum of  $\text{SnO}_2$  thin films with various Sb concentrations at excitation wavelength of 325 nm

#### 4. Conclusion

In our study, transparent conducting  $\text{SnO}_2$  thin films with different concentrations of Sb have been successfully fabricated on glass substrate by using the chemical spray pyrolysis technique. All the synthesized films are polycrystalline in nature and are matched with ICDD card number 00-41-1445 to confirm the tetragonal rutile structure of  $\text{SnO}_2$  films. AFM measurements confirmed a polycrystalline rutile structure for all samples improved with XRD analysis and showed that the maximum roughness was noted for  $\text{SnO}_2$ : 1 at. % Sb thin films. The optical transmittance of the  $\text{SnO}_2$  films increases with doping Sb. These results suggest that spray pyrolysis is a promising fabrication technique for TCOs films composed of Sb doped  $\text{SnO}_2$ . Strong violet emission has been seen in the luminescence spectra.

## References

1. Chi-Fan L, Chun-Hsien K, Tao-Hsing C, Yu-Sheng H. Optoelectronic Properties of Ti-doped SnO<sub>2</sub> Thin Films Processed under Different Annealing Temperatures. *Coatings*. 2020;10(4): 394.
2. Saadeddin I, Pecquenard B, Manaud JP, Decourt R, Labrugère C, Buffeteau T, Campet G. Synthesis and characterization of single- and co-doped SnO<sub>2</sub> thin films for optoelectronic applications. *Applied Surface Science*. 2007;253(12): 5240-5249.
3. Hachoun Z, Ouerdane A, Bouslama M, Ghaffour M, Abdllaoui A, Caodano Y, Ali benamara A. Investigation of the properties of Sb doping on tin oxide SnO<sub>2</sub> materials for technological applications. *Materials Science and Engineering*. 2016;123: 012029.
4. Laxmikanta D, Prasanta KB. Synthesis and characterization of nanostructured Mn(II) doped antimony-tin oxide (ATO) films on glass. *Applied Surface Science*. 2013;280: 33-41.
5. Yuhua X, Shihui G, Li X, Yalu Z, Xueyun Z, Bangmin Z, Li Z, Chengxian L, Xiufeng H, Zhenchao W. Room temperature ferromagnetism of Mn-doped SnO<sub>2</sub> thin films fabricated by sol-gel method. *Applied Surface Science*. 2008;254(22): 7459-7463.
6. Belhamri S, Hamdadou N. Improved Properties of SnO<sub>2</sub> Thin Films Obtained Via Spin Coating Method by Varying the Solution Concentration. *Surface Review and Letters*. 2018;25(7): 1850092.
7. Chi-Fan L, Chun-Hsien K, Tao-Hsing C, Yu-Sheng H. Optoelectronic Properties of Ti-doped SnO<sub>2</sub> Thin Films Processed under Different Annealing Temperatures. *Coatings*. 2020;10(14): 394.
8. Morikawa H, Fujita M. Crystallization and electrical property change on the annealing of amorphous indium-oxide and indium-tin-oxide tin films. *Thin Solid Films*. 2000;359(1): 61-67.
9. Shamala KS, Murthy LCS, Narasimha RK. Studies on tin oxide films prepared by electron beam evaporation and spray pyrolysis methods. *Bull. Mater. Sci*. 2004;27(3): 295-301.
10. Kumar RR, Rao KN, Rajanna K, Phani AR. Novel co-evaporation approach for the growth of Sb doped SnO<sub>2</sub> nanowires. *Mater. Lett*. 2013;106: 164-167.
11. Zhang B, Tian Y, Zhang JX, Cai W. The Ftir studies of SnO<sub>2</sub>:Sb(ATO) films deposited by spray pyrolysis. *Materials Letters*. 2011;65: 1204-1206.
12. Sushant G, Yadav BC, Prabhat KD, Das B. Microstructural, optical and electrical investigations of Sb-SnO<sub>2</sub> thin films deposited by spray pyrolysis. *Materials Research Bulletin*. 2013;48(9): 3315-3322.
13. Xu Y, Yamazaki M, Villars P. Inorganic materials database for exploring the nature of material. *Jpn. J. Appl. Phys*. 2011;50(11S): 11RH02.
14. Allag A, Saâd R, Ouahab A, Abdelmalek N, Brahim G. Effect of solution concentration on the structural, optical and electrical properties of SnO<sub>2</sub> thin films prepared by spray pyrolysis. *Optik*. 2015;127: 2653-2658.
15. Allag A, Saad R, Ouahab A, Attouche H, Kouidri N. Optoelectronic properties of SnO<sub>2</sub> thin films sprayed at different deposition time. *Chin. Phys. B*. 2016;25(4): 046801.
16. Bagheri-Mohagheghi MM, Shahtahmasebi N, Alinejad MR, Youssefi A, Shokooh-Saremi M. The effect of the post-annealing temperature on the nano-structure and energy band gap of SnO<sub>2</sub> semiconducting oxide nano-particles synthesized by polymerizing-complexing sol-gel method. *Physica B*. 2008;403(13-16): 2431-2437.
17. Laghrib S, Amardjia-Adnani H, Abdi D, Pelletier JM. Elaboration et étude des couches minces de SnO<sub>2</sub> obtenu par évaporation sous vide et recuites sous oxygène. *Revue des Energies Renouvelables*. 2007;10(3): 357-366.
18. Junji S, Tasuku K. Structural and electrical properties of Sb-doped SnO<sub>2</sub> thin films prepared by metal organic decomposition. *Thin Solid Films*. 2019;685: 210-215.

19. Klug HP, Alexander LE. *X-Ray Diffraction Procedures*. NY: John & Wiley and Sons; 1954.
20. Patterson AL. The Scherrer formula for X-ray particle size determination. *Phys. Rev.* 1939;56(10): 978.
21. Warren BE. X-ray diffraction methods *J. Appl. Phys.* 1941;12(5): 375.
22. Tauc J. Absorption edge and internal electric fields in amorphous semiconductors. *Mater. Res. Bull.* 1970;5(8): 721-729.
23. Gupta S, Yadav BC, Dwivedi PK, Das B. Microstructural, optical and electrical investigations of Sb-SnO<sub>2</sub> thin films deposited by spray pyrolysis. *Materials Research Bulletin.* 2013;48(9): 3315-3322.
24. Frohlich D, Kezklies R. Band-Gap Assignment in SnO<sub>2</sub> by Two-Photon Spectroscopy. *Phys. Rev. Lett.* 1978;41(25): 1750.
25. Roth AP, Williams DF. Properties of zinc oxide films prepared by the oxidation of diethyl zinc. *Journal of Applied Physics.* 1981;52(11): 6685-6692.
26. Fauzia V, Yusnidar MN, Hanum Lalasari L, Subhan A, Umar AA. High figure of merit transparent conducting Sb-doped SnO<sub>2</sub> thin films prepared via ultrasonic spray pyrolysis. *Journal of Alloys and Compounds.* 2017;720: 79-85.
27. Zheng H, Li L, Sun Z, Yu S, Luo W. Preferential orientation, microstructure and functional properties of SnO<sub>2</sub>:Sb thin film: the effects of post-growth annealing. *Appl. Surf. Sci.* 2016;362: 230-236.
28. Yang W, Yu S, Zhang Y, Zhang W. Properties of Sb-doped SnO<sub>2</sub> transparent conductive thin films deposited by radio-frequency magnetron sputtering. *Thin Solid Films.* 2013;542: 285-288.
29. Rana MPS, Singh F, Joshi K, Negi S, Ramola RC. Influence of electronic excitations on structural, optical and electrical properties of undoped and antimony doped tin oxide thin films. *Thin Solid Films.* 2016;616: 34-42.
30. Feng G, Shu Fen W, Meng Kai L, Xiu Feng C, Su Wen L, Guang Jun Z, Dong X, Duo Rong Y, Luminescence of SnO<sub>2</sub> thin films prepared by spin-coating method. *Journal of Crystal Growth.* 2004;262: 182-185.
31. Patil LA, Shinde MD, Bari AR, Deo VV. Highly sensitive and quickly responding ultrasonically sprayed nanostructured SnO<sub>2</sub> thin films for hydrogen gas sensing. *Sensors and Actuators B.* 2009;143(1): 270-277.
32. Wenhao Y, Shihui Y, Yang Z, Weifeng Z. Properties of Sb-doped SnO<sub>2</sub> transparent conductive thin films deposited by radio-frequency magnetron sputtering. *Thin Solid Films.* 2013; 542: 285-288.
33. Tauc J, Grigorovici R, Vancu A. Optical Properties and Electronic Structure of Amorphous Germanium. *Phys. Status Solidi.* 1996;15: 627.
34. Urbach F. The long-wavelength edge of photographic sensitivity and of the electronic absorption of solids. *Phys. Rev.* 1953;92(5): 1324.
35. Yuheng W, Jin M, Feng J, Xuhu Y, Honglei M, Structural and photoluminescence characters of SnO<sub>2</sub>:Sb films deposited by RF magnetron sputtering. *Journal of Luminescence.* 2005;114(1): 71-76.
36. Kim TW, Lee DU, Yoon YS. Microstructural, electrical, and optical properties of SnO<sub>2</sub> nanocrystalline thin films grown on InP (100) substrates for applications as gas sensor devices. *Journal of Applied Physics.* 200;88(6): 3759.
37. Shinde SS, Shinde PS, Sathe VG, Barman SR, Bhosale CH, Rajpure KY. Electron-phonon interaction and size effect study in catalyst based zinc oxide thin films. *J. Mol. Structure.* 2010;984(1-3): 186.

38. Babar AR, Shinde SS, Moholkar AV, Bhosale CH, Kim JH, Rajpure KY. Sensing properties of sprayed antimony doped tin oxide thin films: solution molarity. *J. Alloys Compd.* 2011;509(6): 3108-3115

### THE AUTHORS

**Habieb H.**

e-mail: habieb.halima@gmail.com

ORCID: 0000-0003-3952-8198

**Hamdadou N.**

e-mail: nasreddine.hamdadou@enp-oran.dz

ORCID: 0000-0003-1880-6881

# On the problem of evaluating the behavior of multicomponent materials in mixed boundary conditions in contact problems

V.A. Babeshko<sup>1✉</sup>, O.V. Evdokimova<sup>2</sup>, O.M. Babeshko<sup>1</sup>

<sup>1</sup>Kuban State University, 149 Stavropolskiya st. Krasnodar, 350040, Russia

<sup>2</sup>Southern Scientific Center RAS, Rostov-on-Don, 344006, Chekhov st, 41, Russia,

✉ e-mail: babeshko41@mail.ru

**Abstract.** For the purposes of evaluating the behavior of multicomponent materials under operating conditions, the paper for the first time constructs in general an exact solution of systems of Wiener-Hopf integral equations of arbitrary order. Systems of these equations arise in mixed problems of continuum mechanics for multicomponent materials of complex rheology. The cases of mixed boundary value problems are considered under the assumption that there is a change of boundary conditions on the inner or outer boundary of a multilayer medium. Such mixed problems are reduced to systems of Wiener-Hopf integral equations, the Fourier transform of the kernels of which is a fairly general meromorphic matrix-a function that does not coincide with any of the special cases for which the system of equations is precisely solved. Earlier, the authors considered the case of a system consisting of two equations. The transfer of these results to the case of an arbitrary number of equations is based on this previously performed work. Systems of Wiener-Hopf integral equations arise in the mechanics of deformable media, geophysics, flaw detection, economics, and in a number of related fields.

**Keywords:** multicomponent materials, systems of Wiener-Hopf integral equation, meromorphic matrix- function in the core, exact solution

**Acknowledgements.** *The work was carried out with the financial support of the Russian Science Foundation, project 22-21-00129.*

**Citation:** Babeshko VA, Evdokimova OV, Babeshko OM. On the problem of evaluating the behavior of multicomponent materials in mixed boundary conditions in contact problems. *Materials Physics and Mechanics*. 2022;48(3): 379-385. DOI: 10.18149/MPM.4832022\_8.

## 1. Introduction

Systems of Wiener-Hopf integral equations play an important role in a wide variety of practice areas. Thus, these equations arise in the problems of strength and fracture [1], wave propagation in elastic bodies [2], acoustics [3], non-destructive testing methods [4], the theory of scattering of electromagnetic waves, and the creation of an electronic element base [5], the theory of waves in a liquid [6], geophysics [7], signal filtering [8], economics and finance [9], in the theory of random processes [10], in the theory of resonances and localization of processes [11] and in other fields.

Recently, their role has increased due to the creation of the block element theory, which allows for the direct solution of boundary value problems for systems of partial differential

equations. The theory of individual Wiener-Hopf equations has been elaborated in detail and published in print in detail. The theory of systems of Wiener-Hopf integral equations is problematic, which are investigated by several approaches: using the singular Sohotsky-Plemel integral [12] and the method of the theory of normalized rings [13]. Both approaches rely on the factorization of matrix functions  $\mathbf{K}(\alpha)$ , which are coefficients of the Riemann-Hilbert matrix functional equations, to which systems of integral equations of the form are reduced

$$\mathbf{K}(\alpha)\mathbf{Q}^+(\alpha) = \mathbf{Q}^-(\alpha) + \mathbf{F}(\alpha).$$

However, factorization of matrix functions in the general case, like a single function, has not yet been possible. Only the types of matrix functions that are functionally commutative, for which equality is true

$$\mathbf{K}(\alpha)\mathbf{K}(\beta) = \mathbf{K}(\beta)\mathbf{K}(\alpha),$$

or reducible to them, as well as triangular, are factorized.

A new universal modeling method developed by the authors, based on the ideas of Mandelbrot fractals in conducting research, has been successfully used in solving boundary value problems for systems of partial differential equations [13]. In this paper, this method is applied to systems of Wiener-Hopf integral equations for the case of their arbitrary order having matrix functions  $\mathbf{K}(\alpha)$  with elements in the form of meromorphic functions. Matrices-functions  $\mathbf{K}(\alpha)$  that are functionally commutative are obtained as a special case in the considered approach.

The simplest method for solving a system of Wiener-Hopf integral equations is to factorize the coefficient of a functional equation, that is, a meromorphic matrix function called a symbol. However, as mentioned above, in the general meromorphic case, the factorization of the symbol could not be carried out. The symbols are factorized only in the variants described above. Thus, if the factorization of the symbol exists, then the result of the factorization will represent quite complex expressions, as well as the entire solution vector. The practice of solving boundary value problems for systems of partial differential equations has clearly shown how difficult the solution can be when using matrix-function factorization [13]. The transition to the search for simpler representations of solutions to boundary value problems, dictated by a new universal modeling method, led to simple problems of factorization of only functions of some functional equations, and not matrix functions. This made it possible to obtain a fairly simple representation of solutions to boundary value problems. Returning to the system of integral equations, it should be noted that the high-level devices of the singular integral or normalized rings themselves rely on simpler approaches that could not "lay" all possible functions in them. These methods were the products of simpler constructions. The solution can be suggested by studying the problem, as in quantum mechanics, for the simplest type of mixed problems associated with the Helmholtz or Schrodinger equation. Therefore, following the mentioned universal method, we use an alternative approach developed in the works of the authors [14,15], which allowed us to solve exactly the system of two integral Wiener-Hopf equations. It consists in reducing the system of Wiener-Hopf integral equations to infinite systems of linear algebraic equations, simpler than functional ones.

Therefore, following the mentioned universal method, we use an alternative approach developed in the works of the authors [14,15], which allowed us to solve exactly the system of two integral Wiener-Hopf equations.

The peculiarity of this approach is that if the matrix-function consists of rational functions, then factorization of matrix-functions may not be necessary to solve a system of integral equations. This determines the research strategy aimed at avoiding factorization of matrix functions in the systems of integral equations under consideration.

### 2. Basic equations

A system of Wiener-Hopf integral equations given on a semi-infinite interval is considered. The system is represented as a single equation with a matrix kernel, called the integral equation symbol, having the form

$$\int_0^\infty \mathbf{k}(x-\xi)\mathbf{q}(\xi)d\xi = \mathbf{f}(x), \quad 0 \leq x < \infty, \quad \mathbf{q} = \{q_1, q_2, \dots, q_N\}$$

$$\mathbf{k}(x) = \frac{1}{2\pi} \int_{\Gamma} \mathbf{K}(\alpha) e^{-i\alpha x} d\alpha, \quad \mathbf{K}(\alpha) = \begin{pmatrix} K_{11}(\alpha) & K_{12}(\alpha) & \dots & K_{1N}(\alpha) \\ \vdots & \vdots & \ddots & \vdots \\ K_{N1}(\alpha) & K_{N2}(\alpha) & \dots & K_{NN}(\alpha) \end{pmatrix}, \quad \mathbf{f} = \{f_1, f_2, \dots, f_N\} \tag{1}$$

We assume that the elements  $K_{mp}(\alpha)$ ,  $m, p = 1, 2, \dots, N$  of the matrix-function  $\mathbf{K}(\alpha)$  are in general meromorphic functions of the variable. Meromorphic functions  $K_{mp}(\alpha)$  and the determinant  $\det \mathbf{K}(\alpha)$  have the following representation and asymptotic behavior [15]

$$K_{mp}(\alpha) = D^{-1}(\alpha)C_{mp}(\alpha), \quad \det \mathbf{K}(\alpha) = D^{-N}(\alpha)\Delta(\alpha), \quad \Delta(\alpha) = \det \|C_{mp}(\alpha)\|.$$

$$K_{mp}(\alpha) = T_{mp} |\alpha|^{-1} (1 + O(\alpha^{-1})), \quad m = p, \quad K_{mp}(\alpha) = T_{mp} \alpha^{-1} (1 + O(\alpha^{-1})),$$

$$m \neq p, \quad |\alpha| \gg 1, \quad p = 1, 2, \dots, N.$$

Here, the functions  $C_{mp}(\alpha)$ ,  $D(\alpha)$ ,  $\Delta(\alpha)$ , are whole functions of the first order and of finite type, that is, of exponential type, in particular, polynomials. It is assumed that whole functions  $D(\alpha)$ ,  $\Delta(\alpha)$  vanish on sets of values  $\pm \zeta_n$  and  $\pm z_n$  and, accordingly, have condensation points at infinity in some wedge-shaped regions of the upper, plus, and lower, minus, parts of the complex plane, as a rule, in the vicinity of the imaginary axis. For the sake of simplicity, we will not complicate the properties of matrix functions that have zero partial indices, and the system of integral equations is uniquely solvable in some  $L_p$ ,  $p > 1$ . The properties of the matrix-function elements are described in more detail in [15] and here we repeat only the following. The determinant  $\Delta(\alpha)$  of the matrix-function has a type  $N\sigma$  and a countable set of zeros  $z_n$  going to infinity, whose distribution density is several  $N$  times greater than zeros  $\xi_n$  of the denominator  $D(\alpha)$  having the type  $\sigma$ . With this in mind, we will construct branches from the zeros of the determinant, each of which will have the density of the zeros of the denominator. To do this, as the first zeros of these branches, we take the sequence of the first zeros  $z_{mp}$ ,  $p = 1, 2, \dots, N$  of the determinant in ascending order of modules or counting counterclockwise. In the future, each next zero  $z_{mp}$  of the branch  $p$  will be taken from the number  $z_m$  with the index  $p + (mp - 1)N$  of the first zero with the added number  $z_{p+(mp-1)N}$ . Using these zeros, we construct  $N$  whole functions in the form of infinite products, as was done in [15], which, after dividing by  $D(\alpha)$ , will give meromorphic functions denoted  $M_p(u)$ . Their zeros are  $\pm z_{mp}$ .

We take the components  $\mathbf{f}(x)$  of the vector of the right part of the system of integral equations (1) in the form  $A_p(\eta) e^{-i\eta x}$ ,  $p = 1, 2, \dots, N$ ,  $\text{Im} \eta = 0$ . Such component values make it possible to obtain arbitrary right-hand sides of the system of integral equations, using Fourier transforms, in the form:

$$f_p(x) = \frac{1}{2\pi} \int_{-\infty}^\infty A_p(\eta) e^{-i\eta x} d\eta, \quad p = 1, 2, \dots, N.$$

Here  $A_p(\eta)$  -the Fourier transforms of functions  $f_p(x)$ .

### 3. Solution Method

We will look for the solution to the system of integral equations (1), for the vector  $\mathbf{f}(x) = \{A_p(\eta)e^{-i\eta x}\}$  of the right part in the following form

$$\varphi_{p\eta}(x) = B_p e^{-i\eta x} + \sum_{m=1}^{\infty} y_{pm} e^{iz_m x}.$$

Here  $B_p, y_{pm}$  do not depend on  $x$ .

In this part of the study, a new universal modeling method developed by the authors is used, and successfully applied to systems of differential equations using the transformation Galerkin [13,16]. The system of Wiener-Hopf integral equations is represented in the form of a system of differential equations of the form

$$\sum_{p=1}^N \prod_{n=1}^{\infty} L_{mpn} \left(i \frac{\partial}{\partial x}\right) \varphi_p(x) = \prod_{s=1}^N D_s \left(i \frac{\partial}{\partial x}\right) f_m(x), \quad m = 1, 2, \dots, N,$$

$$L_{mpn} \left(i \frac{\partial}{\partial x}\right) = \frac{\partial^2}{\partial x^2} + \tau_{mpn}^2, \quad D_p \left(i \frac{\partial}{\partial x}\right) = \frac{\partial^2}{\partial x^2} + \xi_r^2.$$

Following [13,16], Galerkin transformations are applied, leading to separate equations. In the course of the study, Boggio's theorem is generalized to the case of infinite systems of equations. The latter is achieved due to the presence of characteristic equations given by whole functions, the singleness of the zeros of characteristic equations, and the properties of the Dirichlet exponential series as whole functions with the necessary growth index that ensures the uniqueness of the expansion coefficients [11].

As a result of transformations taking into account the properties of the matrix-function elements, similar to those performed in [14,15], we obtain an infinite system of linear algebraic equations, which can be represented in vector form

$$\mathbf{A}\mathbf{Y} = \mathbf{F}_1, \quad \mathbf{A}\mathbf{C}_p\mathbf{Y} = \mathbf{F}_p, \quad p = 1, 2, \dots, N, \quad \mathbf{Y} = \{y_m\},$$

$$\mathbf{A} = \left\| \frac{1}{\xi_r - z_m} \right\|, \quad \mathbf{F}_p = \left\{ -\frac{B_p}{\eta + \xi_r} \right\}, \quad \mathbf{C}_p = \|c_{mm}(p)\|, \quad \mathbf{C}_p^{-1} = \|c_{mm}^{-1}(p)\|. \quad (2)$$

The problem consists of factorization in the form of the sum of the operator of an infinite system, which contains  $N$  times more unknowns than the number of equations. At the same time the requirement of satisfying the initial system of Wiener-Hopf integral equations is met. Like the factorization of the terms of the Wiener-Hopf functional equation in the form of a sum [12] that correlates the number of equations and unknowns, factorization is performed over the operator of an infinite system of equations. The applied operation is new, developed by the authors specifically for this type of infinite systems of linear algebraic equations. Hence, as a result of factorization of the infinite system (2), we obtain exact solutions of individual correct infinite systems of linear algebraic equations equivalent to the Wiener-Hopf equations with complicated right-hand sides

$$\int_0^{\infty} m_p(x-\xi)\varphi_p(\xi)d\xi = h_p(x), \quad x \geq 0, \quad p = 1, 2, \dots, N,$$

$$h_p(x) = \frac{1}{2\pi} \int_{-\infty}^{\infty} \frac{1}{2} (\mathbf{R}_{pv} \mathbf{C}_p^{-1} \mathbf{A}^{-1} F_p + \mathbf{A}^{-1} F_1) e^{-i\eta x} d\eta, \quad (3)$$

$$m_p(x) = \frac{1}{2\pi} \int_{-\infty}^{\infty} M_p(u) e^{-iux} du.$$

$$\varphi_{p\eta}(x) = B_p(\eta) e^{-i\eta x} + \sum_{m=1}^{\infty} y_{sm} e^{iz_{mp}x}. \quad (4)$$

Integral equations have a unique solution, as a consequence of the properties of the constructed functions  $M_p(u)$ .

To obtain solutions to the original system of integral equations, we will look for them in the form of decomposition according to the constructed functions, requiring equality of the left and right parts. As a result, we come to the relations

$$\sum_{s=1}^N K_{ps}(\eta) B_s e^{-i\eta x} = A_p(\eta) e^{-i\eta x},$$

$$\sum_{s=1}^N K_{ps}(\eta) B_s = A_p(\eta), \quad \mathbf{K}(\eta) = \|K_{ps}(\eta)\|, \quad \mathbf{B} = \{B_s\}, \quad \mathbf{A}(\eta) = \{A_p(\eta)\},$$

$$\mathbf{B}(\eta) = \mathbf{K}^{-1}(\eta) \mathbf{A}(\eta).$$

Let us add the found values to the right parts of the expression for  $\varphi_{p\eta}(x)$ ,  $y_{sm}$  (4). Then we get the exact solution of the Wiener-Hopf system of equations for each vector of unknowns in the form

$$\mathbf{Q}_{\eta}(x) = \mathbf{K}^{-1}(\eta) \mathbf{A}(\eta) e^{-i\eta x} + \mathbf{K}^{-1}(\eta) \mathbf{Y}(x),$$

$$\mathbf{Y}(x) = \left\{ \sum_{m=1}^{\infty} y_{pm} e^{iz_{mp}x} \right\}, \quad \mathbf{K}^{-1}(\eta) = \|g_{ps}\|.$$

In coordinate form, the solution can be represented in the form

$$q_{p\eta}(x) = B_p(\eta) e^{-i\eta x} + \sum_{s=1}^N \sum_{m=1}^{\infty} g_{ps} y_{sm} e^{iz_{ms}x}, \quad B_p(\eta) = \sum_{s=1}^N g_{ps} A_p(\eta).$$

Here we see a complete analogy of the representation of the solution vector of a system of Wiener-Hopf integral equations decomposed by solutions of individual Wiener-Hopf integral equations (4), which is similar to decompositions in boundary problems [13].

#### 4. Conclusions

Thus, using examples from the theory of boundary value problems for systems of partial differential equations [13] and systems it is shown that the new universal modeling method makes it easier to investigate and solve them, obtaining a representation of vector solutions decomposed by solutions of scalar problems in multicomponent materials of complex rheologies.

In solving this problem, it should be noted the significant role of transformation academician B.G. Galerkin, whose 150th anniversary was celebrated in 2021 year. Previously, its transformation was used only to a limited extent, avoiding mixed problems [17-19]. The latter makes it possible not only to build simplified representations of complex solutions to the problems under consideration but also to obtain solutions to problems that cannot be investigated by any other methods. At the same time, the article presents for the first time the representation of exact vector solutions of arbitrary systems of Wiener-Hopf

integral equations with a meromorphic matrix-function, which makes it possible to make high-precision management decisions on radiation in multicomponent materials of waves, planned components.

## References

- 1 Freund LB. *Dynamic Fracture Mechanics*. Cambridge University Press; 1998.
- 2 Achenbach JD. *Wave propagation in Elastic Solids*. Amsterdam: North-Holland; 1973.
- 3 Abrahams ID, Wickham GR. General Wiener–Hopf Factorization of Matrix Kernels with Exponential Phase Factors. *SIAM Journal on Applied Mathematics*. 1990;50(3): 819-838.
- 4 Norris AN, Achenbach JD. Elastic wave diffraction by a semi infinite crack in a transversely isotropic material. *The Quarterly Journal of Mechanics and Applied Mathematics*. 1984;37(4): 565-580.
- 5 Sautbekov S, Nilsson B. Electromagnetic scattering theory for gratings based on the Wiener-Hopf method. *AIP Conf. Proc.* 2009;1106: 110-117.
- 6 Chakrabarti A, George AJ. Solution of a singular integral equation involving two intervals arising in the theory of water waves. *Appl. Math. Lett.* 1994;7: 43-47.
- 7 Davis AMJ. Continental shelf wave scattering by a semi-infinite coastline. *Geophys. Astrophys. Fluid Dyn.* 1987;39: 25-55.
- 8 Payandeh Najafabadi AT, Kucerovsky D. Exact solutions for a class matrix Riemann-Hilbert problems. *IMA Journal of Applied Mathematics*. 2014;79: 109-123.
- 9 Fusai G, Abrahams ID, Sgarra C. An exact analytical solution for discrete barrier options. *Finance Stoch.* 2006;10: 1-26.
- 10 Payandeh Najafabadi AT, Kucerovsky D. On distribution of extrema for a class of Lévy processes. *J. Probab. Statist. Sci.* 2011;9: 127-138.
- 11 Vorovich II, Babeshko VA. *Dynamic mixed problems of the theory of elasticity for nonclassical domains*. Moscow: Nauka; 1984. (In Russian).
- 12 Noble B. *Wiener-Hopf method*. Moscow: ILL; 1962. (In Russian)
- 13 Babeshko VA, Evdokimova OV, Babeshko OM. Fractal properties of block elements and a new universal modeling method. *Doklady Physics*. 2021;499: 21-26.
- 14 Babeshko VA. On an effective method for solving some integral equations of elasticity theory and mathematical physics. *Applied Mathematics and Mechanics*. 1967;31(1): 80-89.
- 15 Babeshko VA, Evdokimova OV, Babeshko OM. The Hilbert–Wiener factorization problem of Hilbert - Wiener and the block element method. *Doklady Physics*. 2014;459(5): 557-561.
- 16 Galerkin BGCR. Contribution à la solution générale du problème de la théorie de l'élasticité dans le cas de trois dimensions. *Acad. Sci.* 1930;190: 1047.
- 17 Nowacki W. *Theory of Elasticity Panstwowe*. Warszawa: Wydawnictwo Naukowe; 1970.
- 18 Nowacki W. *Dynamic Problems of Thermoelasticity*. Netherlands: Springer; 1975.
- 19 Nowacki W. *Electromagnetic Effects in Solids Panstwowe*. Warszawa: Wydawnictwo Naukowe; 1983.

## THE AUTHORS

### Babeshko V.A.

e-mail: babeshko41@mail.ru

ORCID: 0000-0002-6663-6357

**Evdokimova O.V.**

e-mail:

ORCID:

**Babeshko O.M.**

e-mail: name1@example.ru

ORCID: 0000-0003-1283-3870

# The nanofluids' viscosity prediction through particle-media interaction layer

V.V. Syzrantsev<sup>1✉</sup>, A.T. Arymbaeva<sup>2</sup>, A.P. Zavjalov<sup>3</sup>, K.V. Zobov<sup>4</sup>

<sup>1</sup>Grozny State Oil Technical University, Isaeva av., Grozny, 364024, Russia

<sup>2</sup>Institute of Inorganic Chemistry of the Siberian Branch of the Russian Academy of Sciences, Lavrentieva av. 3, Novosibirsk, 630090, Russia

<sup>3</sup>Institute of Solid State Chemistry and Mechanochemistry of the Siberian Branch of the Russian Academy of Sciences, 18 Kutateladze str., Novosibirsk, 630128, Russia

<sup>4</sup>Khrstianovich Institute of Theoretical and Applied Mechanics of the Siberian Branch of the Russian Academy of Sciences, 4/1 Institutskaya str., Novosibirsk 630090, Russia

✉ vvveliga@mail.ru

**Abstract.** This work aims to draw a more fundamental understanding of the rheology of nanofluids and the interpretation of the discrepancy in the literature. The rheology of dispersions based on SiO<sub>2</sub> and Al<sub>2</sub>O<sub>3</sub> nanoparticles obtained by four different methods is experimentally investigated in the Newtonian range. It is shown that the viscosity dependence on concentration for nanofluids with particles of different synthesis methods has different values. The parameter of the associated liquid layer model describing the intensity of particles and dispersed medium interaction, as well as the  $\zeta$ -potential of these liquids, were determined. The correlation between the  $\zeta$ -potential and the thickness of the associated liquid layer is shown, and the possibility of their use for predicting the behavior of nanofluids is discussed.

**Keywords:** nanofluids, viscosity, colloid particles, particles distribution, particle-liquid interaction

**Acknowledgements.** No external funding was received for this study.

The rheometry studies were conducted using the equipment of the Center of Collective Use "Scientific Devices" of Buryat State University.

**Citation:** Syzrantsev VV, Arymbaeva AT, Zavjalov AP, Zobov KV. The nanofluids' viscosity prediction through particle-media interaction layer. *Materials Physics and Mechanics*. 2022;48(3): 386-396. DOI: 10.18149/MPM.4832022\_9.

## 1. Introduction

Some of the nanotechnology areas are associated with the use of nanofluids (liquids containing nanoparticles) in various industrial processes. Even a small value of nanoscale additives can both provide special properties to materials and significantly change the conditions of their technological use. Therefore, research in this area is extremely important. In particular, the design of heat engines and heat transfer processes are directly related to the rheological properties of nanofluids due to the variety of their effect on heat transfer [1-3].

A significant number of experiments are presented in the literature regarding the variation of carrier fluid, concentration, size and shape of particles, and their chemical

© V.V. Syzrantsev, A.T. Arymbaeva, A.P. Zavjalov, K.V. Zobov, 2022.

Publisher: Peter the Great St. Petersburg Polytechnic University

This is an open access article under the CC BY-NC 4.0 license (<https://creativecommons.org/licenses/by-nc/4.0/>)

composition. However, despite such significant efforts, the formation of an acceptable unified model of the nanoparticles' influence and the possibility of predicting viscosity has not yet been obtained [4-8]. In general, it has been shown that an increase in concentration or a decrease in particle size leads to an increase in the viscosity value. At the same time, many experiments of different scientific groups came into contradiction with each other and gave results according to the following modified model.

Beginning with Einstein [9] and Brinkman, who developed the first theory [10], significant mathematical efforts have been made to reconcile conflicting data.

The main stages of reconciling can be marked as the semi-empirical relationship between Krieger and Doherty (KD model) [11], the Nielsen power-law model [12], the effect of Brownian particle motion performed by Batchelor [13], Lundgren's dependence in the power series form [14], and the Frankel-Akrivos model performed by Graeme [15], taking into account the radius of the particles and the distance between them. All these works make it possible to predict the liquid viscosity under different conditions, depending on the volume concentration of small particles.

However, the experimental values for the influence of nanoparticles are often much higher than the ones calculated by these models, and an example of this is the Batchelor formula [13], which is widely used for a suspension with microparticles. Moreover, as demonstrated in the experiments of different research groups, different types of nanoparticles – even ones of the same substances – can make different values of the effect. This indicates that the hydrodynamic description implemented in existing models, namely taking into account only one (concentration) or two (concentration and diameter) parameters, is insufficient, and it is necessary to consider the additional factors directly related to the nature of nanoparticles, taking into account the interaction of their surface with the environment.

Furthermore, an additional adhesion force of the liquid in the surroundings of the nanoparticles is proposed as a mechanism for such interactions. Concretely, in certain surroundings of the nanoparticles, the free mobility of the molecules of the dispersion medium decreases. From the model point of view, the three-phase Eshelby method can be used here [16], where an intermediate liquid layer is located between the undisturbed dispersion medium and the solid dispersed phase, which is directly connected with the particle. This layer has its own size and elastic properties. In different models, it is called the intermediate phase, hydrodynamic size, associated layer, etc.

In this model, the parameters of the interfacial layer (its size, elastic properties, and adhesion force to the solid phase) are determined by the effect of active centers present on the surface of nanoparticles, which can differ greatly depending on the method of their production. On this note, we can highlight some synthesis factors that affect the concentration and type of active centers, and these factors include the following: the changes in the stoichiometry of surface atoms, the particle size distribution, and the aggregation of nanoparticles.

It can be assumed that the process of developing many new methods is a tireless attempt to take these three synthesis factors into account; however, so far, these methods have not succeeded in understanding this phenomenon. The difficulty of the situation lies in the fact that the intensity of the interaction of the particles and the liquid is not known in advance. Even for nanoparticles of the same chemical composition but obtained by different methods, the adhesion force can differ due to variations in surface properties such as the presence of surface groups, porosity, etc. Therefore, direct consideration of these factors is hardly possible and will require additional use of spectroscopy and other methods not directly related to rheology. To simplify the analysis, researchers will be forced to use semi-empirical models that can implicitly consider these factors. Strictly speaking, the models mentioned above are

semi-empirical and try to optimize the obtained experimental data with available mathematical dependences of a complex form.

One of the possible options for taking into account the properties of the surface and the aggregability of particles was undertaken in [17-19]. They varied the aggregation parameter in the KD model [11] and obtained the optimal value was 3.34, giving the good fitting of the experimental results of Ethylene glycol+TiO<sub>2</sub> and other nanofluids.

In our previous work, a simple mechanistic approach was presented to describe this mechanism [20]. We proposed using the Batchelor formula to calculate the viscosity, but we considered the particle diameter to be effectively increased by the region of interaction between the surface and the medium (an associated layer was introduced).

Moreover, as an additional complicating factor, it should be noted that at a specific concentration, which primarily depends on the interaction intensity between particles and liquid, the associated layers of neighboring particles can begin to intersect. Therefore, this may be one of the possible mechanisms for the appearance of nonlinear effects, when a nanofluid can become non-Newtonian, as noted by many authors [5,6].

On this note, this work is a study continuation of the nature of such interactions of nanoparticles and the medium based on experimental data on the viscosity of the epoxy resin and distilled water filled with nanoparticles of silicon dioxide and aluminum oxide synthesized by five different methods, which allows variation in the properties of the surface of nanoparticles. In return, this variability, among other aspects, illustrates the reasons for the significant discrepancy between the experimental data of other authors studying nanofluids based on nanoparticles of the same composition but different surface properties.

## 2. Materials and methods

In the experiments, aluminum oxide and silicon dioxide nanoparticles obtained by different methods were used. The first character in the name of the samples encodes the method of obtaining the second means the material: "s" – silica, "a" – alumina. One of the most developed gas-phase methods for the synthesis of nanoparticles is the combustion of a material tetrachloride in a hydrogen flame. Variations of this process allow the production of silicon, titanium, and aluminum oxides on an industrial scale. In this work, commercial nanoparticles (Evonik Industries), Aerosil (As series), and Aerooxide (Aa series) were used. The authors of this work participated actively in the development of a gas-phase method based on the evaporation by the continuous high-energy electron beam and the condensation of the substance in the form of nanoparticles in a carrier gas at atmospheric pressure [21]. Furthermore, silica powders obtained by this method are marketed under the Tarkosil brand and have been fully tested (Ts series) while aluminum oxide powders are produced in smaller volumes and have been partially tested (Ta series). Additionally, the work presents results for commercial nanoparticles (Nanjing XFNANO Materials Tech Co., China) obtained by the liquid-phase method (Ls and La series), and two more types of nanopowders obtained by high-temperature methods were used in this work: silicon dioxide powder obtained in high-temperature plasma method (Ps series) (Plasmotherm, Russia) and aluminum oxides obtained by wire electric explosion method (Ea series) [22].

The average particle size and particle size distribution for the powders were measured by the Nanosizer SALD-7500 (Shimadzu). Figure 1 demonstrates the particle size distribution functions (in form of probability density function) for the series of powders used to create suspensions. In this regard, it is seen that the powders used have similar distribution functions. Average sizes vary in the range of ~ 22–34 nm, and the only exception is the Ea series of the aluminum oxide nanoparticle, for which the average size is approximately twice as large and is ~ 64 nm.

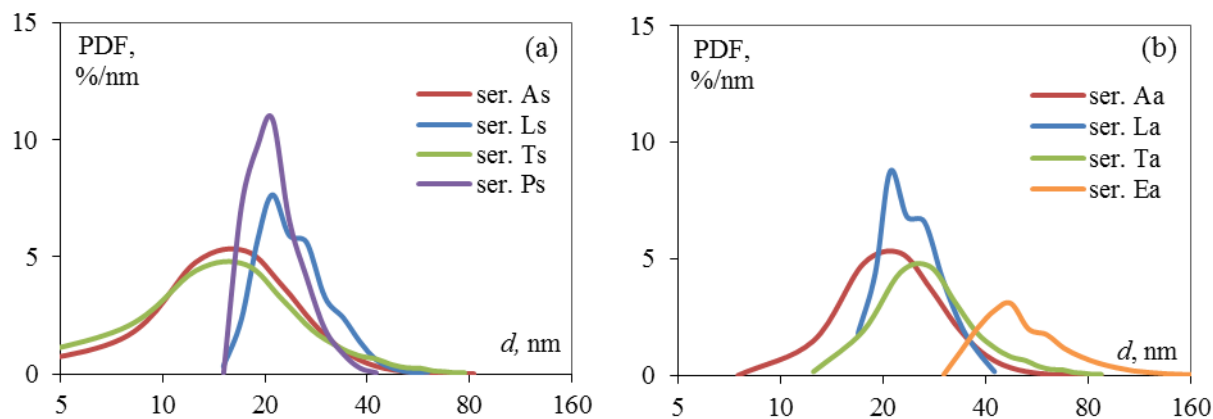


**Fig. 1.** Probability density function (PDF) for size nanoparticles distribution in series: (a) silica  $\text{SiO}_2$ ; (b) alumina  $\text{Al}_2\text{O}_3$

For nanofluid preparation, epoxy resins ED-20 and distilled water were used as a dispersion medium. For the deagglomeration of nanoparticles, the suspensions were sonicated for 30 minutes on a Sonopuls HD 3200 (Bandelin Electronic, Germany). This processing time was selected based on the data of the transparency measuring of an aqueous suspension of nanoparticles of the Ts and As series, partially shown in Fig. 2. It can be observed that the nanofluid transparency increases with the time of ultrasonic treatment, and this is due to the homogenization of the suspension and the transition from strong light blocking by large agglomerates to weak light scattering by nanoparticles [23]. Such deagglomeration process reaches saturation after 20 minutes, but since a more viscous liquid was also used in the experiments, the processing time was increased to 30 minutes. The measurements were carried out immediately after the deagglomeration procedure, during 30-60 minutes, when coagulation was insignificant, which was verified.

The viscosity was measured on an MCR 52 rheometer (Anton Paar, Austria) using the cone/plate (CP) measuring scheme. This system has greater accuracy in contrast to the immersed rotor schemes used in the rheometer. This method works well to combine the values and dependencies in a wide range of values, and there is no need to change the rotor for measurements. Viscosity measurements were carried out over a temperature range of 23 to 60°C for the epoxy resin, and measurements for water were carried out at a temperature of 23°C. The relative error of single measurements ranged from 1% at a temperature of 25°C to 5% at a temperature of 50°C and was determined by the technical characteristics of the rheometer. To reduce the coefficient of error, the viscosity was measured sequentially in four consecutive measurements, and the values were averaged. The temperature measurement accuracy was 0.1°C.

Additional preliminary measurements of relative viscosity  $\mu/\mu_0$  were carried out to determine the effect of temperature and shear rate. Figure 3 shows the temperature dependences of the relative viscosity of the epoxy resin containing various mass concentrations of the Ts series nanoparticles. From Fig. 3, it can be noted that the increase in viscosity caused by the powder occurs proportionally for all presented values of concentration and temperature. On the other hand, Figure 4 shows the dependence of the relative viscosity on the shear rate in the range from 50 to 1000  $\text{s}^{-1}$ . Accordingly, it can be observed that the viscosity coefficient is practically constant at a shear rate of more than 400  $\text{s}^{-1}$  in the studied range of nanoparticle concentrations. Moreover, similar dependences were also obtained for water and other investigated nanoparticles.

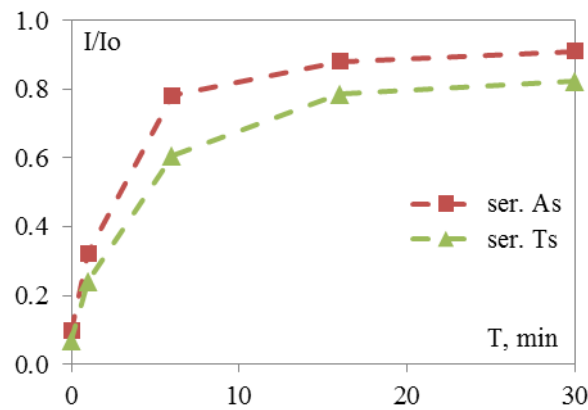


**Fig. 2.** Measurement of the transparency of the suspension dependence on the ultrasonic treatment time for samples of the Ts and As series

Thus, these measurements have demonstrated that for all suspensions, changes in the relative viscosity do not depend on temperature and shear rate within the current experimental variation limits of these parameters. This means that various nonlinear, thixotropic effects, or complex particle dynamics (for example, their agglomeration or sedimentation) did not manifest themselves under the conditions of the performed measurements. So, in the measuring range, the nanofluids showed the Newtonian behavior. Therefore, this issue is not covered further in this work.

On another note, to measure the zeta-potential, the method of electrophoretic light scattering was used. This method is based on dynamic light scattering in a Laser Doppler Anemometer (ELS) configuration. The measurements were carried out in distilled water on a NanoBrook Omni spectrometer (Brookhaven, USA), and the power of a solid-state laser with a 640 nm wavelength measured 35 mW. A special cell AQR2-0007 (Brookhaven Inst. Corp, USA) was used. The electrokinetic potential was calculated using the Smoluchowski formula:  $\zeta = \eta \mu_e / \epsilon \epsilon_0$ , where  $\zeta$  – the zeta potential,  $\epsilon$  – the dielectric constant of the liquid,  $\epsilon_0$  – the electrical constant,  $\eta$  – the viscosity of the initial liquid, and  $\mu_e$  – the electrophoretic mobility.

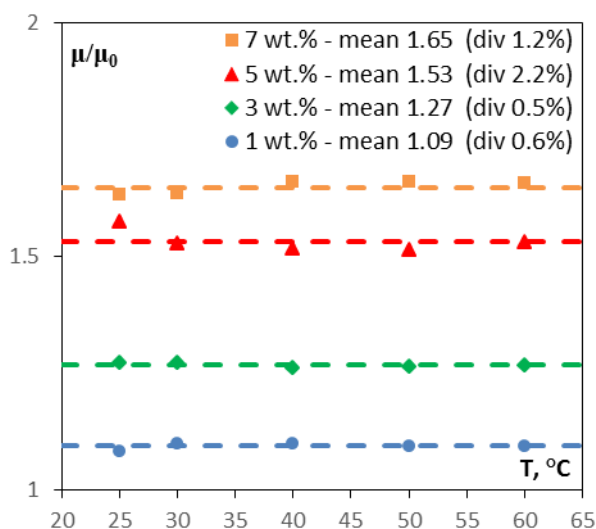


**Fig. 3.** Dependence of the relative viscosity of the epoxy resin with different mass concentrations of Ts particles on temperature. Shear rate  $500 \text{ s}^{-1}$

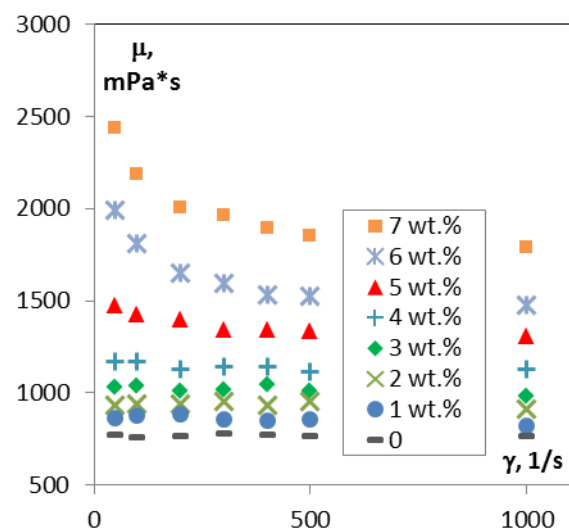


**Fig. 4.** Dependence of the viscosity of the epoxy resin with different mass concentrations of Ts particles on the shear rate. Temperature  $50^\circ\text{C}$

Furthermore, the theoretical background for our calculations is presented in our previous work [20]. Here, we use some different notations, so we rewrite some formulas. We base our calculation model on the Batchelor formula [13], but we use increased volume concentration of the dispersed component due to the associated liquid layer with thickness  $\delta$  (effective volume concentration  $\theta_{eff}$  instead of "clear" volume concentration  $\theta_0$ ). With assumptions about independence of density and associated liquid layer thickness  $\delta$  from particle size, we get the following equations (1-3):

$$\frac{\mu}{\mu_0} = 1 + 2.5\theta_{eff} + 6.25\theta_{eff}^2 = 1 + 2.5K\theta_0 + 6.25K^2\theta_0^2, \quad (1)$$

$$\theta_{eff} = \frac{V_{eff}}{V_{\Sigma}} = \frac{N_{part}}{V_{\Sigma}} \frac{\pi}{6} \int (d + 2\delta)^3 f(d) dd = \underbrace{\frac{N_{part}}{V_{\Sigma}} \frac{\pi}{6} E_3}_{\theta_0} \underbrace{\left(1 + 6\delta \frac{E_2}{E_3} + 12\delta^2 \frac{E_1}{E_3} + 8\delta^3 \frac{1}{E_3}\right)}_K, \quad (2)$$

$$\frac{8}{E_3} \delta^3 + 12 \frac{E_1}{E_3} \delta^2 + 6 \frac{E_2}{E_3} \delta + (1 - K) = 0, \quad (3)$$

where  $K$  – the coefficient of "increase" in the volumetric concentration of the dispersed phase,  $V_{eff}$  – the effective volume of the dispersed phase in the total considered volume  $V_{\Sigma}$ ,  $N_{part}$  – the total number of the dispersed phase particles in the volume  $V_{\Sigma}$ ,  $f(d)$  – the size distribution of the dispersed phase particles, and  $E_i$  – the  $i$ -th moment of particle size distribution.

The same notation is used in our previous work [20]. We calculate  $K$  from the experimental data for  $\mu/\mu_0$  through the fitting by equation (1). As opposed to previous works [20], here we have the data for a particle size distribution function of a dispersed phase (Fig. 3) and directly calculate moments  $E_i$  for equations (1-3). The last calculation step is solving equation (3) for  $\delta$  search (it has only one real root despite the cubic form due to positive coefficients for powers of  $\delta$ ).

### 3. Results and Discussion

Figure 5 shows the dependence of the relative viscosity on the volumetric concentration of nanoparticles of silicon dioxide and aluminum oxide produced by various synthesis methods. Additionally, given are the fitting curves (1) with the value of  $K$ . As observed in Fig. 5, our approximation, which is based on the model of the associated layer, is good for the experimental data while Batchelor's formula does not predict enough values of relative viscosity. The gained  $K$  value allows us to calculate the associated liquid layer thickness  $\delta$  in each measurement's series.

As mentioned previously, nanoparticles dispersed in the medium are complex objects. The core of the system is a solid particle (or aggregate) with its own chemical characteristics and uncompensated charges. Consequently, it is covered by a diffuse layer of ions of the dispersion medium. The parameters of the diffuse layer directly determine the  $\zeta$ -potential of the system. A preliminary study of the functional and chemical composition of the surface of nanoparticles [24,25] showed their difference, which is confirmed by the variation in the value of the  $\zeta$ -potential (Table 1). As mentioned earlier, the distribution functions of the used nanopowders are close (Fig. 3), but some variation in the average particle size is observed. However, it is not possible to reveal the correlation between the particle size and  $\zeta$ -potential. This means that the specific feature of the surface structure and the associated value of the  $\zeta$ -potential is to a greater extent determined by the method of obtaining nanopowders than by the size of the particles.

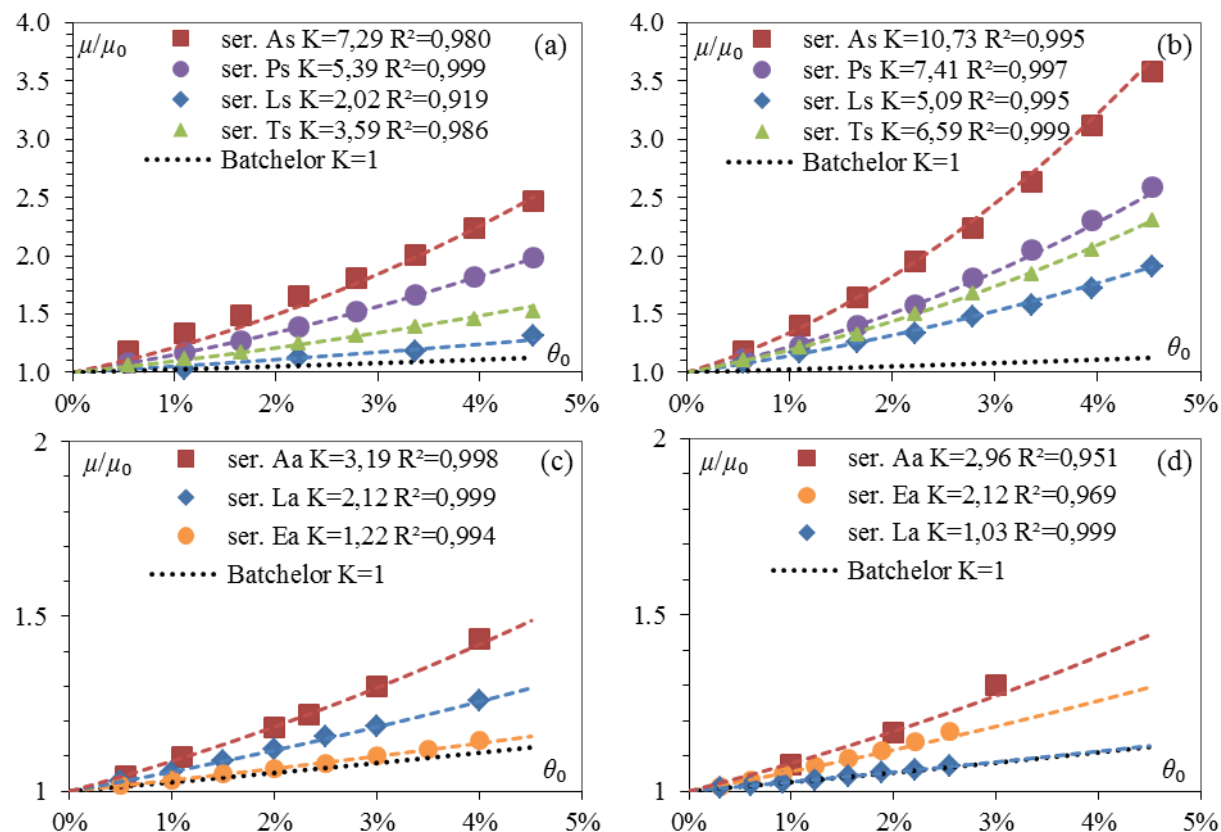


**Fig. 5.** Dependence of the relative viscosity of the medium with nanoparticles in comparison with Batchelor's formula and fitting curves by (1a) form for series: (a), (c) distilled water; (b), (d) epoxy resin; (a), (b) nanoparticles of silica; (c), (d) nanoparticles of alumina

**Table 1.** Comparative characteristics of the powders' series

Matter	Type of nanoparticles	Average particle size, $\langle d \rangle$	$\zeta$ - potential	Associated liquid layer thickness, $\delta$	
		nm		nm	
			mV	Resin	Water
SiO <sub>2</sub>	ser. As	22.7	-36.2±0.5	3.7	3.2
	ser. Ls	28.2	-21.2±1.5	2.8	1.8
	ser. Ts	24.3	-30.2±0.6	3.3	2.5
	ser. Ps	23.8	-24.2±0.7	3.0	2.7
Al <sub>2</sub> O <sub>3</sub>	ser. Aa	27.7	-12.8±0.6	2.2	2.3
	ser. La	27.2	13.3±0.5	0.5	1.8
	ser. Ta	34.3	7.8±0.3	-	-
	ser. Ea	64.3	-17.5±0.4	2.5	1.5

In terms of a mechanistic approach, the nanoparticle moves together with a part of the diffuse layer [26,27]. The size of this part is determined by the structural features of the solid particle and the medium [28], and examples of these features are functional groups on the surface of particles, free bonds of the crystal lattice on the surface, the degree of ionization of the dispersion medium, surface porosity, etc. In the model described earlier (1-3), the parameter  $\delta$  is responsible for the size of this layer. Therefore, the correlation between the value of the  $\zeta$ -potential and the thickness of the associated liquid layer  $\delta$  obtained from the experiments is considered in Fig. 6. For the case of aqueous dispersions, the correlation is not

very high, and we can only speak of a general tendency towards a decrease in the associated layer thickness  $\delta$  as the  $\zeta$ -potential increases. This may be because the viscosity of water is low and its increase in absolute values is insignificant, which can lead to an error in the calculation of the associated layer thickness. For suspensions based on the epoxy resin, we can talk about the presence of an explicit linear relationship. That is, an increase in the  $\zeta$ -potential leads to a decrease in the associated layer thickness. The strongest interaction of particles with the medium is formed by particles with the highest positive  $\zeta$ -potential, and the particles with the highest negative  $\zeta$ -potential have the least interaction with both resin and water.

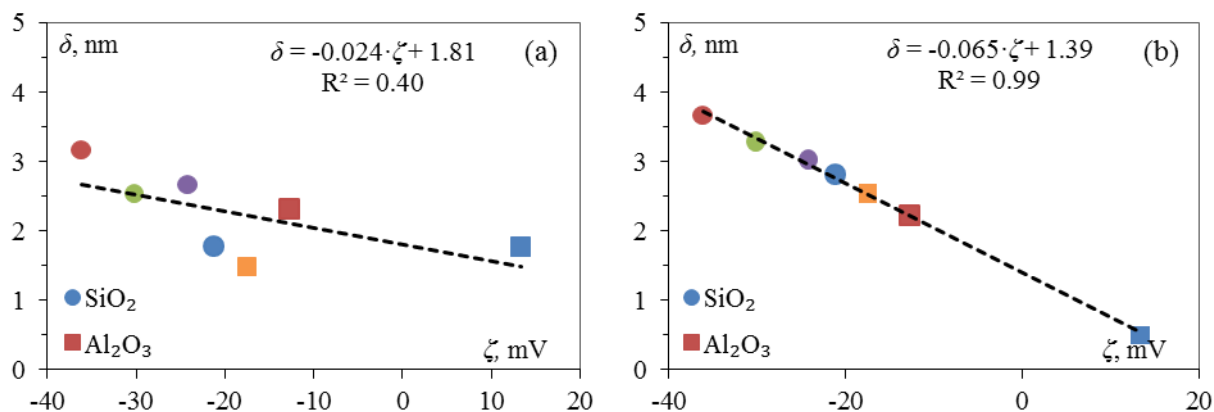


**Fig. 6.** Correlation of the  $\zeta$ -potential and the thickness of the associated layer for suspensions based on: (a) distilled water; (b) epoxy resin

It should be noted that the L-series samples obtained by liquid-phase deposition demonstrate a different behavior compared to other samples obtained by methods of an intense heating of the starting materials. Both samples of the series (Ls and La) have the smallest values of the  $\zeta$ -potential and the associated layer. In the case of alumina particles (La), this is one of the only two samples that show a positive  $\zeta$ -potential. Thus, it can be concluded that the conditions for the synthesis of these samples lead to the creation of a charge structure on the surface of the particles, and this structure interacts with resin and water and is weaker than the one corresponding to the samples obtained by other methods.

Since the direct consideration of the variations in surface-active centers, the presence of porosity, and other surface features is an extremely complex problem, the determination of the  $\zeta$ -potential and the thickness of the associated liquid layer can be an effective substitute for them in the rheology of nanofluids.

Having obtained such dependences of the attached layer thickness  $\delta$  for each liquid and, consequently, the value of K on the value of the  $\zeta$ -potential, we can predict its viscosity. The parameter in the Batchelor equation (1) will be the value of K, which directly depends (3) on the  $\zeta$ -potential of dispersion and the moments of particle size distribution. This equation will be valid for a specific liquid with any nanoparticles, at least in the region where the suspension will retain Newtonian behavior.

To some extent, these factors can explain the occurrence of nonlinear effects [28,29]. If the physical concentration of particles becomes high enough that the associated layers of neighboring particles begin to intersect, then the unperturbed dispersed medium will disappear. Then, the value of the dispersed medium momentum will decrease in comparison with the sum of the momentum of the particles, and the effective viscosity will increase. That is the way for the appearance of the non-Newtonian effects. Calculated predictions here can be difficult since they require preliminary practical measurements to determine the intensity of the interaction between particles and between the associated layers of particles themselves.

It is necessary to note two special points in the obtained ratios of the associated layer thickness and the zeta potential value, which indicate the limitations of this model. The first is the zero value of the associated layer thickness, to which the dependence tends when the zeta potential is more than +20 mV. We assume that at large values of the zeta potential, the dependence ceases to be linear and becomes asymptotic to zero thickness of the associated layer. The second singular point corresponds to the zero value of the zeta potential, where the nanofluid is absolutely unstable and there is no electric double layer. At this point, our model does not apply. It is likely that the dependence will have a discontinuity at this point, with an asymptotic approach to the point ( $\zeta=0$ ,  $\delta=0$ ) on both sides. These features need to be experimentally verified using nanoparticles having the necessary zeta potential values.

#### 4. Conclusion

This study demonstrates that dispersions based on SiO<sub>2</sub> and Al<sub>2</sub>O<sub>3</sub> nanoparticles obtained by different methods have different viscosities, which are apparently determined by the value of the interaction between particles and medium. To determine the intensity of this interaction, a three-phase model of the associated layer is used, which describes the deviation of viscosity from Batchelor's law with high accuracy. The values of the thickness of the associated layer and the  $\zeta$ -potential of the investigated liquids are determined and their correlation is shown. Furthermore, the possibility of using these parameters to predict the behavior of nanofluids is proposed.

#### References

1. Serebryakova MA, Zaikovskii AV, Sakhapov SZ, Smovzh DV, Sukhinin GI, Novopashin SA. Thermal conductivity of nanofluids based on hollow  $\gamma$ -Al<sub>2</sub>O<sub>3</sub> nanoparticles, and the influence of interfacial thermal resistance. *International Journal of Heat and Mass Transfer* 2017;108: 1314-1319.
2. Buongiorno J, Venerus DC, Prabhat N, McKrell T, Townsend J, Christianson R et al. A benchmark study on the thermal conductivity of nanofluids. *Journal of Applied Physics* 2009;106(9): 094312.
3. Kedzierski M, Venerus D, Buongiorno J, Christianson R, Townsend J et al. Viscosity measurements on colloidal dispersions (nanofluids) for heat transfer applications. *Applied Rheology* 2010;20: 44582.
4. Mahbulul IM, Saidur R, Amalina MA. Latest developments on the viscosity of nanofluids. *International Journal of Heat and Mass Transfer* 2012;55(4): 874-885.
5. Bashirnezhad K, Bazri S, Safaei MR, Goodarzi M, Dahari M, Mahian O, et al. Viscosity of nanofluids: A review of recent experimental studies. *International Communications in Heat and Mass Transfer* 2016;73: 114-123.
6. Murshed SMS, Estellé P. A state of the art review on viscosity of nanofluids. *Renewable and Sustainable Energy Reviews* 2017;76: 1134-1152.
7. Minakov AV, Rudyak VY, Pryazhnikov MI. Systematic Experimental Study of the Viscosity of Nanofluids. *Heat Transfer Engineering* 2021;42: 1024-1040.
8. Koca HD, Doganay S, Turgut A, Tavman IH, Saidur R, Mahbulul IM. Effect of particle size on the viscosity of nanofluids: A review. *Renewable and Sustainable Energy Reviews* 2018;82: 1664-1674.
9. Einstein A. A new determination of molecular dimensions. *Ann Phys.* 1906;19: 289-306.
10. Brinkman HC. The Viscosity of Concentrated Suspensions and Solutions. *Journal of Chemical Physics* 1952;20(4): 571-571.
11. Krieger IM, Dougherty TJ. A Mechanism for Non-Newtonian Flow in Suspensions of Rigid Spheres. *Transaction of the Society of Rheology* 1959;3(1): 137-152.

12. Nielsen LE. Generalized Equation for the Elastic Moduli of Composite Materials. *Journal of Applied Physics* 1970;41(11): 4626-4627.
13. Batchelor GK. The effect of Brownian motion on the bulk stress in a suspension of spherical particles. *Journal of Fluid Mechanics* 1977;83(1): 97-117.
14. Lundgren TS. Slow flow through stationary random beds and suspensions of spheres. *Journal of Fluid Mechanics* 1972;51(2): 273-299.
15. Graham AL. On the viscosity of suspensions of solid spheres. *Applied Scientific Research* 1981;37: 275-286.
16. Lurie S, Volkov-Bogorodsky D, Zubov V, Tuchkova N. Advanced theoretical and numerical multiscale modeling of cohesion/adhesion interactions in continuum mechanics and its applications for filled nanocomposites. *Computational Materials Science* 2009;45(3): 709-714.
17. Chen H, Ding Y, Tan C. Rheological behaviour of nanofluids. *New Journal of Physics* 2007;9: 367-367.
18. Chen H, Ding Y, He Y, Tan C. Rheological behaviour of ethylene glycol based titania nanofluids. *Chemical Physics Letters* 2007;444(4-6): 333-337.
19. Chen H, Ding Y, Lapkin A. Rheological behaviour of nanofluids containing tube / rod-like nanoparticles. *Powder Technology* 2009;194(1-2): 132-141.
20. Syzrantsev VV, Zavyalov AP, Bardakhanov SP. The role of associated liquid layer at nanoparticles and its influence on nanofluids viscosity *International Journal of Heat and Mass Transfer* 2014;72: 501-506.
21. Bardakhanov SP, Korchagin AI, Kuksanov NK, Lavrukhin AV, Salimov RA, Fadeev SN, Cherepkov VV. Nanopowders obtained by evaporating initial substances in an electron accelerator at atmospheric pressure. *Doklady Physics* 2006;51: 353-356.
22. Lerner MI, Svarovskaya NV, Psakhie SG, Bakina OV. Production technology, characteristics, and some applications of electric-explosion nanopowders of metals. *Nanotechnologies in Russia* 2009;4: 741-757.
23. Afzal A, Nawfal I, Mahbubul IM, Kumbar SS. An overview on the effect of ultrasonication duration on different properties of nanofluids. *Journal of Thermal Analysis and Calorimetry* 2019;135: 393-418.
24. Syzrantsev V, Paukshtis E, Larina T, Chesalov Y, Bardakhanov S, Nomoev A. Features of Surface Structures of Alumina and Titanium Dioxide Nanoparticles Produced Using Different Synthesis Methods. *Journal of Nanomaterials* 2018;2018: 1-10.
25. Syzrantsev VV, Paukshtis EA, Larina TV. Surface polymorphism of silica nanoparticles. *IOP Conference Series Material Science and Engineering*. 2020;1008: 012030.
26. Mewis J, Wagner NJ. *Colloidal Suspension Rheology*. Cambridge University Press; 2012.
27. Rudyak VY, Belkin AA. On the Effect of Nanoparticles on Fluid Structure. *Colloid Journal* 2019;81: 487-490.
28. Rudyak VY. Modeling of nanofluid flows. Problems, methods, results. *AIP Conference Proceedings*. 2018;2027(1): 020005.
29. Minakov AV, Rudyak VY, Pryazhnikov MI. Rheological behavior of water and ethylene glycol based nanofluids containing oxide nanoparticles. *Colloids and Surfaces A: Physicochemical and Engineering Aspects*. 2018;554: 279-285.

## THE AUTHORS

**Syzrantsev V.V.**

e-mail: vvveliga@mail.ru

ORCID: 0000-0001-5388-8224

**Arymbaeva A.T.**

e-mail: arymbaeva@niic.nsc.ru

ORCID: 0000-0001-5388-8224

**Zavjalov A.P.**

e-mail: zavjalov.alexey@gmail.com

ORCID: 0000-0001-9893-6840

**Zobov K.V.**

e-mail: zobov.kv@gmail.com

ORCID: 0000-0001-5388-8224

# Study numerical and experimental of stress concentration factor on isotropic plate with hole

M.N. Misbah<sup>✉</sup>, R.C. Ariesta, T. Yulianto, D. Setyawan, W.H.A. Putra

Sepuluh Nopember Institute of Technology, Jalan Raya Kampus ITS Sukolilo, Surabaya 60111, Indonesia

✉ [mnmisbah@na.its.ac.id](mailto:mnmisbah@na.its.ac.id)

**Abstract.** The stress concentration factor (SCF) can lead to the failure of ship construction. That problem can occur with hotspot stress expansion in the local area because of the acting load and structural details shapes. However, there is no method for the asses of structure design failure in the minor openings such as a dry hole and scallop dimension. Furthermore, the research aims for evaluating stress concentration performed using the diameter and width (d/W) ratio. The model of plates generates to identify stress phenomena on the isotropic ship plate. The numerical simulation was carried out using finite element analysis and proven by experimental method with the installation of the strain measurement on several working loads of 30% and 60% under yield strength. The plate used for analysis is an A36 steel plate commonly used in the shipbuilding industry. The plate model with the hole was identified, which shows the stress concentration that occurs increases after the d/W of the isotropic plate also increases, then the comparative stress plot. Moreover, based on the numerical and experimental analysis, the comparisons of stress concentration factors within different radius holes have been completed for assessment. Finally, result from numerical and experimental obtained error values below 3%.

**Keywords:** stress concentration factor, ship, numerical, experimental

*Acknowledgements.* The work is supported by Beginners research funding fund from Research Institution Institut Teknologi Sepuluh Nopember, Surabaya. We thank our colleagues from Ship Strength and Construction Laboratory, who provided insight and expertise that greatly assisted the research, although they may not agree with all of the interpretations/conclusions of this paper.

**Citation:** Misbah MNM, Ariesta RCA, Yulianto TY, Setyawan DS, Putra WHAP. Study numerical and experimental of stress concentration factor on isotropic plate with hole. *Materials Physics and Mechanics*. 2022;48(3): 397-406. DOI: 10.18149/MPM.4832022\_10.

## 1. Introduction

Stress Concentration Factor (SCF) is a number that will increase when a plate gets tension force concentrated, such as holes and changes in the cross-section. Recently the sharper radius at the cross-section will influence the increasing SCF value. The plate pressure work per the dimensions of the hole diameter occurs on the plates, the number of the holes, and the axial force that works. The plate holes resulting in a pressure differential force on the other size determine the value. Application of SCF in ship structures like dry holes, corner edge containers, and scallops choose to obtain the best model for reducing stress. The methods performed to determine the SCF model on the plate have several steps. First steps

experiments [1,2], numerical model, regression analysis, finite element [3,4], and artificial intelligence (AI). Numerical model using finite element analysis package software and verifying used experiment tensile test using a universal tensile machine (UTM). To become a numerical example stress intensity factor in evaluating a two-dimensional crack [5,6] is the Stress concentration factor obtained from the plate in a flexible environment. The maximum stress and stress concentration factors appear inconstantly occur at the hole [1]. Reducing SCF is also determined by selecting the appropriate shape. The sharpness of form can construct the concentration of high-stress concentration. Material with a large SCF will quickly fail [2]. This research aims to obtain the result of the stress concentration on the plate material on the vessel. For example, several holes found on the ship structure are all-important, such as lightning holes, which also lead to detection of stress concentration and need analysis to prevent damage on construction with an additional hole or change to optimum shape [3]. This research observed how many errors in the numerical and experimental. Therefore, analysis of the deviation that appears.

## 2. Research Purposes

Stress occurs when the body gets an external force. Especially that happens on the ship hull as a critical area, and to prevent that, external and internal forces will reduce by applying holes to direct a working load focus on the one spot. To predict that stress only appears when to the part and given the treatment so that the structure has good resistance to loading. The research has specific aims:

- a. Obtain the stress concentration factor on a plate with a hole with a various nation of diameter using experimental and numerical
- b. Determine a Comparison of stress testing the value of concentration factor with experimental and numerical verification.

## 3. Research Methods

**Tensile Test.** Tensile testing on the A36 material was carried out to determine the amount of force needed by the material to exceed the yield strength limit to material forces in plastic conditions as input of modelling. The other purpose tensile test is to verify that the material is A36. Furthermore, check the test results in Table 1 and Table 2. Moreover, the material before and after the test is shown in Fig. 1.

Based on the tensile test, the force on the material yield was 44.67 KN, so a various loading model variance was used, with a 30% yield of 13.4 KN and a 60% yield of 26.8 KN, and a 90% yield of 40.2 KN.

Table 1. Material A36 Tensile Test Result (1/2)

Report on Test								
ASTM A36								
No	Material Code	Specification Sample			Tensile Test Result			
		Width	Thick	CSA	Yield Stress	Ultimate Stress	Elongation	Reduct of Area
		mm	mm	mm <sup>2</sup>	Mpa	Mpa	%	%
1	A36	25.35	6	152.1	282.71	335.31	37.94	72.93
2		25.3	6	151.8	296.44	335.97	37.77	72.62
3		25.15	6	150.9	304.84	337.97	32.99	77.87

Table 2. Material A36 Tensile Test Result (2/2)

No	F.Yield (KN)	F.ultimate (KN)	Lo	L1	Wd1	Th1	A1
1	43	51	69.68	96.12	17.3	2.38	41.17
2	45	51	64.86	89.36	16.69	2.49	41.56
3	46	51	69.41	92.31	17.04	1.96	33.4

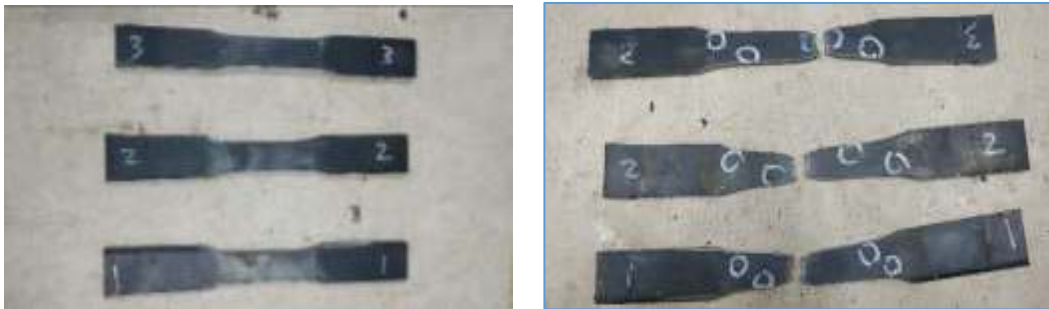


Fig. 1. Tensile Test Specimens A36

**Experimental Model.** The material verification approved the validity by ensuring that it adhered to the issue boundaries mentioned earlier, resulting in a conclusion in good agreement with the facts at the end of the experiment's review [10,11]. Supplying the critical material, A36 steel, and working equipment like a drill, hacksaw, solder, sandpaper, ruler, glue, and tape, are all part of the material preparation process. The specimen dimensions have a length of 300 mm, a width of 60 mm, and a thickness of 6 mm. The test material hole diameter varies between 6 mm, 18 mm, and 30 mm, as shown in Figs. 2-4.

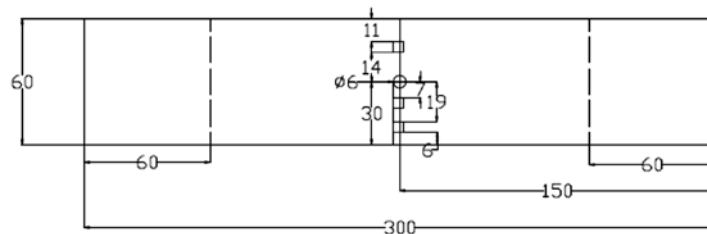


Fig. 2. Test Material Design 1

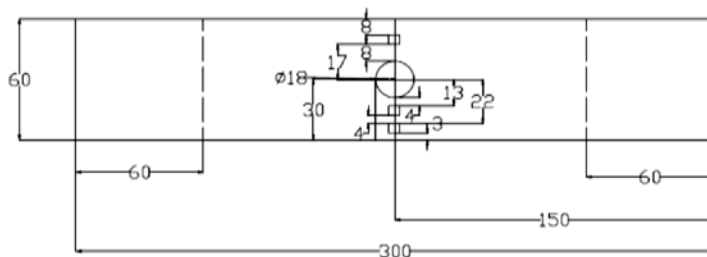
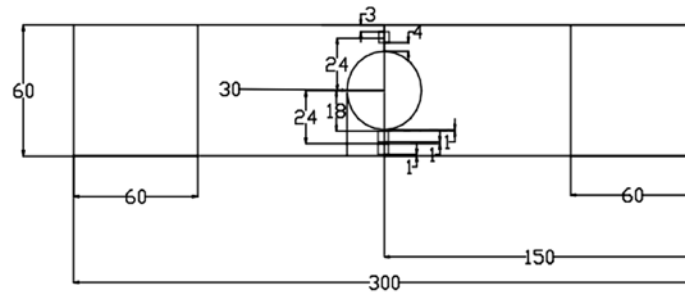


Fig. 3. Test Material Design 2



**Fig. 4.** Test Material Design 3

The sensor used in the experiment is a strain gauge with 350 ohms. Before installing the sensor, polish the surfaces of the steel specimen with sandpaper of grades 150-1200 to achieve a glossy finish and clean with alcohol. The adhesive function joins the sensor with the surface material and the tape patch on it as an additional method to minimize hand contact. There were four sensors installed: one for normal stress distribution and three for stress conversion sensors. The material was tested by tensile testing with three different load variants, as shown in Fig. 5, i.e. 30% yield (13,400 N), 60% yield (26,800 N), and 90% yield (40,200 N). An arrangement of sensor settings with the channel position. The first was at the nearest hole, the second was in the among sensor, the third was on the edge material, and the sensor recorded forces in the Y-axis direction.



**Fig. 5.** Measurement process setup

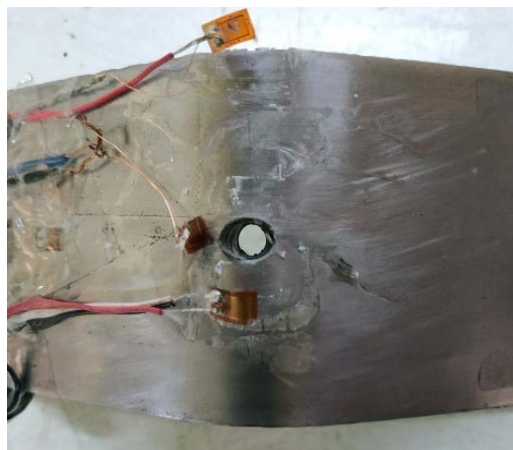


**Fig. 6.** Broken specimen

The sensor will detach after the force enters the plastic zone. Furthermore, measuring the load used to calculate the stress concentration obtained, a broken specimen will be illustrated in Fig. 6.

**Numerical Model.** Steel was chosen as a material commonly used in ship construction. The dimension of a plate with a size of 300 mm × 60 mm × 6 mm was modelled by three different variations of the diameter of the holes, specifically, 6 mm, 18 mm, and 30 mm. The material properties defined such as Young's modulus ( $E$ ), density ( $\rho$ ), and Poisson's ratio ( $\nu$ ) were presented in Table 3.

Table 3. Material properties of steel plate

Material	$E$ (MPa)	$\rho$ (kg/m <sup>3</sup> )	$\nu$
Steel	$210 \times 10^6$	7850	0.26

The numerical simulation will investigate using finite element software ABAQUS<sup>TM</sup>. Eight-node solid linear brick element (C3D8R) implement into the specimen model. Moreover, Steel defines as a homogenous specimen. The boundary condition applied on the top surface was assumed to be clamped on the grip of UTM. Therefore, the load is applied to the bottom of the surface area as a tensile test.

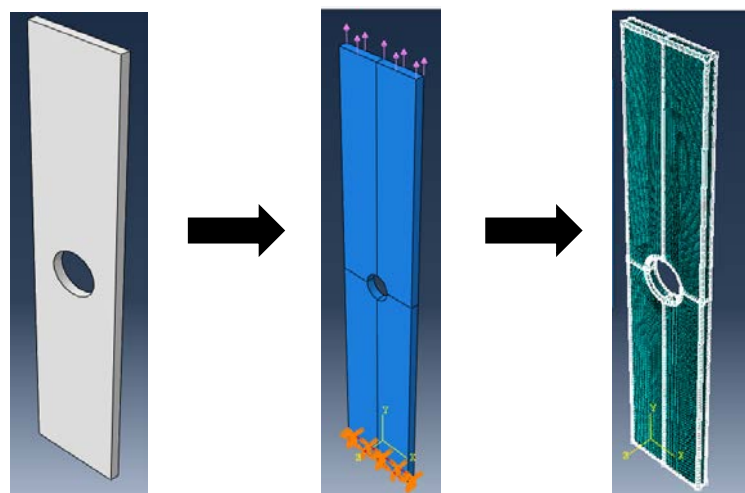


Fig. 6. Specimen model discretization

A Discretization stages cover mesh convergence that aims to ensure the stability of numerical analysis. According to theory, detailed size elements of results will increase the accuracy of the simulation [4]. The results data obtained from the simulation are several stress components such as von Mises stress, Y-axis stress, and X-direction stress. These results use to calculate the stress concentration factor, with the Y-axis stress in the same direction as the tensile test force of each model. When the created model is appropriate, verification was required by performing meshing optimization in software or convergence to obtain a constant stress value at the optimal meshing for further analysis [5]. The final stress is divided into some types of stress obtained from a statistical equation to produce the SCF, stress concentration factors at load variations of 30%, 60%, and 90% of yield strength load.

#### 4. Result and Discussion

Data were read from a strain gauge sensor and attached to the P3 micro Measurement Model to obtain the strain in micro-strain units (106), multiplied by the Modulus of Material (E) generating the stress. The test results are shown in Table 4.

Table 4. Tensile Test Result for Experimental Method

$d$ (mm)	Strain 30%	Strain 60%	$\sigma_{\text{Nom}}$ (MPa)		Strain 30%	Strain 60%	$\sigma_{\text{Max}}$ (MPa)	
6	0.000194	0.000381	40.7	80.10	0.000512	0.001015	107.9	213.2
18	0.000240	0.000496	50.5	104.1	0.000561	0.001159	117.9	243.4
30	0.000350	0.000689	73.4	142.5	0.000753	0.001464	158.1	307.4

The stress concentration factor is obtained by calculating the maximum stress ratio compared to the nominal stress so that the SCF is obtained on the test material using the strain gauge sensor with the results in Table 5.

Table 5. Stress Concentration Factor of Tensile Test Experimental Method

$\sigma_{\text{nom}}$ (MPa)		$\sigma_{\text{max}}$ (MPa)		SCF 30%	SCF 60%
Strain 30%	Strain 60%	Strain 30%	Strain 60%		
40.9	80.10	107.95	213.21	2.64	2.66
50.58	104.14	117.90	243.48	2.33	2.34
73.43	142.56	158.14	307.44	2.15	2.15

The maximum stress data obtained was used to calculate the amount of SCF based on different variations of the hole size. The stress concentration factor (SCF) is a dimensionless factor used to measure stress concentration [6]. The SCF value determines by calculating using Eq (1):

$$SCF = \frac{\sigma_{\text{max}}}{\sigma_{\text{nom}}} \quad (1)$$

It means the ratio of the maximum stress to nominal stress. The nominal stress is total stress in an element under the same loading conditions without a stress concentration to calculate the perforated acting load on the plate [6] Eq.(2):

$$\sigma_{\text{nom}} = \frac{P}{(W-d) \times t} \quad (2)$$

where load (P), a width of material (W), hole diameter (d), and thickness of plate (t). Moreover, the SCF results from empirical calculations can be seen in Tables 6-8 using various loads of 30%, 60%, and 90% yield force.

Table 6. Tensile Stress Y-Axis, load 30% yield

Model	d/w	w=60mm	t=6mm		SCF
		Hole size (d) (mm)	Load		
			(30% yield=13.4 KN)		
			Maximum Stress (MPa)	Nominal Stress (MPa)	
1	0.05	3	105.79	39.18	2.70
2	0.1	6	107.49	41.36	2.60
3	0.3	18	123.24	53.17	2.32
4	0.5	30	159.42	74.44	2.14

Table 7. Tensile Stress Y-Axis, load 60% yield

Model	d/w	w=60mm	t=6mm		SCF
		Hole size (d) (mm)	Load		
			(60% yield=26.8 KN)		
			Maximum Stress (MPa)	Nominal Stress (MPa)	
1	0.05	3	211.58	78.36	2.70
2	0.1	6	214.98	82.72	2.60
3	0.3	18	246.48	106.35	2.32
4	0.5	30	318.83	148.89	2.14

Table 8. Tensile Stress Y-Axis, load 90% yield

Model	d/w	w=60mm	t=6mm		SCF
		Hole size (d) (mm)	Load		
			(90% yield=40.2 KN)		
			Maximum Stress (MPa)	Nominal Stress (MPa)	
1	0.05	3	317.37	117.54	2.70
2	0.1	6	322.50	124.07	2.60
3	0.3	18	369.76	159.52	2.32
4	0.5	30	478.29	223.33	2.14

**Calculation of the Stress Concentration Factor using the Empirical Method.** The empirical calculation method determines using Eq.(3) after obtaining the SCF value based on the FEA simulation test results for each test model selecting Y direction stress for collecting the nominal data is summarised in Table 9 [12].

$$SCF = 3.00 = 3.13 \left(\frac{2r}{D}\right) + 3.66 \left(\frac{2r}{D}\right)^2 - 1.53 \left(\frac{2r}{D}\right)^3. \quad (3)$$

Table 9. SCF Calculation for Empiris Tensile (Roarks Formula)

Variation	r (mm)	W (mm)	d/w	SCF
Model 1	1.5	60	0.05	2.85
Model 2	3		0.1	2.72
Model 3	9		0.3	2.35
Model 4	15		0.5	2.16

**Comparison of the SCF using different methods.** From the Roarks, numerical and experimental results were compared to evaluate that error [12]. All the results of the SCF calculations for each test model are summarised in Table 10.

The stress concentration factor is sensitive to the ratio, and the experiment shows that the higher the ratio value, the higher the maximum stress, and the smaller the SCF value. The average of SCF with various loadings is explained in Table 11.

The graph shows in Fig. 7 a similar trend and pattern, which means the method to evaluate stress concentration factor (SCF) can perform. The value of SCF at 0.1 d/w around 2.7-2.8, in d/w 0.3 that narrow to 2.4, and at d/w is 0.5 that value very close to about 2.2.

Table 10. Comparison of SCF Calculations

d (mm)	(d/W)	Numerical			Experimental		SCF (Roarks Formula)	Empirical Numeric Difference (%)	Numerical Experiments Difference (%)
		30%	60%	90%	30%	60%			
		SCF	SCF	SCF	SCF		SCF		
3	0.05	2.70	2.70	2.70			2.85	5.26	
6	0.1	2.60	2.60	2.60	2.64	2.66	2.72	4.45	1.94
18	0.3	2.32	2.32	2.32	2.33	2.34	2.35	1.38	0.71
30	0.5	2.14	2.14	2.14	2.15	2.15	2.16	0.86	0.62

Table 11. Average of SCF for Tensile Test

Hole Diameter Lingkaran (d) (mm)	W (60 mm)	Numerical Method	Experimental Method	Roarks Formula
	d/W	SCF		
3	0.05	2.70	-	2.85
6	0.1	2.60	2.65	2.72
18	0.3	2.32	2.33	2.35
30	0.5	2.14	2.15	2.16

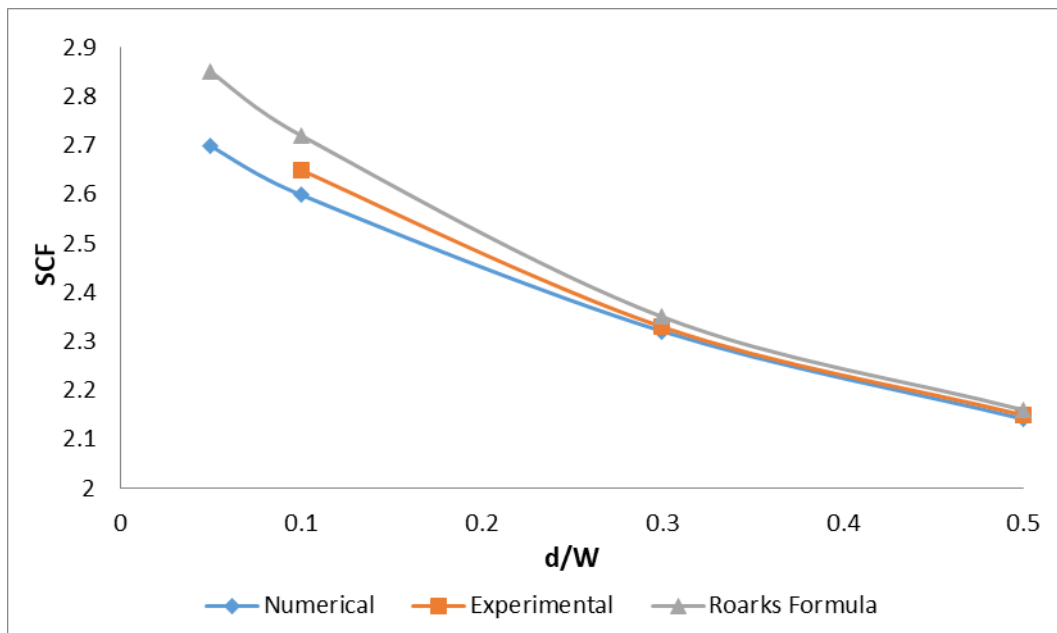


Fig.7. Average of SCF for Tensile Test

## 5. Conclusions

The Experimental (Strain Gauge Sensor) and Numerical (Finite Element Method) measurement methods are used in this study to determine the value of the Stress Concentration Factor (SCF) value, and the results are compared to draw the following conclusions:

1. The numerical method stress concentration factor with a load of 30%, 60%, and 90% did not change at 6 mm, 18 mm, and 30 mm diameters with 2.60, 2.32, and 2.14, respectively. While the experimental method, loading 30%, 60% experienced a change in

6mm diameter from 2.64 (30% load) to 2.66 (60% load), 18mm diameter from 2.33 (30% load) to 2.34 (60% load), 30mm diameter not change remains at the value 2.15.

2. The SCF value calculated using experimental and numerical methods is in good agreement, with a difference of less than 3%.

## References

1. Sarangi H, Murthy K, Chakraborty D. Experimental verification of optimal strain gage locations for the accurate determination of mode I stress intensity factors. *Engineering Fracture Mechanics*. 2013;110: 189-200.
2. Suardana N, Sugita I, Wardana I. Hybrid Acoustic Panel: The Effect of Fiber Volume Fraction and Panel Thickness. *Material Physics and Mechanics*. 2020;44(1): 77-82.
3. Takaki Y, Gotoh K. Approximate weight functions of stress intensity factor for a wide range shapes of surface and an embedded elliptical crack. *Marine Structures*. 2020;70: 1-22.
4. Sujiatanti SH, Yulianto T, Putra WHA, Ariesta RC. Influence of the Cut-out Shape on the Fatigue Ship Structural Detail. In: *Proc. of 6th International Seminar on Ocean and Coastal Engineering, Environmental and Natural Disaster Management*. 2018. p.111-115.
5. Tanaka S, Okada H, Okazawa S, Fujikubo M. Fracture mechanics analysis using the wavelet Galerkin method and extended finite element method. *International Journal for Numerical Methods in Engineering*. 2013;93(10): 1082-1108.
6. Sujiatanti SH, Tanaka S, Shinkawa S, Setoyama T, Yanagihara D. Experimental and numerical studies for buckling and collapse behaviors of a cracked thin steel panel subjected to sequential tensile and compressive loading. *Thin-Walled Structures*. 2020;157: 1-14.
7. Yang CZ, Cho C, Kim HB, Beom G, The effect of biaxial load on stress and strain concentrations in a finite thickness elastic plate containing a circular hole. *International Journal for Numerical Methods in Engineering*. 2008;75(1): 103-126.
8. Sumi Y, Yajima H, Toyosada, Masahiro, Yoshikawa T, Aihara S, Gotoh K, Ogawa Y, Matsumoto T, Hirota K, Hirasawa H, Toyoda M, Morikage Y. Fracture control of extremely thick welded steel plates applied to the deck structure of large container ships. *Journal of Marine Science and Technology*. 2013;18: 497-514.
9. Ariesta RC, Zubaydi A, Ismail A, Tuswan T. Damage evaluation of sandwich material on side plate hull using experimental modal analysis. *Materials Today: Proceedings*. 2021;47: 2310-2314.
10. Ariesta RC, Zubaydi A, Ismail A, Tuswan T, Identification of Damage Size Effect of Natural Frequency on Sandwich Material using Free Vibration Analysis. *Naše More*. 2022;69(1): 1-8.
11. Putri R, Yulianto T, Ariesta RC, Misbah MN. Influence of Stress Concentration Factor due to Scallop Form on the Wrang Plate Structure. *Kapal: Jurnal Ilmu Pengetahuan dan Teknologi Kelautan*. 2022;19(1): 29-41.
12. Misbah MN, Sujiatanti SH, Setyawan D, Ariesta RC and Rahmadianto S. Structural Analysis on the Block Lifting in Shipbuilding Construction Process. *MATECT Web of Conferences*. 2018;177: 01027.
13. Young WC, Budynas RG. *Roark's Formula for Stress and Strain*. New York: McGraw-Hill; 2002.

## THE AUTHORS

**Misbah M.N.**

e-mail: mnmisbah@na.its.ac.id

ORCID: -

**Ariesta R.C.**

e-mail: chandra14@mhs.na.its.ac.id

ORCID: 0000-0002-5510-6369

**Yulianto T.**

e-mail: totoky@na.its.ac.id

ORCID: -

**Setyawan D.**

e-mail: dony@na.its.ac.id

ORCID: 0000-0003-2498-051X

**Putra W.H.A.**

e-mail: wing@na.its.ac.id

ORCID: -

# An out-of-plane oscillating beam nanoresonator with ultrahigh intrinsic quality factor

Chu Manh Hoang<sup>1✉</sup>, Nguyen Van Duong<sup>2</sup>, Dang Van Hieu<sup>2</sup>

<sup>1</sup>International Training Institute for Materials Science, Hanoi University of Science and Technology, No. 1, Dai Co Viet, Hai Ba Trung, Hanoi, Viet Nam

<sup>2</sup>FPT University, Hoa Lac High Tech Park, Hanoi, Viet Nam

✉ [hoangcm@itims.edu.vn](mailto:hoangcm@itims.edu.vn), [hoang.chumanh@hust.edu.vn](mailto:hoang.chumanh@hust.edu.vn)

**Abstract.** An out-of-plane oscillating beam nanoresonator with the ultrahigh intrinsic quality factor based on the motion transformation mechanism from torsion into rotation is reported. The nanoresonator is composed of two resonant beams which are mechanically coupled through two spring beams oscillating in an out-of-phase torsional mode. The out-of-phase torsional oscillation of the two spring beams forms a stationary point in the middle of a supporting beam, which minimizes anchor loss. The low thermoelastic damping (TED) in the nanoresonator is obtained by employing the torsional oscillation mode. The optimal study for minimizing TED has been carried out by varying the representative geometry parameters of the nanoresonator. The nanoresonator with a quality factor over  $10^7$  has been obtained by the proposed oscillation excitation method.

**Keywords:** beam nanoresonator, out-of-plane oscillation, torsional oscillation, thermoelastic damping

**Acknowledgements.** This work is financially supported by the Vietnam Ministry of Education and Training, Project number B2020-BKA-23-CTVL.

**Citation:** Hoang CM, Duong NV, Hieu DV. An out-of-plane oscillating beam nanoresonator with ultrahigh intrinsic quality factor. *Materials Physics and Mechanics*. 2022;48(3): 407-418. DOI: 10.18149/MPM.4832022\_11.

## 1. Introduction

Mechanical resonators have recently attracted much interest because of their wide range of applications in sensing, timing, and physical measurements [1-5]. An important parameter for the performance evaluation of mechanical resonators is the quality factor ( $Q$ ). A resonator with a high  $Q$  implies a higher sensitivity in sensors, a good frequency resolution in filters, and low phase noise in oscillators. In order to maximize  $Q$ , it is fundamental to understand physical mechanisms limiting  $Q$ . Physical mechanisms of energy dissipation can be described by two categories: extrinsic and intrinsic losses [6-12]. The extrinsic losses are acoustic radiation, surface loss, and air friction, while the intrinsic losses include material loss, anchor loss, and thermoelastic damping (TED). Besides, the operation modes and imperfection of resonators/attached masses also affect the factor  $Q$  [8,9,11]. Under low vacuum conditions, losses in mechanical resonators are often generated from extrinsic damping mechanisms such as air damping [6-12]. Under high vacuum conditions, extrinsic dampings become negligible, and intrinsic damping mechanisms such as anchor loss and TED need to be taken into account.

© Chu Manh Hoang, Nguyen Van Duong, Dang Van Hieu, 2022.

Publisher: Peter the Great St. Petersburg Polytechnic University

This is an open access article under the CC BY-NC 4.0 license (<https://creativecommons.org/licenses/by-nc/4.0/>)

Anchor loss is often dominated by the radiation of elastic energy through anchors to the substrate [13,14]. This loss can be eliminated by using virtual supports [15] or by connecting the beam to the nodal points of spring beams [16]. Anchor loss can also be reduced by using extensional mode resonators [17]. Recent research have also been conducted on TED that shows to be another intrinsic damping source affecting the upper limit of  $Q$  [18-21]. The TED damping relates to the irreversible process of heat flow generated by compressed and extended regions between various parts of an oscillation structure [19-21]. For a material having a positive coefficient of thermal expansion, the compression in an oscillation structure leads to a higher temperature region while the tensile stress on its opposite side results in a lower temperature region. The strength of TED depends on the oscillation frequency, the relevant thermal relaxation time constant, and on the stress distribution in the oscillation structure. These, in turn, depend on the structural geometry and also on the material properties which are themselves functions of temperature. Resonators with high  $Q$  values can be obtained by operating the device at a low temperature [22]. Recently, engineered resonators for reducing TED have also been introduced [22-28]. These resonators can be in-plane flexural oscillation or out-of-plane oscillation. In a recent study [16], a flexural free-free resonator is studied and the TED  $Q$  has obtained around  $10^6$ . The numerical evaluation of TED in microelectromechanical systems has been reported [29], in which the numerical results on TED of the flexural free-fixed beam resonators have been compared with analytical solutions [19]. To obtain a high  $Q$  resonator, it is necessary to consider not only anchor loss but also TED. The TED dissipation is generated from the extension and compression in the flexural vibrations of the mechanical resonator. Several out-of-plane (OP) vibrational resonators have been reported [26-28]. However, an OP vibrational beam nanoresonator operating in the MHz regime with the ultrahigh intrinsic  $Q$  in considering both anchor loss and TED has not yet been studied with much interest and needs to be reported.

In this paper, we propose an OP vibrational beam nanoresonator. The OP vibration is carried out by the motion transformation from torsion into rotation. The application of the torsional oscillation mode is to minimize TED, while the out-of-phase oscillation is to suppress energy dissipation caused by anchor loss. Anchor loss is first investigated by decomposing the structure of the nanoresonator. Then, TED in the nanoresonator depending on its representative geometry parameters is investigated in detail. The  $Q$ -factor of the nanoresonator is optimized by considering the design of the cross-section and aspect ratio of the beams to minimize TED. The dependence of the  $Q$ -factor of the nanoresonator on the width and length of the beams is then explored. The nanoresonator with the  $Q$ -factor over  $10^7$  is obtainable by eliminating the intrinsic damping mechanisms.

## 2. The concept of nanoresonator and analysis model

As introduced, TED and anchor losses are the main intrinsic damping sources that affect the upper limit of the  $Q$ -factor. For a mechanical resonator, its vibration is composed of flexural and/or torsional components, while TED is caused by flexural vibrations [19]. Flexural vibrations cause alternating tensile and compressive strains on opposite sides of the neutral axis leading to thermal imbalance. The irreversible heat flow, which is driven by the temperature gradient, makes the vibrational energy to be dissipated. Because of the shear strain, the TED loss in a pure torsional vibration is zero, however, in general, a nanoresonator usually includes a mixture of flexure and pure torsion vibrations. On the other hand, anchor loss can be minimized by using the support points with small displacement [15,16]. Taking these two requirements into account, we design an OP vibrational beam nanoresonator as shown in Fig. 1. Two resonant beams with length  $L_b$  are connected to two free ends of two spring beams with length  $L_s/2$ , which oscillate in the torsional mode. The two remaining ends of the two spring beams are connected to the middle of a supporting beam. The dimensional parameters of the nanoresonator are denoted in Fig. 1.

The  $Q$ -factor of a mechanical resonator is proportional to the ratio of the stored mechanical energy to the dissipated energy per cycle of oscillation. The totally dissipated energy is the sum of energy dissipated by a variety of physical mechanisms. We assume that the nanoresonator is operated under high vacuum conditions. Intrinsic losses including material loss, anchor loss, and thermoelastic damping are remained. The nanoresonator is assumed to be made of single-crystal silicon whose material loss is negligible [30]. In the current design, anchor loss can be eliminated [15]. Therefore, TED is considered to be a dominant damping source.

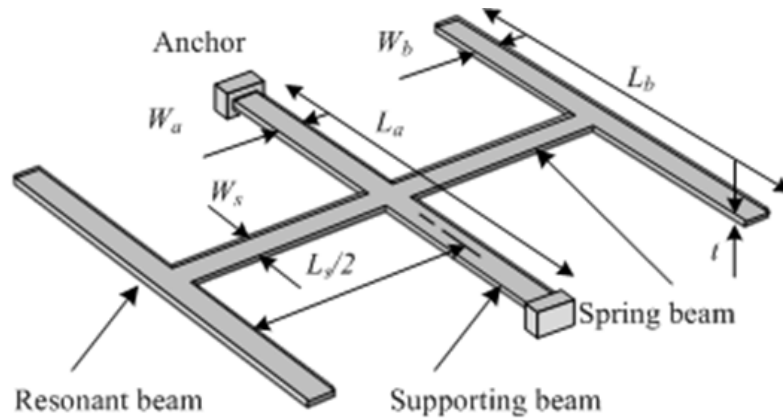


**Fig. 1.** Schematic drawing of the OP vibrational beam nanoresonator based on the motion transformation mechanism from torsion into rotation

According to the theory of thermoelasticity, the heat transfer equation involving TED is known as

$$\rho C_p \frac{\partial T}{\partial t} - \nabla \cdot (\kappa \nabla T) = -\frac{E\alpha T_0}{1-2\nu} \frac{\partial \varepsilon}{\partial t}, \quad (1)$$

where  $T$  is temperature and  $\varepsilon$  is the elastic strain. The definition and value of other parameters in Eq. (1) are shown in Table 1. The term on the left of Eq. (1) is the heat source showing the heat generation rate per unit volume.  $\varepsilon$  is defined by

$$\varepsilon = \varepsilon_x + \varepsilon_y + \varepsilon_z = \nabla \cdot u, \quad (2)$$

where  $u$  is displacement.

Table 1. Physical parameters of single-crystal silicon used for simulation

Parameters	Definition	Values
$E$	Young's modulus	165 [GPa]
$\alpha$	Coefficient of thermal expansion	$2.6 \times 10^{-6}$ [1/K]
$T_0$	Ambient and initial beam temperature	300 [K]
$\rho$	Density	2330 [kg/m <sup>3</sup> ]
$C_p$	Specific heat capacity	700 [J/(kg K)]
$C_v$	Heat capacity $C_v = \rho C_p$	$1.63 \times 10^6$ [J/(m <sup>3</sup> K)]
$\kappa$	Thermal conductivity	90 [W/(m K)]
$\nu$	Poisson's ratio	0.28

In the theory of dynamics and vibration, the equation of motion is established on the basis of the following force equilibrium:

$$\rho \frac{\partial^2 u}{\partial t^2} = \nabla \cdot \sigma, \quad (3)$$

where  $\sigma$  is the mechanical stress tensor. Furthermore, according to the theory of thermoelasticity, the relation between  $\sigma$  and  $\varepsilon$  is given by

$$\sigma = C\varepsilon - DT, \quad (4)$$

where  $C$  is the stiffness matrix and  $D$  is the thermal expansion coefficient matrix [23].

In harmonic vibration, the temperature  $T$ , displacement  $u$ , and velocity  $v$  have forms as:

$$\begin{cases} T = \mathfrak{S}(xi) \exp(i\omega t) \\ u = U(xi) \exp(i\omega t) \\ v = V(xi) \exp(i\omega t) = i\omega U \end{cases} \quad (5)$$

where  $\omega (= i\lambda)$  is the complex angular frequency, which consists of resonant and damping components;  $\mathfrak{S}(xi)$ ,  $U(xi)$ , and  $V(xi)$  are the amplitudes of node temperature, node displacement, and node velocity, respectively.

By substituting Eqs. (2), (4), and (5) into Eqs. (1) and (3), equations for estimating TED in the nanoresonator are given by a 3-order matrix [31]

$$AX = \lambda BX, \quad (6)$$

where  $A$  and  $B$  are coefficient matrices, which are derived by applying the standard Galerkin finite element formulation for Eq. (1). The components of matrices  $A$  and  $B$  depend on the thermal conductivity  $\kappa$ , the density  $\rho$ , the specific heat of mass  $C_p$ , the elastic modulus  $E$ , the thermal expansion coefficient  $\alpha$ , and Poisson's ratio  $\nu$ . The eigenvector is  $X = (\mathfrak{S}, U, V)^T$ , namely a vector combining nodal temperature, displacement, and velocity together. Equation (6) is a generalized eigenvalue equation and the eigenvalue  $\lambda$  is dependent on the representative dimension parameters of the nanoresonator and TED. As presented, the strength of damping caused by TED depends on the structural geometry and also on the material properties which are themselves functions of temperature. It is assumed that the nanoresonator is operated at room temperature. In the following section, the dependence of TED on the representative geometry parameters of the nanoresonator is investigated.

The natural resonant angular frequency  $\omega_r$  and the  $Q$ -factor of the nanoresonator according to the real and imaginary parts of  $\lambda$  are as follows [18,23]:

$$\omega_r = |Im(\lambda)|, \quad (7)$$

$$Q = \frac{1}{2} \frac{|Im(\lambda)|}{|Re(\lambda)|}, \quad (8)$$

where  $Q$  is the fraction of energy lost per radian, and the factor 1/2 arises from the fact that the mechanical energy of the nanoresonator is proportional to the square of its amplitude.

To obtain information about the  $Q$ -factor of the nanoresonator, it is of interest to know its eigenfrequency. To do this, an eigenfrequency analysis is carried out to find eigenvalues. The  $Q$ -factor of the nanoresonator is calculated by solving the coupled thermoelastic equations by the finite element method in Comsol multiphysics. In this study, the used Comsol module is the MEMS module. The mechanical and thermal problems are coupled through the mechanical and thermal coupling equations as shown in Eq. (6). The mechanical and thermal boundary conditions imposed on the nanoresonator are as follows. Displacement fields at the anchor's boundary is zero and at remained boundaries are free and zero at the initial condition. The nanoresonator is set in an insulated environment and its initial temperature is room temperature. There is no temperature deviation in the nanoresonator at the initial condition. The surfaces of the nanoresonator are set to be thermal isolation conditions. In this research, it is assumed that the nanoresonator is made of single-crystal silicon material. The physical parameters of single-crystal silicon used for simulation are shown in Table 1.

### 3. Results and discussion

As presented above, nanoresonators oscillating in the pure torsional mode are interested due to negligible thermoelastic damping, which is explained by isovolumetric strain in the pure

torsional oscillation. However, the torsional resonator normally contains flexural vibration components which significantly generate TED [19]. Therefore, the torsional resonator needs to be optimized to obtain the lowest TED, i.e. the highest  $Q$ -factor.

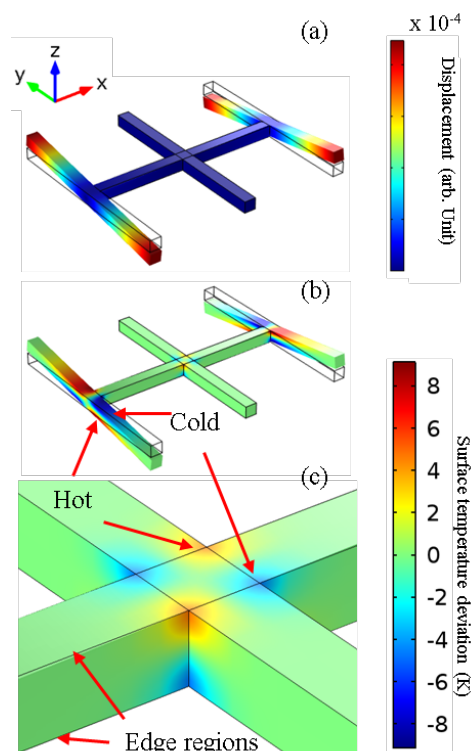


**Fig. 2.** Perspective view of displacement (a) and temperature distribution (b) of the out-of-phase OP torsional mode of the proposed nanoresonator. In the magnified image of the interconnection between the supporting beam and the torsional spring beam (c), the temperature distribution is clearly seen. The dimensions of the resonant, spring, and supporting beams are  $W_{b,s,a} = 60$  nm,  $t = 60$  nm, and  $L_{b,s,a} = 1$   $\mu$ m

Figures 2 (a) – (b) show the perspective view and temperature distribution of the nanoresonator in the out-of-phase torsional oscillation mode. This operation mode is the sixth mode of the nanoresonator. As seen in Fig. 2a, the two resonant beams, as well as the two spring beams, oscillate in the out-of-phase mode. Due to the out-of-phase torsional oscillation of the two spring beams, extension and compression regions are periodically distributed around the torsional axis at the four edge regions as shown in Fig. 2c.

For a comprehensively modal analysis, the first five modes of the nanoresonator are also shown in Figs. 3a–e. The resonant frequency  $f$  and quality factor  $Q$  of the first five modes and the interested sixth mode are presented in Table 2. It is clear that the out-of-phase torsional oscillation mode has a much higher  $Q$  value than the remaining modes, except for mode 1. This can be explained that the other modes appear as anchor loss due to the flexural vibration of the spring and supporting beams or the torsional vibration of the supporting beam and TED loss due to the flexural vibration of the spring and supporting beams. Mode 4 is also a torsional mode; however, this torsional mode is the in-phase OP mode, so the moment imbalance occurs at the anchors that cause anchor losses. The moment imbalance also makes the supporting beam to perform flexural vibrations, which causes TED. The anchor and TED losses in mode 4 are the cause that we did not choose for investigating further. For mode 1, its  $Q$  value is comparable to that of mode 6; however, the anchor loss of this mode is not negligible due to the displacement of the anchor and the TED loss is caused by the flexural

oscillating spring beam. The resonant frequency of mode 1 is also two times lower than that of mode 6. Moreover, the requirements for high  $Q$  nanoresonators are both anchor loss and TED having to be suppressed. Mode 6 fulfills these requirements, so it is chosen for investigation. Therefore, in the following, we will investigate the characteristics of the out-of-phase OP torsional oscillation mode of the nanoresonator. The characteristics of the nanoresonator have been investigated by the finite element method. Here, we have meshed the nanoresonator with the swept mesh method from the top down. This meshing method is chosen due to the symmetrical structure of the nanoresonator. The meshing element is cube-shaped; its size is 20 nm wide  $\times$  20 nm long  $\times$  6 nm high. The size of such meshing element is suitable for our current calculation facility and acceptable for calculation errors. We have also investigated the convergence of calculation on the meshing size. When we decrease the meshing size from 30 nm to 15 nm, the discrepancy of  $f$  and  $Q$  is less than 1% and 17 %, respectively.

Table 2. The  $f$  and  $Q$  values of the first six modes for the nanoresonator with the dimensions of the resonant, spring, and supporting beams  $W_{b,s,a} = 60$  nm,  $t = 60$  nm, and  $L_{b,s,a} = 1$   $\mu$ m

Mode order	Mode definition	$f$ (MHz)	$Q$
1	1 <sup>st</sup> out-of-plane cantilever mode	42.113	$1.753 \times 10^7$
2	1 <sup>st</sup> in-plane cantilever mode	61.853	$2.385 \times 10^6$
3	2 <sup>nd</sup> in-plane cantilever mode	76.023	$1.593 \times 10^6$
4	In-phase torsion mode	81.862	$9.531 \times 10^6$
5	2 <sup>nd</sup> out-of-plane cantilever mode	83.911	$2.020 \times 10^6$
6	Out-of-phase OP torsion mode	86.854	$2.291 \times 10^7$

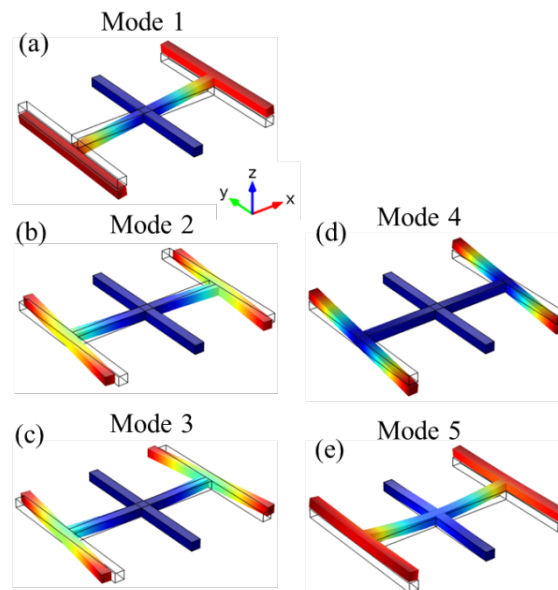


**Fig. 3.** (a)–(e) show resonant modes from 1–5, which have lower  $Q$  than the out-of-phase OP torsional mode, Fig. 2

As above presented, the intrinsic energy dissipation in the nanoresonator is caused by not only TED but also anchor loss. Therefore, it firstly needs to prove that the anchor loss in the nanoresonator in the out-of-phase torsional mode is negligible. It is well-known that the anchor loss is minimal by locating anchors at the stationary points of vibration beams, however, it is challenging to evaluate quantitatively the anchor loss in the nanoresonator having a complex structure. Therefore, we will estimate the anchor loss in terms of investigating TED in the

nanoresonator by decomposing its structure. The anchor loss can be caused by propagating elastic energy through the interconnection between the spring beam and the supporting beam and the two ends of the supporting beam attached to the substrate. To estimate the anchor loss caused by the interconnection between the spring beam and the supporting beam, we compare the  $Q$ -factor of the asymmetrical nanoresonator as shown in Fig. 4a, which is composed of only half the proposed symmetrical nanoresonator in Fig. 1. The asymmetrical nanoresonator has the  $Q$ -factor of  $1.195 \times 10^7$  lower than that of the symmetrical nanoresonator ( $2.291 \times 10^7$ ). For comparison, the temperature distribution of the asymmetrical nanoresonator is shown in Fig. 4b. Thus, the temperature gradient has appeared in this nanoresonator, which is caused by the extension and compression strain in the flexural vibration of the supporting beam. The supporting beam perform flexural vibrations due to the torsional torque generated by the rotational motion of the spring beam. In contrast, the temperature gradient does almost not appear in the proposed symmetrical nanoresonator, Figs. 2c-d. This means that the anchor loss caused by propagating the elastic energy through the interconnection between the spring beam and the supporting beam is minimized in the proposed symmetrical nanoresonator. It can also be derived from the damping analysis in the asymmetrical and symmetrical nanoresonators that the weakening of the mechanical coupling between the two OP rotating oscillators leads to the increment of TED, i.e. the decrement of the  $Q$ -factor. This can be explained that the compression and extension strain of the supporting beam becomes larger when the mechanical coupling strength between the two OP rotating oscillators is weakened.

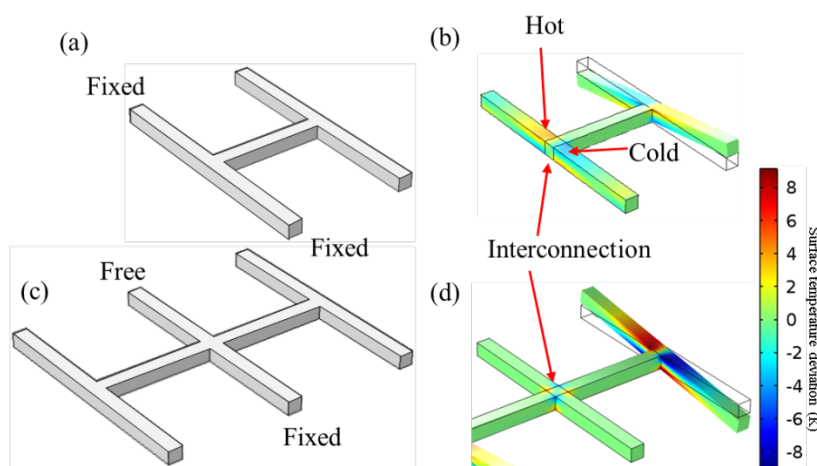


**Fig. 4.** (a) and (b) are schematic drawings and temperature distributions of the asymmetrical nanoresonator, respectively; (c) and (d) are schematic drawings and temperature distributions of the nanoresonator with one free supporting beam end in the out-of-phase torsion mode, respectively

To estimate the energy dissipation caused by propagating the elastic energy through the two anchors to the substrate, we use the nanoresonator with a fixed-free supporting beam as shown in Fig. 4c. The  $f$  and  $Q$  values of this nanoresonator in the out-of-phase torsional mode are almost the same as those of the symmetrical nanoresonator. This can be explained that the torsional spring beam takes the main role in determining the resonant oscillation of both the asymmetric and symmetrical nanoresonators. The deviation of  $f$  and  $Q$  of these two nanoresonators are only  $4.14 \times 10^{-3} \%$  and  $6.25 \times 10^{-2} \%$ , respectively. This also confirms that the out-of-phase torsional oscillation mode does not cause the displacement of the two anchors. Therefore, the elastic energy loss through the two anchors to the substrate is negligible. However, the nanoresonator with the supporting beam clamped at both two ends is considered to

be more robust than that clamped at one end. This is explained due to the higher stiffness of the supporting beam clamped at both two ends.

Thus, by decomposing the structure, we have shown that the anchor loss in the proposed nanoresonator is negligible. Furthermore, we have investigated the same operation mode in the three nanoresonators, the asymmetrical, symmetric, and fixed-free supporting beam nanoresonators, so the relation of the results from the three nanoresonators can be derived. Therefore, the intrinsic energy dissipation is dominant due to TED.

In the following, we will focus on investigating TED in the nanoresonator oscillating in the out-of-phase torsional mode. For the design purpose of one high- $Q$  OP vibrational beam nanoresonator, the dependence of TED on the dimensions of the supporting beam has been investigated. The resonant frequency of the nanoresonator does almost not depend on  $L_a$  and  $W_a$ . When  $L_a$  and  $W_a$  increase, the  $Q$ -factor of the nanoresonator slightly decreases. This can be explained that the mechanical coupling between the two torsional oscillations on both sides of the supporting beam is being weakened, which leads to the increment of TED.

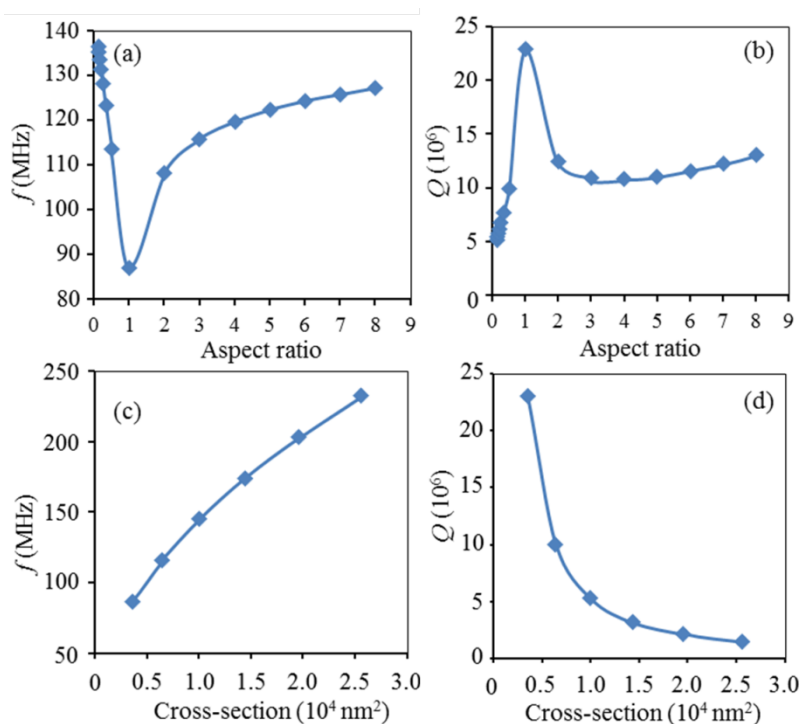


**Fig. 5.** (a) and (b) are  $f$  and  $Q$  of the OP vibrational beam nanoresonator investigated as functions of aspect ratio, respectively; (c) and (d) are  $f$  and  $Q$  of the OP vibrational beam nanoresonator investigated as functions of cross-section, respectively

The  $f$  and  $Q$  values of the OP vibrational beam nanoresonator have been investigated as a function of the aspect ratio of beams (wide  $W$  to thick  $t$  ratio). In the investigation, the thickness and length of the beams are fixed at 60 nm and 1  $\mu\text{m}$ , respectively, while the width is varied. Figures 5a–b show the investigated results. The frequency response shows an 87 MHz minimum at the aspect ratio of 1, however, the  $Q$ -factor obtains a maximum of  $2.3 \times 10^7$ . For the aspect ratio of 1, the  $Q$ -factor obtains the highest value. This may be explained that TED in the torsional oscillation with the aspect ratio of 1 is mainly caused by the four edge regions of the torsional oscillation beam and the flexural vibration of the resonant beam. Thus, to maximize the  $Q$ -factor of the nanoresonator, the aspect ratio of the spring beam should be chosen to 1, i.e. the cross-section of the spring beam is square-shaped. Based on such criteria,  $f$  and  $Q$  of the nanoresonator have then been investigated as functions

of cross-section while keeping the aspect ratio to be 1. The investigated results are shown in Figs. 5c–d.  $f$  increases with the cross-section, while the  $Q$ -factor decreases quickly according to the cross-section. When the cross-section decreases from  $2.56 \times 10^4 \text{ nm}^2$  (120 nm wide  $\times$  120 nm high) to  $36 \times 10^2 \text{ nm}^2$  (60 nm wide  $\times$  60 nm high),  $f$  decreases a factor of 2.68, however, the  $Q$ -factor increases more than one order of the magnitude (16 times).

In the following investigation, the OP vibrational beam nanoresonator with the 60 nm  $\times$  60 nm cross-section has the highest  $Q$  value chosen to investigate the dependence of  $Q$  on  $L_s$ .  $L_s$  varied from 0.5  $\mu\text{m}$  to 1.75  $\mu\text{m}$ . The investigated results are shown in Fig. 6 (a). The  $Q$ -factor strongly depends on  $L_s$ . When  $L_s$  is varied from 0.5  $\mu\text{m}$  to 1.75  $\mu\text{m}$ , the  $Q$ -factor of the OP vibrational beam nanoresonator increases a factor of 5.9 from  $8.68 \times 10^6$  to  $5.15 \times 10^7$ . In contrast with  $Q$ ,  $f$  decreases a factor of 1.8 from 120 MHz to 66 MHz.

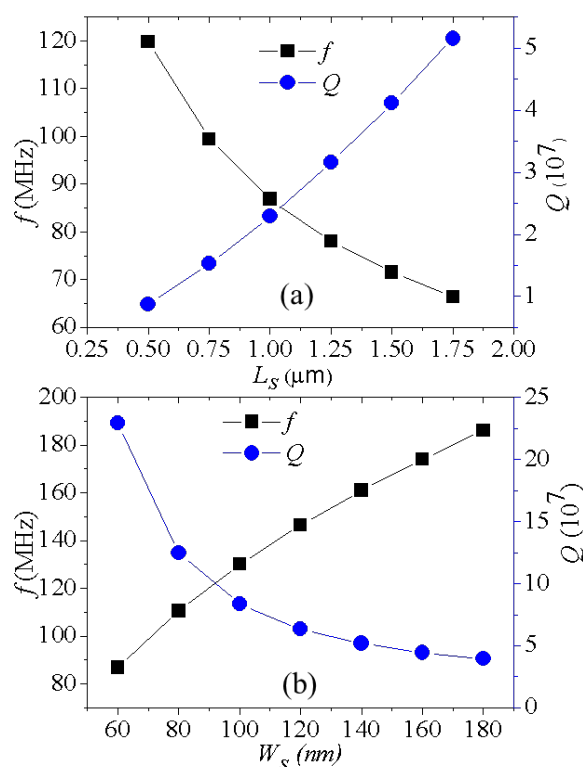


**Fig. 6.** The resonant frequency and quality factor of the OP vibrational beam nanoresonator were investigated as functions of  $L_s$  (a) and  $W_s$  (b), respectively

From the investigated result in Fig. 5b, the  $Q$ -factor of the OP vibrational beam nanoresonator achieves the maximum value when the aspect ratio of the spring beam is 1. However, for application in practical design, in addition to the study on the  $Q$ -factor depending on the length of the spring beam, we have also investigated the  $Q$ -factor of the nanoresonator as a function of  $W_s$ . In this case, the thickness of the spring beam is kept to be 60 nm, while  $W_s$  is varied. The investigated results are shown in Fig. 6b. The  $Q$ -factor decreases a factor of 5.8 from  $2.29 \times 10^7$  to  $3.94 \times 10^6$ , while  $f$  increases two times from 86.9 MHz to 186 MHz. Thus,  $f$  and  $Q$  of the OP vibrational beam nanoresonator strongly depend on the length and width of the spring beam. Here, the spring beam takes part as a torsional oscillation in the nanoresonator. As proved in the previous section, when  $W_s$  varies, the aspect ratio of the torsional spring beam differs from 1, this means that TED increases, which leads to the decrement of the  $Q$ -factor.

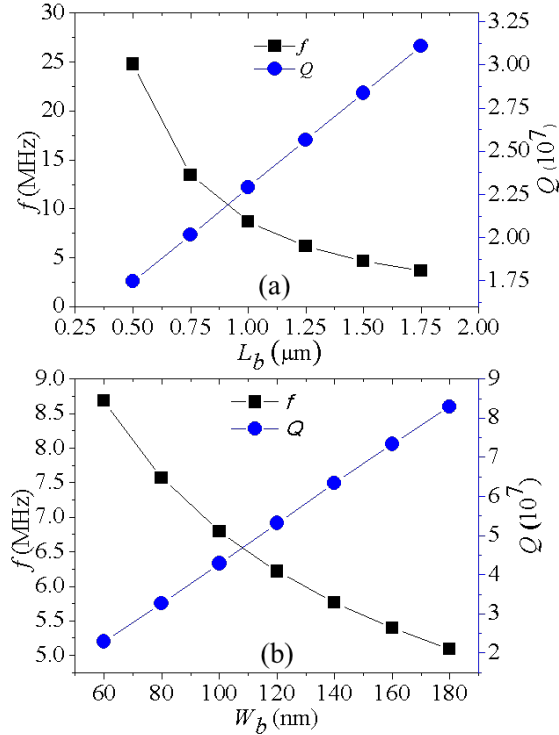


**Fig. 7.** (a) and (b) show the  $f$  and  $Q$  of the OP vibrational beam nanoresonator investigated as functions of  $L_b$  and  $W_b$ , respectively

The  $f$  and  $Q$  values have also been investigated as functions of  $L_b$  and  $W_b$ . The results are shown in Figs. 7a - b. As seen in Fig. 7, the  $Q$ -factor linearly increases with  $L_b$  and  $W_b$ . In Fig. 7a, the cross-section of the beams is 60 nm wide  $\times$  60 nm high. When  $L_b$  increases from 0.5  $\mu\text{m}$  to 1.75  $\mu\text{m}$ , the  $Q$ -factor increases a factor of 1.8 from  $1.75 \times 10^7$  to  $3.11 \times 10^7$ , while  $f$  decreases a factor of 6.8 from 248 MHz to 36.6 MHz. When  $W_b$  increases from 60 nm to 180 nm (Fig. 7b), the  $Q$ -factor increases a factor of 3.6 from  $2.29 \times 10^6$  to  $8.29 \times 10^7$ , while  $f$  decreases a factor of 1.7 from 87 MHz to 51 MHz. In this investigation, the thickness of the resonant beam is fixed at 60 nm. The increment of the  $Q$ -factor with  $W_b$  can be explained by Zener's TED theory [19,20]. The energy distribution exhibits a Lorentzian behavior as a function of  $\omega_r \tau$ , ( $Q^{-1} = \Delta_M (\omega_r \tau / (1 + (\omega_r \tau)^2))$ ), where,  $\tau$  ( $= \sqrt{\tau_\sigma \tau_\delta}$ ) is thermal relaxation time, in which  $\tau_\sigma$  and  $\tau_\delta$  are the relaxation times of the stress and strain, respectively,  $\Delta_M$  is a dimensionless quantity called the relaxation strength of the elastic modulus). The energy distribution appears a maximum value when  $\omega_r \tau = 1$  [19,20]. For the resonating beam with dimensions of 60 nm wide  $\times$  60 nm high  $\times$  0.5  $\mu\text{m}$  long,  $\tau$  ( $= \rho C_p t^2 / \pi^2 \kappa$ ) is evaluated to be  $2.64 \times 10^{-13}$ , so in the investigated range of  $W_b$ ,  $\omega_r < 1/\tau$ . When  $W_b$  increases,  $\omega_r$  decreases due to the increment of the rotational inertia while  $\tau$  is constant,  $\omega_r \tau$  is consequently decreased. Thus, the  $Q$  value increases with  $W_b$  due to lesser energy dissipated.

#### 4. Conclusion

We have presented the design and simulation analysis of an OP vibrational beam nanoresonator. Based on the motion transformation mechanism from torsion into the rotation, the OP vibrational beam nanoresonator having ultrahigh intrinsic  $Q$ -factor in considering both anchor loss and TED is designed and simulated. The torsional oscillation is used to minimize TED, while the out-of-phase vibration is employed to form the stationary points for suppressing anchor loss. The optimal design flow for the OP vibrational beam resonator has been carried out. The torsional spring beam should have a square shape to minimize TED.

The OP vibrational beam nanoresonator with the  $Q$ -factor over  $10^7$  is achievable by optimizing its representative geometry parameters.

## References

1. Naik AK, Hanay MS, Hiebert WK, Feng XL, Roukes ML. Towards single-molecule nanomechanical mass spectrometry. *Nature Nanotechnology*. 2009;4: 445-450.
2. Xu Y, Lin JT, Alphenaar BW, Keynton RS. Viscous damping of microresonators for gas composition analysis. *Applied Physics Letters*. 2006;88(14): 143513.
3. Van Beek JTM, Puers R. A review of MEMS oscillators for frequency reference and timing applications. *Journal of Micromechanics and Microengineering*. 2012;22(1): 013001.
4. Li M, Tang HX, Roukes M. Ultra-sensitive NEMS-based cantilevers for sensing, scanned probe and very high-frequency applications. *Nature Nanotechnology*. 2007;2: 114-120.
5. Connell ADO, Hofheinz M, Ansmann M, Bialczak RC, Lenander M, Lucero E, Neeley M, Sank D, Wang H, Weides M, Wenner J, Martinis JM, Cleland AN. Quantum ground state and single-phonon control of a mechanical resonator. *Nature*. 2010;464: 697-703.
6. Ilgamov MA. Flexural vibrations of a plate under changes in the mean pressure on its surfaces. *Acoustical Physics*. 2018 64(5): 605-611.
7. Ilgamov MA. Bending and stability of a thin plate under vacuuming its surfaces. *Doklady Physics*. 2018;63(7): 244-246.
8. Ilgamov MA. Frequency spectrum of a wire micro- and nanoresonator. *Doklady Physics*. 2020;65(9): 326-329.
9. Ilgamov MA, Khakimov AG. Influence of pressure on the frequency spectrum of micro- and nanoresonators on hinged supports. *Journal of Applied and Computational Mechanics*. 2021;7(2): 977-983.
10. Hoang MC. Air damping models for micro- and nano-mechanical beam resonators in molecular-flow regime. *Vacuum*. 2016;126: 45-50.
11. Van HD, Van TL, Hane K, Hoang C M. Models for analyzing squeeze film air damping depending on oscillation modes of micro/nano beam resonators. *Archive of Applied Mechanics*. 2021;91(1): 363-373.
12. Bao M, Yang H. Squeeze film air damping in MEMS. *Sensors and Actuators A: Physical*. 2007;136(1): 3-27.
13. Photiadis DM, Judge JA. Attachment losses of high Q oscillators. *Applied Physics Letters*. 2004;85(3): 482-484.
14. Hao Z, Erbil A, Ayazi F. An analytical model for support loss in micromachined beam resonators with in-plane flexural vibrations. *Sensors and Actuators A: Physical*. 2003;109(1-2): 156-164.
15. Kotani S, Hoang CM, Sasaki T, Hane K. Micromirrors connected in series for low voltage operation in vacuum. *Journal of Vacuum Science & Technology B*. 2013;31(4): 42001.
16. Hassani FA, Tsuchiya Y, Mizuta H. Optimization of quality-factor for in-plane free-free nanoelectromechanical resonators. *IET Micro & Nano Letters*. 2013;18(12): 886-889.
17. Taş V, Olcum S, Aksoy MD, Atalar A. Reducing Anchor Loss in Micromechanical Extensional Mode Resonators. *IEEE Transactions on Ultrasonics, Ferroelectrics, and Frequency Control*. 2010;57: 448-454.
18. Yi YB, Matin MA. Eigenvalue Solution of Thermoelastic Damping in Beam Resonators Using a Finite Element Analysis. *Journal of Vibration and Acoustics*. 2007;129(4): 478-483.
19. Zener C. Internal Friction in Solids, I: Theory of Internal Friction in Reeds. *Physical Review*. 1937;52: 230-235.
20. Lifshitz R, Roukes ML. Thermoelastic Damping in Micro- and Nanomechanical Systems. *Physical Review B*. 2000;61: 5600-5609.
21. Bostani M, Karami Mohammadi A. Thermoelastic damping in microbeam resonators

- based on modified strain gradient elasticity and generalized thermoelasticity theories. *Acta Mechanica*. 2018;229: 173.
22. Photiadisa DM, Houstona BH, Liu X, Bucaro JA, Marcus MH. Thermoelastic loss observed in a high Q mechanical oscillator. *Physica B*. 2002;316-317: 408-410.
  23. Guo X, Yi YB, Pourkamali S. A finite element analysis of thermoelastic damping in vented MEMS beam resonators. *International Journal of Mechanical Sciences*. 2013;74: 73-82.
  24. Duwel A, Candler RN, Kenny TW, Varghese M. Engineering MEMS Resonators with Low Thermoelastic Damping. *Journal of Microelectromechanical Systems*. 2006;15: 1437-1445.
  25. Guo X, Yi YB. Suppression of thermoelastic damping in MEMS beam resonators by piezoresistivity. *Journal of Vibration and Acoustics*. 2014;333(3): 1079-1095.
  26. Losby J, Burgess JAJ, Diao Z, Fortin DC, Hiebert WK, Freeman MR. Thermo-mechanical sensitivity calibration of nanotorsional magnetometers. *Journal of Applied Physics*. 2012;111(7): 07D305.
  27. Torres FA, Meng P, Ju L, Zhao C, Blair DG, Liu KY, Chao S, Martyniuk M, Jeune IR, Flaminio R, Michel C. High quality factor mg-scale silicon mechanical resonators for 3-mode optoacoustic parametric amplifiers. *Journal of Applied Physics*. 2013;114(1): 014506.
  28. Houston BH, Photiadis DM, Marcus MH, Bucaro JA, Liu X, Vignola JF. Thermoelastic loss in microscale oscillators. *Applied Physics Letters*. 2002;80(7): 1300.
  29. Ardito R, Comi C, Corigliano A, Frangi A. Solid damping in micro electro mechanical systems. *Meccanica*. 2008;43: 419-428.
  30. Petersen KE. Silicon as mechanical material. *Proceedings of the IEEE*. 1982;70: 420-57.
  31. Yi YB. Geometric effects on thermoelastic damping in MEMS resonators. *Journal of Sound and Vibration*. 2008;309: 588-599.

## THE AUTHORS

### **Chu Manh Hoang**

e-mail: hoangcm@itims.edu.vn

ORCID: 0000-0001-5808-8736

### **Nguyen Van Duong**

e-mail: manhduong415@gmail.com

ORCID: 0000-0003-3880-9828

### **Dang Van Hieu**

e-mail: hieudv2@fe.edu.vn

ORCID: 0000-0001-7774-775X

# Ab initio calculations of electronic band structure of ideal and defective CdMnS

Matanat A. Mehrabova<sup>1✉</sup>, Natig T. Panahov<sup>2</sup>, Niyazi H. Hasanov<sup>3</sup>

<sup>1</sup>Institute of Radiation Problems of Azerbaijan National Academy of Sciences, B. Vahabzade str., 9, Baku, AZ-1143, Azerbaijan

<sup>2</sup>Azerbaijan University of Architecture and Construction, A. Sultanova str. 5, Baku, AZ-1073, Azerbaijan

<sup>3</sup>Baku State University, Z. Khalilov str., 23, Baku, AZ-1148, Azerbaijan

✉ m.mehraboav@science.az

**Abstract.** The purpose of this work was to calculate the electronic band structure of ideal and defective Cd<sub>1-x</sub>Mn<sub>x</sub>S. Ab initio, calculations are performed in the Atomistix Toolkit program within the Density Functional Theory and Local Spin Density Approximation on Double Zeta Double Polarized basis. We have used Hubbard  $U$  potential  $U_{Mn} = 3.59$  eV for  $3d$  states for Mn atoms. Supercells of 8 and 64 atoms were constructed. After the construction of Cd<sub>1-x</sub>Mn<sub>x</sub>S ( $x = 6.25\%$ ;  $25\%$ ) supercells, atom relaxation and optimization of the crystal structure were carried out. Electronic band structure, and density of states were calculated, and total energy have been defined in antiferromagnetic and ferromagnetic phases. Our calculations show that the band gap increases with the increases in Mn ion concentration. It has been established that defects such as interstitial Cd(S) atom, Cd(S) vacancy or Frankel pair in the crystal structure lead to increasing band gap, shifting of Fermi level towards the valence or conduction band.

**Keywords:** ab initio calculations, DFT, semimagnetic semiconductors, electronic band structure, defect

**Acknowledgements.** No external funding was received for this study.

**Citation:** Mehrabova MA, Panahov NT, Hasanov NH. Ab initio calculations of electronic band structure of ideal and defective CdMnS. *Materials Physics and Mechanics*. 2022;48(3): 419-427. DOI: 10.18149/MPM.4832022\_12.

## 1. Introduction

CdS (band gap 2.43 eV) is an attractive semiconductor in the photoconductive, photovoltaic, and optoelectronic materials [1-5]. They have large applications as photoconductors in the visible and near ultra-violet spectral regions, in semiconductor lasers, nonlinear optical devices [6], photovoltaic solar cells, thin film transistors, display devices [7] and also for tagging biological molecules [8]. Doping of transition metals such as Mn, Fe, Ni, Co, etc. in nonmagnetic CdS is very important to make this material multifunctional, that influences the electronic structure, produces unique magnetic and magneto-optical properties with unparalleled opportunities in the field of spintronics [9]. Cd<sub>1-x</sub>Mn<sub>x</sub>S thin films have also drawn large attention because of their magnetic and magneto-optical properties [10,11]. Room temperature CdS- based semimagnetic semiconductors (SMSC), such as Mn-doped

CdS are a very good photoluminance compound due to  $d$  states at the top of the valence band and intra- $d$  shell transitions [12].

This work is devoted to ab initio calculations of  $\text{Cd}_{1-x}\text{Mn}_x\text{S}$  SMSC by using Density functional theory (DFT). DFT have been successfully used for theoretical investigations of magnetic materials [13-17]. The Mn-CdS sheet with 16 atom supercell is analyzed by Kumar S., Kumar A., Ahluwalia P.K. [18]. The electronic band structure of wurtzite CdS calculated by Rantala et al. using two different self-consistent ab initio Local Density Approximation (LDA) methods [19]. Nabi [20] investigated electronic and magnetic properties of Mn-doped CdS in the wurtzite phase, using ab-initio calculations based on LDA, Generalized Gradient Approximation (GGA) and LDA +  $U$  exchange and correlation functional. It is found that Mn:CdS does not allow the hopping of electrons and d-d super exchange interactions are observed in Mn:CdS [20]. Ahmed N., Nabi A., Nisar J., Tariq M., Javid M.A., and Nasim M.H. [12] investigated the electronic band structure of  $\text{Cd}_{1-x}\text{Mn}_x\text{S}$  ( $x = 6.25\%$ ) using spin-polarized DFT within the framework of GGA, its extension via on-site Hubbard  $U$  interactions (GGA +  $U$ ), and a model for exchange and correlation of potential Tran modified Becke-Johnson (TB-mBJ).

Band structure of defective CdMnS has been investigated less [20] in comparison with other SMSC. The purpose of this work was to calculate the electronic band structure of ideal and defective  $\text{Cd}_{1-x}\text{Mn}_x\text{S}$  SMSC in both.

## 2. Methods and results

Ab initio calculations are performed in the Atomistix Toolkit (ATK) program within the DFT and Local Spin Density Approximation (LSDA) on the Double Zeta Double Polarized (DZDP) basis. We have used Hubbard  $U$  potential  $U_{Mn} = 3.59$  eV for 3d states for Mn atoms [5-10]. Ideal supercells of 8 (Fig. 1) and 64 (Fig. 2) atoms were constructed. After the construction of  $\text{Cd}_{1-x}\text{Mn}_x\text{S}$  ( $x = 0; 6.25\%; 25\%$ ) supercells, atom relaxation and optimization of the crystal structure were carried out to eliminate forces and minimize stresses. Electron band structure (EBS) and density of states (DOS) were calculated, and the total energy has been defined in AFM and FM phases.

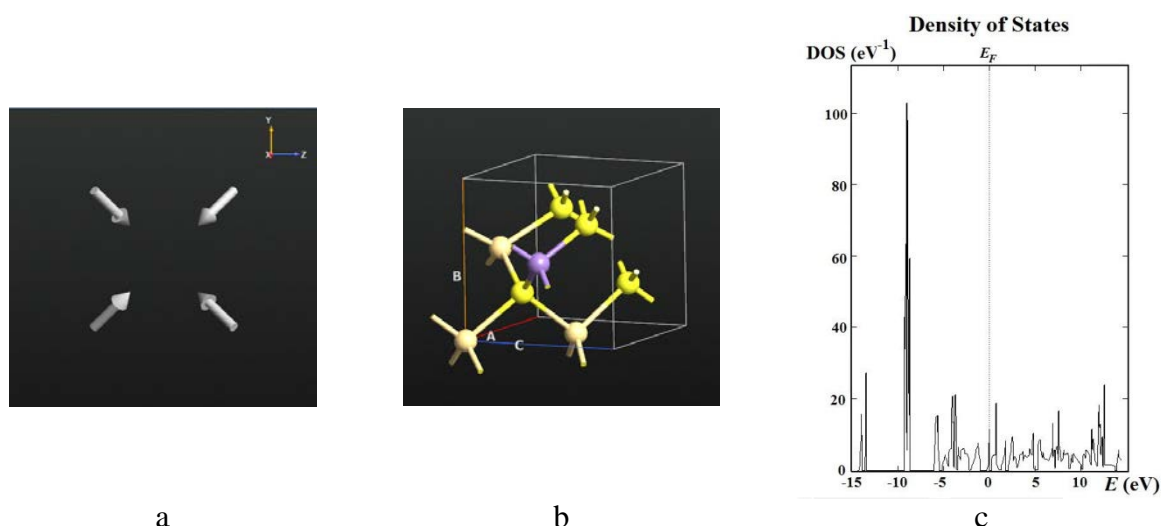


**Fig. 1.**  $\text{Cd}_{1-x}\text{Mn}_x\text{S}$ ,  $x=0.25$  supercell: a – forces; b – bulk configuration; c – density of states

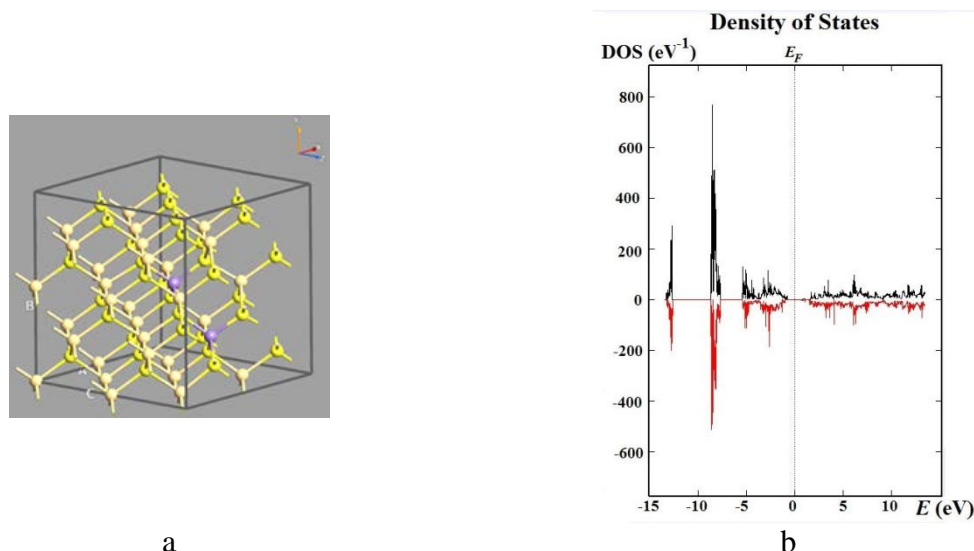


**Fig. 2.**  $\text{Cd}_{1-x}\text{Mn}_x\text{S}$ ,  $x = 0.0625$  supercell: a – bulk configuration; b – density of states

The electron band structure of  $\text{Cd}_{1-x}\text{Mn}_x\text{S}$  ( $x = 0.0625$ ) SMSC is determined from the projected density of states (PDOS) (Fig. 3). The obtained PDOS plots are presented in Fig. 3. The analysis of these graphs shows that in the valence band, the electron band structure of  $\text{Cd}_{1-x}\text{Mn}_x\text{S}$  consists of three parts: (1) the upper part of the valence band is mainly formed by  $p$ -orbitals of S and Cd atoms,  $s$ -orbitals of Cd and Mn atoms with some contribution of  $d$ -orbitals of Mn atoms; (2) the middle part is formed by  $d$ -orbitals of Cd atoms, which are 8–9 eV lower than the valence band maximum (3) the lower part is formed by  $s$ -orbitals of S and Mn atoms, and  $p$ -orbitals of Mn atoms which are located 13 eV lower than the valence band maxim. The bottom of the conductivity band is formed by  $s$ - and  $p$ -orbitals of Mn atoms and  $p$ -orbitals of Cd atoms,  $d$ -orbitals of S atoms (Fig. 3).

The band gap for the  $\text{Cd}_{1-x}\text{Mn}_x\text{S}$  SMSC with  $x = 0.25$  supercells is equal to  $E_g = 1.6$  eV and total energy is equal to  $E_t = -6698.61546$  eV. For the  $x = 0.0625$  supercell band gap is equal to  $E_g = 1.25$  eV and total energy is equal to  $E_t = 59267.92943$  eV. The calculated band gap much closer to theoretical 1.25 eV, 1.27 eV [12,20] and experimental value [26]. The values of band gap with GGA calculations and effect of Hubbard "U" term on band gap using GGA+U calculations were used in [12,20].

Calculations show that the band gap increase with an increase in Mn ion concentration (Table 1). These theoretical results have a good agreement with experimental results [27]. The optical transmission of the  $\text{Cd}_{1-x}\text{Mn}_x\text{S}$  thin films show that the band gap increases with the increases in manganese ion concentration.

Table 1. Band gap and total energy for  $\text{Cd}_{1-x}\text{Mn}_x\text{S}$

$x$	$E_g$ , eV	$E_t$ , eV
0	0.83	-1910,95
0.0625	1.25	-59267,93
0.25	1.6	-6698,62

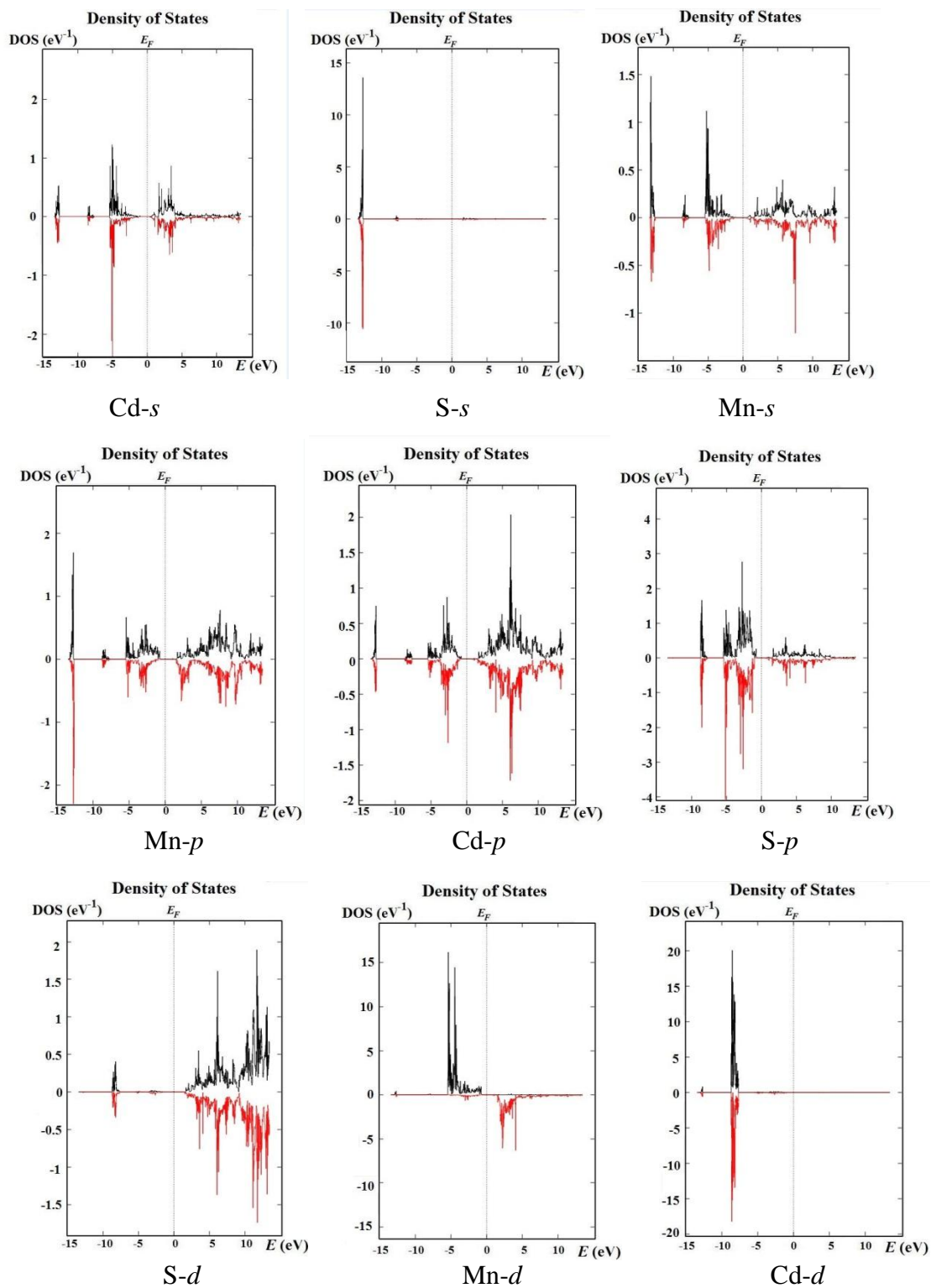


**Fig. 3.** PDOS of  $\text{Cd}_{1-x}\text{Mn}_x\text{S}$  ( $x = 0.0625$ ) SMSC

EBS and DOS of the defective  $\text{Cd}_{30}\text{Mn}_2\text{Se}_{32}$  supercell are calculated. We consider vacancy-type defects. Atom relaxation and optimization of the crystal structure were carried out, and forces and stresses were minimized (Fig. 4).

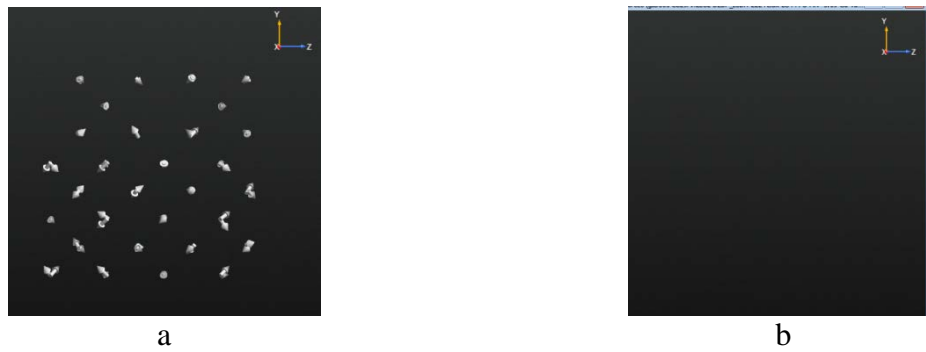


**Fig. 4.** Forces: a – before optimization; b – after optimization

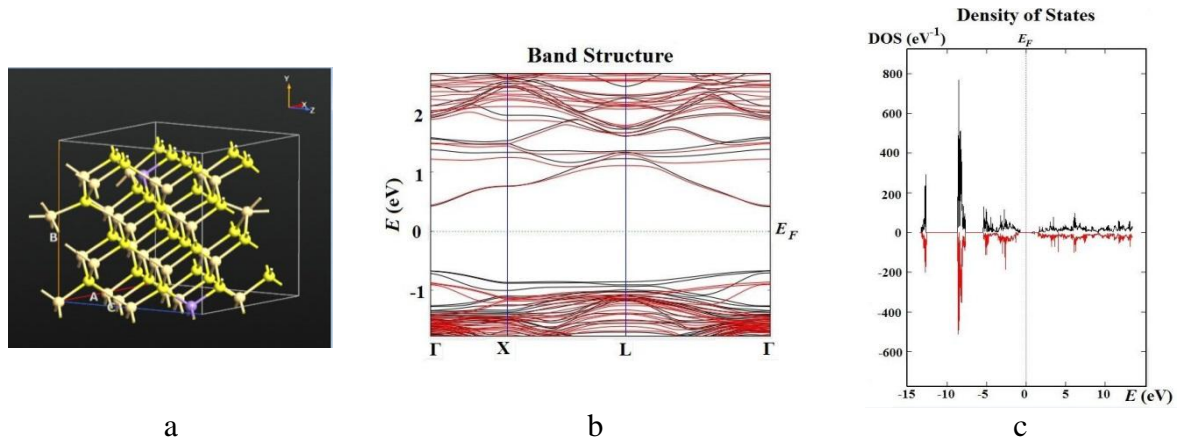


**Fig. 5.** S vacancy in  $Cd_{1-x}Mn_xS$ ,  $x = 0.625$ ; a – bulk configuration; b – EBS; c – DOS

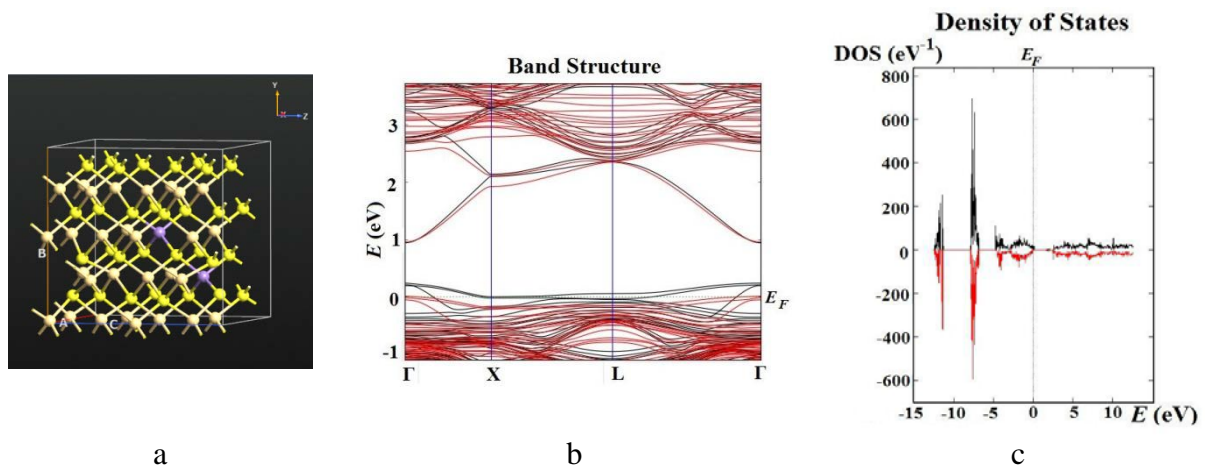


**Fig. 6.** Cd vacancy in  $Cd_{1-x}Mn_xS$ ,  $x = 0.625$ ; a – bulk configuration; b – EBS; c – DOS

In the case of S vacancy ( $V_S$ ), the band gap is  $E_g = 1.3$  eV, and the total energy equals  $E_t = -58907.65$  eV (Fig. 5); for Cd vacancy ( $V_{Cd}$ ) the band gap is  $E_g = 1.55$  eV, the total energy is  $E_t = -57712.51$  eV (Fig. 6). Figures 5 and 6 show that Cd or S vacancy in a crystal leads to an increase in the band gap, as a change in the total energy occurs, the Fermi level shifts towards the valence or conduction band.

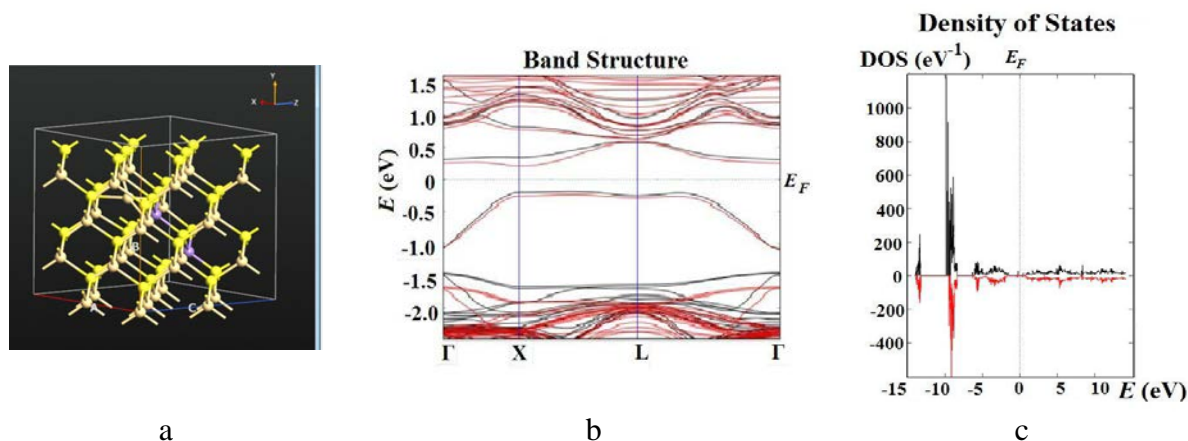


**Fig. 7.** Interstitial Cd atom in  $\text{Cd}_{1-x}\text{Mn}_x\text{S}$ ,  $x = 0.625$ ; a – bulk configuration; b – EBS; c – DOS

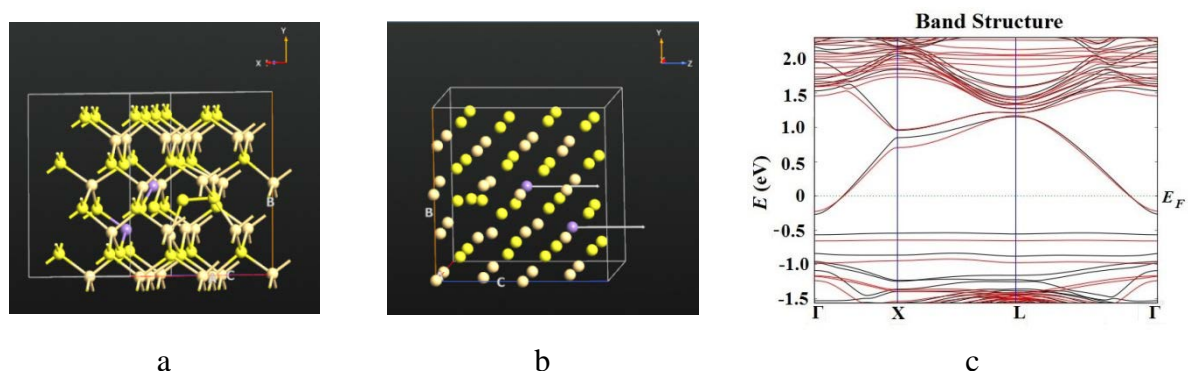


**Fig. 8.** Interstitial S atom in  $\text{Cd}_{1-x}\text{Mn}_x\text{S}$ ,  $x = 0.625$ ; a – bulk configuration; b – magnetic moments; c – EBS

Supercell of  $\text{Cd}_{1-x}\text{Mn}_x\text{S}$  of 64 atoms with interstitial Cd ( $I_{\text{Cd}}$ ) atom and interstitial S ( $I_{\text{S}}$ ) atom were constructed. After the construction of  $\text{Cd}_{1-x}\text{Mn}_x\text{S}$  ( $x=6.25\%$ ) supercell with interstitial Cd or S atom, atom relaxation and optimization of crystal structure were carried out. Electron band structure, density of states were calculated, and total energy have been defined (Fig. 7,8). In the case of interstitial Cd atom, the band gap is equal to  $E_g=1.35$  eV, total energy is equal to  $E_T=-60817.73$  eV (Fig. 7). For the interstitial S atom, the band gap is equal to  $E_g=1.75$  eV, and total energy is equal to  $E_T=-59624.67$  eV (Fig. 8). Figures 7 and 8 show that interstitial Cd or S atoms in crystal structure lead to an increase in the band gap.

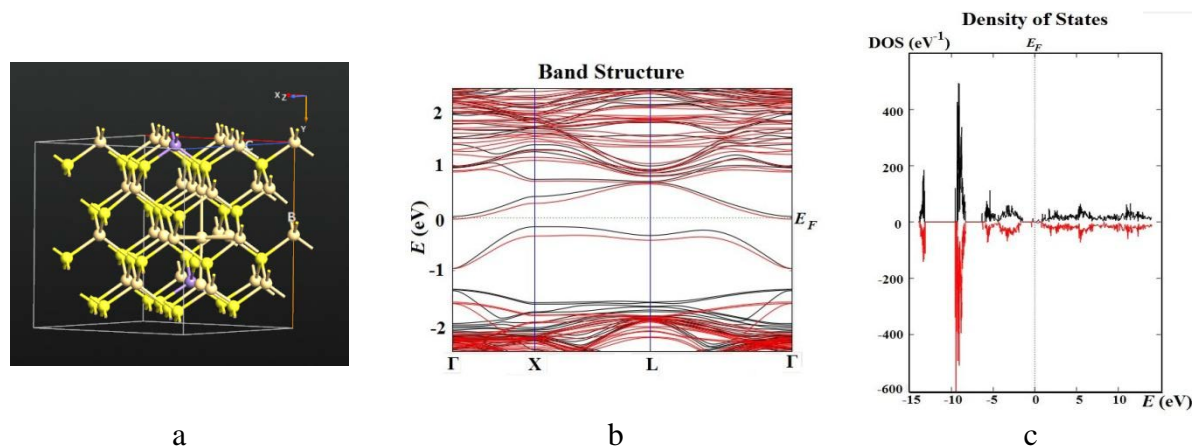


**Fig. 9.** Frenkel pair in  $\text{Cd}_{1-x}\text{Mn}_x\text{S}$ ,  $x = 0.625$ ; a – bulk configuration; b – EBS; c – DOS

Supercell of  $\text{Cd}_{1-x}\text{Mn}_x\text{S}$  of 64 atoms with Frankel pair was constructed. After the construction of  $\text{Cd}_{1-x}\text{Mn}_x\text{S}$  ( $x=6.25\%$ ) supercell with Frankel pair, atom relaxation and optimization of crystal structure were carried out. Electron band structure, density of states were calculated, and total energy have been defined. In the case of Frankel pair, the band gap is equal to  $E_g=2$  eV, total energy is equal to  $E_t=-60817.77$  eV (Fig. 9).

It can be concluded that vacancy, interstitial atom, or Frenkel pair type defects in crystal lead to an increase in the band gap, Fermi level shifts towards the valence or conduction band (Table 2).

Table 2. Band gap and total energy for Interstitial Cd (S) atom and Cd (S) vacancy in  $\text{Cd}_{1-x}\text{Mn}_x\text{S}$ ,  $x=0.25$

$x=0.0625$	Ideal	$V_{Cd}$	$V_S$	$I_{Cd}$	$I_S$	$FP$
$E_g$ , eV	1.25	1.55	1.3	1.35	1.75	2
$E_t$ , eV	-59267.93	-57712.51	-58907.65	-60817.73	-59624.67	60817.77

### 3. Conclusion

Ab initio calculations have been performed to analyze the electronic band structure of an ideal and defective  $\text{Cd}_{1-x}\text{Mn}_x\text{S}$  SMSC ( $x = 0.25; 0.0625$ ). It has been defined that with an increase in Mn ion concentration in the  $\text{Cd}_{1-x}\text{Mn}_x\text{S}$ , there is an increase in the band gap and an increase in the total energy. The calculations show that the defects as a vacancy, interstitial atom, or Frenkel pair in a crystal lead to an increase in the band gap, shifting the Fermi level towards the valence or conduction band.

### References

1. Munde BS, Ravangave LS. Physical and spectroscopic characterization of chemically deposited  $\text{Cd}_{1-x}\text{Mn}_x\text{S}$  thin films. *IOSR Journal of Applied Physics*. 2017;9(3): 85-89.
2. Munde BS, Mahewar RB, Ravangave LS. Study of spectroscopic properties of  $\text{Cd}_{0.6}\text{Mn}_{0.4}\text{S}$  chemical bath deposited thin film for solar cell applications. *International Journal of Research and Analytical Reviews*. 2018;5(3): 962-966.
3. Mali AE, Gaikwad AS, Borse SV, Ahire RR. Influence of  $\text{Mn}^{2+}$  magnetic ions on the properties of  $\text{Cd}_{1-x}\text{Mn}_x\text{S}$  thin films synthesized by chemical bath deposition. *Journal of Nano- and Electronic Physics*. 2021;13(1): 01004.
4. Girish M, Sivakumar R, Sanjeeviraja C. Tuning the properties of  $\text{Cd}_{1-x}\text{Mn}_x\text{S}$  films deposited by nebulized spray pyrolysis. *Optik - International Journal for Light and Electron Optics*. 2021;227(4): 166088.
5. Potapenko KO, Kurenkova AY, Bukhtiyarov AV, Gerasimov EY, Cherepanova SV, Kozlova EA. Comparative Study of the Photocatalytic Hydrogen Evolution over  $\text{Cd}_{1-x}\text{Mn}_x\text{S}$  and  $\text{CdS}-\beta-\text{Mn}_3\text{O}_4-\text{MnOOH}$  Photocatalysts under Visible Light. *Nanomaterials*. 2021;11(2): 355.
6. In-Hwan C, Peter YY. Structural and optical properties of cubic-CdS and hexagonal-CdS thin films grown by MOCVD on GaAs substrates using a single source precursor  $\text{C}_{14}\text{H}_{30}\text{CdN}_2\text{S}_4$ . *Physica Status Solidi (b)*. 2005;242: 1610-1616.
7. Basudev P, Ashwani KS, Asim KR. Conduction studies on chemical bath-deposited nanocrystalline CdS thin films. *Journal of Crystal Growth*. 2007;304(2): 388-392.

8. Feng W, Wee BT, Yong Z, Xianping F, Minquan W. Luminescent nanomaterials for biological labeling. *Nanotechnology*. 2006;17: R1-R13.
9. Wu XJ, Shen DZ, Zhang Z, Liu KW, Li BH, Zhang JY, Lu YM, Zhao DX, Yao B, Ren XG, Fan XW. Characterization of Cd<sub>1-x</sub>FexS diluted magnetic semiconductors grown at near phase conversion temperature. *Solid State Communications*. 2007;141: 344-347.
10. Franciosi W, Niles DW, Reifenberger R, Quaresima C, Copozi M, Perfetti P. Electronic structure of Cd<sub>1-x</sub>MnxS ternary semimagnetic alloys. *Physical Review B*. 1990;41: 5969-5978.
11. Badera N, Godbole B, Srivastava SB, Vishwakarma PN, Chandra LSSh. Jain D, Sathe VG, Ganesan V. Photoconductivity in Cd<sub>1-x</sub>MnxS thin films prepared by spray pyrolysis technique. *Solar Energy Materials and Solar Cells*. 2008;92: 1646-1651.
12. Ahmed N, Nabi A, Nisar J, Tariq M, Javid MA, Nasim MH. First principle calculations of electronic and magnetic properties of Mn-doped CdS (zinc blende): a theoretical study. *Materials Science-Poland*. 2017;35(3): 479-485.
13. Masrour R, Hlil EK. Correlation of electronic structure and magnetic moment in Ga<sub>1-x</sub>MnxN: First-principles, mean field and high temperature series expansions calculations. *Physica A*. 2016;456: 215-221.
14. Mounkachi O, Salmani E, El Moussaoui H, Masrour R, Hamedoun M, Ez-Zahraouy H, Hlil EK, Benyoussef A. High blocking temperature in SnO<sub>2</sub> based super-paramagnetic diluted magnetic semiconductor. *Journal of Alloys and Compounds*. 2014;614: 401-407.
15. Rkhioui A, Masrour R, Hlil EK, Benyoussef A, Hamedoun M, Bahmad L. Electronic and Magnetic Properties of Ga<sub>1-x</sub>MxA (M = Mn and Cr; A = As and N): Ab Initio Study. *Journal of Superconductivity and Novel Magnetism*. 2015;28: 3419-3428.
16. Masrour R, Rkhioui A, Hlil EK, Hamedoun M, Benyoussef A, Bahmad L. Calculated Ab-Initio of Co-doped Zn<sub>1-x-y</sub>AxB<sub>y</sub>O (A=Mo; B=Mn, Cr). *Journal of Superconductivity and Novel Magnetism*. 2015;28: 125-129.
17. Rkhioui A, Masrour R, Hlil EK, Bahmad L, Hamedoun M, Benyoussef A. Study of Electronic and Magnetic Properties of Zn<sub>1-x</sub>MxO (M = Mn and Cr) by ab initio Calculations. *Journal of Superconductivity and Novel Magnetism*. 2013;26: 3469-3474.
18. Kumar S, Kumar A, Ahluwalia PK. First principle study of manganese doped cadmium sulphide sheet. *AIP Conference Proceedings*. 2014;1591(1): 1732.
19. Rantala TT, Rantala TS, Lantto V, Vaara J. Surface relaxation of the (1010) face of wurtzite CdS. *Surface Science*. 1996;352-354: 77-82.
20. Nabi A. The electronic and the magnetic properties of Mn doped wurtzite CdS: First-principles calculations. *Computer Material Science A*. 2016;112: 210-218.
21. Mehrabova MA, Orujov HS, Hasanov NH, Kazimova AI, Abdullayeva A. Ab Initio Calculations of Defects in CdMnSe Semimagnetic Semiconductors. *Mechanics of Solids*. 2020;55(1): 108-113.
22. Mehrabova MA, Hasanov NH, Huseynov NI, Kazimova AI. Ab initio calculations of defects in Cd<sub>1-x</sub>MnxTe(Se) semimagnetic semiconductors. *Journal of Radiation Researches*. 2020;7(2): 39-42.
23. Mehrabova MA, Orujov HS, Nuriyev HR, Hasanov NH, Abdullayeva AA, Suleymanov ZI. Ab-initio calculations of electronic structure of CdFeTe and optical properties. *Conference Proceedings Modern Trends In Physics*. 2019: 39-42.
24. Mehrabova MA, Hasanov NH, Huseynov NI, Kazimova AI, Asadov FG. Effect of defects on electronic structure of Cd<sub>1-x</sub>MnxSe semimagnetic semiconductors. *Journal of Radiation Reserches*. 2018;5(2): 46-50.

25. Mehrabova MA, Nuriyev HR, Orujov HS, Nazarov AM, Sadigov RM, Poladova VN. Defect formation energy for charge states and electrophysical properties of CdMnTe. *Proc. SPIE Photonics, Devices and Systems VI, SPIE*. 2015;9450: 945001-9450010.
26. Srivastava P, Kumar P, Singh K. Room temperature ferromagnetism in magic-sized Cr-doped CdS diluted magnetic semiconducting quantum dots. *Journal of Nanoparticle Research*. 2011;13(10): 5077-5085.
27. Al-Jawad SMH. Optoelectronic characteristics and optical properties for Cd<sub>1-x</sub>Mn<sub>x</sub>S nanocrystalline thin films prepared by chemical bath deposition. *International Journal of Application or Innovation in Engineering & Management*. 2014;3(2): 329-333.

## THE AUTHORS

### **Mehrabova M.A.**

e-mail: mehrabova@mail.ru

ORCID: 0000-0003-4417-0522

### **Panahov N.T.**

e-mail: panahovn@yahoo.com

ORCID: 0000-0002-9178-0641

### **Hasanov N.H.**

e-mail: n.h.hasanov@rambler.ru

ORCID: 0000-0002-5122-4712

# Seismic behavior of heritage building with isotropic and orthotropic material properties: a comparative analysis

Kamran<sup>1✉</sup>, Shakeel Ahmad<sup>2</sup>, Rehan A. Khan<sup>2</sup>

<sup>1</sup>Department of Civil Engineering, Indian Institute of Technology Roorkee, Roorkee 247667, India

<sup>2</sup>Department of Civil Engineering, Aligarh Muslim University, Aligarh 202002, India

✉ [kmm890@gmail.com](mailto:kmm890@gmail.com)

**Abstract.** Restoration and retrofitting of heritage buildings is a complex analysis. In actual practice, building materials of heritage masonry buildings are anisotropic. However, in practice, these building materials had been considered isotropic to optimize the analysis. The present study is a comparative analysis of these two approaches. A heritage school building in northern India underlying seismic zone IV has been considered for the analysis. The seismic performance analysis of the buildings has been carried out through numerical modeling using the SAP2000. Analysis has been carried out for one set of isotropic and three sets of orthotropic material parameters. Normal and shear stresses had been observed and compared with stress calculated from the empirical relationships provided in the standard code of practice.

**Keywords:** heritage building, orthotropic material, seismic performance, Chamoli earthquake, modal analysis

**Acknowledgements.** *The authors are highly grateful to UGC for providing grants (File no. 3.44/2012 (SAP II)) for undertaking this work.*

**Citation:** Kamran, Ahmad S, Khan RA. Seismic behavior of heritage building with isotropic and orthotropic material properties: a comparative analysis. *Materials Physics and Mechanics*. 2022;48(3): 428-442. DOI: 10.18149/MPM.4832022\_13.

## 1. Introduction

The understanding of the failure mechanism of masonry structures under lateral loads is of utmost importance, as it fails miserably under lateral load [1-5]. Doors and windows opening are highly vulnerable [6]. The investigation of seismic behaviour of any heritage buildings (typically masonry structures) is combined with several difficulties such to find its original design plans. Moreover, modifications have occurred to the structure due to changes of use or combined with renovations over time [7,8]. Unfortunately, documentations on modifications of the structure are also not available either. To find the seismic performance of structures it is very useful to find old records of historical earthquakes in the region. Due to the non-availability of codes at the time of construction, the design of masonry buildings was based on personal experience resulting in very thick and uneconomic structures. In order to minimize the effort of the material survey, parameters must be defined with reference to present codes or reference values of similar structures. Masonry is a composite, non-homogeneous and anisotropic material. It may be of stones, bricks, adobe, or tiles bonded together with mortar. Masonry structures are load-bearing and perform a variety of functions like supporting loads,

subdividing space, providing thermal insulation and weather protection, etc. Being a heterogeneous material, behaviour of masonry depends on the mechanical properties of its components, the arrangement of the units, the interfaces between them, and the interaction of these units with other structural members and materials used in the building (e.g. timber or steel beams and columns and timber floors) [9-12].

Camathias U. [13] has conducted theoretical and experimental research and found various parameters of masonry construction which affect the strength, stability, and performance of masonry structures are found, need to be considered in the design. It is a vital issue to understand the lateral load resisting system of such structures for their comprehensive structural analysis. The earthquake waves hitting perpendicular to the longer side of the wall are more vulnerable than that hitting parallel to the longer side of the wall. This is mainly due to the height-to-thickness ratio of the masonry wall [13]. The historic masonry walls have confirmed the high vulnerability and low shear capacity when exposed to seismic actions whereas the shear strength of masonry increases with the pre-compression up to a limit and becomes constant at higher pre-compression [15]. Nowadays, finite element analyses have become the most important tool for the analysis of historical structures [10,16]. Sarhosis V. et al. [17] have found that 3D simulation approach is more reliable to investigate the real seismic response than 2D analysis. Parajuli H.R. [18] investigated the effects of various earthquake ground motions on finite element model (FEM) have confirmed that old masonry structures were found very weak in resisting seismic forces. The article is devoted to the important applied problem – the seismic resistance estimation of ground buildings. Due to the high risks of destruction during the earthquake, the old building should be modified to resist enough stability. In the case of the impossibility to carry out laboratory experiments, computer simulation is a reasonable technique. The nonlinear analysis technique is widely used by other scientific groups [19]. The author described the current state of the art in the direction is seismic impact simulations, however, not only finite-element methods show good results. For example, due to the hyperbolicity of the considered dynamic problem, the grid-characteristic method recently showed perfect precision [20].

In the present study, the seismic behaviour of the masonry heritage school (STS High School, Aligarh) building has been analysed. It is a brick masonry structure, established in 1875 A.D. It is a residential school in seismic zone IV with the strength of 2000 students. Figure 1 shows a northwest view of the school building.



**Fig. 1.** STS High School Front NorthWest view [21]

## 2. Mathematical Modelling Techniques

The following modelling techniques can be adopted [10,14].

(1) *Detailed micro modelling*: Units and mortar joints are represented by continuum elements whereas the unit-brick interface is represented by discontinuous elements.

(2) *Simplified Micro modelling*: Expanded units are represented by continuum elements whereas the behaviour of the mortar joints and the unit-mortar interface is lumped in discontinuous elements. These interface elements represent the preferential crack locations where tensile and shear cracking occur.

(3) *Macro-modelling*: Units, mortar, and unit-mortar interface are smeared out in the continuum. It is more practice-oriented due to the reduced time and memory requirements as well as user-friendly mesh generation.

These three types of modelling techniques of a masonry sample have been shown in Fig. 2.

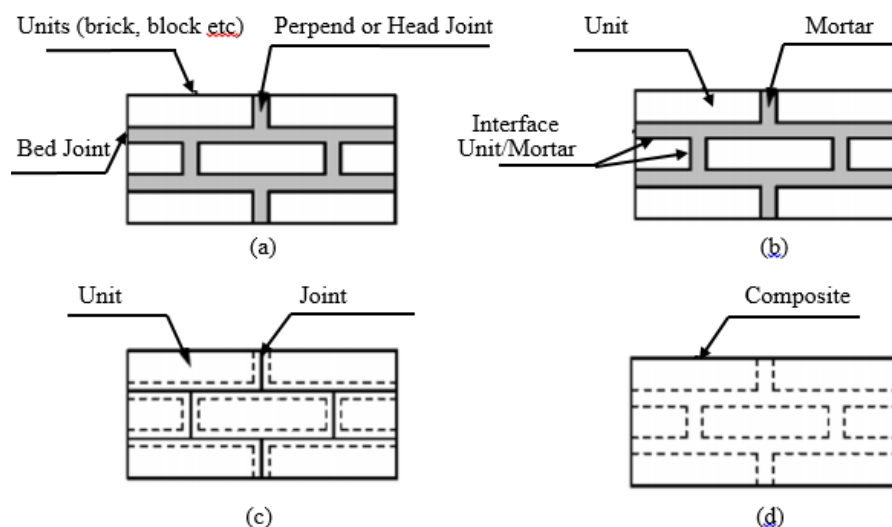


**Fig. 2.** Modeling Techniques for Brick Masonry (a) typical masonry sample, (b) detailed micro modeling, (c) simplified micro-modeling, (d) macro-modeling [22]

## 3. Numerical Modeling of the Heritage Building

The case study structure is load-bearing. Since it is a very large structure, the heterogeneous micro modelling is not possible, therefore, the homogeneous macro modelling is used for Finite Element (FE) modelling of the unreinforced masonry heritage structure. Since the ground and first-floor plans are almost similar, see Figs. 3,4 and the building is almost symmetrical, therefore, only half of the building is considered for numerical analysis. It is also a reasonable approach in order to make a computationally efficient finite element model. All the walls in the structure except the veranda walls are 304.8 mm thick while the veranda walls are 228.6 mm thick. The height of the ground floor is 5.13 m and the height of the first floor is 4.65 m while the height of the first floor of veranda wall is 3.84 m. SAP2000 software is used for analysis in which the homogeneous masonry units are modelled using shell elements because it has good agreement with finite element software and experimental results [23]. The building rests on very firm soil with about 1.5 m deep masonry strip footing. The support condition, therefore, is taken as fixed in the software model. Masonry columns are provided in the buildings. Some are solid and some are hollow from the inside. Hollow columns are not considered in the software design model. The building is having an arched roof supported on iron girders which are resting on masonry walls. Columns and iron girders are modeled using frame elements in the software model. The results obtained will be

generalized for the whole building. Figure 5 shows 3D view of the software model of the structure with co-ordinate axes.

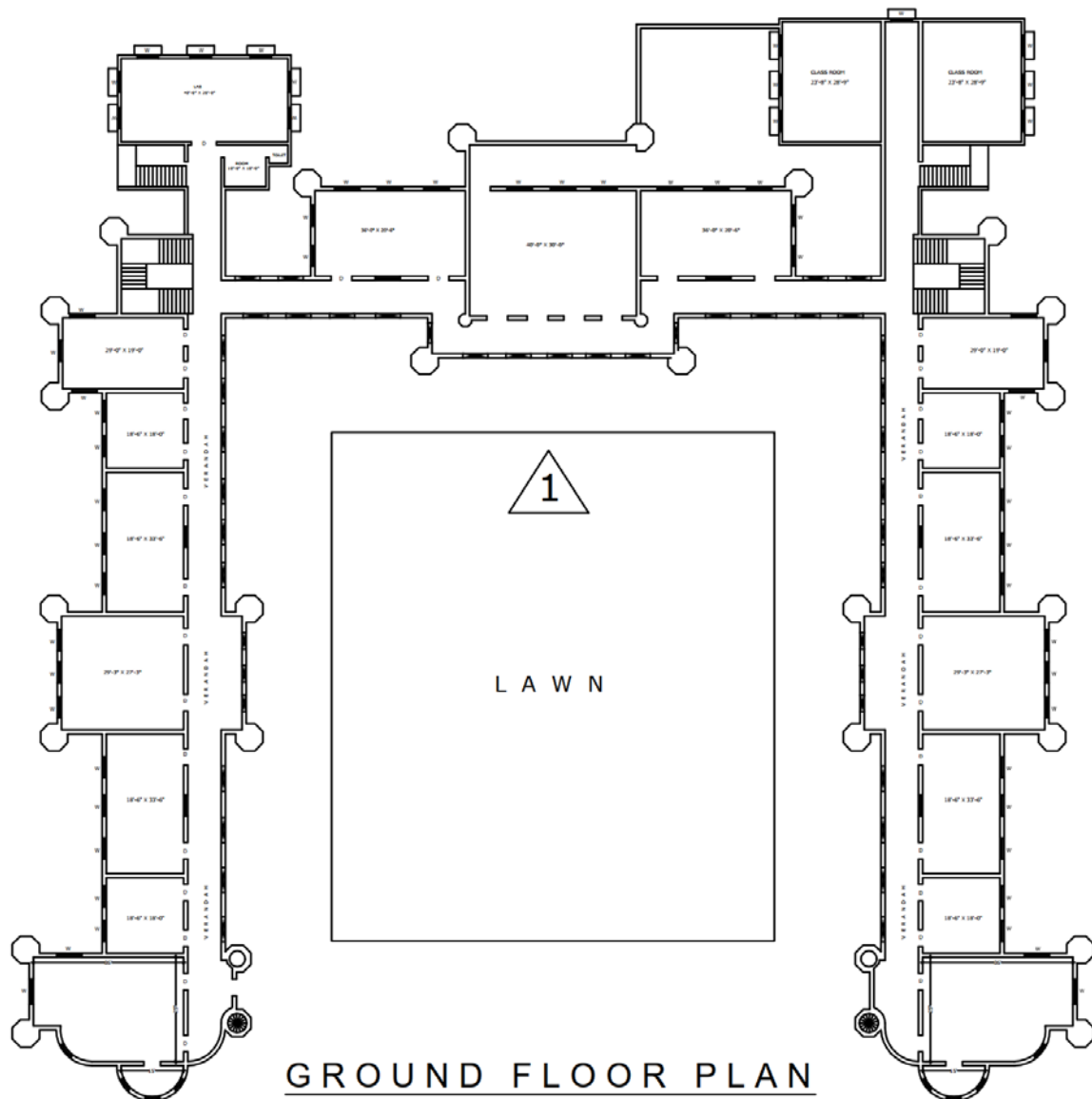
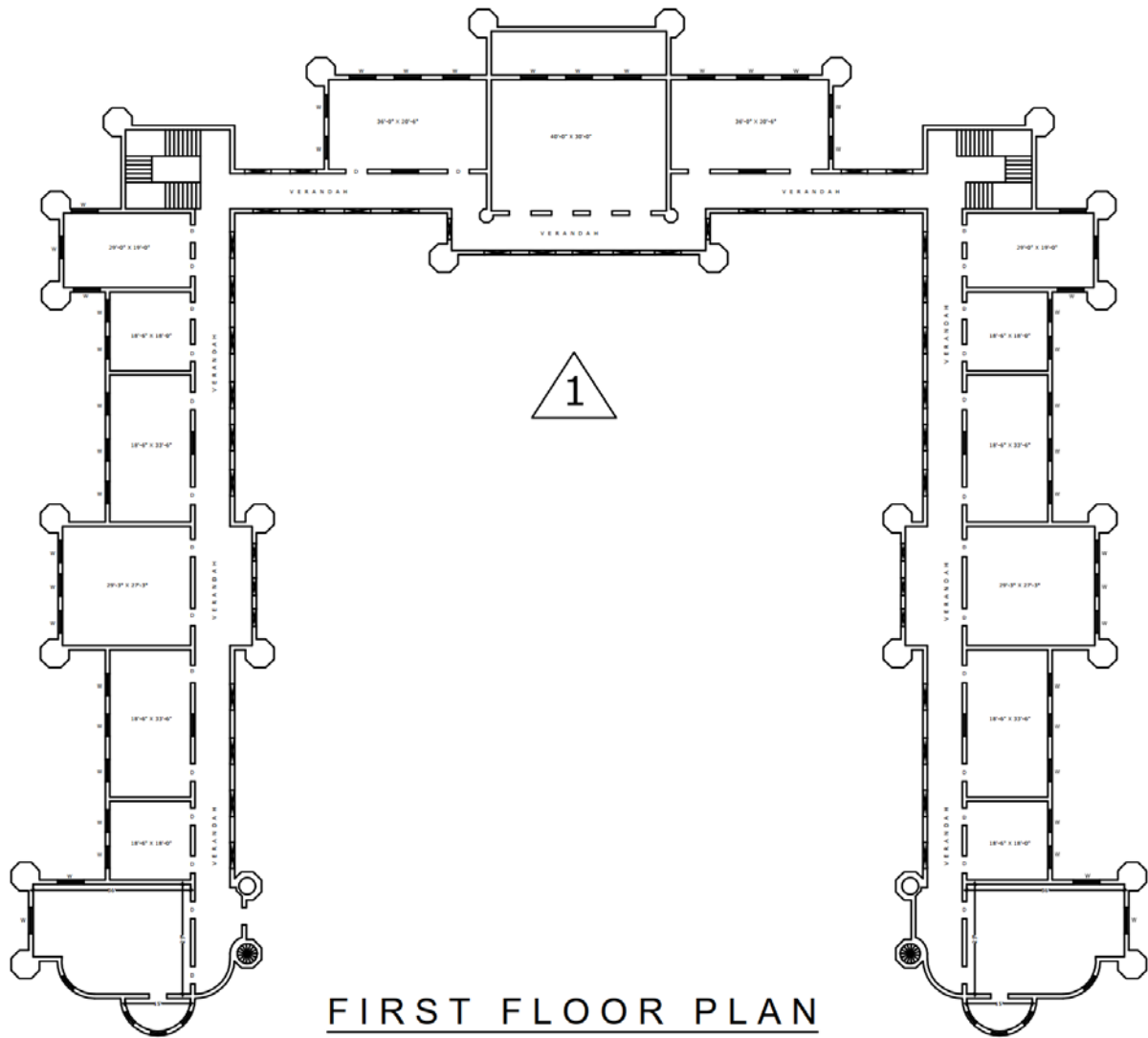


**Fig. 3.** Typical Ground Floor Plan



FIRST FLOOR PLAN

**Fig. 4.** Typical First Floor Plan

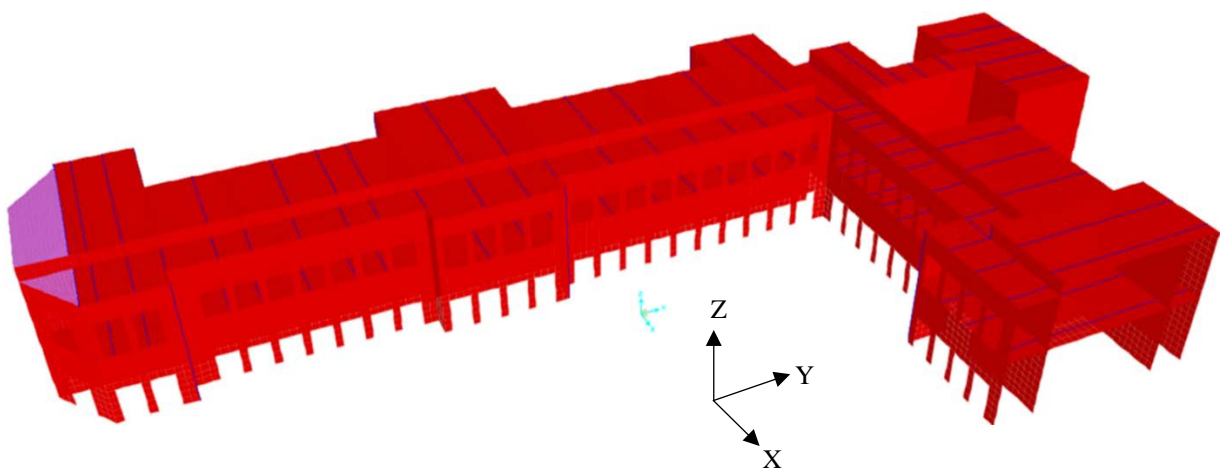


**Fig. 5.** 3D view of the half structure

#### 4. Analysis and Discussion

In order to examine the exact nonlinear behavior of structures, a nonlinear time history analysis has to be carried out. In this method, the ground motion record is applied to the structures in the form of time history. Chamoli earthquake in the form of ground acceleration has a magnitude of 6.5 on the Richter scale and was recorded at an epicentral distance of 8.72 km. Figure 6 shows the recorded time history data of Chamoli Earthquake. This time history follows the provisions given in FEMA P695 [24], therefore it is used as input ground motion for the analysis.

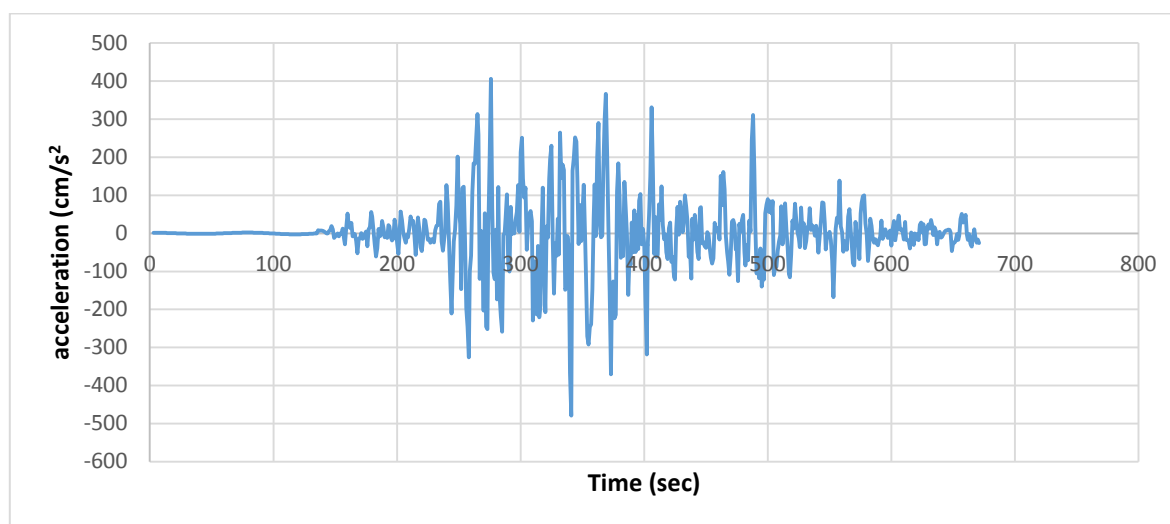


**Fig. 6.** Time history of Chamoli Earthquake

According to FEMA 273 [25], in order to determine the mechanical properties of existing masonry, test prisms shall be extracted from an existing wall and tested in compression, tension, etc. Since the structure in the present study is a heritage institutional building; it was not allowed to extract the prism from there. In absence of the actual data for the existing building, material properties have been taken after studying the literature. The values taken for old unreinforced brick masonry with lime mortar do not show much variation worldwide. According to F. Paris [26], values of compressive strength and modulus of Elasticity for Old brick masonry with lime mortar can be taken as 2.40 - 4.00 MPa and 1200 - 1800 MPa respectively.

The material properties as shown in Table 1 have been taken from recent literature [27] on seismic analysis of a hundred years old unreinforced masonry buildings in Nepal. The building is having much similarities, in age, construction type and material, etc., with the presently studied building. Also, Nepal is located very near so a similarity can be observed in the material, workmanship, techniques, climate, and other structural parameters. So using the same material properties for the present study is justified. With these data, the heritage building is analyzed using SAP2000 software [28].

**Table 1.** Mechanical properties of the materials [27]

Materials	Young's Modulus, $E$ (N/mm <sup>2</sup> )	Poisson Ratio, $\mu$	Mass Density (kN/m <sup>3</sup> )	Compressive Strength (MPa)	Tensile Strength, (MPa)
Brick Masonry	1708	0.15	21	4	0.4

Materials are said to be orthotropic when their properties are different in three mutually perpendicular directions. For the present orthotropic analysis, the values of elastic and shear moduli in three perpendicular directions are taken such that the equivalent of these are nearly equal to isotropic moduli. The values of moduli are given below in Table 2. The values of other required parameters are taken the same as given in Table 1.

Table 2. Material Parameters

Properties of material	Case 1	Case 2	Case 3
$E_x$ (MPa)	1200	800	1000
$E_y$ (MPa)	1000	1200	800
$E_z$ (MPa)	800	1000	1200
$G_x$ (MPa)	500	300	400
$G_y$ (MPa)	400	500	300
$G_z$ (MPa)	300	400	500

Using the above material properties, various modes shapes, and stresses in the structure are obtained from the finite element model.

Natural frequencies and mode shapes of the building have been obtained through modal analysis. The first 3 natural frequencies and corresponding time periods of each case of analysis are given in Table 3. The mode shapes of the case study building are similar for each case. The first three mode shapes are shown in Fig. 7. The natural frequencies decrease and time period increase (Table 3). In each case, the natural frequencies are closely spaced.

Table 3. Natural Frequencies with corresponding time periods

Mode	Isotropic material Case		Orthotropic material case					
	Frequency (Cycles/sec)	Time Period (sec)	Case 1		Case 2		Case 3	
			Frequency (Cycles/sec)	Time Period (sec)	Frequency (Cycles/sec)	Time Period (sec)	Frequency (Cycles/sec)	Time Period (sec)
1	8.35348	0.11971	6.62155	0.15102	6.17824	0.16186	5.92898	0.16866
2	8.75714	0.11419	6.95845	0.14371	6.21843	0.16081	6.23321	0.16043
3	8.87935	0.11262	7.12476	0.14036	6.43689	0.15535	6.37783	0.15679

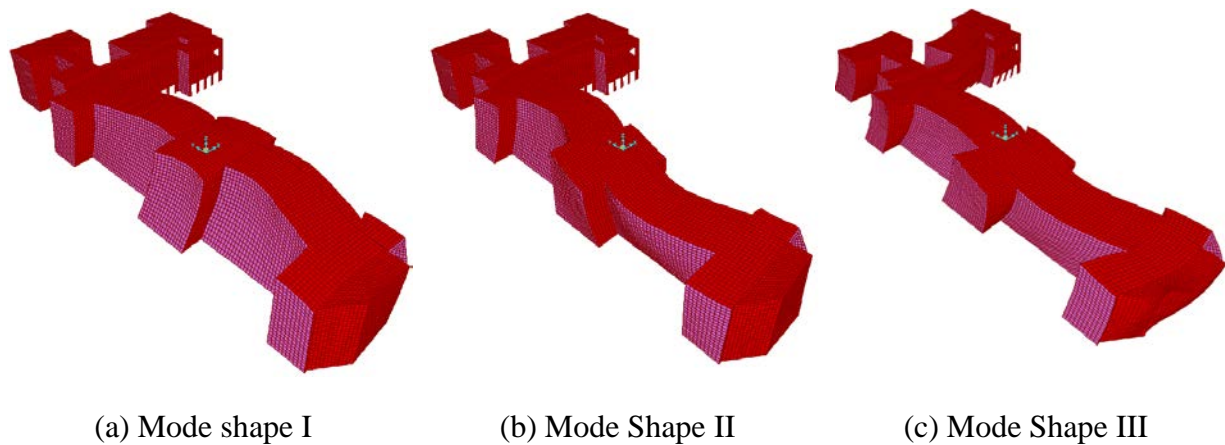


**Fig. 7.** First Three Natural Mode Shape

The time history in the form of ground acceleration is applied in X and Y directions. The direct principal and maximum shear stresses for different parts of the structure are found. The permissible values of the stresses are given in IS-1905 [29]. For the present case, the permissible values of compressive, tensile, and shear stresses can be taken as 1.1 MPa, 0.07 MPa, and 0.25 MPa respectively.

**For Isotropic Material Case.** As shown in Fig. 8, most part of the structure remains under compression within a permissible limit. The maximum values of compressive and tensile stresses are found to be 0.810 MPa and 0.222 MPa respectively. The tensile stresses are exceeded at slab and beam wall junctions. As shown in Fig. 9, the structure is experiencing shear stress within a permissible limit i.e. within 0.25 MPa. The maximum value of shear stress is found to be 0.130 MPa.

As shown in Fig. 10, here also most part of the structure remains under compression within a permissible limit. The maximum values of compressive and tensile stresses are found to be 0.818 MPa and 0.254 MPa respectively. The tensile stress is exceeded at all the joints and roofs. As shown in Fig. 11, the structure is having shear stress within permissible limits. The maximum value of shear stress is found to be 0.132 MPa.

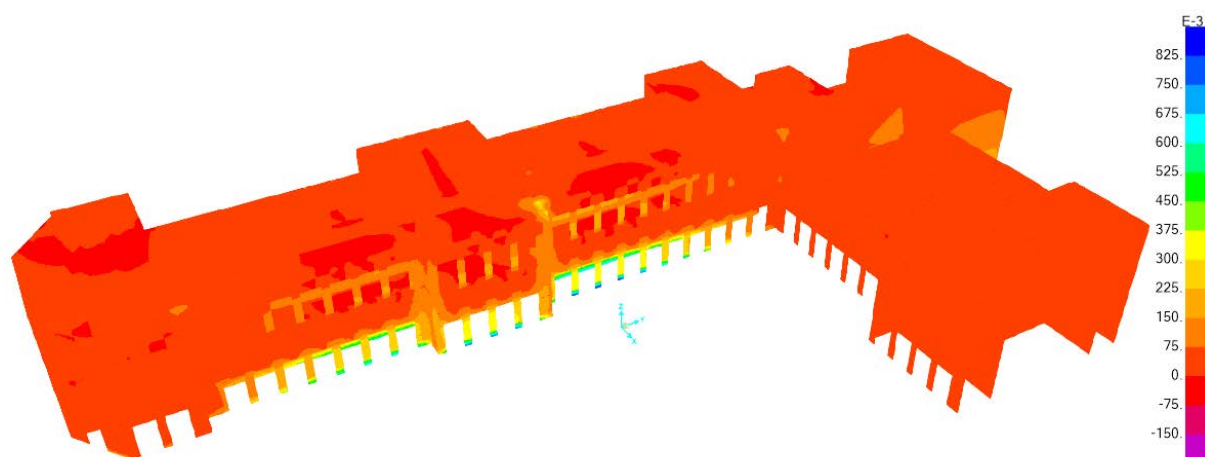


**Fig. 8.** Direct Principle Stress (MPa) due to Earthquake in X direction in isotropic case

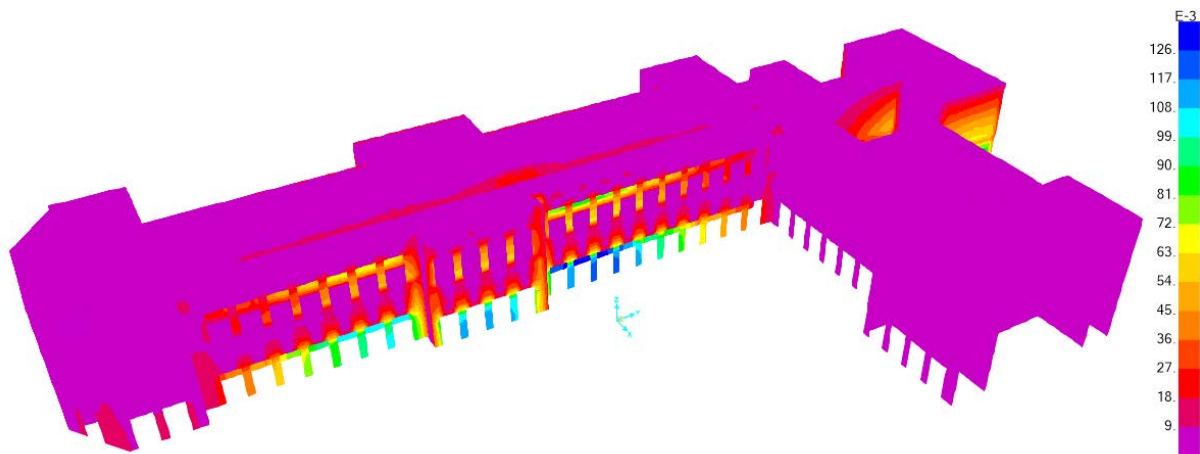


**Fig. 9.** Maximum Shear Stress (MPa) due to Earthquake in X-direction in isotropic case

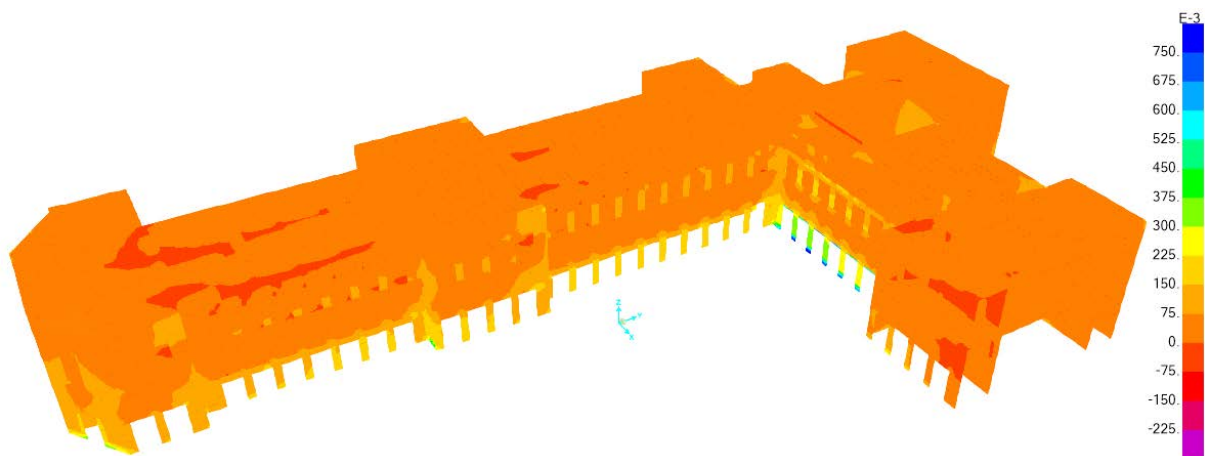


**Fig. 10.** Direct Principle Stress (MPa) due to Earthquake in Y direction in the isotropic case

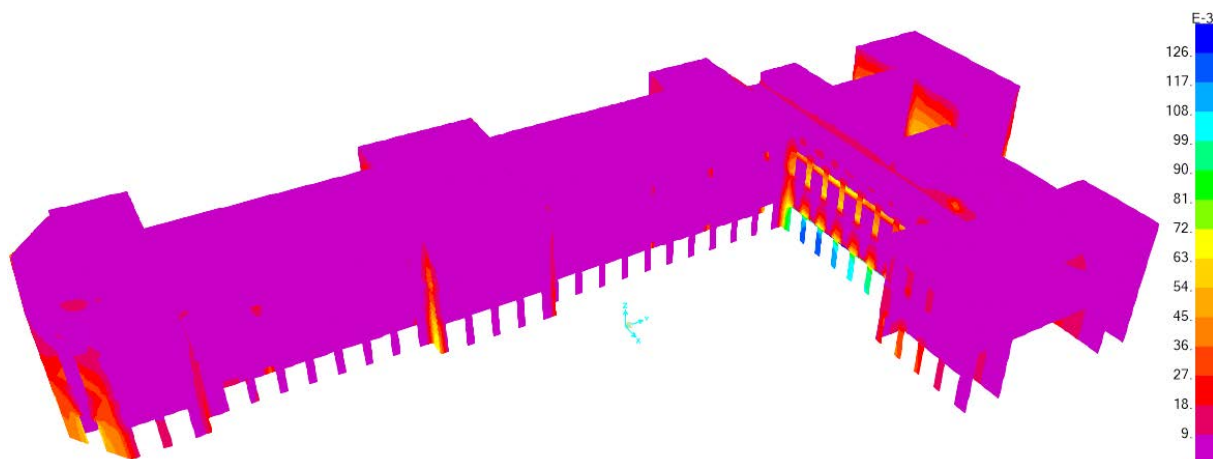


**Fig. 11.** Maximum Shear Stress (MPa) due to Earthquake in Y-direction in the isotropic case

The shear stress contours in the heritage building were found to be the same in all orthotropic cases when compared to the isotropic material case but the maximum values of the shear stresses were found to be different in each case, therefore, only the maximum value of shear stress has been provided in each orthotropic case. On the other hand, the direct

principal stress contours were found to be different from each other with their maximum values, therefore, the figures of direct stress contour results have been provided in each respective case.

**For Orthotropic: Case 1.** As shown in Fig. 12, most part of the structure remains under compression within a permissible limit. The maximum values of compressive and tensile stresses are found to be 0.618 MPa and 0.206 MPa respectively. The tensile stress is exceeded at roof and beam-wall junctions. The shear stress contours were found to be the same as shown in Fig. 9, however, the maximum value of shear stress is found to be 0.099 MPa, which is within a permissible limit, i.e. 0.25 MPa.

As shown in Fig. 13, here also most part of the structure remains under compression within a permissible limit. The maximum values of compressive and tensile stresses are found to be 0.694 MPa and 0.199 MPa respectively. The tensile stress is exceeded at all the joints and roofs. The shear stress contours were found to be the same as shown in Fig. 11, however, the maximum value of shear stress is found to be 0.111 MPa, which is within a permissible limit.

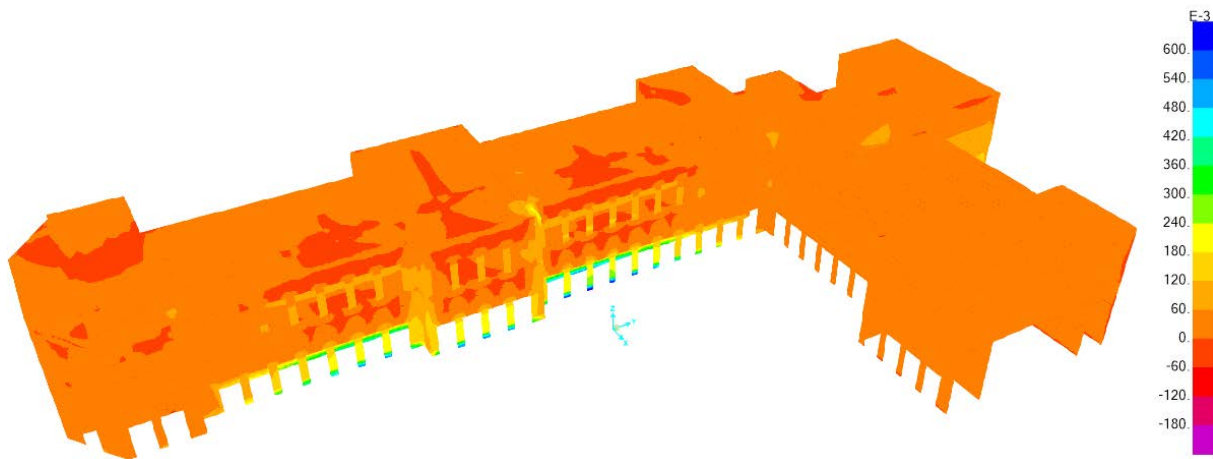


**Fig. 12.** Direct Principle Stress (MPa) due to Earthquake in X direction in orthotropic case I

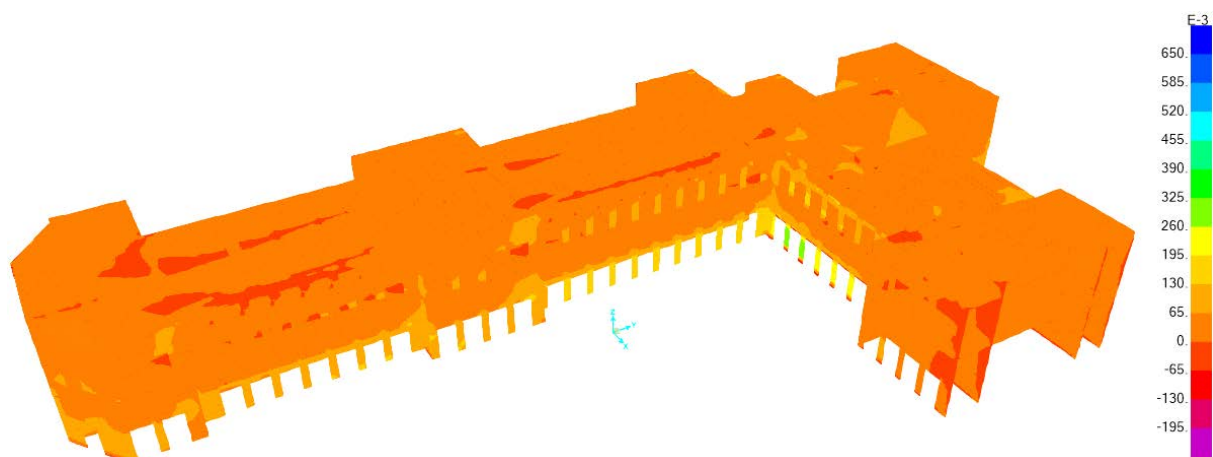


**Fig. 13.** Direct Principle Stress (MPa) due to Earthquake in Y direction in orthotropic case I

**For Orthotropic: Case 2.** As shown in Fig. 14, most part of the structure remains under compression within a permissible limit. The maximum values of compressive and tensile stresses are found to be 0.696 MPa and 0.167 MPa respectively. The tensile stress is exceeded

at the roof and beam-wall junction. The shear stress contours were found to be the same as shown in Fig. 9, however, the maximum value of shear stress is found to be 0.113 MPa, which is within a permissible limit, i.e. 0.25 MPa.

As shown in Fig. 15, here also most part of the structure remains under compression within a permissible limit. The maximum values of compressive and tensile stresses are found to be 0.687 MPa and 0.196 MPa respectively. The tensile stress is exceeded at all the joints and roofs. The shear stress contours were found to be the same as shown in Fig. 11, however, the maximum value of shear stress is found to be 0.120 MPa, which is within a permissible limit.

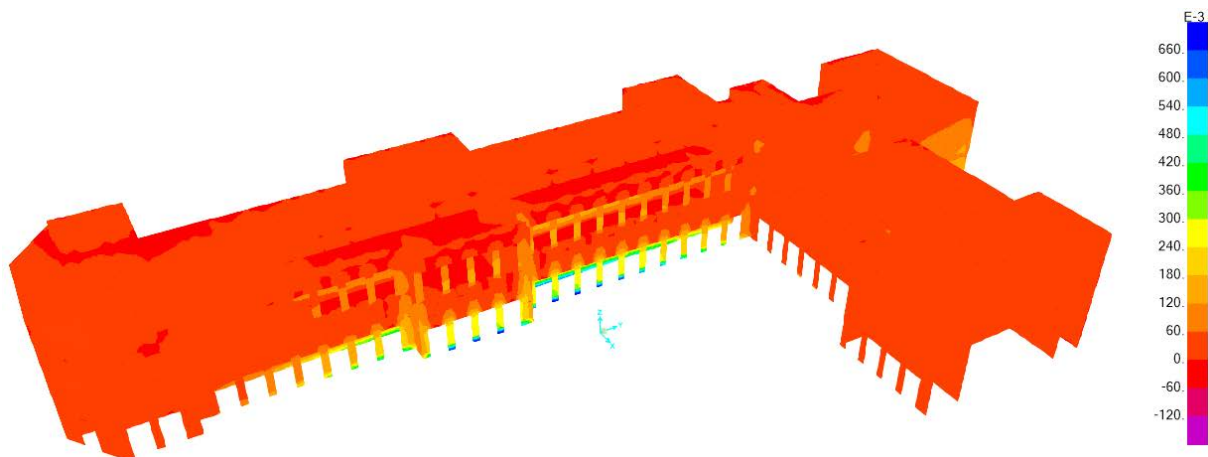


**Fig. 14.** Direct Principle Stress (MPa) due to Earthquake in X direction in orthotropic case II

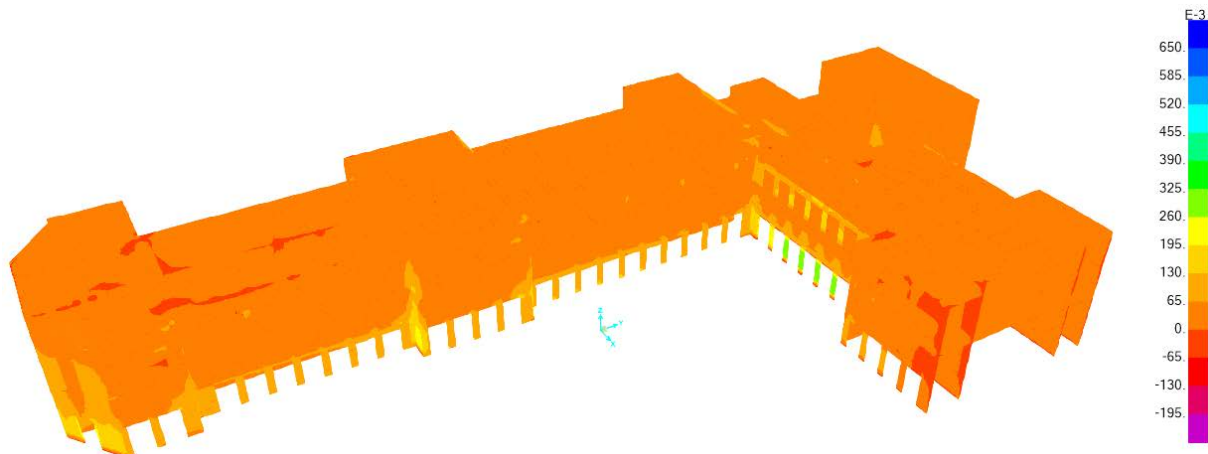


**Fig. 15.** Direct Principle Stress (MPa) due to Earthquake in Y direction in orthotropic case II

**For Orthotropic: Case 3.** As shown in Fig. 16, most part of the structure remains under compression within a permissible limit. The maximum values of compressive and tensile stresses are found to be 0.565 MPa and 0.193 MPa respectively. The tensile stress is exceeded at the roof and beam-wall junction. The shear stress contours were found to be the same as shown in Fig. 9, however, the maximum value of shear stress is found to be 0.091 MPa, which is within a permissible limit, i.e. 0.25 MPa.

As shown in Fig. 17, here also most part of the structure remains under compression within a permissible limit. In a few places, the maximum values of compressive and tensile stresses are found to be 0.605 MPa and 0.175 MPa respectively. The tensile stress is exceeded

at all the joints and roofs. The shear stress contours were found to be the same as shown in Fig. 9, however, the maximum value of shear stress is found to be 0.097 MPa, which is within a permissible limit.

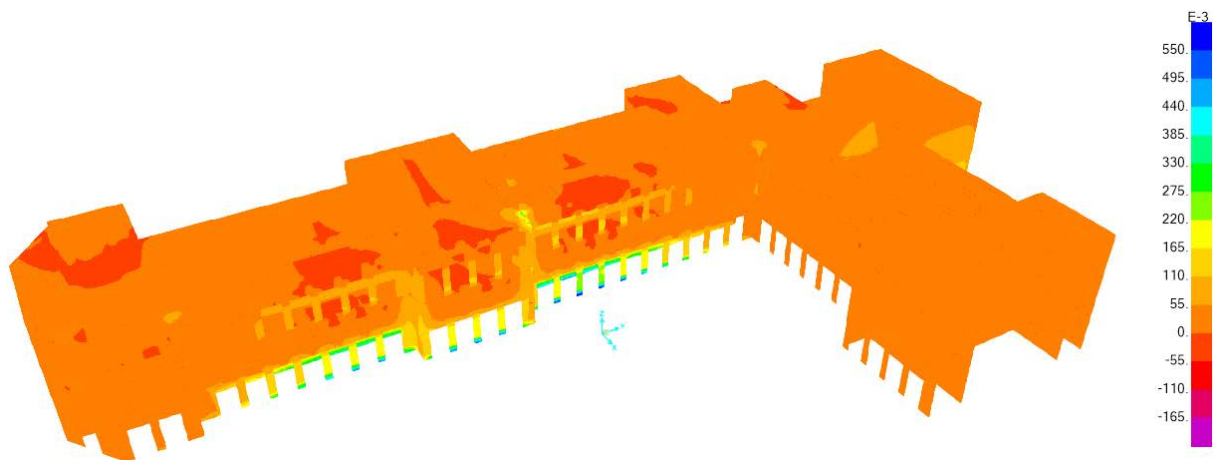


**Fig. 16.** Direct Principle Stress (MPa) due to Earthquake in X direction in orthotropic case III

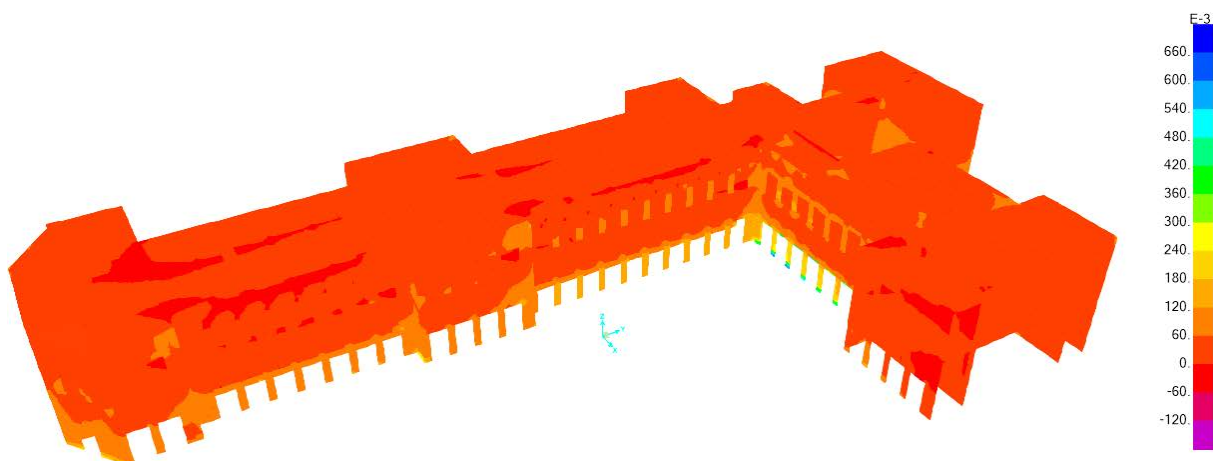


**Fig. 17.** Direct Principle Stress (MPa) due to Earthquake in Y direction in orthotropic case III

**Table 4.** Maximum value of Stresses due to Earthquake in X direction

Type of Stress	Isotropic material Case	Orthotropic material cases		
		Case 1	Case 2	Case 3
Compressive (MPa)	0.810	0.618	0.696	0.565
Tensile (MPa)	0.222	0.206	0.167	0.193
Shear (MPa)	0.130	0.099	0.113	0.091

**Table 5.** Maximum value of Stresses due to Earthquake in Y direction

Type of Stress	Isotropic material Case	Orthotropic material cases		
		Case 1	Case 2	Case 3
Compressive (MPa)	0.818	0.694	0.687	0.605
Tensile (MPa)	0.254	0.199	0.196	0.175
Shear (MPa)	0.132	0.111	0.120	0.097

## 5. Conclusion

The present study shows that the mode shapes of all cases of analysis are found to be similar (Fig. 6) and their corresponding natural frequencies are closely spaced in each material case, see Table 3. But the values of natural frequencies of the isotropic cases have been found higher than all orthotropic cases. In orthotropic cases, the value of natural frequencies of case 1 is found to be higher than case 2, and case 2 values are found to be higher than case 3.

Due to the earthquake in X-direction, see Table 4, the maximum value of compressive, tensile, and shear stresses of the isotropic cases are found to be higher than the values of all orthotropic cases. The maximum value of compressive stress of orthotropic case 2 value is found to be higher than case 1 and case 1 value is found to be higher than the case 3 whereas the maximum value of tensile stress of orthotropic case 1 value is found to be higher than case 3 and case 3 value is found to be higher than the case 1 whereas the maximum value of shear stress of orthotropic case 2 value is found to be higher than case 1 and case 1 value is found to be higher than the case 2.

Due to the earthquake in Y-direction, see Table 5, the maximum value of compressive, tensile, and shear stresses of the isotropic cases are found to be higher than the values of all orthotropic cases. The maximum value of compressive stress of orthotropic case 1 value is found to be higher than case 2, and case 2 value is found to be higher than case 3. Similarly, the maximum value of tensile stress of orthotropic case 1 is found to be higher than case 2, and case 2 value is found to be higher than case 3 whereas the maximum value of shear stress of orthotropic case 2 value is found to be higher than case 1, and case 1 value is found to be higher than case 3.

In all cases of analysis, the tensile stresses are exceeded the permissible limit whereas the compressive and shear stresses are found to be within the permissible limit. The tensile stresses are exceeded mostly at the corners of walls, roof level, and beam-wall junctions. The maximum value of compressive stress in all cases is found to be at the bottom of walls and piers whereas the maximum value of shear stress is found to be at the corners of walls and piers.

The portions around the openings are found highly vulnerable. There is a requirement for retrofitting to overcome the exceeded stresses.

## References

1. Sayin E, Yon B, Calayir Y, Gor M. Construction failures of masonry and adobe buildings during the 2011 Van earthquakes in Turkey. *Structural Engineering and Mechanics*. 2014;51(3): 503-518.
2. Ferreira TM, Vicentea R, Varum H. Seismic vulnerability assessment of masonry facade walls: development, application and validation of a new scoring method. *Structural Engineering and Mechanics*. 2014;50(4): 541-561.
3. Adhikari BR. *Gorkha Earthquake 2015: Cause and Effect*. A CESS NEPAL Publication; 2015.
4. Maio R, Estêvão JM, Ferreira TM, Vicente R. The seismic performance of stone masonry buildings in Faial island and the relevance of implementing effective seismic strengthening policies. *Engineering Structures*. 2017;141: 41-58.
5. Orlando M, Betti M, Spinelli P. Assessment of structural behaviour and seismic retrofitting for an Italian monumental masonry building. *Journal of Building Engineering*. 2020;29: 101115.
6. Altin S, Kuran F, Anil O, Kara ME. Rehabilitation of heavily earthquake damaged masonry building using steel straps. *Structural Engineering and Mechanics*. 2008;30(6): 651-664.
7. Wang Q, Chai Z, Wang L. Seismic capacity of brick masonry walls externally bonded

- GFRP under in-plane loading. *Structural Engineering and Mechanics*. 2014;51(3): 413-431.
8. Ortega J, Vasconcelos G, Rodrigues H, Correia M. Assessment of the influence of horizontal diaphragms on the seismic performance of vernacular buildings. *Bulletin of Earthquake Engineering*. 2018;16(9): 3871-904.
  9. Ahmad S, Khan RA, Gupta H. Seismic performance of a masonry heritage structure. *Int J Eng Adv Technol*. 2014;3(4): 335-340.
  10. Maio R, Ferreira TM, Estêvão JM, Pantò B, Calio I, Vicente R. Seismic performance-based assessment of urban cultural heritage assets through different macro element approaches. *Journal of Building Engineering*. 2020;29: 101083.
  11. Couto R, Bento R, Gomes RC. Seismic performance and fragility curves of historical residential buildings in Lisbon downtown affected by settlements. *Bulletin of Earthquake Engineering*. 2020;18(11): 5281-5307.
  12. Makoond N, Pelà L, Molins C. A Risk Index for the Structural Diagnosis of Masonry Heritage (RISDiMaH). *Construction and Building Materials*. 2021;284: 122433.
  13. Camathias U. *Seismic Performance Evaluation of a Historic Unreinforced Masonry Building Structure*. Master Thesis. Ljubljana, Slovenia: Swiss Federal Institute of Technology, Institute of Structural Engineering, University of Ljubljana; 2013.
  14. Sirajuddin M, Sunil J, Narayanan Sambu Potty. Non Linear seismic analysis of masonry structures. *Journal of Design and Built Environment*. 2012;9(1).
  15. Capozucca R. Shear behaviour of historic masonry made of clay bricks. *The Open Construction & Building Technology Journal*. 2011;5(1): 89-96.
  16. DeJong MJ. *Seismic assessment strategies for masonry structures*. PhD Thesis. USA: Massachusetts Institute of Technology; 2009.
  17. Sarhosis V, Asteris PG, Mohebkah A, Xiao J, Wang T. Three dimensional modelling of ancient colonnade structural systems subjected to harmonic and seismic loading. *Structural Engineering and Mechanics*. 2016;60(4): 633-653.
  18. Parajuli HR, Kiyono J, Taniguchi H, Toki K, Furukawa A, Maskey PN. Parametric study and dynamic analysis of a historical masonry building of Kathmandu. *Disaster Mitigation of Cultural Heritage and Historic Cities*. 2010;4(1): 149-156.
  19. Sharma A, Golubev VI, Khare RK. Seismic Evaluation of Two-Storied Unreinforced Masonry Building with Rigid Diaphragm Using Nonlinear Static Analysis. In: *Smart Modelling for Engineering Systems*. Singapore: Springer; 2021. p.175-187.
  20. Favorskaya A, Golubev V. Study the elastic waves propagation in multistory buildings, taking into account dynamic destruction. In: *Proc. International Conference on Intelligent Decision Technologies*. Singapore: Springer; 2020. p.189-199.
  21. Kamran, Ahmad S, Khan RA. Seismic Performance of a heritage school building. *Procedia engineering*. 2017;173: 1763-1770.
  22. Lourenço PB. Computations on historic masonry structures. *Progress in Structural Engineering and Materials*. 2002;4(3): 301-319.
  23. Kheirollahi M. Equivalent frame model and shell element for modeling of in-plane behavior of Unreinforced Brick Masonry buildings. *Structural Engineering and Mechanics*. 2013;46(2): 213-229.
  24. *Quantification of Building Seismic Performance Factors*. Washington DC: Federal Emergency Management Agency; 2009.
  25. *Guidelines for the seismic rehabilitation of buildings*. Washington DC: Federal Emergency Management Agency; 1997
  26. Parisi F, Augenti N. Experimental data analysis for mechanical modelling of existing brick masonry structures. In: *15 WCEE*. LISBOA; 2012.
  27. Khadka SS. Seismic performance of traditional unreinforced masonry building in Nepal. *Kathmandu University Journal of Science and Technology*. 2013;9(1): 15-28.

28. *SAP2000. Reference Manual. Computers and Structures*. Berkeley: University of Ave; 2015.
29. Standard I. *Code of practice for structural use of unreinforced masonry*. New Delhi: Bureau of Indian Standards: 1987.

## THE AUTHORS

### **Kamran**

e-mail: kmrn890@gmail.com  
ORCID: 0000-0001-6456-3089

### **Shakeel Ahmad**

e-mail: shakeel60in@yahoo.co.in  
ORCID: 0000-0002-9516-3296

### **Rehan A. Khan**

e-mail: rehan\_iitd@rediffmail.com  
ORCID: 0000-0001-6891-9521

# Calculation of the stress level in modeling the inter-dislocation interaction of aluminum bronze

A.Yu. Nikonov<sup>✉</sup>, A.A. Bibko, D.V. Lychagin

Institute of Strength Physics and Materials Science SB RAS, 2/4, pr. Akademicheskii, Tomsk, 634055, Russia

✉ [anickonoff@ispms.ru](mailto:anickonoff@ispms.ru)

**Abstract.** The behavior of a polycrystal during deformation depends on the deformation of its constituent grains, their boundaries, and the degree of interaction. In this case, the deformation of a single grain is determined by its orientation and morphology. An urgent task is to estimate the stress level for individual grains of a polycrystalline aggregate of aluminum bronze. This problem can be solved by molecular dynamics simulation of crystallites with different crystallographic and geometric characteristics. Based on the results of the active plastic deformation simulation, the main types of dislocations are identified and their role in plastic deformation and hardening is determined. It has been established that the orientation of the lateral faces under moderate deformations has little effect on the fraction of dislocations of various types and the stress. A noticeable effect is exerted by the compression axis crystallographic orientation and the sample height.

**Keywords:** aluminum bronze, molecular dynamics method, deformation, stress, dislocation interaction

**Acknowledgements.** This research was funded by the Research Program 20-72-10184 of the Russian Science Foundation for 2020-2023.

**Citation:** Nikonov AYu, Bibko AA, Lychagin DV. Calculation of the stress level in modeling the inter-dislocation interaction of aluminum bronze. *Materials Physics and Mechanics*. 2022;48(3): 443-451. DOI: 10.18149/MPM.4832022\_14.

## 1. Introduction

The density of defects capable of resisting shear determines the hardening of a crystalline material during deformation. These are defects whose motion determines the possibility of plastic deformation itself. Such defects at moderate degrees of deformation include point defects, dislocations, twins, and, under certain conditions, grain boundaries. Active plastic deformation at low and moderate temperatures leads to an increase in the number of dislocations and deformation twins, which, in turn, will resist shear to gliding dislocations. The possibility of shear in an individual slip system will be determined by the shear stress. The magnitude of the stress depends on the Schmid factor and the local stress in the region of the shear system. Accounting for substructural strain hardening is a complex problem. From the results of studying the structure by transmission electron microscopy, the moments of the processes of motion and interaction of dislocations remain unclear. This gap can be filled, in particular, by molecular dynamics simulation. Naturally obtaining the distribution of stresses with a well-chosen potential of the interaction of atoms and setting the boundary conditions, we have the opportunity to study in detail the processes in a small volume of material.

Using atomic simulation, it is possible to track changes in homogeneous nucleation of dislocations in single crystals under uniaxial loadings changes as a function of crystallographic orientation. In copper studies at 10 and 300 K along with the dislocation nucleation factor determined by the conventional Schmid factor (shear stress in the direction of slip), the influence of the stress normal to the slip plane (Schmid and non-Schmid terms) is taken into account [1,2]. Molecular dynamics simulation of the loadings of TiAl alloys in the  $\langle 001 \rangle$  direction at temperatures 10 and 300 K made it possible to determine the dependence of tensile and compressive strength on temperature and the reasons for this effect [3]. The strengthening structural element is stacking-fault tetrahedra (SFT). The modeling of their formation mechanisms and the dependence of the formation on the stacking fault energy and the crystallographic orientation of loading are the subject of works [4,5]. The influence of the stacking fault energy of FCC metal grains with different morphology on stress-strain curves has been studied. The influence of grain morphology on the mechanical characteristics and the relationship between the formation of sessile dislocations and hardening has been established [6]. The nucleation of dislocations, formation of twins, the interaction of dislocations and twins, and the relationship of these processes with the mechanical behavior of FCC metals are studied in the works [7,8].

In the manufacture of products using the 3D surfacing method, a mixed grain structure is formed. One of the characteristic features of which are the formations of large grains elongated in the direction of the surfacing plane. In this regard, the question of the behavior of individual grains with different crystallographic orientations and morphology under loading becomes topical. This will make it possible to predict mechanical properties and obtain products with an optimal grain structure.

Using aluminum bronze as a model material and data on the crystallographic and morphological characteristics of the product obtained by 3D electron-beam surfacing [9], the following problem was posed. Establish for individual grains (single crystals) the influence of the compression axis crystallographic orientation and lateral faces and their morphology on structural changes during deformation and their relation to stress by molecular dynamics simulation.

## 2. Materials and methods

Simulation of plastic deformation by compression of single crystals aluminum bronze (Cu-13at.% Al) was carried out by molecular dynamics. The crystal has the form of a tetragonal prism with dimensions  $30a \times 60a \times 30a$  ( $h/d=2$ ) and  $30a \times 30a \times 30a$  ( $h/d=1$ ) along X, Y, and Z axes ( $a$  is the lattice constant of the aluminum bronze). The deformation was determined by moving at a constant speed of 5 m/s with two rigid 5Å-thick atomic layers in the plane X0Z above and below the sample. The LAMMPS software package and the interparticle potential constructed using the embedded atom method were used for simulating. The equations of motion of atoms were integrated by the Verlet high-speed method. The OVITO [10] program allows consideration of movement and interaction of locations in crystal structures. This is achieved by applications of the program. The common neighbor analysis [11] was used to determine the structural location of each atom and to determine the type of crystal lattice (BCC, FCC, HCP). The dislocation extraction algorithm [12] converted the initial atomistic representation into a linear representation of dislocations and the determination of their Burgers vectors. The analysis made it possible to systematize dislocation complexes that carry out sliding along with Shockley dislocations or are barriers to sliding [13].

### 3 The relationship between the structural changes and the deformation curve

The results of molecular dynamic simulation showed that plastic deformation of single crystals of aluminum bronze is carried out by the generation of Shockley dislocations from the places of stress concentration. Originating at the vertices of the sample, they slip in the octahedral plane through the crystal. In single crystals oriented for sliding along three (orientation of the load axis  $Y - [111]$ ) and four (orientation of the load axis  $Y - [100]$ ) equally loaded planes, it becomes possible to interact with dislocations in adjacent planes. As a result, slip is performed by complex defects consisting of Shockley dislocations and dislocations of other types [13,14]. Areas with a higher dislocation density are formed in these crystals. When simulating, they are observed near the loaded layers. The lateral surfaces of the crystal are set free. The interacting dislocations in the thickenings carry out oscillations. After some time, the dislocation or dislocation complex breaks away from the thickening and goes through the crystal.

Consideration of the deformation of Ni and Cu-13at.% Al single crystals with the compression axis orientation  $[111]$  showed that, regardless of the magnitude of the stacking fault energy (SFE), their stress-strain curves consist of areas of increase and decrease in the values of the acting stress [13]. These curves characterize the process at the micro-level and describe elementary slip events (Fig. 1). The highlighted section of the stress-strain curve can be compared with the processes of changes in the dislocation structure in the simulated volume. The stress reduction section coincides with the sliding of the dislocation complex from one cluster to another dislocation cluster (A in Fig. 1 and Fig. 2a). No displacements are observed in stress-strain curve areas (B in Fig. 1 and Fig. 2b). Shockley partial dislocations take an active part in the formation of dislocation complexes. Thus, the areas of softening on the stress-strain curve are due to relaxation (decrease) of stress because of sliding of dislocations. If the increase in load is not accompanied by sliding, then an increase in stress is observed on the curve.

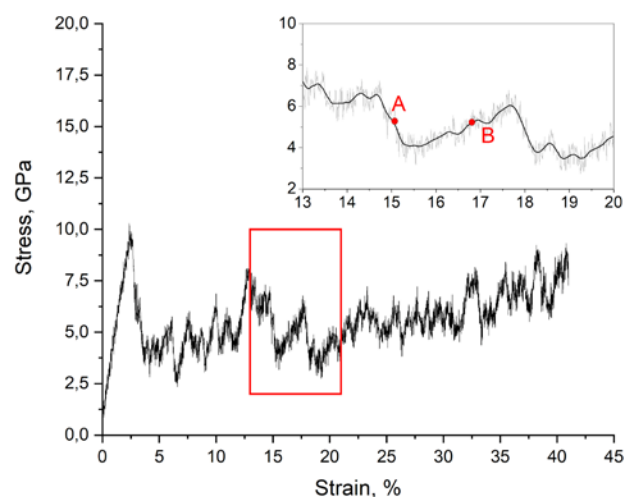


**Fig. 1.** The stress-strain curve of Cu-Al alloy single crystal with a highlighted fragment, that shows areas of hardening and softening

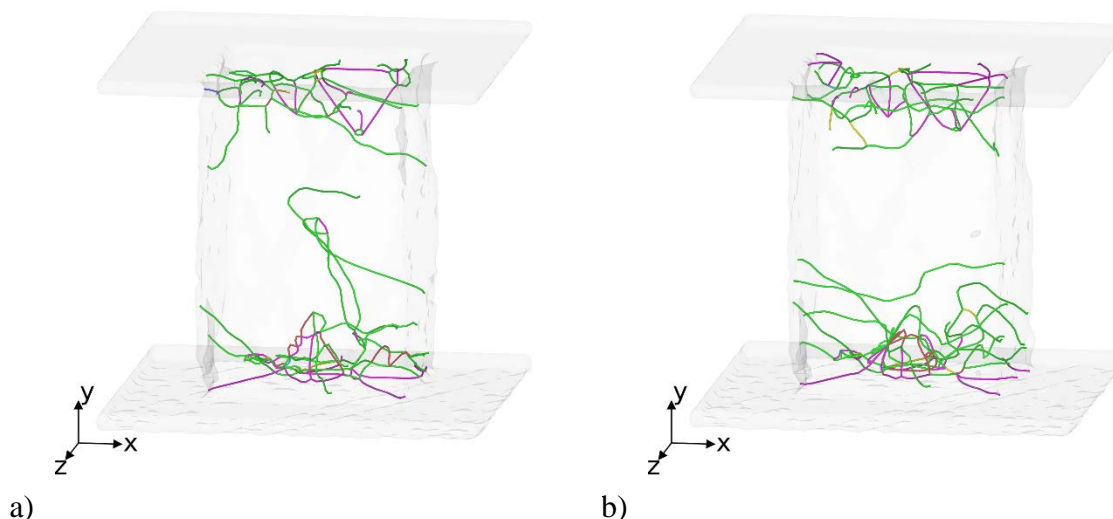


**Fig. 2.** The evolution of the dislocation structure of Cu-Al alloy single crystal at strain: (a) 15%; (b) 16.8%

It can be assumed that the stress level that the dislocation structure withstands under load is related to the strength of dislocation configurations from interacting dislocations. In this case, it speaks of a substructural hardening mechanism. The contribution to the resistance to dislocation motion associated with a dislocation structure without sub boundaries depends on the density of dislocations. The empirical formula gives a proportional relationship with the square root of the average dislocation density for a uniform distribution of dislocations [15]. In the formation of dislocation clusters, the inversely proportional relationship between the stress and the distance between dislocation clusters is usually considered. Nickel has a high SFE, and dislocation clusters are observed in it from the very beginning of plastic deformation. Therefore, the stress level at the second stage of the deformation curves is associated with the distance between these clusters [15]. Alloy Cu-13at.% Al has a low SFE value. The dislocation clusters are formed already at developed deformation during the transition to the third stage of the strain hardening curves. Deformation can also occur by twinning. The tendency to form clusters or deformation by twinning depends on the crystallographic orientation, temperature, and strain rate.

The molecular dynamics method provides a unique opportunity to isolate dislocations of different types and makes it possible to determine the fraction of the length of each of them in the volume of the simulated crystal. The fraction of the length of each type of dislocation and calculated stress depending on the strain is shown in Fig. 3. The most mobiles are complete perfect dislocations  $\frac{a}{2}\langle 110 \rangle$  (blue) and Shockley partial dislocations  $\frac{a}{6}\langle 112 \rangle$  (green). The detailed mechanism of sliding of a complete dislocation in an FCC crystal by splitting into partial ones is considered in [13]. Partial dislocations make up the bulk of dislocations and provide the main deformation of the crystal. Other types of dislocations are observed in the simulated crystal. Stair-rod dislocations  $\frac{a}{6}\langle 110 \rangle$  (magenta), Hirsch  $\frac{a}{3}\langle 001 \rangle$  (yellow), and Frank partial dislocation  $\frac{a}{3}\langle 111 \rangle$  (cyan) are highlighted separately. Dislocations of other types  $\frac{a}{3}\langle 110 \rangle$ ,  $\frac{a}{3}\langle 112 \rangle$ ,  $\frac{a}{6}\langle 013 \rangle$ ,  $\frac{a}{6}\langle 114 \rangle$ , and some others are combined into one group (red). These dislocations form stationary configurations or low-mobility dislocation complexes [14]. Slow dislocation complexes provide sliding simultaneously along two adjacent planes. This option is realized only for the orientations of the deformation axes [100] and [111]. According to the simulation results, upon deformation of single crystals with the [110] compression axis,

dislocations of different slip systems practically do not interact. This orientation has the lowest stress level. The main dislocation type is Stair-rod dislocations.

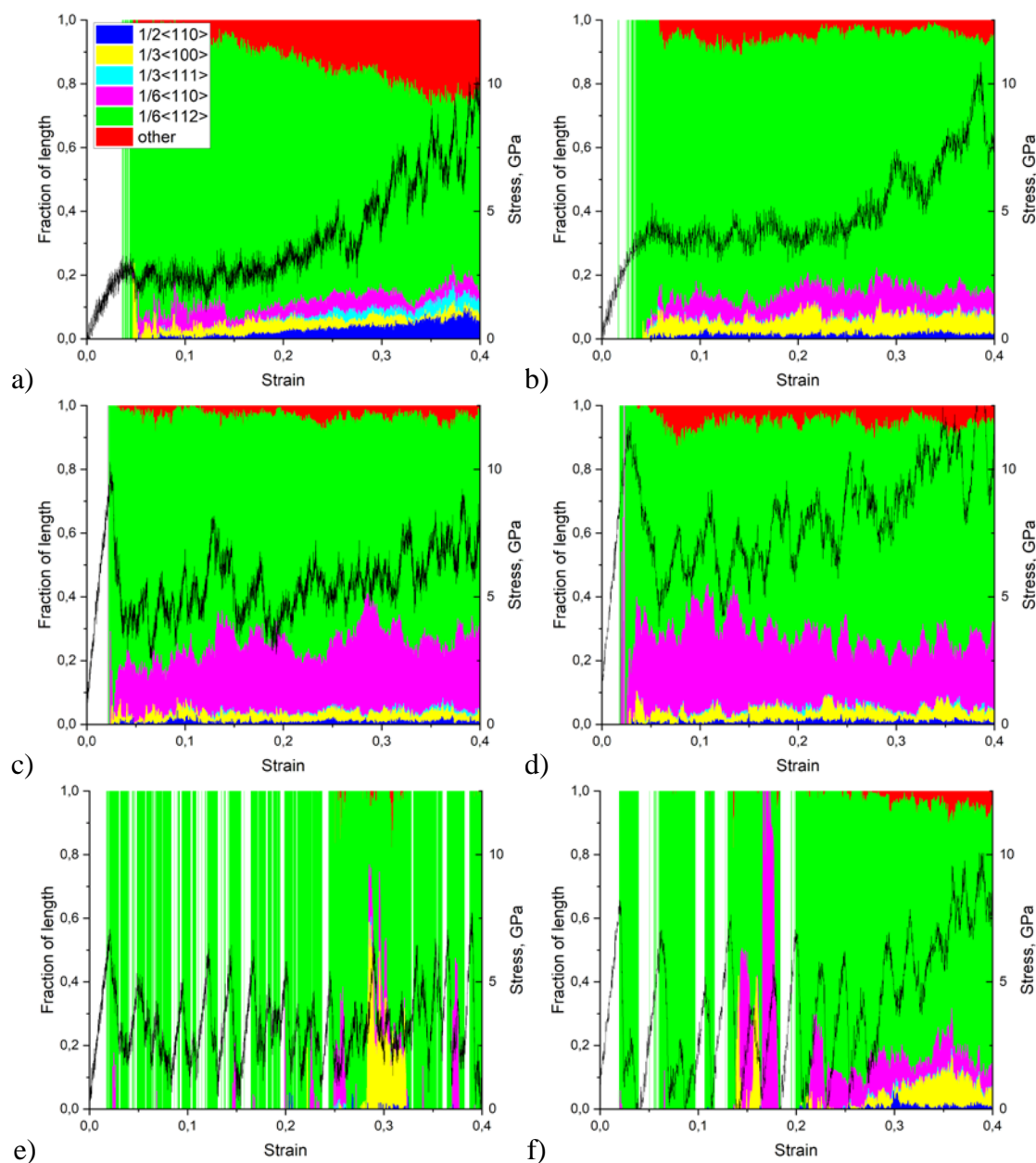


**Fig. 3.** The fraction of the length of each type of dislocation (P) depending on the strain in [100] single crystal with {001} lateral faces (a, b), [111] single crystal with {111}/{112} lateral faces (c, d) and [110] single crystal with {110}/{001} lateral faces (e, f). The black line is the stress-strain curve. Samples with an h/d ratio equal to 2 (a, c, e) and 1 (b, d, f)

The ratio of the share of Stair-rod dislocations to Shockley dislocation differs for materials with different SFE. For [111] nickel single crystals, this ratio is 0.67, and for the Cu-13at.% Al alloy one is 0.25. The ratio of these values is 2.7, which corresponds to the ratio of the operating stress levels of these materials. An analysis of the dislocation structure of these materials showed that a higher SFE favors the formation of tetrahedral complexes from Stair-rod dislocations. These complexes are stable dislocation configurations in a noticeable range of increasing stresses, making it difficult for dislocations to slip. These data show the important role of Stair-rod dislocations in deformation resistance and their contribution to

hardening, as well as tetrahedral complexes from these dislocations. However, the formation of tetrahedral complexes depends on the number of equally loaded slip systems. Their formation is observed for the orientations [100] and [111]. Tetrahedral complexes are not formed when the deformation axis is oriented [110]. The difference in dislocation formation for orientations at the corners of the stereographic triangle causes different stress levels (Fig. 3 a, c, e). The stress comparison is carried out using the approximated average of stress fluctuations for deformation of 0.4. A comparison of the stress values for samples with  $h/d = 2$  gives a value of 7.5 ... 9 GPa for the [100] and [111] orientations, and for the [110] orientation this value is lower and amounts to 5 GPa. An important feature is the lack of hardening for the latter orientation. This corresponds to the case of weak interdislocation interaction. The increased stress is caused not only by the density of the barriers to slip dislocations, but also determined by crystallographic and geometric factors. They determine the initial conditions for shear in a slip system.

Therefore, when considering the influence of the compression axis on the density of the barriers and the stress level, take into account the influence of the crystallographic orientation of the lateral faces and the height of the sample. Changes in these parameters reveal the role of the geometric (morphological) factor in the development of the shift. A comparison of the influence of the crystallographic orientation of the lateral faces was made for the orientations [100] and [110]. [100]-monocrystals are modeled with lateral faces {001} and {110}. For this orientation, 8 shear systems (4 planes, 2 directions in each plane) are equally loaded. As noted in [14], sliding, in this case, is accomplished by complex defects in adjacent planes. The difference in the orientation of the lateral faces has little impact on the fraction of the types of dislocations formed. This seems to be associated with a slightly higher stress value for [100]-single-crystal lateral faces: {001} – 9 GPa and {110} – 7.5 GPa. The general development patterns of the dislocation structure in both single crystals are identical. In [110]-monocrystals were examined with two sets of lateral faces: {110}/{001} and {111}/{112}. In both cases, there is a weak interaction of gliding dislocations and a change in the local stress near the same average level of 5 GPa. A short-term increase in stress is associated with the formation of Stair-rods or Hirsch dislocations, and a decrease with their disappearance.

One of the parameters describing grain morphology is their shape. It can be described by the shape factor, which characterizes the degree of deviation of the shape from the equiaxial one. Three main axes of the ellipse inscribed in the grain can be taken as the shape parameters. In axially symmetric form, the degree of inequality is described by the ratio of the longest axis of the ellipse to the shortest axis. As a variable parameter when simulating single crystals in the form of the tetragonal prism, we took the ratio of the sample height to its width. We used the ratios of these parameters equal to two and one. In these cases, we also have a difference in the scheme of principal stresses in such samples in the presence of end face friction. The geometric position of the main stress concentrators, which are the tops of the sample and the end face ribs, changes as well. Their position relative to the deformed volume for single crystals with different  $h/d$  ratios will differ. Reducing the height of the sample increases the probability of interaction between dislocations of different slip systems. This is reflected in the simulation results. If we compare orientations with different ratios of specimen height to width (Fig. 3), then the following conclusions can be drawn:

1. The strain stress of a single crystal with  $h/d = 1$  is equal to or slightly higher than in single crystals with  $h/d = 2$ .
2. A change in the sample height leads to a redistribution of the fraction of low-mobility dislocations, which play the role of barriers to the development of shear.

In fact, by reducing the height of the sample at a constant width, we increase the volume fraction of stress concentrators, activate a large volume fraction of dislocation sources, and, therefore, increase the rate of accumulation of dislocations per unit volume, the probability of

interaction of dislocations and the formation of low-mobility dislocations that prevent slip. As a result, the formed dislocation structure provides a higher level of stress. This effect illustrates a somewhat different understanding of the action of the Hall-Petch equation. In this case, it is not the limitation of the path of dislocations by grain boundaries that are taken as a basis, but a higher probability of barrier-breaking by dislocations inside the grain. Although, technically, as the height of the sample decreases, the average grain size decreases.

In addition, for a more complete analysis of the influence of the shear geometry on the stress level, it is important to consider the orientation of the shear directions and planes relative to the lateral faces. For the loading scheme between two punches with free lateral faces, the shear planes are in different conditions. In the deformed volume, depending on the crystallographic orientation of the faces, one can distinguish a volume in which there are no reverse stresses from the opposite punch and the shift is freely carried out towards the free surfaces [6-8]. The deformation is higher in this area. The presence of these areas somewhat reduces the amount of stress required for deformation. This causes a lower stress in [100] single crystals ( $h/d=2$ ) with {110} lateral faces as compared to {001}. Dislocations in this volume reach the surface more easily without accumulating in the crystal. If the shear planes are limited by the punches of the testing machine, then thickening of dislocations occurs near them. We also note that as the height of the sample decreases, the rate of accumulation increases.

#### 4 Conclusion

The results of simulating single crystals of aluminum bronze made it possible to establish a relationship between dislocations of a certain type, dislocation complexes, their mobility, and deformation curves. The fraction of the main types of dislocations, which determines the magnitude of the stress, has been identified. The leading role in shear resistance, in the formation of mobile and stable dislocation complexes (tetrahedral), belongs to Stair-rod dislocations. It is shown that the decrease in stress is associated with the process of dislocation slip. The rise in stress corresponds to the period of no-slip, and the hardening value is determined by the dislocation interactions.

The influence of crystallographic and geometric (morphological) factors on the type of dislocations and their role in strengthening is considered. The shear in adjacent slip planes is realized by complex defects, and it is observed for the [100] and [111] orientations. For all orientations, there is a connection between the formation of the Stair-rod and other sedentary dislocations and the level of the acting stress. The orientation of the lateral faces has little effect on the formation of dislocations and stress. The main influence is exerted by the geometric arrangement of the planes relative to the base stress concentrators and lateral faces, as well as the volume fraction of the stress concentrators. These changes are manifested largely with a decrease in the height of the sample compared to the orientation of the lateral faces.

The simulation results make it possible to establish the texture and morphological parameters of the grain structure, which provide the greatest value of substructural hardening. The grain orientation relative to the applied load should be grouped near the  $\langle 100 \rangle$  and  $\langle 111 \rangle$  poles. The shape of the grains should be closer to the equiaxed. The increase in the Hall-Petch contribution is achieved by reducing the grain size. These results can be extended to FCC materials and used as criteria for obtaining the optimal structure of products.

#### References

1. Tschopp MA, Spearot DE, McDowell DL. Atomistic simulations of homogeneous dislocation nucleation in single crystal copper. *Modelling and Simulation in Materials Science and Engineering*. 2007;15(7): 693-709.
2. Tschopp MA, McDowell DL. Influence of single crystal orientation on homogeneous dislocation nucleation under uniaxial loading. *Journal of the Mechanics and Physics of Solids*. 2008;56(5): 1806-1830.
3. Arifin R, Astuti F, Baqiya MA, Winardi Y, Wicaksono YA, Darminto, et al. Structural Change of TiAl Alloy under Uniaxial Tension and Compression in the  $\langle 001 \rangle$  Direction: A Molecular Dynamics Study. *Metals*. 2021;11(11): 1760.
4. Kumar Panda A, Divakar R, Singh A, Thirumurugesan R, Parameswaran P. Molecular dynamics studies on formation of stacking fault tetrahedra in FCC metals. *Computational Materials Science*. 2021;186: 110017.
5. Liang Q, Weng S, Fu T, Hu S, Peng X. Dislocation reaction-based formation mechanism of stacking fault tetrahedra in FCC high-entropy alloy. *Materials Chemistry and Physics*. 2022;282: 125997.
6. Yuan L, Jing P, Shivpuri R, Xu C, Xu Z, Shan D, et al. Atomistic simulation of the stacking fault energy and grain shape on strain hardening behaviours of FCC nanocrystalline metals. *Philosophical Magazine*. 2019;99(22): 2818-2840.
7. Mianroodi JR, Svendsen B. Effect of twin boundary motion and dislocation-twin interaction on mechanical behavior in Fcc metals. *Materials*. 2020;13(10): 1-12.
8. Rohith P, Sainath G, Goyal S, Nagesha A, Srinivasan VS. Role of axial twin boundaries on deformation mechanisms in Cu nanopillars. *Philosophical Magazine*. 2020;100(5): 529-550.
9. Khoroshko E, Filippov A, Tarasov S, Shamarin N, Moskvichev E, Fortuna S, et al. Strength and Ductility Improvement through Thermomechanical Treatment of Wire-Feed Electron Beam Additive Manufactured Low Stacking Fault Energy (SFE) Aluminum Bronze. *Metals*. 2020;10(12): 1568.
10. Stukowski A. Visualization and analysis of atomistic simulation data with OVITO—the Open Visualization Tool. *Modelling and Simulation in Materials Science and Engineering*. 2010;18(1): 015012.
11. Honeycutt JD, Andersen HC. Molecular dynamics study of melting and freezing of small Lennard-Jones clusters. *Journal of Physical Chemistry*. 1987;91(19): 4950-4963.
12. Stukowski A, Bulatov VV, Arsenlis A. Automated identification and indexing of dislocations in crystal interfaces. *Modelling and Simulation in Materials Science and Engineering*. 2012;20(8): 085007.
13. Nikonov AY, Dmitriev AI, Lychagin DV, Lychagina LL, Bibko AA, Novitskaya OS. Numerical Study and Experimental Validation of Deformation of  $\langle 111 \rangle$  FCC CuAl Single Crystal Obtained by Additive Manufacturing. *Metals*. 2021;11(4): 582.
14. Lychagin D, Dmitriev A, Nikonov A, Alfyorova E. Crystallographic and Geometric Factors in the Shear Development in  $\langle 001 \rangle$  FCC Single Crystals: Molecular Dynamics Simulation and Experimental Study. *Crystals*. 2020;10(8): 666.
15. Kozlov E, Koneva N. Nature of hardening of metallic materials. *Russian Physics Journal*. 2002;1: 1-23.

## THE AUTHORS

**Nikonov A.Yu.**

e-mail: anickonoff@ispms.ru

ORCID: 0000-0002-0980-0317

**Bibko A.A.**

e-mail: [bibko.geology@gmail.com](mailto:bibko.geology@gmail.com)

ORCID: 0000-0003-1155-0078

**Lychagin D.V.**

e-mail: [lychagindv@mail.ru](mailto:lychagindv@mail.ru)

ORCID: 0000-0002-0544-9371

# Influence of Ni-Al interphase boundary orientation on the interdiffusion rate at temperatures above aluminum melting point: a molecular dynamics study

G.M. Poletaev<sup>1</sup>✉, R.Y. Rakitin<sup>2</sup>

<sup>1</sup>Altai State Technical University, Lenin Str. 46, 656038 Barnaul, Russia

<sup>2</sup>Altai State University, Lenin Str. 61, 656049 Barnaul, Russia

✉ [gmpoletaev@mail.ru](mailto:gmpoletaev@mail.ru)

**Abstract.** The influence of the orientation of Ni-Al interphase boundary relative to the nickel crystal lattice on the intensity of interdiffusion at temperatures above the melting temperature of aluminum was studied by the method of molecular dynamics. It was observed that the boundary between the crystalline and liquid phases was, in fact, shifted by two or three atomic planes into the aluminum phase – a thin layer of aluminum near the boundary retained a crystalline structure that repeated the nickel lattice. As the temperature increased, the thickness of the Al crystalline layer near the boundary decreased. The concentration curves were obtained after modeling interdiffusion at various temperatures for (111) and (001) orientations of the interphase boundary with respect to the Ni lattice. The parts of the curves responsible for the diffusion of Al atoms into crystalline Ni turned out to be similar for both orientations. However, the more sloping parts related to the diffusion of Ni atoms into liquid Al differed: diffusion of Ni atoms into Al proceeded more intensively at the (111) boundary orientation and slower at orientation (001).

**Keywords:** molecular dynamics, diffusion, interphase boundary, nickel, aluminum

**Acknowledgements.** No external funding was received for this study.

**Citation:** Poletaev GM, Rakitin RY. Influence of Ni-Al interphase boundary orientation on the interdiffusion rate at temperatures above aluminum melting point: a molecular dynamics study *Materials Physics and Mechanics*. 2022;48(3): 452-458. DOI: 10.18149/MPM.4832022\_15.

## 1. Introduction

Intermetallic compounds of Ni-Al system and alloys based on them, due to the combination of properties such as low density, high yield strength at elevated temperatures, good resistance to oxidation and corrosion, have a high potential for their use as high-temperature structural materials [1-4]. The technology for producing intermetallic compounds and alloys is based on diffusion, the process of which in such systems is complex and multifactorial. In the diffusion zone at the interface of two metals, for example, in the process of combustion synthesis, both solid ordered and disordered phases can be present simultaneously, as well as liquid mixtures with different content of components [5-7]. Knowledge of diffusion kinetics, characteristics, and mechanisms of diffusion in metal systems, in particular in the Ni-Al system, is necessary for a more detailed understanding of the processes occurring at high-

temperature synthesis and is also of great importance for the entire field of research and creation of intermetallic compounds and binary alloys.

In previous works [8, 9], we studied the self-diffusion of individual Ni, Ti, and Al atoms in liquid alloys of Ni-Al and Ti-Al two-component systems. Ordered and disordered alloys with compositions  $A_{75}B_{25}$ ,  $A_{50}B_{50}$ , and  $A_{25}B_{75}$  (A and B are alloy components), as well as pure metals, were considered. In particular, the characteristics of self-diffusion were obtained for the considered systems: the diffusion activation energy and the pre-exponential factor in the corresponding Arrhenius equation.

This work is devoted to the molecular-dynamics study of the influence of the orientation of the interfacial boundary relative to the crystal lattice of Ni on the rate of interdiffusion in the solid-liquid phase contact of Ni and Al, i.e. at temperatures above the melting point of Al, but below the melting point of Ni.

## 2. Description of the model

EAM potentials from [10] were used to describe interatomic interactions in Ni-Al system in the molecular dynamics model. These potentials were obtained in [10] on the basis of comparison with both experimental and first-principle data on various properties and structures of pure metals and intermetallic compounds NiAl and  $Ni_3Al$ . They have proven themselves in various studies and have been successfully tested in a wide range of mechanical and structural-energy properties of the alloys of the systems under consideration [9-11].

The computational cells contained about 90 thousand atoms and had the form of rectangular parallelepipeds (Fig. 1). The interphase boundary was created at the center of the computational cell along the yz-plane. Along the y and z axes, an infinite repetition of the cell was simulated, that is, periodic boundary conditions were imposed. In this case, the dimensions along these axes were selected in such a way that they were multiple, with the minimum possible deviation, of the repetition periods of both Ni and Al crystal lattices (initially, aluminum was created in a crystalline state). The unequal thermal expansion of metals for each specific temperature at which the simulation was carried out was also taken into account. Rigid conditions were imposed along the x-axis: the atoms at the left and right ends of the computational cell (colored in gray in Fig. 1) remained immobile during the computer experiment.

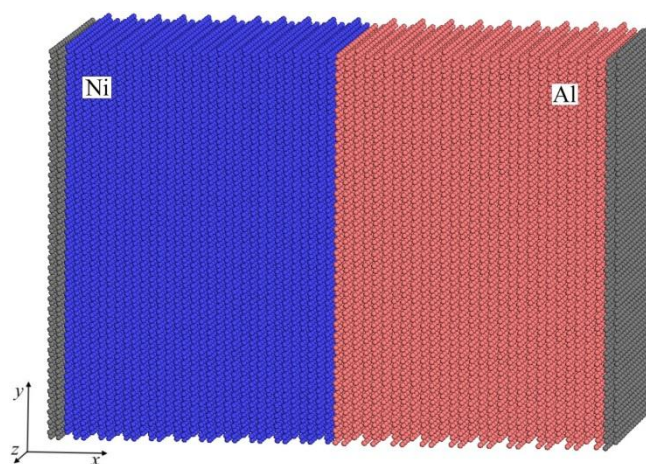


**Fig. 1.** Computational cell for simulating interdiffusion at the Ni-Al boundary before setting the temperature (gray atoms at the ends of the cell remained immobile during the simulation)

Both metals were initially created in the crystalline state. In this work, a solid-liquid phase contact was considered, that is, aluminum was in a liquid state during the simulation and its initial orientation did not matter. Nevertheless, to confirm this and refine the results,

we considered four initial orientations of the interphase boundary relative to the fcc crystal lattices of Ni and Al: 1) (111):(111), 2) (111):(001), 3) (001):(001), 4) (001):(111). The (111) plane is the most densely packed - its filling density with atoms (if their radius is taken equal to half the distance to the nearest neighbors in an ideal crystal) is 90.7%. The filling density of the (001) plane is 78.6%.

The temperature in the model was set through the initial velocities of atoms according to the Maxwell distribution. To keep the temperature constant during the simulation, a Nose-Hoover thermostat was used. The time integration step in the molecular dynamics method was 2 fs [12-14]. The potentials used, among other things, describe well the melting points of Ni and Al: 1710 and 990 K in our model respectively (reference values: 1726 and 933 K). The temperature varied in the range from 1200 K to 1800 K. The melting of aluminum in the model occurred much faster than interdiffusion, in a few picoseconds. Simulation of interdiffusion was carried out for several hundred picoseconds.

### 3. Results and discussion

After the melting of aluminum, a part of it near the interphase boundary remained in the crystalline state, repeating the nickel lattice. That is, the interface between the solid and liquid phases actually moved two or three atomic planes deep into the aluminum. Figure 2 shows examples of this phenomenon. This is explained by the fact that the Ni-Al bond is much stronger than the Al-Al bond [10], and therefore, in particular, the melting temperatures of intermetallic compounds of the Ni-Al system significantly exceed the melting temperature of aluminum [1,2]. Therefore, for the destruction of Ni-Al bonds at the interphase boundary, the considered temperatures are not enough. Because of this, the detachment of Ni atoms and their entrainment into liquid aluminum at the initial stage of the computer experiment, obviously, becomes more complicated and does not occur as quickly as it would be in direct contact of nickel with the liquid phase. Subsequently, despite the mixing of the components and blurring of the boundary, this effect persisted (Fig. 3), but became less noticeable with increasing temperature.

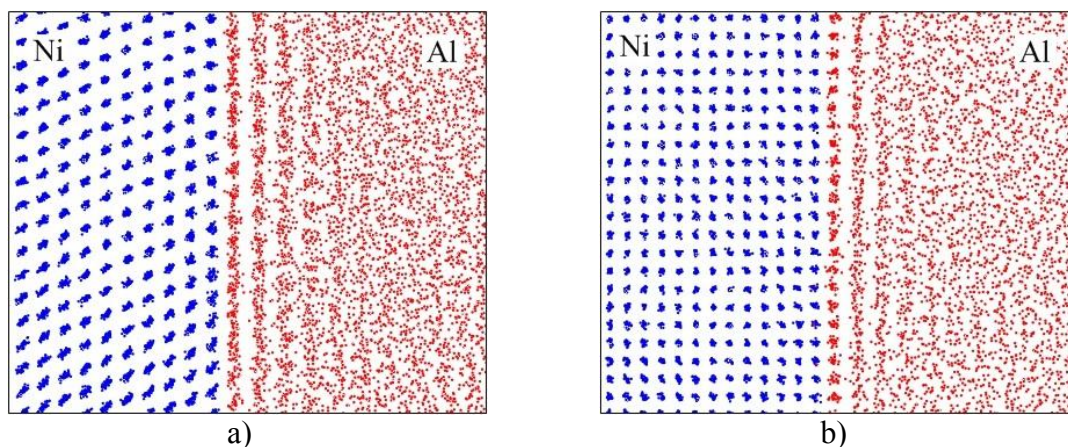


**Fig. 2.** Formation of a crystal structure in Al near the interphase boundary at a temperature above the melting point of aluminum (1300 K): a) (111) orientation; b) (001) orientation

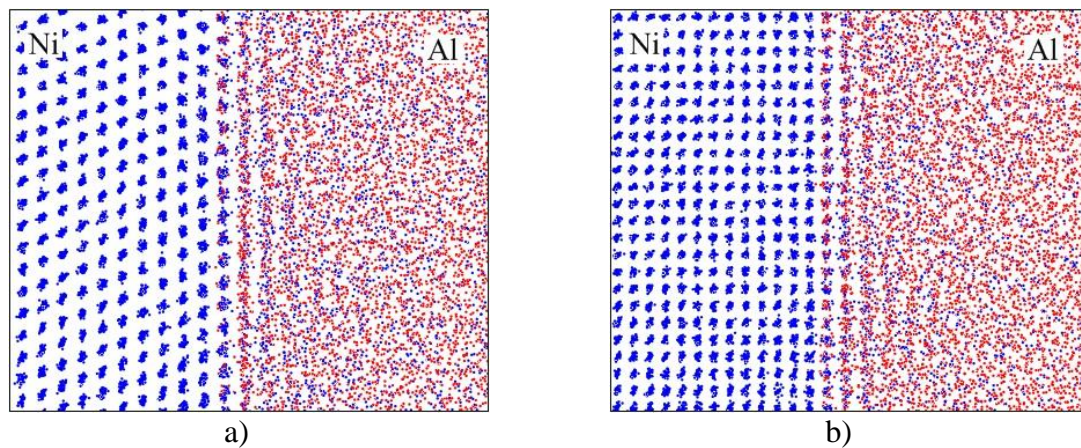


**Fig. 3.** Distribution of atoms in computational cells after simulation for 500 ps at a temperature of 1400 K: a) (111) orientation; b) (001) orientation

Despite the phenomenon described above, the mutual diffusion at the Ni-Al interface during solid-liquid contact was intense enough to be modeled using the molecular dynamics method. A significant predominance of the diffusion of Ni atoms deep into liquid Al was observed compared to the diffusion of Al atoms into crystalline Ni (Fig. 3), which is explained, first of all, by the difference in the aggregate states of Ni and Al.

Figure 4 shows the concentration curves obtained at temperatures of 1400 and 1600 K after simulation for 500 and 300 ps, respectively, for the four interphase boundary orientations considered. The curves were plotted by analyzing the concentration of Ni atoms in a layer 5 Å thick when this layer was displaced by 1 Å along the x-axis. The obtained concentration curves are qualitatively similar to those obtained experimentally for this system [6,7].

The relatively steep left part is the diffusion of Al atoms deep into the Ni crystal lattice. Obviously, it proceeds much more slowly than the diffusion of Ni atoms into liquid Al (the right, more sloping part on the concentration curves). In connection with the above-described phenomenon of the preservation of the crystal structure in the aluminum phase in a small layer near the interface, the concentration curves at a temperature of 1400 K show a change from the steep to the sloping part at concentrations well below 50% (Fig. 4a). However, as the temperature increased, this boundary shifted and approached 50% (Fig. 4b).

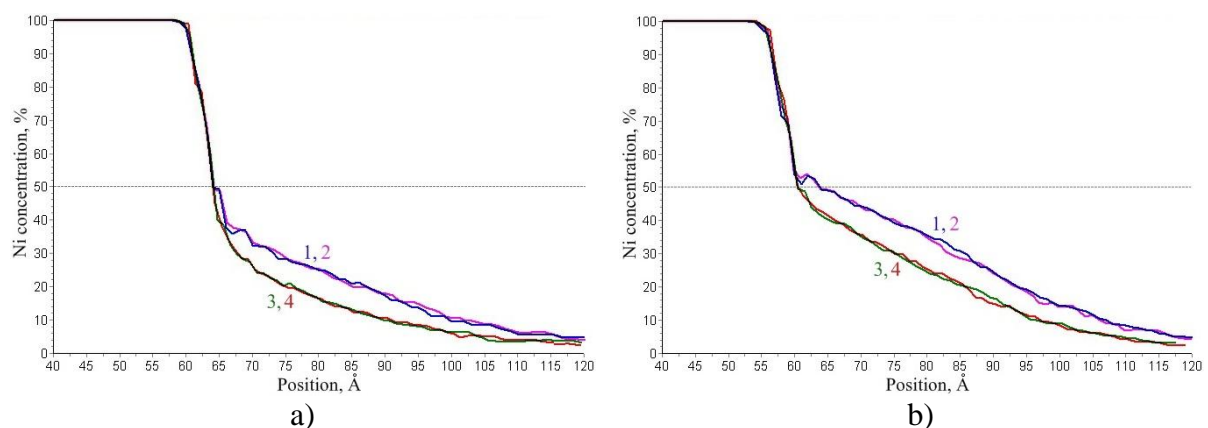


**Fig. 4.** Distribution of the concentration of Ni atoms in the computational cells: a) after 500 ps at a temperature of 1400 K; b) after 300 ps at a temperature of 1600 K. The numbers indicate the considered orientations: 1) (111):(111), 2) (111):(001), 3) (001):(001), 4) (001):(111)

The left parts, as can be seen, turned out to be identical and have no difference for all considered interphase boundary orientations. Also similar, as expected, were the results obtained for the same orientation of the boundary relative to the Ni lattice, but for different initial orientations of the Al lattice (1, 2 and 3, 4 in the figures). However, on the right part for the (111) and (001) orientations, the curves did not coincide: for the (111) orientation, in all cases, the concentration curves were located above the (001) curves, which primarily indicates an easier detachment of Ni atoms from the boundary with the orientation (111) and entrainment in aluminum compared to the (001) orientation. That is, with the (111) orientation, interdiffusion proceeds more intensively than with the (001) orientation.

A similar effect of the orientation of the interface is observed when the crystallization front moves in metals: crystallization from the interface, which has a relatively looser (001) orientation in the fcc lattice, moves 1.3-1.5 times faster than from the interface, which has the densest orientation (111) [15-18]. This behavior can be explained by the difference in the depth of potential wells in which atoms are located at the interface. Near the interface between metals in solid-liquid-phase contact, as well as at the liquid-crystal interface, the main role is played by the difference between the free energies of an atom near the interface in the liquid phase and "built-in" into the crystal boundary. This value can be compared with the energy of an adatom on the corresponding free surface of the crystal, or with the activation energy of its migration over the given surface. For example, using computer simulations, in [19] it was shown that the activation energy of diffusion of adatoms over the free (001) surface of fcc metals is almost two times higher than over the (111) surface.

#### 4. Conclusion

The method of molecular dynamics was used to study the influence of the orientation of the interphase boundary relative to the nickel crystal lattice on the intensity of interdiffusion at temperatures above the temperature of aluminum, that is, at solid-liquid-phase contact of metals. It was noticed that near the interphase boundary a small layer of aluminum with a thickness of two or three atomic planes remained in the crystalline state, repeating the nickel lattice, and therefore the boundary between the crystal and the liquid metal actually shifted deeper into the aluminum. In the process of interdiffusion and blurring of the boundary, this effect persisted, but with increasing temperature, the thickness of the crystalline layer near the boundary decreased.

For the considered orientations (111) and (001) of the interphase boundary with respect to the Ni lattice, the concentration curves were obtained after modeling interdiffusion at different temperatures. The parts of the curves responsible for the diffusion of Al atoms into crystalline Ni turned out to be similar for both orientations. However, the more sloping parts related to the diffusion of Ni atoms into liquid Al differed: diffusion of Ni atoms into Al proceeded more intensively at the (111) boundary orientation and slower with a relatively "loose" orientation (001), which, apparently, is due to the difference in the energies of the Ni atoms in the aluminum phase and those embedded in the boundary of crystalline nickel.

#### References

1. Miracle DB. The physical and mechanical properties of NiAl. *Acta Metallurgica et Materialia*. 1993;41(3): 649-684.
2. Westbrook JH, Fleischer RL. *Intermetallic Compounds: Structural Applications*. New York: Wiley; 2000.
3. Tresa P, Sammy T. Nickel-based superalloys for advanced turbine engines: chemistry, microstructure and properties. *Journal of Propulsion and Power*. 2006;22(2): 361-374.
4. Lima MSF, Ferreira PI. Microstructure and mechanical properties of Ni-Al and Ni-Al-B alloys produced by rapid solidification technique. *Intermetallics*. 1996;4(2): 85-90.

5. Rogachev AS, Shkodich NF, Vadchenko SG, Baras F, Kovalev DY, Rouvimov S, Nepapushev AA, Mukasyan AS. Influence of the high energy ball milling on structure and reactivity of the Ni + Al powder mixture. *Journal of Alloys and Compounds*. 2013;577: 600-605.
6. Celko L, Klakurkova L, Svejcar J. Diffusion in Al-Ni and Al-NiCr interfaces at moderate temperatures. *Defect and Diffusion Forum*. 2010;297-301: 771-777.
7. Sondermann E, Kargl F, Meyer A. Influence of cross correlations on interdiffusion in Al-rich Al-Ni melts. *Physical Review B*. 2016;93(18): 184201-184205.
8. Poletaev GM. Self-diffusion in liquid and solid alloys of the Ti-Al system: molecular-dynamics simulation. *Journal of Experimental and Theoretical Physics*. 2021;133(4): 455-460.
9. Poletaev GM, Bebikhov YuV, Semenov AS, Starostenkov MD. Self-diffusion in melts of Ni-Al and Ti-Al systems: molecular dynamics study. *Letters on Materials*. 2021;11(4): 438-441.
10. Purja Pun GP, Mishin Y. Development of an interatomic potential for the Ni-Al system. *Philosophical Magazine*. 2009;89(34-36): 3245-3267.
11. Levchenko EV, Ahmed T, Evteev AV. Composition dependence of diffusion and thermotransport in Ni-Al melts: A step towards molecular dynamics assisted databases. *Acta Materialia*. 2017;136: 74-89.
12. Poletaev GM, Zorya IV, Rakitin RY, Iliina MA. Interatomic potentials for describing impurity atoms of light elements in fcc metals. *Materials Physics and Mechanics*. 2019;42(4): 380-388.
13. Chen C, Zhang F, Xu H, Yang Z, Poletaev GM. Molecular dynamics simulations of dislocation-coherent twin boundary interaction in face-centered cubic metals. *Journal of Materials Science*. 2022;57: 1833-1849.
14. Poletaev GM, Zorya IV. Effect of light element impurities on the edge dislocation glide in nickel and silver: molecular dynamics simulation. *Journal of Experimental and Theoretical Physics*. 2020;131(3): 432-436.
15. Mendeleev MI, Zhang F, Song H, Sun Y, Wang CZ, Ho KM. Molecular dynamics simulation of the solid-liquid interface migration in terbium. *The Journal of Chemical Physics*. 2018;148(21): 214705.
16. Zhang HY, Liu F, Yang Y, Sun DY. The molecular dynamics study of vacancy formation during solidification of pure metals. *Scientific Reports*. 2017;7: 10241.
17. Mendeleev MI, Rahman MJ, Hoyt JJ, Asta M. Molecular-dynamics study of solid-liquid interface migration in fcc metals. *Modelling and Simulation in Materials Science and Engineering*. 2010;18(7): 074002.
18. Sun DY, Asta M, Hoyt JJ. Kinetic coefficient of Ni solid-liquid interfaces from molecular-dynamics simulations. *Physical Review B*. 2004;69(2): 024108.
19. Liu CL, Cohen JM, Adams JB, Voter AF. EAM study of surface self-diffusion of single adatoms of fcc metals Ni, Cu, Al, Ag, Au, Pd, and Pt. *Surface Science*. 1991;253(1-3): 334-344.

## THE AUTHORS

**Poletaev G.M.**

e-mail: gmpoletaev@mail.ru

ORCID: 0000-0002-5252-2455

**Rakitin R.Y.**

e-mail: [movehell@gmail.com](mailto:movehell@gmail.com)

ORCID: 0000-0002-6341-2761

### **Submission of papers:**

Manuscript should be submitted (**both MS Word and PDF**) by e-mail to: **mpmjournal@spbstu.ru**

After a confirmation of the paper acceptance, the authors should send the signed hard copy of the "Transfer of Copyright Agreement" form (available at <http://www.mpm.spbstu.ru> section "Authors") by regular post to "Materials Physics and Mechanics" editorial office:

*Periodicals Editorial Office, Institute of Advanced Manufacturing Technologies, Peter the Great St.Petersburg Polytechnic University, Polytechnicheskaya, 29, St.Petersburg 195251, Russia.*

The scanned copy of the signed "Transfer of Copyright Agreement" should be send by e-mail to: **mpmjournal@spbstu.ru**.

### **Filetype:**

Authors are invited to send their manuscripts **as MS Word file with PDF format copy**.

MS Word file should be prepared according to the general instructions bellow; we are kindly asking the authors to look through the detail instruction at: <http://www.mpm.spbstu.ru>.

### **Length:**

Papers should be limited to 30 typewritten pages (including Tables and Figures placed in the proper positions in the text).

### **Structure of the manuscript:**

**PAPER TITLE: CENTERED,**

**TIMES NEW ROMAN 14 BOLD, CAPITAL LETTERS**

**A.B. Firstauthor<sup>1</sup>, C.D. Secondauthor<sup>2\*</sup>** -Times New Roman 12, bold, centered

<sup>1</sup>Affiliation, address, country - Times New Roman 10, centered

\*e-mail: e-mail of the corresponding author - Times New Roman 10, centered

**Abstract.** Times New Roman 12 font, single line spacing. Abstract should not exceed 12 lines.

**Keywords:** please, specify paper keywords right after the abstract.

**Paper organization.** Use Times New Roman 12 font with single line spacing. Use *Italic* font in order to stress something; if possible, please, use **bold** for headlines only.

**Page numbering.** Please, do not use page numbering.

**Tables, Figures, Equations.** Please, see the sample file at <http://www.mpm.spbstu.ru> for more details.

### **References**

References should be subsequently numbered by Arabic numerals in square brackets, e.g. [1,3,5-9], following the sample style below:

[1] Koch CC, Ovid'ko IA, Seal S, Veprek S. *Structural Nanocrystalline Materials: Fundamentals and Applications*. Cambridge: Cambridge University Press; 2007.

[2] Hull D, Bacon DJ. *Introduction to Dislocations*. 5nd ed. Amsterdam: Butterworth-Heinemann; 2011 Available from: <https://www.sciencedirect.com/science/book/9780080966724?via%3Dihub> [Accessed 19th June 2018].

[3] Romanov AE, Vladimirov VI. Disclinations in crystalline solids. In: Nabarro FRN (ed.) *Dislocations in Solids*. Amsterdam: North Holland; 1992;9. p.191-402.

[4] Mukherjee AK. An examination of the constitutive equation for elevated temperature plasticity. *Materials Science and Engineering: A*. 2002;322(1-2): 1-22.

- [5] Soer WA, De Hosson JTM, Minor AM, Morris JW, Stach EA. Effects of solute Mg on grain boundary and dislocation dynamics during nanoindentation of Al–Mg thin films. *Acta Materialia*. 2004;52(20): 5783-5790.
- [6] Matzen ME, Bischoff M. A weighted point-based formulation for isogeometric contact. *Computer Methods in Applied Mechanics and Engineering*. 2016;308: 73-95. Available from: [doi.org/10.1016/j.cma.2016.04.010](https://doi.org/10.1016/j.cma.2016.04.010).
- [7] Joseph S, Lindley TC, Dye D. Dislocation interactions and crack nucleation in a fatigued near-alpha titanium alloy. To be published in *International Journal of Plasticity*. *Arxiv*. [Preprint] 2018. Available from: <https://arxiv.org/abs/1806.06367> [Accessed 19th June 2018].
- [8] Pollak W, Blecha M, Specht G. *Process for the production of molded bodies from silicon-infiltrated, reaction-bonded silicon carbide*. US4572848A (Patent) 1983.
- [9] Brogan C. *Experts build pulsed air rig to test 3D printed parts for low carbon engines*. Available from: <http://www.imperial.ac.uk/news/186572/experts-build-pulsed-test-3d-printed/> [Accessed 19th June 2018].

### **Правила подготовки статей:**

Рукопись (**английский язык, MS Word и копия PDF**) должна быть направлена в редакцию журнала по электронной почте: **mpmjournal@spbstu.ru**.

После подтверждения принятия статьи в печать, авторы должны отправить подписанные:

1. Соглашение о передаче авторских прав (<http://www.mpm.spbstu.ru>, раздел «Авторам»);
2. Экспертные заключения о том, что материалы статьи не содержат сведений, составляющих государственную тайну, и информацию, подлежащую экспортному контролю; по адресу:

*Россия, 195251, Санкт-Петербург, Политехническая, д. 29, Санкт-Петербургский политехнический университет Петра Великого, Институт передовых производственных технологий, Редакция периодических изданий.*

Скан-копии подписанных документов просим направить по электронной почте: **mpmjournal@spbstu.ru**

### **Тип файла:**

Редакция принимает **файлы MS Word с копией в формате PDF**. Статья должна быть подготовлена в соответствии с настоящей инструкцией, мы просим авторов также следовать более подробным инструкциям на сайте журнала <http://www.mpm.spbstu.ru> в разделе «Авторам».

### **Длина статьи:**

Статья не должна превышать 30 страниц формата А4, включая Таблицы и Рисунки, размещенные непосредственно в соответствующих местах.

### **Общие правила оформления статьи:**

**НАЗВАНИЕ СТАТЬИ: ВЫРОВНЯТЬ ПО ЦЕНТРУ,**

**ШРИФТ, TIMES NEW ROMAN 14 BOLD, ЗАГЛАВНЫЕ БУКВЫ**

Автор(ы): **А.Б. Первыйавтор<sup>1</sup>, В.Г. Автор<sup>2\*</sup>** - шрифт Times New Roman 12, bold, по центру

<sup>1</sup>Наименование организации, адрес, страна - шрифт Times New Roman 10, по центру

\* e-mail автора, представившего статью - шрифт Times New Roman 10, по центру

**Аннотация.** Аннотация статьи составляет не более 12 строк. Используйте шрифт Times New Roman 12, одинарный межстрочный интервал.

**Ключевые слова:** укажите ключевые слова после аннотации.

**Как организовать текст статьи.** Используйте шрифт Times New Roman 12, одинарный межстрочный интервал. При необходимости выделить какую-либо информацию используйте *курсив*. Используйте **полужирный** шрифт только для заголовков и подзаголовков.

**Номера страниц.** Пожалуйста, не используйте нумерацию страниц

**Таблицы, Рисунки, Уравнения.** Подробные правила оформления данных элементов статьи приведены в инструкции на сайте журнала <http://www.mpm.spbstu.ru>

### **Литература**

Ссылки приводятся в тексте в квадратных скобках [1,3,5-9]. Стиль оформления ссылок:

[1] Koch CC, Ovid'ko IA, Seal S, Veprek S. *Structural Nanocrystalline Materials: Fundamentals and Applications*. Cambridge: Cambridge University Press; 2007.

[2] Hull D, Bacon DJ. *Introduction to Dislocations*. 5nd ed. Amsterdam: Butterworth-Heinemann; 2011 Available from: <https://www.sciencedirect.com/science/book/9780080966724?via%3Dihub> [Accessed 19th June 2018].

[3] Romanov AE, Vladimirov VI. Disclinations in crystalline solids. In: Nabarro FRN (ed.) *Dislocations in Solids*. Amsterdam: North Holland; 1992;9. p.191-402.

[4] Mukherjee AK. An examination of the constitutive equation for elevated temperature plasticity. *Materials Science and Engineering: A*. 2002;322(1-2): 1-22.

- [5] Soer WA, De Hosson JTM, Minor AM, Morris JW, Stach EA. Effects of solute Mg on grain boundary and dislocation dynamics during nanoindentation of Al–Mg thin films. *Acta Materialia*. 2004;52(20): 5783-5790.
- [6] Matzen ME, Bischoff M. A weighted point-based formulation for isogeometric contact. *Computer Methods in Applied Mechanics and Engineering*. 2016;308: 73-95. Available from: [doi.org/10.1016/j.cma.2016.04.010](https://doi.org/10.1016/j.cma.2016.04.010).
- [7] Joseph S, Lindley TC, Dye D. Dislocation interactions and crack nucleation in a fatigued near-alpha titanium alloy. To be published in *International Journal of Plasticity*. *Arxiv*. [Preprint] 2018. Available from: <https://arxiv.org/abs/1806.06367> [Accessed 19th June 2018].
- [8] Pollak W, Blecha M, Specht G. *Process for the production of molded bodies from silicon-infiltrated, reaction-bonded silicon carbide*. US4572848A (Patent) 1983.
- [9] Brogan C. *Experts build pulsed air rig to test 3D printed parts for low carbon engines*. Available from: <http://www.imperial.ac.uk/news/186572/experts-build-pulsed-test-3d-printed/> [Accessed 19th June 2018].

# МЕХАНИКА И ФИЗИКА МАТЕРИАЛОВ

48 (3) 2022

Учредители: Санкт-Петербургский политехнический университет Петра Великого,

Институт проблем Машиноведения Российской академии наук

Издание зарегистрировано федеральной службой по надзору в сфере связи,  
информационных технологий и массовых коммуникаций (РОСКОМНАДЗОР),

свидетельство ПИ №ФС77-69287 от 06.04.2017 г.

## Редакция журнала

Профессор, д.т.н., академик РАН, А.И. Рудской – главный редактор

Профессор, д.ф.-м.н., член-корр. РАН, Д.А. Индейцев – главный редактор

Профессор, д.ф.-м.н. И.А. Овидько (1961 - 2017) – основатель и почетный редактор

Профессор, д.ф.-м.н. А.Л. Колесникова – ответственный редактор

Доцент, к.т.н. А.С. Немов – ответственный редактор

А.Ю. Ромашкина, к.т.н. – выпускающий редактор

Л.И. Гузилова – редактор, корректор

## Телефон редакции

+7(812)552 77 78, доб. 224

E-mail: [mpmjournal@spbstu.ru](mailto:mpmjournal@spbstu.ru)

Компьютерная верстка А.Ю. Ромашкина

---

Подписано в печать 29.07.2022 г. Формат 60x84/8. Печать цифровая  
Усл. печ. л. 10,0. Тираж 100. Заказ \_\_\_\_.

---

Отпечатано с готового оригинал-макета, предоставленного автором  
в Издательско-полиграфическом центре Политехнического университета Петра  
Великого. 195251, Санкт-Петербург, Политехническая ул., 29.  
Тел.: +7(812)552 77 78, доб. 224.

- Effect of Si<sup>+</sup> ion irradiation of  $\alpha$ -Ga<sub>2</sub>O<sub>3</sub> epitaxial layers on their hydrogen sensitivity .....301-307**  
N.N. Yakovlev, A.V. Almaev, P.N. Butenko, A.N. Mikhaylov, A.I. Pechnikov, S.I. Stepanov,  
R.B. Timashov, A.V. Chikiryaka, V.I. Nikolaev
- Non-equilibrium phonon gas in a chalcogenide semiconductor with exponential temperature dependence of conductivity.....308-314**  
K.D. Mynbaev, N.V. Sovtus
- Optimization of powder metallurgy process parameters to enhance the mechanical properties of AZ91 magnesium alloy .....315-327**  
Naveen Kumar, Ajaya Bharti
- A study on mechanical and dielectric properties of B<sub>4</sub>C and Al dispersed single-layered epoxy-based polymer composites fabricated through molding and curing route.....328-341**  
S. Vignesh, J.T. Winowlin Jappes, S. Nagaveena, K. Sankaranarayanan, R. Krishna Sharma, N.C. Brintha
- Comparison of mechanical strain measurement accuracy of fiber-optic sensor and smart-layer .....342-354**  
G.S. Shipunov, M.A. Baranov, A.S. Nikiforov, F.R. Khabibrakhmanova
- Deformation and mechanical stresses in a magnet with thin-walled quasi-force-free winding.....355-366**  
G.A. Shneerson, A.V. Khlybov, A.A. Belov, A.P. Nenashev, A.A. Parfentiev, S.A. Shimanskiy
- Preparation and characterization of undoped and antimony doped tin oxide thin films synthesized by spray pyrolysis.....367-378**  
H. Habieb, N. Hamdadou
- On the problem of evaluating the behavior of multicomponent materials in mixed boundary conditions in contact problems.....379-385**  
V.A. Babeshko, O.V. Evdokimova, O.M. Babeshko
- The nanofluids' viscosity prediction through particle-media interaction layer .....386-396**  
V.V. Syzrantsev, A.T. Arymbaeva, A.P. Zavjalov, K.V. Zobov
- Study numerical and experimental of stress concentration factor on isotropic plate with hole .....397-406**  
M.N. Misbah, R.C. Ariesta, T. Yulianto, D. Setyawan, W.H.A. Putra
- An out-of-plane oscillating beam nanoresonator with ultrahigh intrinsic quality factor ...407-418**  
Chu Manh Hoang, Nguyen Van Duong, Dang Van Hieu
- Ab initio calculations of electronic band structure of ideal and defective CdMnS.....419-427**  
Matanat A. Mehrabova, Natig T. Panahov, Niyazi H. Hasanov
- Seismic behavior of heritage building with isotropic and orthotropic material properties: a comparative analysis.....428-442**  
Kamran, Shakeel Ahmad, Rehan A. Khan
- Calculation of the stress level in modeling the inter-dislocation interaction of aluminum bronze .....443-451**  
A.Yu. Nikonov, A.A. Bibko, D.V. Lychagin
- Influence of Ni-Al interphase boundary orientation on the interdiffusion rate at temperatures above aluminum melting point: a molecular dynamics study.....452-458**  
G.M. Poletaev, R.Y. Rakitin